



McFarlane, Andrew Robert (2012) *The application of inelastic neutron scattering to investigate methane reforming catalysts*. PhD thesis.

<http://theses.gla.ac.uk/4098/>

Copyright and moral rights for this thesis are retained by the author

A copy can be downloaded for personal non-commercial research or study, without prior permission or charge

This thesis cannot be reproduced or quoted extensively from without first obtaining permission in writing from the Author

The content must not be changed in any way or sold commercially in any format or medium without the formal permission of the Author

When referring to this work, full bibliographic details including the author, title, awarding institution and date of the thesis must be given

The Application of Inelastic Neutron Scattering to Investigate Methane Reforming Catalysts



Andrew Robert McFarlane

School of Chemistry

University of Glasgow

Submitted in fulfilment of the requirements for the degree of

Doctor of Philosophy

I declare that, except where due reference is made, that this thesis for the degree of Doctor of Philosophy is my own work and has not been submitted for any other degree at this institution or elsewhere.

Andrew Robert McFarlane
University of Glasgow
September 2012

*And above all, give me the humility,
Which will make me,
Not proud of what I have discovered,
But concious of what I do not know,*

W. Barclay

Acknowledgements

First and foremost, I would like to thank my supervisor David Lennon for giving me the opportunity to work on this project. His guidance (especially during many morning running sessions) and his belief in me over the last five years has been incredible and it has been a privilege to work under his supervision.

Secondly, I am extremely grateful to Stewart Parker for all he has taught me, especially with regards to neutrons, and for always being the optimist when it came to assigning peaks in my spectra. I'll be back down to the Cherry Tree soon.

Special thanks also goes to Ian Silverwood. His patience with me when explaining and teaching all things spectroscopic was second to none, as was his knowledge of Oxford pubs, a portion of which I have hopefully passed on.

I also want to thank everybody in the lab for their help and friendship including Neil, Liam, Robbie, Clement (careful with that Transit, it's a rental!), Lauren (I really want that Jack Wills bedding) and June. Liam, we'll always have America, and Robbie, that night at ISIS was unforgettable!

Colin How and Jim Gallagher are also thanked for all their help with the TEM studies. Outside of work I'd like to thank my Mum and Dad for bankrolling me thus far and for making me do my homework for all these years, it seems it might have actually paid off.

Lastly, I wish to thank my wonderful wife Kirsty, for her constant love, friendship and understanding, and for bringing our lovely daughter Izzy into the world. Her big smiles when I get home make the lack of sleep worth while!

Thank you all.

Abstract

Hydrocarbonaceous overlayers formed on a range of nickel alumina and gold-doped nickel alumina catalysts during both the H₂O and CO₂ reforming of methane has been examined using a number of techniques including thermal studies, XRD, TEM IR and Raman spectroscopy. These techniques have allowed both qualitative and quantitative analysis of the carbon and hydrogen components of coke to be achieved. Both amorphous carbon and filamentous carbon has been observed. Results show that changing the catalyst preparation routine effects the morphology of the carbon in both the CO₂ and H₂O reforming reactions. The “dry” and steam reforming reactions were also studied by inelastic neutron scattering. This technique has permitted quantitative measurements of the extent of hydrogen retention for the first time and has allowed elementary steps associated with the reaction to be explored from a new perspective.

As well as determining the nature and quantity of the hydrocarbonaceous overlayers, the source of the coke has also been considered in the CO₂ reforming reaction. Isotopic substitution reactions have been employed to achieve this. Temperature programmed oxidation measurements using a ¹³CO₂ feedstream identify a clear role for the oxidant in the carbon retention process.

The combination of techniques outlined above has permitted a series of elementary reactions to be proposed for both reforming reactions. Elementary surface reactions involving hydrogen are shown to be fast and efficient compared to those involving carbon. Furthermore, oxidation of carbon to CO is slower than that of carbon polymerisation. These statements are true for both CO₂ and H₂O reforming and suggest the CO₂ reforming reaction has the potential to represent a en-

environmentally friendly alternative to the industrially preferred steam reforming process.

As well as increasing the understanding of these two highly relevant reaction systems, a range of inelastic neutron scattering reactors have been designed, built and tested under reforming conditions in order to accomplish the quantitative hydrogen measurements. An evaluation of these reactors, as well as a description of the development of the INS technique as a quantitative tool is given.

Contents

Contents	v
List of Figures	ix
List of Tables	xvi
Nomenclature	xvii
1 Introduction	1
1.1 Reforming of Methane	1
1.1.1 CO ₂ Reforming of Methane	2
1.1.2 Steam Reforming of Methane	5
1.1.3 Carbon Deposition in Methane Reforming	6
1.1.4 Gold Doping in Ni/Al ₂ O ₃ Reforming Catalysts	8
1.2 Techniques	9
1.2.1 Vibrational Spectroscopy	10
1.2.1.1 Infrared Spectroscopy	10
1.2.1.2 Fourier Transform Spectrometry	11
1.2.1.3 Transmission Infrared Spectroscopy	15
1.2.1.4 Diffuse Reflectance Infrared Spectroscopy	15
1.2.1.5 Raman Spectroscopy	16
1.2.1.6 Inelastic Neutron Scattering (INS)	18
1.2.2 X-ray Diffraction	22
1.2.3 Transmission Electron Microscopy	23

2	Experimental and Development of Inelastic Neutron Scattering Technique for Analysis of Heterogeneous Catalyst Samples	25
2.1	Experimental	25
2.1.1	Catalyst Preparation	25
2.1.1.1	Catalysts Resulting in Amorphous Carbon For- mation	26
2.1.1.2	Catalysts Resulting in Filamentous (Graphitic) Carbon Formation	27
2.1.2	Microreactor Rig and Reactor Design	27
2.1.3	Microreactor Conditions	30
2.1.3.1	CO ₂ Reforming	30
2.1.3.2	H ₂ O Reforming	32
2.1.4	Inelastic Neutron Experiments	32
2.1.4.1	CO ₂ Reforming	33
2.1.4.2	H ₂ O Reforming	35
2.1.5	Post-reaction Analysis of Microreactor and INS Samples .	36
2.2	INS Reaction Testing Apparatus	38
2.3	Reactor Designs	42
2.3.1	Stainless Steel U-Tube	42
2.3.2	Inconel [®] Reactor	44
2.3.3	Quartz U-Tube Reactor	46
2.4	Performance Results	48
2.5	Discussion of Performance and Challenges	53
2.6	Calibration and Quantification of Hydrogen Modes	55
2.6.1	Development of Method and Calibration of INS Spectrometer	55
2.6.1.1	Experimental	56
2.6.1.2	Discussion	60
3	CO₂ Reforming of Methane	61
3.1	Amorphous Carbon Characterisation	62
3.1.1	Results	62
3.1.1.1	Microreactor Studies	62
3.1.1.2	Inelastic Neutron Scattering Measurements, TOSCA	68

CONTENTS

3.1.1.3	Inelastic Neutron Scattering Measurements, MAPS	71
3.1.1.4	Post-reaction Temperature Programmed Oxidation of INS Samples	78
3.1.1.5	Post-Reaction Raman scattering and Infrared spectroscopy	80
3.1.1.6	Post Reaction Transmission Electron Microscopy (TEM) and X-ray Diffraction (XRD)	84
3.1.2	Discussion	88
3.2	Graphitic Carbon Characterisation	92
3.2.1	Results	93
3.2.1.1	Microreactor Studies	93
3.2.1.2	INS Sample Preparation, Carbon Analysis and INS Measurements for Ni/Al ₂ O ₃	105
3.2.1.3	Isotopic Substitution Experiments	122
3.2.2	Discussion	127
4	Steam Reforming of Methane	131
4.1	Amorphous Carbon Characterisation	133
4.1.1	H ₂ O Calibration	133
4.1.2	Microreactor Results	136
4.1.3	Inelastic Neutron Scattering Measurements	141
4.1.4	Post INS Characterisation	148
4.1.4.1	Raman	148
4.1.4.2	X-ray Diffraction Measurements	151
4.1.4.3	Transmission Electron Microscopy	153
4.2	Discussion	153
4.3	Graphitic Carbon Characterisation	156
4.3.1	Results	157
4.3.1.1	Microreactor Studies	157
4.3.1.2	Inelastic Neutron Scattering Results	160
4.3.2	Discussion	176
4.4	High Temperature INS Steam Reforming	177
4.4.1	Results	178

CONTENTS

4.4.1.1	Microreactor Studies	178
4.4.1.2	Inelastic Neutron Scattering Studies	181
4.4.2	Discussion	183
5	Conclusions and Future Work	184
	References	187

List of Figures

1.1	Schematic of an Interferometer	12
1.2	Constructive and destructive interference patterns that result from varying path length	13
1.3	Possible interactions between IR radiation and sample	14
1.4	Schematic of diffuse reflectance technique	15
1.5	Raman scattering energy diagram	17
1.6	Stokes, Rayleigh and Anti-Stokes Bands	17
1.7	Schematic of the TOSCA spectrometer	20
1.8	Schematic of the MAPS spectrometer	21
1.9	Schematic of the MERLIN spectrometer	22
1.10	K-shell x-ray fluorescence	24
2.1	Schematic of Microreactor Apparatus	28
2.2	Calibration of mass spectrometer response (Mass 44) to known quantities of graphite	31
2.3	Picture of ISIS gas handling system	39
2.4	Schematic of ISIS catalyst preparation arrangement	40
2.5	Schematic of stainless steel U-tube reactor	43
2.6	Schematic of Inconel [®] reactor cell	44
2.7	Picture of assembled Inconel [®] reactor	45
2.8	Picture of assembled Inconel [®] reactor	45
2.9	Picture of high temperature quartz reactor	47
2.10	Picture of quartz reactor in furnace	48
2.11	Medium energy INS spectra (2017cm ⁻¹)	49
2.12	High energy INS spectra (4840cm ⁻¹)	50

LIST OF FIGURES

2.13	INS spectra of the $\nu(\text{C-H})$ and (O-H) region for different known masses of polystyrene	57
2.14	Best linear fit of INS peak area against known sample mass of polystyrene	58
2.15	INS spectra of the $\nu(\text{C-H})$ and $\nu(\text{O-H})$ region for different known masses of brucite	59
2.16	Best linear fit of INS peak area against known sample mass of brucite	60
3.1	Temperature-programmed reaction (500 - 1300 K) of a 2:1 mixture of CH_4 and CO_2 over $\text{Ni}/\text{Al}_2\text{O}_3$ catalyst	62
3.2	Temperature-programmed reaction (500 - 1300 K) of a 2:1 mixture of CH_4 and CO_2 over $\text{Ni-Au}/\text{Al}_2\text{O}_3$ catalyst	63
3.3	Extended reaction at 1073 K of a 2:1 mixture of CH_4 and CO_2 over $\text{Ni}/\text{Al}_2\text{O}_3$ catalyst	64
3.4	Extended reaction at 1073 K of a 2:1 mixture of CH_4 and CO_2 over $\text{Ni-Au}/\text{Al}_2\text{O}_3$ catalyst	65
3.5	Temperature-programmed oxidation profile for $\text{Ni}/\text{Al}_2\text{O}_3$ after isothermal micro-reactor runs at 1073 K.	66
3.6	Temperature-programmed oxidation profile for $\text{Ni-Au}/\text{Al}_2\text{O}_3$ after isothermal micro-reactor runs at 1073 K.	67
3.7	TOSCA INS spectrum of the alumina support after 6 hours reaction of a 2:1 mixture of CH_4 and CO_2 at 1073 K	68
3.8	TOSCA INS spectrum of the $\text{Ni}/\text{Al}_2\text{O}_3$ catalyst after 6 hours reaction of a 2:1 mixture of CH_4 and CO_2 at 1073 K	69
3.9	TOSCA INS spectrum of the $\text{Ni-Au}/\text{Al}_2\text{O}_3$ catalyst after 6 hours reaction of a 2:1 mixture of CH_4 and CO_2 at 1073 K	70
3.10	MAPS Mitre plot of Low energy-transfer INS spectra of post reaction $\text{Ni}/\text{Al}_2\text{O}_3$	72
3.11	MAPS High energy-transfer INS spectra	73
3.12	MAPS Medium energy-transfer INS spectra	75
3.13	MAPS Low energy-transfer INS spectra	76
3.14	Temperature-programmed oxidation profile for $\text{Ni}/\text{Al}_2\text{O}_3$ INS runs after 6 hours reaction at 1073 K	78

LIST OF FIGURES

3.15	Temperature-programmed oxidation profile for Ni/Al ₂ O ₃ INS runs after 6 hours reaction at 1073 K	79
3.16	Raman spectra of Ni/Al ₂ O and Ni-Au/Al ₂ O catalysts after reaction and INS measurement	81
3.17	Transmission IR spectra of Ni/Al ₂ O (b) Ni-Au/Al ₂ O catalysts after reaction and INS measurement	83
3.18	TEM of Ni/Al ₂ O post INS reaction.	85
3.19	TEM of Ni-Au/Al ₂ O post INS reaction.	86
3.20	Powder XRD patterns of post-reaction (a) Ni/Al ₂ O and (b) Ni-Au/Al ₂ O catalyst samples	87
3.21	Temperature-programmed reduction profile (400 - 1000 K) for Ni/Al ₂ O ₃ catalyst.	94
3.22	Temperature-programmed reduction profile (400 - 1000 K) for Ni-Au/Al ₂ O ₃ catalyst	95
3.23	Temperature-programmed reaction profile (350 - 1150 K) for Ni/Al ₂ O ₃ catalyst	96
3.24	Temperature-programmed reaction profile (350 - 1150 K) for Ni-Au/Al ₂ O ₃ catalyst	97
3.25	Isothermal reaction profile at 898 K of a 1:1 mixture of CH ₄ and CO ₂ over Ni/Al ₂ O ₃ catalyst	99
3.26	Isothermal reaction profile at 898 K of a 1:1 mixture of CH ₄ and CO ₂ over Ni-Au/Al ₂ O ₃ catalyst	100
3.27	Temperature-programmed oxidation profile for Ni/Al ₂ O ₃ catalyst post reaction at 898 K	101
3.28	Temperature-programmed oxidation profile for Ni-Au/Al ₂ O ₃ catalyst post reaction at 898 K	102
3.29	Temperature programmed hydrogenation profile for Ni/Al ₂ O ₃ catalyst after 3 hours reaction of a 1:1 mixture of CH ₄ and CO ₂ at 898 K	103
3.30	Temperature programmed hydrogenation profile for Ni-Au/Al ₂ O ₃ catalyst after 3 hours reaction of a 1:1 mixture of CH ₄ and CO ₂ at 898 K.	104

LIST OF FIGURES

3.31 Isothermal reaction profile at 898 K of a 1:1 mixture of CH ₄ and CO ₂ over Ni-Au/Al ₂ O ₃ catalyst	106
3.32 Temperature-programmed oxidation profile for Ni/Al ₂ O ₃ catalyst after 3 hours reaction of a 1:1 mixture of CH ₄ and CO ₂ at 898 K in the INS Inconel [®] reactor	108
3.33 High energy transfer INS spectrum of reacted Ni/Al ₂ O ₃ after 6 hours reaction of a 1:1 mixture of CH ₄ and CO ₂ at 898 K	110
3.34 Medium energy transfer INS spectrum of reacted Ni/Al ₂ O ₃ after 6 hours reaction of a 1:1 mixture of CH ₄ and CO ₂ at 898 K	112
3.35 Low energy transfer INS spectrum of reacted Ni/Al ₂ O ₃ after 6 hours reaction of a 1:1 mixture of CH ₄ and CO ₂ at 898 K	113
3.36 Powder X-ray diffraction pattern of Ni/Al ₂ O ₃ recorded after reaction and INS measurement	115
3.37 Transmission electron micrographs of Ni/Al ₂ O ₃ recorded after reaction and INS measurement	116
3.38 Colour-coded energy map transmission electron micrograph of Ni/Al ₂ O ₃ recorded after reaction and INS measurement	117
3.39 UV-vis spectra of Ni/Al ₂ O ₃ as received, Ni/Al ₂ O ₃ post dry reforming reaction and Barium sulphate	119
3.40 Raman measurement of post INS reaction Ni/Al ₂ O ₃ catalyst, 325nm laser	120
3.41 Raman measurement of post INS reaction Ni/Al ₂ O ₃ catalyst, 532nm laser	121
3.42 Isothermal reaction profile at 898 K of a 1:1 mixture of ¹² C ¹ H ₄ and ¹³ C ¹⁶ O ₂ over Ni/Al ₂ O ₃ catalyst.	124
3.43 Temperature-programmed oxidation profile for Ni/Al ₂ O ₃ catalyst after 1.5 hours isothermal run at 898 K of a 1:1 mixture of (a) ¹² C ¹ H ₄ and ¹³ C ¹⁶ O ₂ and (b) ¹² C ¹ H ₄ and ¹² C ¹⁶ O ₂ over Ni/Al ₂ O ₃ catalyst	126
3.44 Schematic diagram illustrating some of the main reactions active during the “dry” reforming of methane and the formation of filamentous carbon.	130

LIST OF FIGURES

4.1	Mass 18 (H ₂ O) response of oxidation of varying known flow rates of H ₂ in O ₂	134
4.2	Average mass 18 (H ₂ O) response vs H ₂ O flow rate	135
4.3	Variation of H ₂ O flow rate (based on mass 18 (H ₂ O) response)	136
4.4	Temperature programmed reaction for steam reforming over 45 wt % Ni/Al ₂ O ₃ catalyst	137
4.5	Isothermal reaction for steam reforming at 893 K over 45 wt % Ni/Al ₂ O ₃ catalyst	138
4.6	Temperature programmed oxidation of catalyst after extended isothermal reaction at 893 K (Figure 4.5)	139
4.7	Mass 15 (methane) Temperature programmed hydrogenation of catalyst after extended isothermal reaction at 893 K	140
4.8	Extended reaction at 893 K of 18 sccm CH ₄ and 30 sccm H ₂ O over reduced Ni/Al ₂ O ₃ catalyst	141
4.9	Extended reaction at 893 K of 5.6 CH ₄ and 30 H ₂ O over reduced Ni/Al ₂ O ₃ catalyst	142
4.10	INS spectra of catalyst (a) after reduction (b) after reaction (INS18) (c) after hydrogenation (INS18H) of reaction-deposited layer recorded with incident neutron energy of 4840 cm ⁻¹	144
4.11	Subtracted INS spectra of catalyst overlayers recorded with incident neutron energy of 4840 cm ⁻¹ (a) after reaction (INS18) and (b) after hydrogenation INS18H of reaction-deposited layer	145
4.12	INS spectra of catalyst (a) after reduction (b) after reaction (c) after hydrogenation of reaction-deposited layer recorded with incident neutron energy of 2017 cm ⁻¹	147
4.13	Diffuse reflectance UV-Vis spectra of samples after (a) reaction at low methane flow (INS6) and (b) reaction at high methane flow followed by hydrogen treatment (INS18H)	149
4.14	Raman spectra of catalyst after (a) reaction at low methane flow (INS6) and (b) reaction at high methane flow followed by hydrogen treatment (INS18H).	150
4.15	UV-Raman spectra of (a) KBr diluent, (b) catalyst after reaction with low methane flow (INS6), and (c) glucose reference	151

LIST OF FIGURES

4.16 X ray diffraction pattern for the catalysts (a) as received, (b) INS6 post reaction, (c) INS18 hydrogenated in the microreactor post-reaction and (d) INS18H after reduction, reaction and hydrogen treatment	152
4.17 Transmission Electron Micrograph of INS6 after reduction and re-action at low methane flow	154
4.18 Transmission Electron Micrograph of INS18 after reduction, reac-tion and hydrogen treatment	155
4.19 Temperature-programmed reaction (500 - 1200 K) of a 1:1 mixture of CH ₄ and H ₂ O over reduced Ni/Al ₂ O ₃ catalyst	158
4.20 Extended microreactor reaction at 898 K of a 1:1 mixture of CH ₄ and H ₂ O over reduced Ni/Al ₂ O ₃ catalyst.	159
4.21 Temperature-programmed oxidation profile for Ni/Al ₂ O ₃ catalyst post reaction at 898 K	161
4.22 Extended reaction at 898 K of a 1:1 mixture of CH ₄ and H ₂ O over reduced Ni/Al ₂ O ₃ catalyst.	162
4.23 Temperature-programmed oxidation profile for Ni/Al ₂ O ₃ catalyst post INS reaction at 898 K	164
4.24 High energy transfer INS spectrum of reacted Ni/Al ₂ O ₃	166
4.25 Medium energy transfer INS spectrum of reacted Ni/Al ₂ O ₃	167
4.26 UV-vis spectra of (red) Ni/Al ₂ O ₃ as received, (blue)Ni/Al ₂ O ₃ post steam reforming reaction and (black) Barium sulphate	169
4.27 Raman measurement of post INS reaction Ni/Al ₂ O ₃ catalyst, 532nm laser	170
4.28 Raman measurement of (a) post INS reaction Ni/Al ₂ O ₃ catalyst and (b) reduced Ni/Al ₂ O ₃ , 325nm laser	171
4.29 Powder X-ray diffraction pattern of Ni/Al ₂ O ₃ recorded (a) after reduction and (b) after reaction and INS measurement	173
4.30 Transmission electron micrographs of Ni/Al ₂ O ₃ recorded after re-action and INS measurement	174
4.31 Colour-coded energy map transmission electron micrograph of Ni/Al ₂ O ₃ recorded after reaction and INS measurement	175

LIST OF FIGURES

4.32	Extended reaction at 1123 K of a 1:1 mixture of CH ₄ and H ₂ O over reduced Ni/Al ₂ O ₃ catalyst	179
4.33	Temperature-programmed oxidation profile for Ni/Al ₂ O ₃ catalyst post reaction at 1123 K	180
4.34	High energy transfer INS spectrum of reacted Ni/Al ₂ O ₃ (1123 K)	182

List of Tables

2.1	Summary of the catalysts used in this project	26
2.2	Summary of INS Vibrational Assignments Pre and Post Methanol Adsorption	52
3.1	Summary of the TOSCA INS Vibrational Assignments Pre and Post Methane Reforming	71
3.2	Summary of the MAPS INS Vibrational Assignments Pre and Post Methane Reforming	74
3.3	Carbon and hydrogen retention values for Ni/Al ₂ O ₃ post micro-reactor and INS CO ₂ reforming.	77
3.4	Carbon and hydrogen retention values for Ni-Au/Al ₂ O ₃ post micro-reactor and INS CO ₂ reforming.	77
3.5	Summary of the Raman and Infrared Vibrational Assignments Post Methane Reforming for Ni/Al ₂ O ₃ and Ni-Au/Al ₂ O ₃	84
3.6	Carbon and hydrogen retention values for Ni/Al ₂ O ₃ post micro-reactor and INS CO ₂ reforming.	107
3.7	Summary of the MAPS INS Vibrational Assignments Post Methane Reforming	114
3.8	Summary of the Raman Vibrational Assignments Post Methane Reforming	123
4.1	Carbon and hydrogen retention values for post H ₂ O reforming at a 2:1 steam to methane ratio.	146
4.2	Summary of the INS Vibrational Assignments Pre and Post Methane Steam Reforming	148

LIST OF TABLES

4.3	Carbon and hydrogen retention values for Ni/Al ₂ O ₃ post micro-reactor and INS CO ₂ reforming.	168
4.4	Summary of the INS Vibrational Assignments Pre and Post Methane Steam Reforming	168
4.5	Summary of the Raman Vibrational Assignments Post Methane Reforming	172
5.1	Summary of the Ni/Al ₂ O ₃ C : H ratios for dry and steam reforming systems which lead to amorphous and graphitic carbon deposition. Microreactor TPO values are also given.	185

Chapter 1

Introduction

1.1 Reforming of Methane

The supply of oil is one of the most important factors to both the current and future world order. This is not simply due to its use as a fuel, but also as a precursor to fine chemicals and plastics. Its value really cannot be overstated. As energy consumption in the developing world grows, so too does the demand for oil. It is well known however, that stocks are dwindling and prices are increasingly unstable. Currently, it is estimated that there is around 1.4 billion barrels of oil proven - only enough to last between 45 and 50 years of consumption at current rates [1]. Much of this includes non-traditional sources of oil such as tar sands, and some care needs to be taken when discussing the supply in terms of time as it does not take into account fluctuations in consumption or crude price versus extraction price. Nonetheless, it has become vital to secure alternative energy sources and chemical feed-stocks that do not rely on sources of oil. Possible candidates currently under investigation for replacing traditional oil include Liquefied Petroleum Gas (LPG), ethanol, biofuels and hydrogen [2].

The relative abundance of natural gas makes the reforming of methane into a chemical feedstock and fuel a very interesting prospect [3][1][4]. Methane is a greenhouse gas and is sometimes burned at the source as flare gas to make H_2O and CO_2 (also a greenhouse gas but to a lesser extent). However, for methane to be utilised to its fullest potential it can be converted to syngas (CO and H_2),

which is then able to be reacted further to make more valuable compounds or used as a direct energy source via the hydrogen produced [5]. Examples of these further reactions are the polymerisation of CO to make C_nH_n longer chain hydrocarbons either with the Fischer-Trøpsch reaction [6] or the Mobil process (via methanol) [7]. Syngas can also be used in ammonia synthesis [8]. There are a number of different ways to convert CH_4 to syngas including oxidation with CO_2 (“dry” reforming) or H_2O (steam reforming) and catalytic partial oxidation (CPOX). It is the first two examples that are the focus of this work.

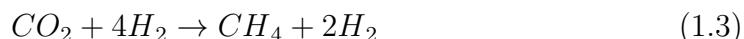
1.1.1 CO_2 Reforming of Methane

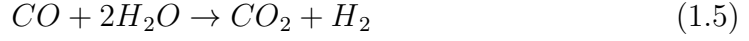
Using CO_2 as the oxidant in methane reforming has environmental benefits as both reactants are undesirable greenhouse gasses. Being able to react both of these species on a commercial scale into something more valuable is a very interesting prospect. Furthermore, the synthesis gas produced has a lower $H_2:CO$ ratio which is more suited to Fischer-Trøpsch synthesis [6][9]. Another possible application of CO_2 reforming is the production of hydrogen from biomass gasification [10][11].

In principle, the chemical equation for the dry reforming reaction is inherently simple (equation 1.1)



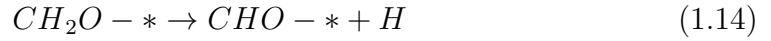
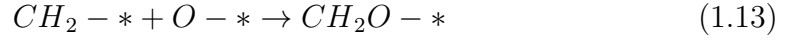
In practice however, there are a large number of elementary reactions and competing side reactions which can result in decreased syngas yields, varying CO : H_2 ratios and catalyst deactivation over extended periods of time. Cui et al and Froment are among those that have outlined the following side reactions [12][13]:



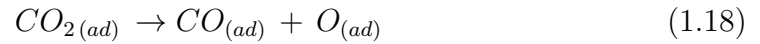


These include the Boudouard reaction (equation 1.2), methanation reactions (equations 1.3 and 1.4), water-gas shift / reverse water-gas shift reactions (equations 1.6 and 1.5) and methane cracking (equation 1.7). As well as potential side reactions, the reforming reaction itself can be broken down into a number of elementary reactions, which again increases the level of complexity. Firstly, methane has to dissociate in order to be able to recombine to form products. The loss of the first hydrogen from methane to CH_3 and H (equation 1.9) is well documented in the literature as rate limiting step [5]. Further dissociation of the methane is then thought to occur either by complete stepwise loss of hydrogen to $C_{(ad)}$ and $4H_{(ad)}$ (equations 1.8 - 1.12), or possibly via an oxygen insertion step at an intermediate point in the dissociation process (equations 1.13 and 1.14). If the complete dissociation route occurs, then C_{ad} will combine with adsorbed oxygen from the oxidant to give CO (equations 1.15 - 1.26) (Surface sites are denoted by *)



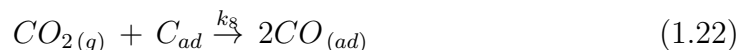


What the above equations highlight is the sheer complexity of the CO₂ reaction that is not immediately apparent on first glance. When the dissociation of the oxidant (CO₂) and its side reactions are also considered (equations 1.17 - 1.19, 1.2 1.6 and 1.5), the difficulty in understanding the surface chemistry increases again.



Finally, both formation of CO and H₂ (via associative desorption) has to be considered (equations 1.20-1.23):

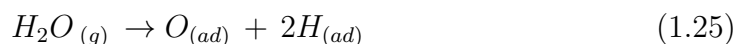




1.1.2 Steam Reforming of Methane



The steam reforming of hydrocarbons is industrially favoured over the CO₂ process due to the high ratio of hydrogen produced which can then be used as a primary fuel [2]. The reaction itself shares many of the complexities associated with the CO₂ reforming process including; dissociative adsorption of methane (equations 1.8 - 1.12), oxidation of surface carbon (or carbonaceous intermediates) (equations 1.13 - 1.16), product forming steps (equations 1.15 - 1.26) and competing side reactions (equations 1.2 - 1.7). However, rather than elementary steps involving CO₂, the oxidant is H₂O [12][13]:



These elementary reactions result in a more complicated system than is perhaps first imagined, and a number of these steps contribute to the current problems associated with the steam reforming reaction on an industrial scale.

Although the overall reaction is less endothermic than CO₂ reforming [14] it is an energetically expensive technology due to high reaction temperatures and the corrosive nature of steam which makes maintaining reactor integrity and catalyst performance challenging, however continued focus on this reaction and its associated problems are only likely to increase as oil reserves decrease, and gas reserves become exploited [4].

As well as high reaction temperatures and steam corrosion of reactors there are other issues with this reaction that make it the focus of research. Although a number of metals are catalytically active for this reaction such as Rh and Ru [15; 16; 17] it is nickel that finds most application, due mainly to its low cost. The

problem with nickel catalysts in both the steam and “dry” reforming reactions however, is that they suffer from serious coke build-up. The industrial significance of this extensive coking is that it leads to the blocking of pores and halts access of hydrocarbon to surface active sites [18]. Unchecked, this leads to serious pressure drop in fixed bed reactors due to inter-particle growth and ultimately results in reactor shut-down [19; 20; 21; 22]. This coke build-up may be mitigated through careful management of the reaction conditions, for example in steam reforming with control of the $H_2O:CH_4$ ratio and/or temperature [19]. Doping the catalyst with elements such as molybdenum [23], sulphur [5], gold [24], silver [25] or tin [26] can also prove successful. Despite their benefits, these dopants have not generally proved economically viable and running at high steam ratios is expensive [27]. It would be beneficial therefore to find a process by which to operate the reaction using nickel catalysts at low steam ratios, whilst still minimising the deposition of carbon.

1.1.3 Carbon Deposition in Methane Reforming

It is perhaps surprising that more work has not gone into the characterisation of coke and its methods of formation, considering the costs that dealing with it on an industrial scale incurs. In addition to the deactivation of catalysts, it blocks reactors, affects heat transfer and leads to other inefficiencies [22][21].

As well as attempting to better understand the elementary steps involved in the reactant breakdown / product forming reactions, this project also aims to better understand the elementary steps that result in carbon deposition and subsequent polymerisation such as the dissociation of $CH_{(ad)}$ equation 1.12, the CO reduction reaction (equation 1.26) and the polymerisation reaction (equation 1.27) . These reactions result in substantial carbon laydown and lead to significant problems with catalyst deactivation [21]. Characterising and better understanding this carbon is another major theme of this study.





As already mentioned, nickel catalysts are commonly used for both CO₂ - and steam-reforming due to economic considerations, however they are known to deactivate rapidly through coke formation [28][21]. An abundant literature exists on describing the nature of this surface carbon that is formed during the reaction [29; 30; 31; 32; 33; 34; 35]. Various broad classifications of carbon forms are used for the carbon linked to deactivation [21][2]. Highly reactive monatomic carbon has been suggested to function as a reaction intermediate, commonly denoted C α . In addition to CO production, this carbon may dissolve in nickel to form a bulk carbide, C γ , or polymerise to constructs of amorphous carbon, C β (equation 1.28).



Further, the growth of filamentous carbon may cause physical damage to the catalyst and generate pressure rises within the reactor (equation 1.29).



However, this mechanical growth process does not inhibit chemical activity [36][27]. Chemical inhibition is caused by encapsulating carbon, which covers the nickel surface and prevents reactants from accessing the active catalytic sites. At high temperatures crystalline graphite (Cc) may form, which will also have a deactivating effect. It is therefore important to examine and better understand the nature and formation of the coke in order to improve the reforming reaction. In any coke-forming reaction, a range of the carbon species mentioned above can be formed and the conversion between materials and their morphology is complex but irrespective of the type of carbon formed they all provide considerable challenges in their characterisation. As a result, often the only effort made in quantifying carbon is with thermal measurements, particularly temperature programmed oxidation (TPO) and thermo-gravimetric analysis (TGA) [2] [37]. These techniques may however, misrepresent the materials true nature (for example by catalytically lowering the oxidation temperature of the coke being investigated [38]) and

large carbon motifs can mask minority species. Carbon NMR may be used in some cases [39], but investigation of the deposits *in-situ* on a nickel catalyst is difficult, due to its magnetic qualities which result in poor resolution and line-broadening. Infrared spectroscopy is difficult due to their high absorbance [40], Raman may have difficulty with fluorescence, and XRD is challenged by their lack of long-range order. It has been shown however that with great care optical spectroscopy is possible on highly absorbing, coked, catalyst samples [41][42][43] and vibrational spectroscopy with neutrons can also be used on completely absorbing materials [44][45]. Characterisation methods combining vibrational spectroscopy with thermal methods consequently promise a more complete investigation into the materials deposited on catalyst surfaces.

This project will use a number of techniques including those mentioned above to attempt to characterise the carbon forming during both the dry and steam reforming reactions. By using vibrational characterisation in conjunction with the thermal methods, a more complete investigation into how and what materials are deposited on catalysts can be attempted. By accurately characterising and quantifying the coke deposited on the catalyst during the reaction, it may be possible to suggest improvements to the system that reduce this carbon formation during operation whilst still using economically favourable nickel catalysts (and at low steam ratios in the case of the steam reforming reaction).

1.1.4 Gold Doping in Ni/Al₂O₃ Reforming Catalysts

As discussed earlier, this study focusses on nickel catalysts which is due to their predominance in the industrial scene. Pioneering work from Clausen, Nørskov and co-workers has demonstrated that gold-doped nickel catalysts may be used in the steam reforming of methane in order to minimise deactivation [24; 46]. If the most active sites on nickel catalysts are those which are located at steps and edges [47; 48], the gold atoms in the promoted catalysts are thought to block these sites that are responsible for coking. However, it is not possible to exclusively attribute this effect to improved coking resistance and an electronic effect may need to be additionally invoked [48]. Model studies have shown that the addition of gold slightly decreases the ability of the catalyst to dissociate methane.

More importantly, however, the active monatomic carbon intermediate $C\alpha$ is destabilised, so that it is more likely to be oxidised (to CO) than to polymerise into coke,[24]. Rostrup-Nielsen has demonstrated that a larger ensemble of active metal sites is required to form coke than is needed for the desired reaction [49]. Well dispersed metal groups or other interspersed dopants will therefore disrupt the larger ensembles and thus improve catalyst longevity. The use of sulphur in the SPARG (Sulfur PAssivated ReforminG) process is an example of this effect [49]. In contrast to the steam reforming of methane, the use of gold-modified catalysts in the “dry” reforming reaction is much less studied. In 1999 a patent was granted for the the synthesis and subsequent use of nickel catalysts on zeolites for CO_2 reforming, with promotion by, amongst other things, gold [36]. Zhu has also reported on the use of a Ni/Au catalyst for “dry” reforming [50]. Triantafyllopoulos and Neophytides have examined the doping of nickel with gold for partial oxidation processes, with gold being hypothesised to increase the lifetime, stability and concentration of CH_x species [51]. Finally, Guzzi et al. have recently examined the CO_2 reforming of methane on Ni/Au spinels. In this communication, gold is thought to be inhibiting the conversion of monatomic carbon to carbon nanotubes and graphite in much the same way as proposed by Clausen above [47; 52]. The work of Triantafyllopoulos also agrees with this conclusion. As well as studying reforming performance and carbon build-up on Ni/ Al_2O_3 catalysts, this thesis has examined the CO_2 reforming reaction over a gold doped analogue in order to evaluate the generality of whether gold offers any improvement in coke resistance or reaction performance.

1.2 Techniques

It has already been discussed that in order to achieve a more complete understanding of the the nature of the hydrocarbonaceous overlayers formed during both the “dry” and steam reforming reactions that a wide range of analytical probes and techniques will be required. This investigation employs a number of tools including; vibrational spectroscopy, electron microscopy, and microreactor techniques, in order to elucidate the chemistry occurring on the catalyst surface. A brief description of these techniques and their application in the field of

heterogeneous catalysis is discussed presently.

1.2.1 Vibrational Spectroscopy

1.2.1.1 Infrared Spectroscopy

Vibrations in molecules or solid lattices can be excited by the absorption of photons. Infrared (IR) spectroscopy measures this interaction using light of wavelength between about 700 nm and 1 mm ($14000\text{-}10\text{ cm}^{-1}$). This range is divided into three regions with respect to their relation to the visible spectrum; near- ($> 4000\text{ cm}^{-1}$), mid- ($4000\text{-}400\text{ cm}^{-1}$) and far-infrared ($< 400\text{ cm}^{-1}$) [40][53]. The energy of the radiation varies with frequency, thus each region is best suited for the analysis of certain phenomena. The low energy of the far-infrared region is suited to the analysis of the rotational structure of gases, mid-IR is most useful in the study of fundamental molecular vibrations, whilst near-IR can excite vibrational overtones. Molecular vibrations have energies which correspond to the energy of light in the mid-infrared region, and is the region we are most interested in. Molecular vibrations occur when a molecule absorbs photons with a specific energy causing transitions between vibrational levels. Each functional group has its own discrete vibrational energy, so if a molecule or surface species is subject to photons with a broad range of energy (*i.e.* the mid infrared range) a complete picture of all the discrete functional groups is possible. This is a slight simplification however as infrared vibrations are subject to certain selection rules and active modes are only those that involve a change in dipole moment [40]. There is also the complication that, in practice, catalyst supports such as alumina absorb all energy below certain wavelengths. This results in an optical “cut-off” that makes it hard to study samples much below 1000 cm^{-1} . The first studies of adsorbed species was carried out by Terenin *et al* in the 1940s using near infrared to study hydroxyl groups on oxides [54]. Mid-IR studies on catalysts was pioneered by Eischens and Pliskin [55] and has since developed into a powerful tool for catalyst characterisation. Infrared is a highly popular tool and is excellent in the identification of organic molecules. Amongst the reasons for its popularity are its simplicity to run the experiment, the large quantities of data it can give and the fact that it is relatively inexpensive to run. Samples can be easily run

in solid liquid or gas phases. This also makes it highly versatile for a range of experiments and especially good for viewing catalysis reactions.

1.2.1.2 Fourier Transform Spectrometry

Historically, infrared spectrometers tended to work via a grating system. Radiation that enters the machine can be filtered using two gratings, so as to allow only a small range of wavelengths go on to interact with the sample. Smaller gratings give shorter wavelength ranges and so result in higher frequency resolution. A large drawback of this though is the fact that most of the radiation hits the side walls of the grating and so the total amount of energy getting through the system is small. High resolution therefore equals low energy. In practical terms this means that it is time consuming to build up a well resolved spectra especially parts of the spectra with low baseline transmittance (as it is hard to separate from the background noise) [53]. Current infrared spectrometers operate using the Fourier transform (FTIR). The first FTIR measurement was carried out in 1949 by Fellgett [56][53]. Interferometry allows all the frequencies to be measured simultaneously in the same experiment. The time saved in carrying out this type of experiment over the traditional experiment is considerable and is known as Fellgett's advantage.

Of central importance to a Fourier Transform spectrometer is the interferometer, which is a piece of apparatus that splits and recombines a beam of radiation to allow analysis of the beam. Figure 1.1 shows a schematic of an interferometer. It consists of a beamsplitter, which transmits and reflects equal portions of the radiation, and two planar mirrors aligned perpendicularly to each other. One mirror is held in a fixed position, whilst the other can be moved to vary the path length the radiation travels. The difference in path length between the two beams is known as the retardation and is equal to double the difference between the distances of the two mirrors from the beamsplitter. Figure 1.2 describes a perfectly collimated monochromatic radiation source with wavelength λ . When the two mirrors are equidistant from the beamsplitter (zero retardation), the radiation will take the same amount of time to travel along each path, and will thus be in phase when the two beams are recombined. However, if the moving

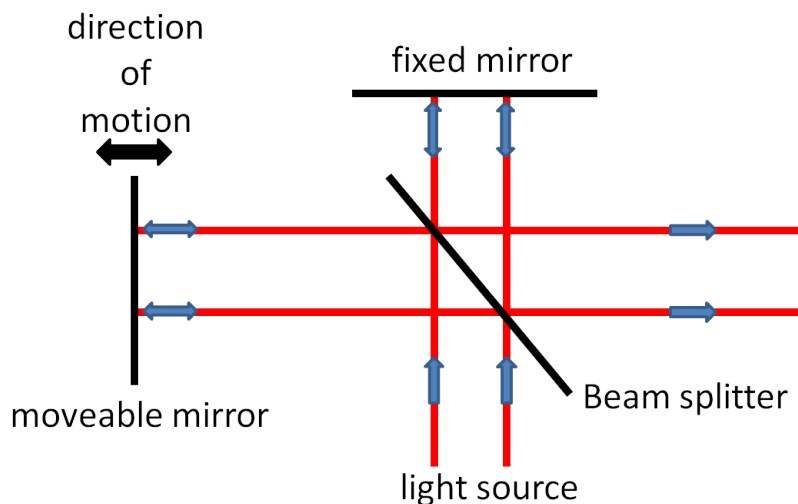


Figure 1.1: Schematic of an Interferometer [53]

mirror is displaced by a distance equivalent to a quarter of the wavelength of the incoming radiation (one half-wavelength retardation), the beams will recombine completely anti-phase and destructively interfere, resulting in no emitted signal. On one complete wavelength retardation, the waves combine again to give totally constructive interference. In practice, depending on where the moveable mirror is placed, different patterns of constructive and destructive interference occur and the resultant variation in the intensity of the beams reaching the detector is what gives the spectral information in an FTIR spectrometer. By using a black-body radiation source, a complete spectrum can be produced. There are a number of ways that infrared light can interact with a sample. Figure 1.3 shows three possible scenarios. In (a), the IR radiation does not interact with the sample and all the energy is transmitted. Scenario (b) shows that the sample absorbs some of the energy (corresponding to distinct molecular vibrations). The transmitted beam's energy is then weaker than the incident energy. Reflectance can also occur after absorption (c), and gives similar information to (b). It is the latter two scenarios that this project utilises.

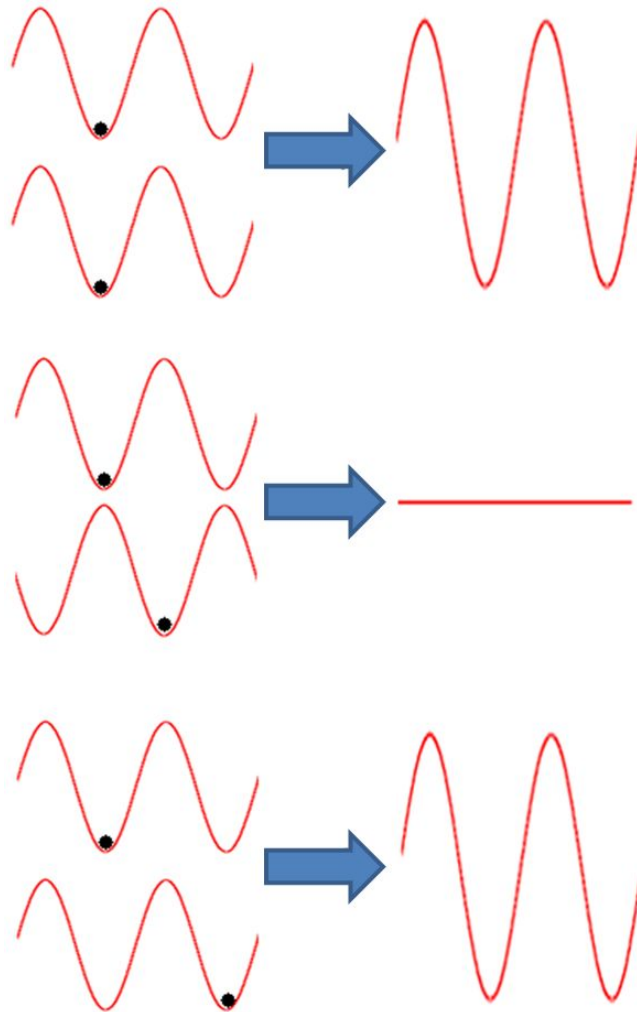


Figure 1.2: Constructive and destructive interference patterns that result from varying path length. From top to bottom, Zero retardation, one half-wavelength retardation and one complete wavelength retardation [53].

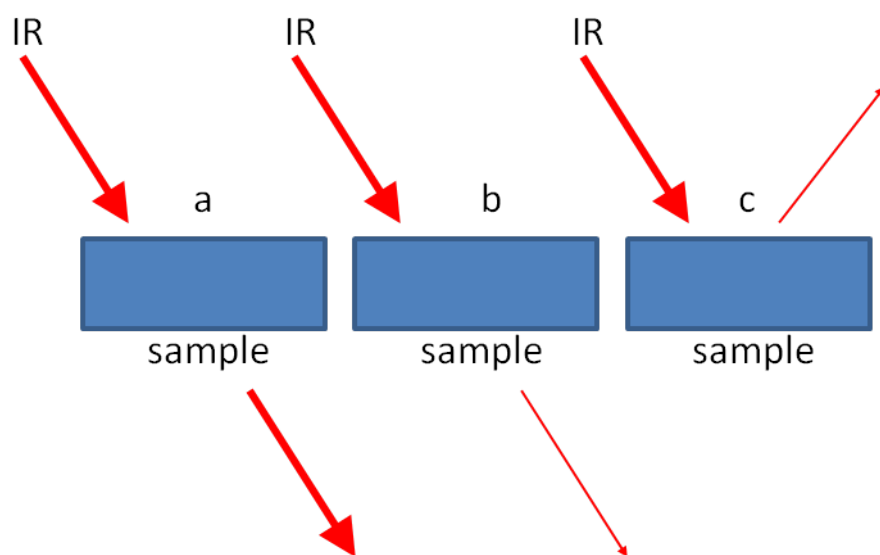


Figure 1.3: Possible interactions between IR radiation and sample: (a), no interaction, (b), sample absorbs energy and transmits, (c), sample absorbs energy and reflects [53]

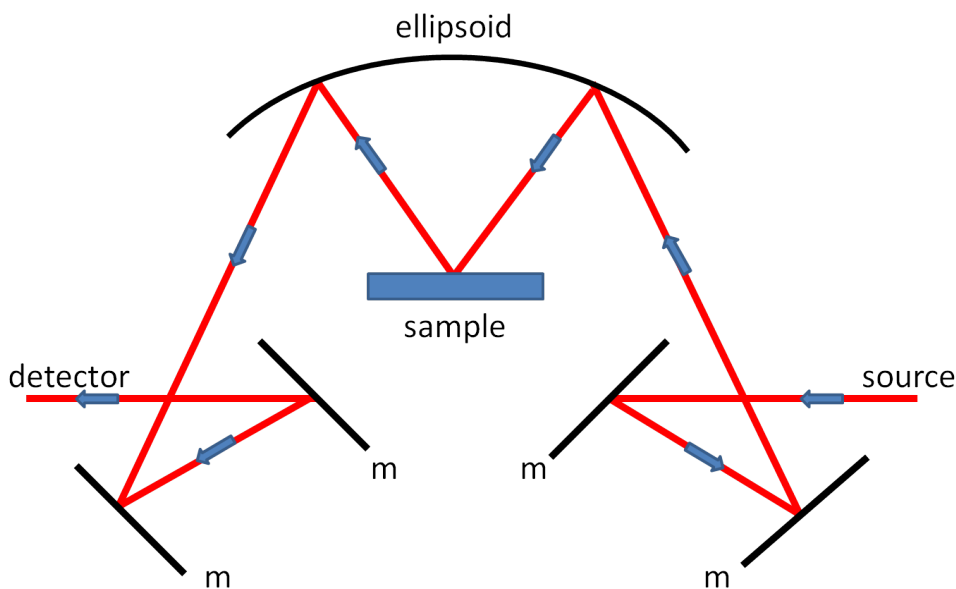


Figure 1.4: Schematic of diffuse reflectance technique [53]

1.2.1.3 Transmission Infrared Spectroscopy

Probably the simplest form of IR spectroscopy to perform is transmission 1.3b. The sample to be studied is first pressed into a disk (either self supporting or mixed with an optically neutral compound such as KBr). The sample is then supported in the path of the infrared beam. The light that is transmitted from the sample will be different to that of the incident beam in that any photons that have been absorbed by a vibrating species will have been at least partially lost. The key benefit of transmission infrared spectroscopy is in its inherent simplicity as very little technical apparatus other than the spectrometer is required. It has some limitations however, one of which is that post reaction catalyst samples are normally black, and it can be very difficult to press a disk sufficiently thin to allow any light through at all.

1.2.1.4 Diffuse Reflectance Infrared Spectroscopy

Diffuse Reflectance spectra result from the scattering of light from a powdered sample which has absorbed incident radiation 1.3c. Light is scattered by reflec-

tion, refraction and diffraction and is collected by elliptical mirrors before being focussed onto a detector 1.4. Most of the light beam is reflected so the angle between the reflected beam and the sample is equal to the angle between the incident beam and the sample. Light which is reflected in this manner, as would happen with a mirror, is known as specular reflection and is likely to have interacted little with the sample. The light which is diffusely reflected will exit in every direction and will have transferred energy to the sample. The key to DRS is to maximise the non-specular signal with respect to the specular and thus select the light which has strongly interacted with the sample being studied. The drawback to this technique is that the the ratio of the non-specular reflection to the incident beam is very low, and so a sensitive detector must be used. A Fourier transform spectrometer is ideal for exploiting this technique which is known as Diffuse Reflectance Infrared Fourier Transform Spectroscopy or DRIFTS [53]. As diffuse reflector sample cells have become commercialised, so has the technique grown in popularity. The major advantage of diffuse reflectance over the more traditional transmission technique is that the sample is a self supported powder and is not required to be pressed as a disk. Other benefits are that using a powder sample allows gas to freely diffuse around the material and provides a greater surface area for interaction with gases, and that by having less processing decreases the likelihood of the introduction of artefacts or even changing the system being analysed.

1.2.1.5 Raman Spectroscopy

Whilst infrared spectroscopy relies on the molecule adsorbing photons of the same energy as its vibrations, Raman spectroscopy involves the inelastic scattering of photons from the molecule being studied [40][57]. Figure 1.5 shows how photons interacting with a sample can behave, while figure 1.6 shows the resultant spectrum [40]. When monochromatic light interacts with a sample, most of the light is elastically scattered without loss or gain of energy - Rayleigh scattering (figures 1.5 and 1.6). Essentially this involves exciting the molecule from its ground state to an unstable virtual excited state, before the molecule returns to its ground state releasing the same energy as it took to excite it. If however, a molecule in

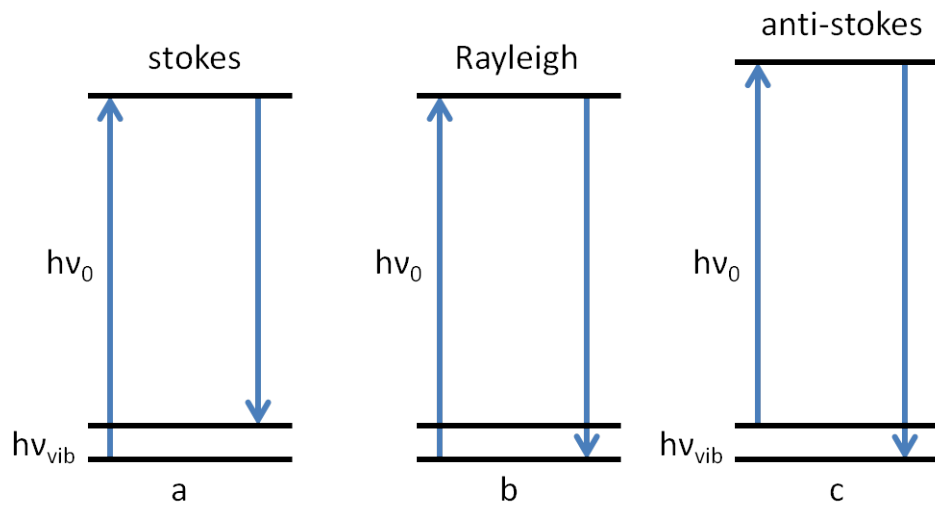


Figure 1.5: Raman scattering energy diagram (a), Stokes band, (b), Rayleigh band, (c), Anti-Stokes band. [40]

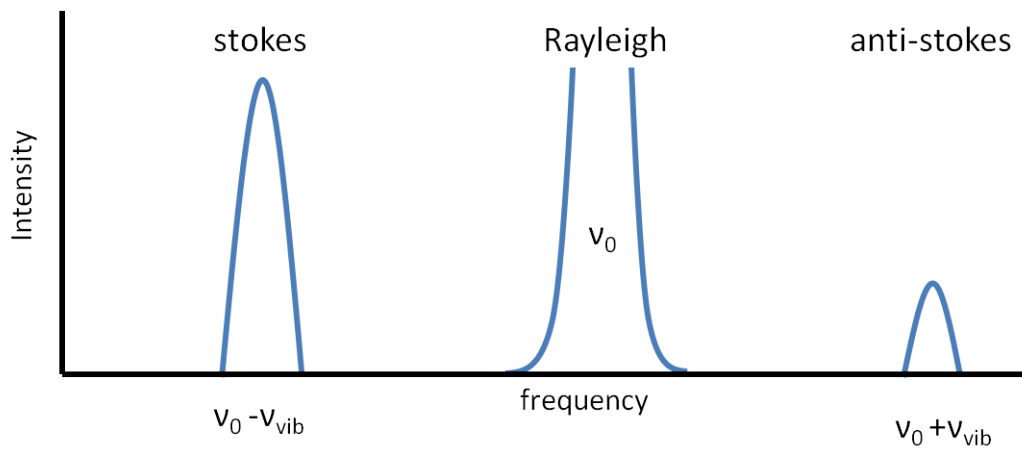


Figure 1.6: Stokes, Rayleigh and Anti-Stokes Bands [40]

its excited state returns to the first vibrational level the scattered photon has less energy than it did initially with the resultant intensity $\propto \nu_0 - \nu_{vib}$. This gives a Raman peak called a Stokes band (figures 1.5a and 1.6). It should be noted that there is also the possibility of an anti-Stokes band, but this around 10^3 times less intense than the Stokes band (figures 1.5 c and 1.6).

As in infrared spectroscopy, not all vibrations are observable, however the selection rules are different to infrared in that only those vibrations which result in a change of polarisability of the molecule are observable. A practical example of this are H_2 , N_2 , O_2 stretching vibrations which are Raman active but infrared inactive. These selection rules can often make infrared and Raman complementary and can be enlightening when used together. Raman spectroscopy has a number of advantages over infrared spectroscopy. The first is that it is possible to carry out measurements on black samples. Another is that due to the lack of “windows” in the sample handling apparatus, it is possible to obtain spectra at wavenumbers below 1000 cm^{-1} . Lastly, due to the fact that Raman spectroscopy is carried out using lasers, it is possible to obtain a spectrum from a significantly smaller sample than infrared. This last advantage however, can also be a possible shortcoming, in that samples can easily be overheated and decomposed. Finally, sample fluorescence can have a huge bearing on the spectral background which can make it difficult to achieve a suitable signal to noise ratio [40; 57; 58; 59].

1.2.1.6 Inelastic Neutron Scattering (INS)

Inelastic neutron scattering (INS) is analogous to that of Raman spectroscopy and electron energy loss spectroscopy (EELS). Unlike infrared where a photon excites a vibrational transition with resulting absorption or emission, INS and Raman are measurements based on the collision of a particle with a nucleus of a species of interest (e.g. a molecule on a surface). Raman is the collision of a photon, whereas INS is the collision of a neutron. One of the major differences between infrared, Raman and INS is that as a neutron has mass (1.009 amu), it is possible to measure the change in energy and the change in momentum of the neutron after the collision has occurred [40]. This gives rise to two interesting

features of INS. Firstly, it results in a two-dimensional spectrum (energy transfer (i.e. vibration) at a given momentum transfer) and also, it means that there are no inherent selection rules in the technique. As there are no selection rules, all vibrations are theoretically possible and visible [44][60]. However, the large cross section of hydrogen (82.0 barn) compared to other atoms, e.g. carbon (5.55 barn) means that in practice an INS spectrum for a carbonaceous species will be dominated by vibrational modes involving hydrogen [45][44]. A good example of this is the carbonyl stretch which although has a strong band in infrared spectroscopy, is effectively invisible to INS. The two dimensional spectrum allows determination of whether a vibration is associated with a light atom (e.g. hydrogen) or a heavy atom (e.g metal lattice modes) [44], and can also even be used to probe magnetic modes [61]. Another interesting feature is that as atomic nuclei have a size of around 0.1 % of the entire atom, neutrons are highly penetrating and can therefore probe the bulk of a sample.

$$S(Q, n\omega_i) \propto \frac{(QU_i)^{2n}}{n!} \exp [-(QU_{Tot})^2] \sigma \quad (1.30)$$

Equation 3.1 shows the scattering law. The intensity (S) is related to both momentum (Q) and the frequency (ω_i). i is the mode at frequency ω and $n = 1, 2$ or 3 for a fundamental band, overtone (or binary combination) or secondary overtone (or tertiary combination) respectively. U_i and U_{tot} are the root-mean square displacements of the atoms in the particular vibration or of all the atoms in the sample respectively. The exponential term is the Debye-Waller factor. This part of the equation is critical from a practical perspective, and requires that measurements are taken as close to 0 Kelvin as possible (typically below 30 K) [44; 60]. Lastly, σ is the cross-sectional area of the atoms involved in the mode.

For this study, INS spectra were recorded using the TOSCA (fig 1.7) MAPS (fig 1.8) and MERLIN spectrometers, located at the ISIS Facility, Rutherford Appleton Laboratory, Oxfordshire, U.K. A brief description of each of the spectrometers is given presently.

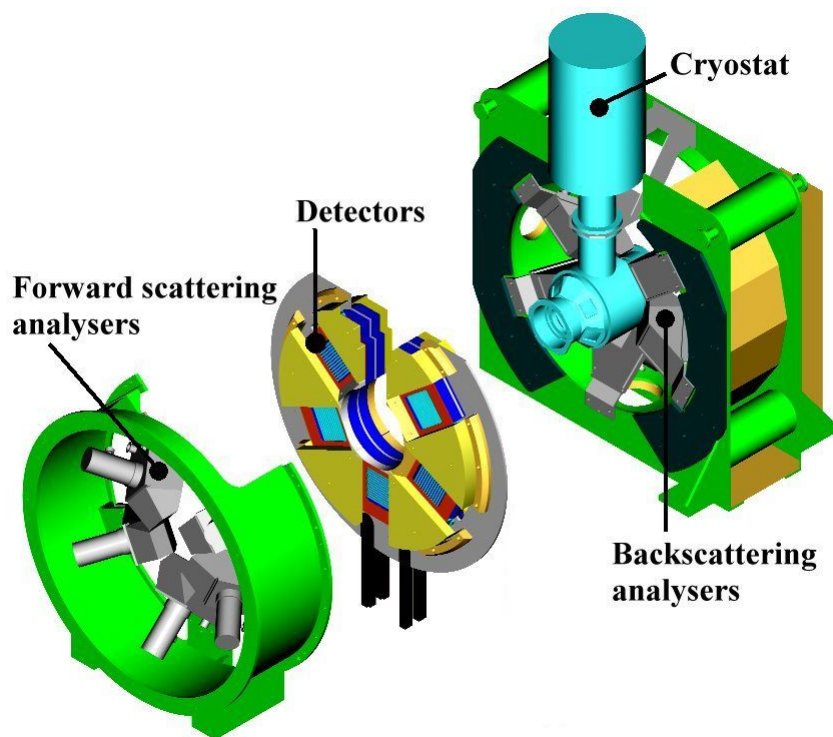


Figure 1.7: Schematic of the TOSCA spectrometer [62][63]

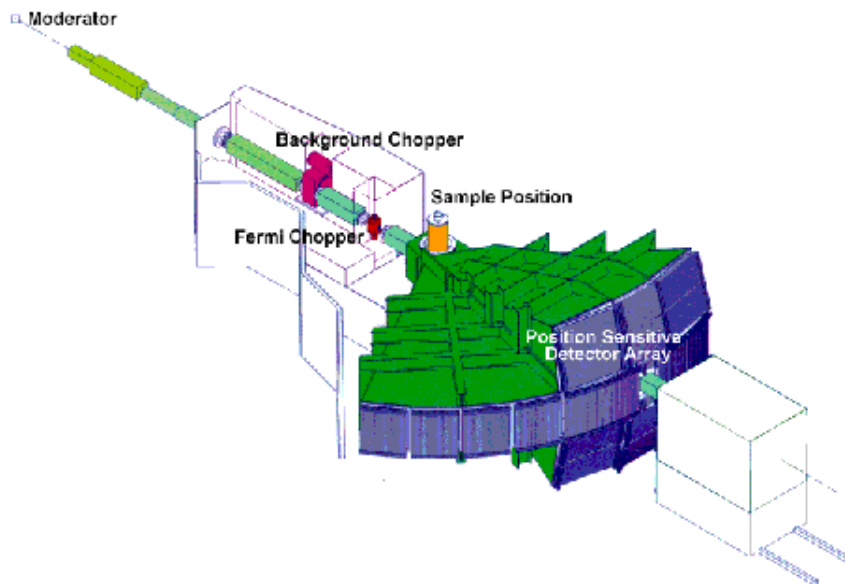


Figure 1.8: Schematic of the MAPS spectrometer [64]

TOSCA is an indirect geometry instrument [62][63][65] and this has traditionally been the spectrometer design of choice when measuring catalyst samples [44; 60; 66; 67; 68; 69]. This is mainly due to its simple design. All incident neutrons are allowed to interact with the sample, and a simple beryllium filter allows only neutrons with a specific final energy to reach the detectors. This makes it very easy to collect data across the whole range of energy (40 cm^{-1} up to 4500 cm^{-1}) but has the downside of losing any momentum information and also loses resolution towards higher wavenumbers.

More recently, studies have been carried out on the MAPS spectrometer at ISIS [64][70]. MAPS is a direct geometry instrument and is almost the opposite to TOSCA in how it functions. Neutrons entering the instrument do so with a wide range of energies. Before interacting with the sample, a “chopper” is used to select a discrete energy range (see figure 1.8). This can be tuned to highlight specific areas across the spectrum from 40 cm^{-1} up to 4500 cm^{-1} . Once the neutrons have interacted with the sample, all energies of scattered neutrons are

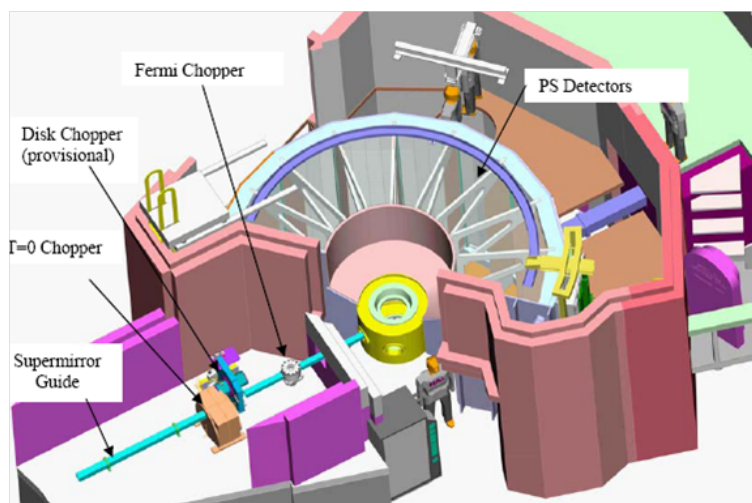


Figure 1.9: Schematic of the MERLIN spectrometer [71; 72; 73]

measured using a wide detector bank and so information on momentum transfer as well as energy transfer can be measured. A larger detector bank is required on MAPS compared to TOSCA in order to compensate from the loss of incident flux due to the choppers. This coupled to the fact that different incident energies are required to cover the full vibrational range, means that sample collection times can be in the order of 24 hours or more for a single sample.

Finally, some measurements have also been carried out on the MERLIN spectrometer 1.9 [71; 72; 73]. Like MAPS it is a direct geometry instrument, which uses a Fermi chopper to monochromate the incident neutron beam to give incident energies in the range $72 - 8060 \text{ cm}^{-1}$. It does however differ from MAPS in that it has a larger detector bank which allows it to have a higher count rate and so better signal to noise ratios. The drawback of MERLIN is that it has an inferior resolution to that of MAPS, which could be a major problem when trying to separate vibrational modes (e.g. C-H and O-H stretches).

1.2.2 X-ray Diffraction

X-rays have a wavelength in the angström range. X-ray diffraction (XRD) allows the investigation of the bulk phases (structural properties) of catalysts. XRD

is a measure of the elastic scattering of x-ray photons by atoms in a periodic lattice. When a powdered sample is analysed e.g. a supported metal catalyst, a diffraction pattern occurs as a fraction of the the particles will be oriented in such a way as a crystal plane is at an angle θ to the incident energy giving rise to scattered monochromatic x-rays that are in phase and so produce constructive interference. The lattice spacing is defined by the Bragg equation (1.31) and is characteristic for any given compound. This diffraction pattern is therefore characteristic for any given compound and allows for determination of the phases present in a sample.

$$n\lambda = 2d\sin\Theta \quad (1.31)$$

1.2.3 Transmission Electron Microscopy

Whereas XRD is a measure of the scattering of x-rays by electrons, Transmission Electron Microscopy (TEM) is a measure of electron scattering by both electrons and the nucleus. TEM allows the visualisation of catalyst surfaces due to the small de Broglie wavelength of electrons compared to that of visual light. When an electron interacts with a sample a number of possibilities can result including zero energy loss, electron diffraction, x-ray diffraction, backscattering, Auger and energy loss amongst them.

In TEM transmitted and diffracted electrons are utilised. A primary beam of electrons interacts with the sample. The transmitted electrons are attenuated with respect to density and thickness which gives a two dimensional projection of the sample (bright field imaging). The diffracted electrons give a dark field image. It is well known that samples emit x-rays when they are subjected to electron bombardment. X-ray fluorescence occurs when a core hole - formed due to the loss of an electron - is filled with an electron from a higher shell. The energy associated with this transition is characteristic of a specific compound. Figure 1.10 describes how an electron from the L shell falls into the K shell hole created by the loss of an electron. As the electron falls, an x-ray of energy $K\alpha$ is emitted. In practice this allows TEM images to be combined with information

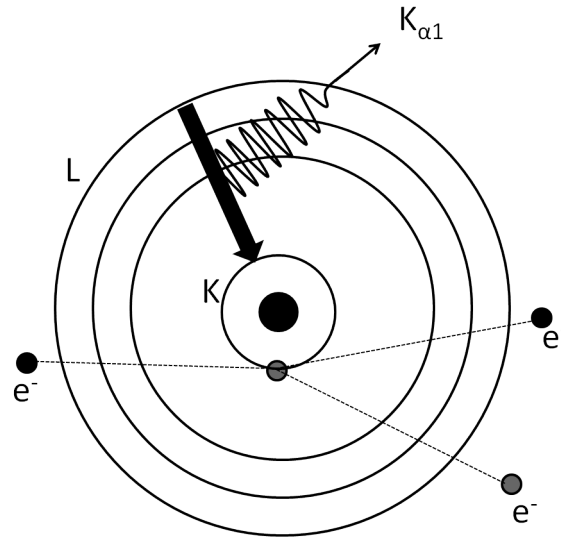


Figure 1.10: K-shell x-ray fluorescence

from backscattered x-rays. This makes it possible to generate an elemental map - a 2-D image that can be colour coded to highlight the specific elements present in a brightfield image.

Chapter 2

Experimental and Development of Inelastic Neutron Scattering Technique for Analysis of Heterogeneous Catalyst Samples

2.1 Experimental

Both the CO₂ and H₂O methane reforming studies carried out in this study use similar catalysts, reaction apparatus and reaction conditions. The resultant, post-reaction samples were also studied in a similar manner. The following experimental details can be assumed to be the same for each section except where explicitly stated.

2.1.1 Catalyst Preparation

Four catalysts were used in this study, two Ni/Al₂O₃ catalysts that either facilitate the formation of amorphous or graphitic carbon in both the “dry” and steam reforming reactions and two Ni-Au/Al₂O₃ catalysts that also favour amorphous or graphitic carbon deposition. A summary of the catalysts and what carbon is deposited on their surface is presented in table 2.1. The catalysts were prepared by colleagues at the University of Keele and the preparation routine is as follows:

Catalyst	Resultant Carbon Formed
45 wt % Ni/Al ₂ O ₃	Amorphous Carbon
5 wt % gold-doped 45 wt % Ni/Al ₂ O ₃	Amorphous Carbon
26 % (w/w) Ni/Al ₂ O ₃	Filamentous Carbon
5 mol % Au 20 wt % Ni/Al ₂ O ₃	Filamentous Carbon

Table 2.1: Summary of the catalysts used in this project and their resultant carbon

2.1.1.1 Catalysts Resulting in Amorphous Carbon Formation

The following catalysts were prepared by colleagues at the University of Keele. A 45 wt % Ni/Al₂O₃ catalyst and a 5 wt % gold-doped 45 wt % Ni/Al₂O₃ catalyst were prepared by wet impregnation of α -alumina (Sumitomo, lot no. YE6 Y01, BET surface area 1.93 m² g⁻¹) with nickel nitrate and hydrogen tetrachloroaurate, followed by calcination at 1173 K. For the non-doped material, nickel nitrate hexahydrate was dissolved in a minimal amount of water, to which alumina was added subsequently. Water was driven off the suspension using a hot plate, before drying in an oven at 393 K for 6 days. Finally, the material was calcined in static air by heating to 773 K at 1 K min⁻¹, then to 1173 K at 5 K min⁻¹. The temperature was maintained for one hour before cooling to room temperature. This procedure resulted in a 45.1 wt% Ni/Al₂O₃ catalyst. The doped material followed the same synthesis, but used nickel nitrate hexahydrate with hydrogen tetrachloroaurate (III) trihydrate and alumina to generate a catalyst 43.1 % Ni and 4.77 % Au by mass. Hydrogen tetrachloroaurate(III) trihydrate (99.9 % purity) was supplied by Acros Organics and nickel(II) nitrate hexahydrate (99.8 %) by BDH.

2.1.1.2 Catalysts Resulting in Filamentous (Graphitic) Carbon Formation

As with the previous section, catalysts were synthesised by colleagues at the university of Keele. The preparation of both the Ni and the Ni-Au is as follows:

A 26 % (w/w) Ni/Al₂O₃ catalyst was prepared by wet impregnation of -alumina (Alfa Aesar, 99.98%, < 1 micron APS powder, surface area 10 m² g⁻¹) with nickel nitrate hexahydrate, Ni (NO₃)₂.6H₂O, (Acros Organics, 99 %). The mixture was stirred whilst heating at 353 K. Water was driven off the suspension using a hot plate, before drying in an oven at 393 K for 6 days. The material was then calcined in static air by heating in a furnace (Carbolite RHF 1600) to 773K at 1 K/min, then to 873K at 5 K/min. This temperature was maintained for one hour before cooling the sample to room temperature at 10 K/min. Following calcination, the catalyst was ground using a pestle and mortar and sieved to a particle size <106 μm using a stainless steel Laboratory Test Sieve (BS410/1986).

Similarly, 60 g of 5 mol % Au 20 wt % Ni/Al₂O₃ was prepared. 59.32 g of nickel nitrate hexahydrate, Ni(NO₃)₂.6H₂O, (Fischer Scientific) was dissolved into solution and 48 g of dried alpha aluminium oxide, α-Al₂O₃, (Alfa Aesar) was added, as above. Gold was added in the form of gold chloride trihydrate, HAuCl₄.3H₂O, (Acros Organics) to a level of 5 mol % with respect to the nickel content, which equated to 4.06 g. This was suspended in a minimal amount of water and added to the Ni(NO₃)₂ solution. The mixture was stirred whilst gently heating at ca. 353 K. All samples were dried in ceramic boats at 373 K overnight and then activated by calcination. The material was calcined in static air by heating in a furnace (Carbolite RHF 1600) to 773 K at 1 K min⁻¹, then to 873 K at 5 K min⁻¹. This temperature was maintained for one hour before cooling the sample to room temperature at 10 K min⁻¹. Following calcination, the catalysts were ground using a pestle as with the Ni/Al₂O₃ sample above.

2.1.2 Microreactor Rig and Reactor Design

As part of this investigation, a reactor rig has been constructed in order to carry out reforming reactions on a scale of 5-100 mg catalyst sample size. The schematic of the microreactor used for reaction testing is shown in figure 2.1. This appara-

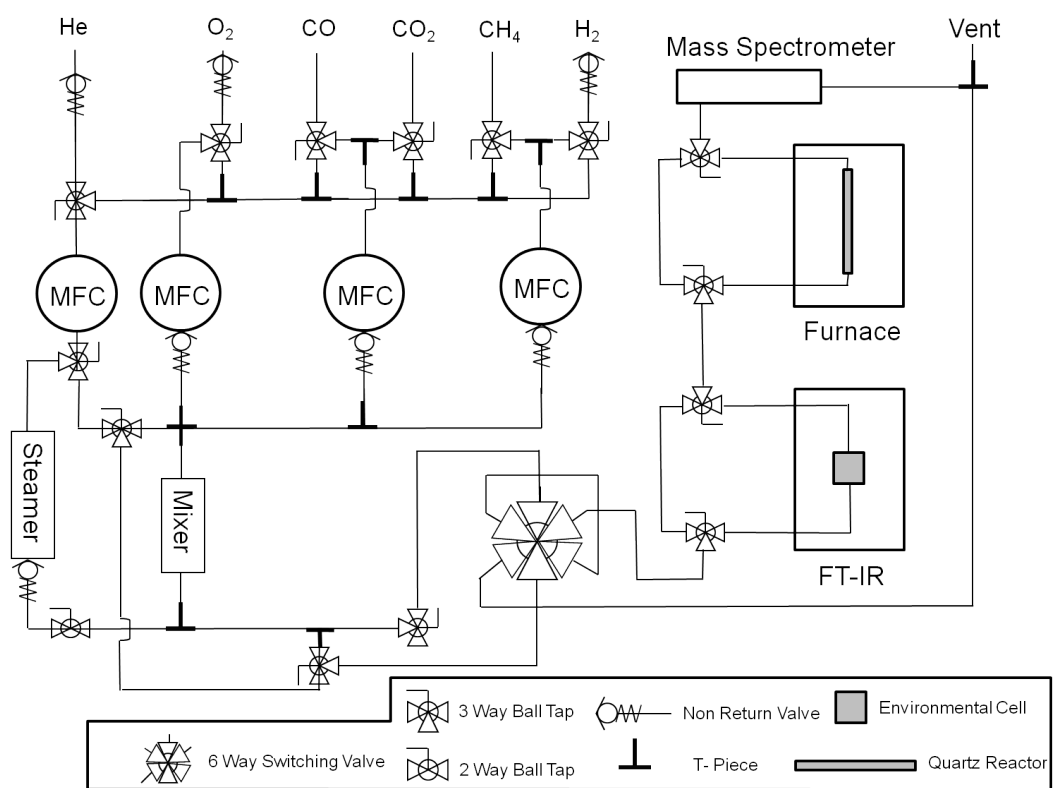


Figure 2.1: Schematic of Microreactor Apparatus

tus was designed to be flexible and allows both CO₂ and H₂O reforming reactions to be studied simply by altering the direction of the He carrier gas. All reaction testing and thermal measurements (TPO,TPH etc) were performed using this apparatus with the exception of the samples that were prepared for inelastic neutron scattering studies. These studies required construction of a second reaction rig that will be discussed later.

Four mass flow controllers (Hastings HFC302 controlled by Teledyne THPS-400) are connected with 1/8" stainless steel tube to a mixing volume containing glass beads. The gasses connected to the apparatus were as follows: H₂ (BOC, 99.999 %), He (BOC, 99.999 %), CH₄ (CK gas, 99.95 %), CO (CK gas, certified 4.872 % in Ar), ¹²CO₂ (CK gas, 99.995 %), ¹³CO₂ Cambridge Isotope Laboratories 99 % and 5% O₂/He mix (BOC). Helium is used as a diluent, and a portion of its flow may be passed through a saturator filled with deionised water. This is immersed in an oil bath on a stirrer-hotplate (IKA RCT basic with ETS-D5 control), set to a temperature not exceeding 353 K, depending upon the experiment. The gas lines downstream of the saturator are heated to 353 K using heating tape (Electrothermal engineering HT95508) controlled by a PID controller (Ero Electronic LFS). The reactor itself is a quartz tube of 6 mm O.D. which passes through a tube furnace (Carbolite MTF 10/15/30, max T 1000 °C) and is connected to the steel tubing with 1/4" Cajon compression fittings. The catalyst is held in the centre of the reactor using quartz wool. Two three-way taps either side of the tube furnace allow the direction of the gas flow to bypass the reactor. *In-situ* DRIFTS measurements are also possible (as is transmission IR) via the environmental cell (Specac) and FTIR spectrometer (Bruker Vertex 70) incorporated into the reaction rig. The spectrometer can also be bypassed via two three-way taps. The exhaust line is also heated and has a T piece fitting with one outlet attached to the heated quartz inlet capillary of a Hiden HPR20 quadrupole mass spectrometer and the other is attached to a K-type thermocouple that can be pressed against the quartz wool inside the reactor to give a more accurate measurement of the catalyst bed temperature. This thermocouple was connected to the mass spectrometer the software of which automatically recorded the temperature. Differential pumping allows this system to accept gas inputs at above ambient pressures.

2.1.3 Microreactor Conditions

Reaction testing for both CO₂ and H₂O studies were performed in a quartz-tube micro-reactor using the University of Glasgow microreactor arrangement described above. The two different catalyst preparations (45 wt % and 26 wt % inherently favoured different forms of carbon retention. The reaction conditions below are presented as a general set-up, with any differences in the the specific test regimes mentioned.

2.1.3.1 CO₂ Reforming

Approximately 5-20 mg of the 45 wt % Ni/Al₂O₃ catalyst or 5 mol % gold-doped 45 wt % Ni/Al₂O₃ catalysts were loaded into the reactor between quartz wool plugs. Prior to reaction, the catalysts were reduced for 2 h at 1123 K under a flow of 3 sccm (standard cubic centimetres per minute) H₂ in 40 sccm He. Reactions used 2 sccm CH₄ with 1 sccm CO₂ diluted in 40 sccm He as before. The reaction conditions provide a total gas hourly space velocity (GHSV, defined as the ratio of the total volumetric flow at the inlet and the reactor bed volume) of $1.2 \times 10^4 \text{ hr}^{-1}$ and a space time (the volume of the catalyst bed divided by the flow) of 0.3 s [20] Initial micro-reactor measurements were recorded in a temperature-programmed mode (300-1150 K). The results from those runs were used to select a temperature for isothermal measurements. The isothermal temperature selected (1073 K) used for the micro-reactor was selected due to constraints with the INS apparatus. All reactions were performed at least twice, so that the results presented here are representative of the trends observed. These conditions are those which resulted in amorphous carbon laydown.

The 26 wt % Ni/Al₂O₃ catalyst favoured graphitic carbon formation. This catalyst used 5.6 sccm CH₄ with either 5.6 sccm ¹²CO₂ or ¹³CO₂ diluted in 40 sccm/min He. The reaction conditions provide a gas hourly space velocity (GHSV) of $2.4 \times 10^4 \text{ hr}^{-1}$ and a space time of 0.15 s [20]. Isothermal reactions were performed at 898 K in both the microreactor and the INS experiments.

Post reaction temperature-programmed oxidation measurements of both regimes

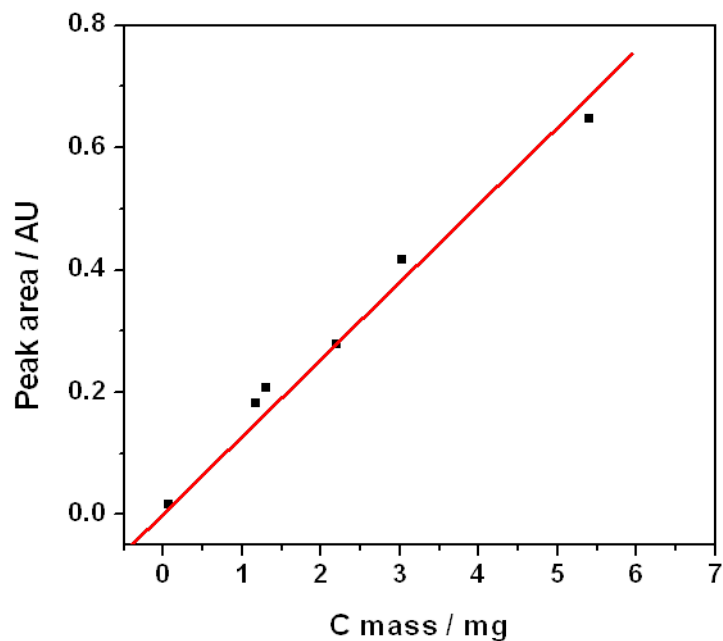


Figure 2.2: Calibration of mass spectrometer response (Mass 44) to known quantities of graphite. The line is best fit to the data

were performed *in-situ* after reaction using 20 sccm of a 5% O₂/He mix using a temperature ramp of 10 K min⁻¹ to 1223 K. Temperature-programmed hydrogenation (TPH) experiments were also performed *in-situ* using 5 sccm H₂ diluted in 40 sccm He with a ramp to 1223 K at 10 K min⁻¹. The raw data were normalized against the total recorded pressure to remove the effects of pressure variation and to give a percentage composition of the exhaust gases. The instrumental response was calibrated by oxidation of known masses of graphite (Sigma-Aldrich, >99.5%), as well as the thermal decomposition of calcium carbonate (BDH, >98%). Figure 2.2 shows the calibration of the response of the micro-reactor to known quantities of graphite. It can be seen from figure 2.2 that the response is linear and will permit the quantification of unknown masses of carbon that form on the surface during the reforming process.

2.1.3.2 H₂O Reforming

In order to study amorphous carbon deposition in the methane steam reforming reaction approximately 5-20 mg of the 45 wt % Ni/Al₂O₃ catalyst was reduced in the same manner as the CO₂ reforming reaction. Flow of H₂O was established first by heating the oil bath to the desired temperature before passing helium through the saturator. Once a steady mass 18 signal was observed on the mass spectrometer, a methane flow rate was selected to give an H₂O ratio of 3 to 1.8 CH₄. Due to the inherent difficulties in controlling steam compared to gases, the exact H₂O flow rate varied from experiment to experiment, but was always in the region of 3 ± 0.5 sccm. For graphitic steam reforming, reactions were performed using a 1:1 ratio of reactant to oxidant. This ratio should accelerate deactivation and provide a stronger INS signal for evaluation than the amorphous analogue. Due to the inherent difficulties in controlling steam compared to gasses, the exact H₂O flow rate varied from experiment to experiment, but was always in the region of 5 ± 1 sccm. Temperature programmed reaction was performed using a temperature ramp of 10 K/min to 1223 K. Isothermal measurement temperature was 898 K for the low temperature studies and 1123 K for the high temperature studies. Post-reaction TPO and TPH procedures were also analogous to the CO₂ reforming studies.

2.1.4 Inelastic Neutron Experiments

INS measurements were performed at the ISIS Facility of the STFC Rutherford Appleton Laboratory using the TOSCA, MAPS and MERLIN spectrometers described previously. In order to achieve reasonable resolution over a wide spectral range (40 - 4000 cm⁻¹), spectra on the MAPS spectrometer were measured at 4840, 2017 and 484 cm⁻¹.

Due to sensitivity constraints, large catalyst masses (ca. 10 g) are typically required for INS studies of heterogeneous catalysts, which is around 200 times more sample than is normally used in conventional micro-reactor measurements. In order to achieve this, reaction apparatus was constructed to accommodate the larger catalyst masses. The following section details the construction of this

apparatus as well as the development of the inelastic neutron scattering technique. A brief experimental section detailing the reaction conditions for both the steam and CO₂ reforming reactions are described presently.

2.1.4.1 CO₂ Reforming

2.1.4.1.1 Catalyst Favouring Retention of Amorphous Carbon

For amorphous carbon studies, a charge of approximately 20 g of the 45 wt % Ni/Al₂O₃ catalyst or 5 mol % gold-doped 45 wt % Ni/Al₂O₃ catalysts was loaded into the stainless steel u-tube reactor described later in this section. The samples were reduced by heating to 1023 K at 5 K min⁻¹ in flowing hydrogen (140 ml min⁻¹ H₂ diluted with 1250 ml min⁻¹ He) and held at this temperature until hydrogen consumption ceased. Maintaining the helium flow, the sample temperature was increased to 1073 K and reaction commenced by flowing CO₂ and CH₄ and He over the catalyst at respective flow rates of 35, 70 and 1250 sccm. This resulted in a GHSV of 4.9 x 10³ h⁻¹ and a space time of 0.72 s. Reaction was maintained for 6 hours with methane conversions comparable to those observed with the micro-reactor arrangement. It should be noted that it was not possible to match the GHSV between the microreactor and the INS measurements. This is solely due to is the increased mass of catalyst required for the INS experiments coupled to the maximum output of the mass flow controllers that restricts the maximum space velocities achievable. There is also a limitation on vented gas emissions allowable within the ISIS experimental arrangement. The gasses used in these experiments were as follows; research grade H₂, CO₂ and CH₄ were supplied by CK gases, with purities of 99.95 %, 99.995 %, and 99.999 % respectively. The He diluent was UHP grade from Air Products (99.9992 %).

After 6 hours on-stream, the heating was stopped and the sample isolated and allowed to cool to ambient temperature. The quartz reactor was transferred to an indium-sealed gas tight aluminium sample cell inside an argon-filled glove box (MBraun UniLab MB-20-G, [H₂O] < 1 ppm, [O₂] < 2 ppm). The cell was then transferred to the INS spectrometer, for the recording of INS spectra at 20 K. Background measurements were also performed on the alumina used in the

catalyst synthesis. A sample of the α -alumina was initially treated in flowing hydrogen at 823 K for 2 hrs ($140 \text{ ml min}^{-1} \text{ H}_2$ diluted with $1250 \text{ ml min}^{-1} \text{ He}$); subsequently CO_2 and CH_4 and He were passed over the sample at the same temperature (respective flow rates of 70, 35 and 1250 sccm) in order to provide a blank control experiment. Methane conversion was not detected to any extent under these conditions.

After these INS measurements, any radioactivity emerging from the INS cell was allowed to decay to a safe level before the catalysts were recovered and further analysed.

2.1.4.1.2 Catalyst Favouring Retention of Graphitic Carbon

For graphitic carbon studies, approximately 10 g of the 26 % (w/w) Ni/ Al_2O_3 catalyst was loaded between quartz wool plugs in the Inconel [®] reactor described later. The sample was reduced at 883 K for 2 h in a flow of 50 sccm H_2 (CK gas, 99.999 %) in 1500 sccm He (Air products 99.9992 %). The H_2 was then purged from the system whilst cooling, before the catalyst was isolated under the inert gas and transferred to the spectrometer for the background spectrum to be recorded at 20 K.

After the background spectrum had been recorded, the cell was removed from the spectrometer and reconnected to the gas handling system. This allows the initial sample to be reacted without being disturbed - which should result in good background subtractions. The methane reforming reaction was then initiated by establishing flows of 80 sccm CH_4 (CK gas, 99.95 %), 80 sccm CO_2 (CK gas, 99.995 %) and 1500 sccm He (GHSV = $1.2 \times 10^4 \text{ h}^{-1}$, space time = 0.3 s) and heating the catalyst to 898 K. These conditions were maintained for 6 h, at which point heating was stopped, the reactor purged, and isolated. The sample is then quenched in liquid nitrogen before being analysed by INS [74; 75]. The spectrum of the reduced catalyst was subtracted from the spectrum of the reacted catalyst for background subtraction. In this way, spectra only relate to material formed during the reaction stage. All INS spectra were recorded at 20 K.

2.1.4.2 H₂O Reforming

2.1.4.2.1 Catalyst Favouring Retention of Amorphous Carbon

As before, larger samples in the region of 7 g had to be prepared for INS measurements. In order to produce steam, a portion of He was passed through a heated saturator which is described in the following chapter. Amorphous carbon samples were prepared in the Inconel[®] reactor using the 45 wt % Ni/Al₂O₃ catalyst. The sample was reduced at 898 K for 2 h in a flow of 50 sccm H₂ diluted in 1500 sccm He. The H₂ was then purged from the system using He whilst the sample cooled at which point it was transferred to the spectrometer for a background spectrum to be recorded.

The reduced sample was then reconnected to the gas manifold. The saturator was then run at 343 K with a flow of 150 sccm through it. This gave an unstable and approximate flow of 30 sccm H₂O. Two samples were prepared; the first reacted 5.85 sccm CH₄ with the steam (around a 1 H₂O : 1 CH₄ ratio). The second sample had a flow of 18 sccm CH₄ (around a 1 H₂O : 3 CH₄ ratio). The first showed 100 % methane conversion, the second showed approximately 80 %. After INS spectra were collected from the second sample it was subsequently heated to 773 K under a flow of 1500 sccm He and 50 sccm H₂, then held for over an hour. Gas phase H₂ was then purged as the system cooled, and the sample isolated after 10 min. The mass spectrometer detected production of CH₄, CO and O₂ in this hydrogenation step. In subsequent sections, these samples are referred to as INS6 and INS18, relating to the approximate methane flow rate used in their preparation. INS18H refers to the sample post hydrogenation. It should be noted that as INS18 was converted to INS18H, it was not available for further characterisation.

2.1.4.2.2 Catalyst Favouring Retention of Graphitic Carbon

Graphitic carbon samples were prepared using the 26 % (w/w) Ni/Al₂O₃ catalyst. The sample was reduced at 898 K for 2 h in a flow of 50 sccm H₂ diluted in 1500 sccm He. The H₂ was then purged from the system using He

whilst the sample cooled at which point it was transferred to the spectrometer for a background spectrum to be recorded.

The reduced sample was then reconnected to the gas manifold. The methane reforming reaction was then initiated by establishing flows of 1500 sccm He (split into 150 sccm through the bubbler and 1350 sccm to act as diluent). Once a stable mass 18 signal was detected, a flow rate of methane was established to match the H₂O at a 1:1 ratio (For this study, the methane flow rate was 78 sccm). The reaction was carried out at 898 K and was maintained for 6 h, at which point heating was stopped, the reactor purged, and isolated. The sample is then quenched in liquid nitrogen before being analysed by INS [74; 75].

For the high temperature graphitic reactions, the conditions had to be altered to accommodate pressure constraints associated with the quartz u-tube reactor described in the following chapter. Reduction temperatures and flow rates were the same as the low temperature graphite studies however the isothermal reaction flow rates were 10 sccm He (through saturator), 40 sccm (as diluent) and 5 sccm CH₄ in order to keep the operating pressure below 2 bar. This pressure limit is due to the inherent weakness between the joints that fuse the stainless steel to the quartz. The INS sample was reacted for 6 hours before being isolated, cooled and transferred into an aluminium sample can via the glovebox described earlier.

2.1.5 Post-reaction Analysis of Microreactor and INS Samples

Elemental analysis was carried out using an Exeter Analytical C440 Elemental Analyser. Temperature-programmed oxidation and hydrogenation measurements of post-reaction INS samples was undertaken by loading *ca.* 10 mg of reacted sample into the quartz micro-reactor then performing comparable procedures to those described for the in-situ TPO measurements. Visual inspection of the pre- and post-TPO samples showed the samples had changed from black to green indicating that the TPO runs had fully oxidised the residual carbon.

Raman scattering measurements were undertaken using two separate instruments. For CO₂ reforming resulting in amorphous carbon, a custom instrument was used which utilises backscattering geometry, 532 nm excitation wavelength,

spectral resolution of 6.5 cm^{-1} and laser power at the sample of 20 mW so as not to damage the sample[76]. Samples were ground with KBr in an approximately 15:1 ratio and the self supporting discs were held in the laser focus. Data were collected for approximately two minutes. All other Raman measurements were recorded on a Horiba Jobin Yvon LabRam HR confocal Raman microscope using 532 nm and 352nm laser excitation; taking care to ensure that no laser-induced decomposition occurred. Temperature-programmed hydrogenation/Raman scattering experiments were performed by loading ca. 5 mg of a post-reaction sample into a Linkam CCR1000 environmental chamber interfaced to the Raman spectrometer. The cell was then heated at 10 K min^{-1} to 700 K under a 10 sccm N_2/H_2 mix for 30 mins before re-recording the Raman spectrum.

Infrared absorption measurements were performed using a Bruker Vertex 70 FTIR spectrometer. Thin discs were pressed without diluent in a 13 mm diameter die under 10 tonnes of applied pressure. Spectra were recorded using a high D* MCT detector at 4 cm^{-1} resolution and 512 scans were summed.

Powder X-ray diffraction measurements were carried out on a Siemens D5000 diffractometer with a Cu_α source and beryllium detector. Approximately 200 mg of sample were placed in a rotating sample holder. Measurements were taken from $5 - 85^\circ$ at $1.3^\circ\text{ min}^{-1}$.

Transmission electron microscopy (TEM) measurements were undertaken using a Technai T20 microscope with an accelerating voltage of 200 keV. Samples were dispersed in methanol before being deposited on holey carbon film ($300\ \mu\text{m}$ mesh grid, Agar scientific) prior to inspection. Elemental mapping was performed via energy filtered imaging of the nickel, carbon and oxygen K-edges (40, 20 and 35 eV slit widths for 855, 284 and 532 eV energy levels respectively) using the three window technique with a a Gatan image filter. Powder X-ray diffraction measurements were carried out on a Siemens D5000 diffractometer with a Cu_α source and beryllium detector. Approximately 200 mg of sample were placed in a rotating sample holder. Measurements were taken from $5 - 85^\circ$ at $1.3^\circ\text{ min}^{-1}$.

UV-vis measurements were performed using a Perkin-Elmer lambda 850. This utilises tungsten-halogen and D_2 lamps, coupled to an R6872 photomultiplier detector to record spectra. *Ca.* 10 mg sample was diluted in 50 mg Barium Sulphate (Fisher technical grade) and placed in the Harrick high temperature

diffuse reflectance sample chamber (with SiO₂ windows). Spectra were recorded between 600-250 nm with a resolution of 0.1 nm. Barium sulphate was also used as a reflectance standard.

2.2 INS Reaction Testing Apparatus

Although still in relative infancy compared to other spectroscopies, INS is increasingly being used for the characterization of heterogeneous catalysts [77][69][78][60]. As already discussed, there are a number of reasons for this. Firstly, as it is a non-optical technique, INS can characterise black samples (such as reacted catalysts). It can also probe a wide wavenumber range (10-4500 cm⁻¹) and finally, as the technique is uniquely sensitive to hydrogen atoms, spectra can be obtained that emphasise a hydrogenous component that has been adsorbed onto a catalyst. Despite this upwards trend in research activity, there has been little work done on addressing the issues with sample preparation associated with the handling of relatively large quantities of the potentially hazardous chemicals that can be present in catalytic systems. The inherent insensitivity of neutrons means that samples have to be prepared on a scale of *ca.* 10 g. This in turn necessitates the scale up of reactants such as helium, hydrogen and oxygen to flow rates of litres per minute. This dearth of developmental work is no doubt in part due to the fact that there are only a handful of neutron scattering facilities worldwide and that there is not yet a sufficient user group requiring the apparatus to be constructed. Nevertheless, some literature does exist on the development of sample cells and reactor systems. Nicol has described sample cells that are capable of studying chemisorbed species (e.g. hydrogen) in a flow-through environment [79]. Mitchell *et al.* have also described cells that are able to carry out investigations into adsorption systems [44] that include a combination of flow-through and batch style reactors made from either aluminium or stainless steel. Lastly, Turner *et al.* have described apparatus for studying catalysts and catalytic processes using neutron scattering [80; 81]. The difference between this final body of work and the previous two examples is that the systems designed are for neutron diffraction measurements rather than inelastic neutron scattering measurements. Although the apparatus is for different measurements, some of the sample handling issues



Figure 2.3: Picture of ISIS gas handling system. Reactor and furnace can be seen on the right of the fume hood and the gas manifold and mass spectrometer are on the left of the picture.

are relevant to investigations of reactive catalytic systems generally.

The lack of established INS catalyst preparation hardware has necessitated that an aspect of this project be focussed on the development of a suitable gas handling arrangement and subsequent reactors that can handle these large sample sizes and maintain steady-state reaction conditions for extended periods of time. Other considerations for reactor design is that it should be capable of high temperatures, pressures and be resistant towards hydrogen embrittlement. A reaction system and a number of reactor configurations are hereby described that have enabled INS samples to be prepared. The performance of the reactors will also be evaluated.

Inelastic neutron scattering reactions and measurements were carried out at the ISIS spallation neutron source, Rutherford Appleton Laboratory, Oxfordshire. The reaction system broadly comprises a gas manifold, reactor and furnace and exhaust gas analyser. A picture of the gas control apparatus is given in figures 2.3 and the schematic of the reaction rig in 2.4. Components are connected using 1/4" o.d. stainless steel tubing and Swagelok tube fittings. Gas flow is controlled by four Hastings model HFC302 mass flow controllers attached to a

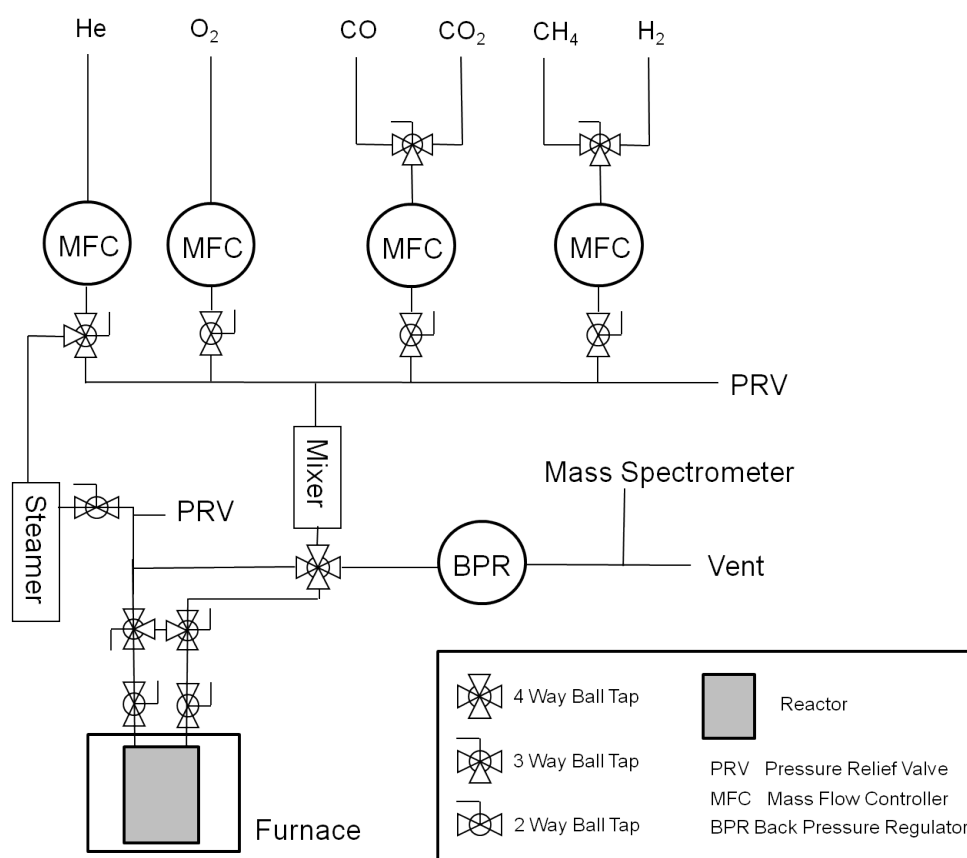


Figure 2.4: Schematic of ISIS catalyst preparation arrangement

Teledyne THPS-400 controller. These controllers have been calibrated for nitrogen use but use of gas correction factors allows other gases to be accurately metered. One controller has a maximum flow rate of 1500 sccm to allow for the larger flow rate of the carrier gas, one has 150 sccm, and two have 200 sccm (all with respect to nitrogen). Pressure is controlled up to 20 bar using a back pressure regulator (BPR, Parker Veriflo ABP-1ST-43-PP-X4) which is positioned after the mass flow controllers. Pressure relief valves (PRV, Parker HPRV S4A-BN-K1-319) are present before and after a heated saturator vessel in order to prevent over-pressurisation. The saturator itself provides the facility to force gas through a liquid to provide a vapour pressure of liquid reactants, such as water for the steam reforming of methane. The saturator can be filled without removal and an overflow ensures that the liquid volume does not exceed safe limits. The bubbler has a thermocouple (Trip-TC) in contact with its outer surface and is wrapped in heating tape (Farnell, power 40 W/m, part no. 397-750) and insulated. This is connected to an over-temperature trip (Eurotherm 2132i) set below the boiling point of the liquid to prevent excessive pressurisation of the vessel. A second thermocouple is immersed in the saturator liquid and is connected to a PID controller (Eurotherm 3508) to control the heating on the saturator. A mixing vessel, ensures turbulent flow by forcing the gas mixture to pass between Ballotini glass spheres encased in a wide bore length of Swagelok. To prevent condensation in the mixing volume, the output from the saturator joins the other gases downstream. All lines carrying vapor from the saturator are trace-heated with heating tape that is controlled with PID controllers (Eurotherm 3508) and insulated. Other thermocouples are attached to components of large mass to ensure they are maintained at the required elevated temperature. Overall, these thermocouple and heating tape arrangements ensure the unit operates without cold spots in the apparatus that would otherwise cause water vapour to condense in the line. The entire line can be evacuated for leak-testing and to purge any residual gases before or after reaction. The reactor is held inside a bucket furnace (Instron SFL, model no: TF105/3/12/F controlled by Eurotherm 3508) and can be isolated using high-temperature valves (Parker NV series, rated to 811 K) on the input and output connections. The valves sit above the furnace and are shielded by the use of thin, circular, loose-fitting steel baffles and ceramic

tiles that sit in and above the furnace bore to minimise heat loss. Depending on the configuration of reactor used, the reactor can then be isolated from the line and either (i) transferred to a glove-box (MBraun UniLab MB-20-G, $[\text{H}_2\text{O}] < 1 \text{ ppm}$, $[\text{O}_2] < 2 \text{ ppm}$) for further processing of air sensitive samples (u-tube configurations), or (ii) loaded directly into the neutron beam (Inconel[®] in-situ configuration). After the reactor, it is possible to install a cold-trap that could be used to condense liquid products (e.g long chain Fischer-Tröpsch products) if desired. Monitoring of the reaction is followed in real-time using a quadrupole Mass Spectrometer (MS, Spectra Microvision plus) which samples the exhaust line. Flow is controlled into the instrument by a needle valve. The mass spectrometer can be used as a qualitative and to an extent quantitative indicator of the reaction progress. It would also be possible to install other analytical techniques, such as GC, to provide fully quantitative reaction data if so desired.

2.3 Reactor Designs

As the project has progressed, limitations in the reactor cells have become apparent and has resulted in the development of second and third generation reactors. Their development, and relative strengths and weaknesses are discussed herein.

2.3.1 Stainless Steel U-Tube

The initial reactor was a simple design in the form of two 3/4 inch tubes connected using reducing unions and a 1/4 inch tube bent into a U-shape. The design for this reactor is shown in figure 2.5. Spot welded wire gauzes at the lower end of the large tubes provided supports to hold quartz Raschig rings on the inlet and the catalyst on the outlet. The inlet arm was designed to pre-heat the gas before encountering the catalyst and the Raschig rings were used to ensure a convoluted flow path to achieve this objective as well as to allow for further mixing of the gas. Shut-off valves were located directly above the reactor inlet and outlet allowing the sample to be isolated under helium after reaction. This allows the sample to be disconnected from the reaction rig and transferred to the

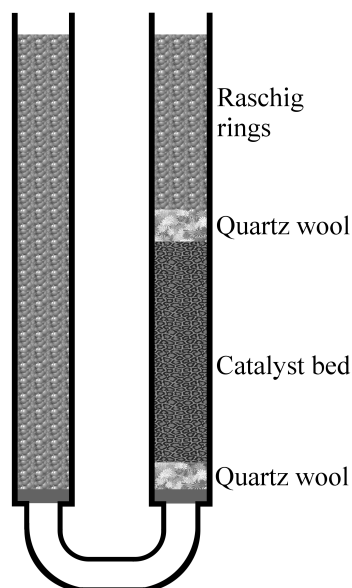


Figure 2.5: Schematic of stainless steel U-tube reactor

glovebox without being subject to the atmosphere. The reactor was held inside a bucket furnace (Instron) attached to a temperature controller (Eurotherm), with a quartz wool plug inserted to minimise heat loss due to convection. This design is capable of reacting around 10 g of catalyst and was rated up to 12 bar. The U-tube arrangement is reasonably straight-forward and inexpensive to construct, and can be easily applied to follow specific reaction treatments, e.g. acquisition of INS spectrum of a catalyst after a timed exposure to a particular mixture of gases at a specified temperature. However, there are limitations. Firstly, the stainless steel has a maximum operating temperature of around 700 K especially when using corrosive substances such as steam. This makes it impossible to use for high temperature systems. This has quite specific implications for reforming reactions as higher temperatures helps to negate influences from the water gas shift reaction - a serious consideration at 700 K. The main flaw however, is in handling treated samples. The reactor design is unsuitable for direct transfer into the neutron beam line and therefore requires that the reacted catalysts and resultant overlays have to be externally transferred into a suitable isolatable aluminium sample can which results in disturbance of the sample during the

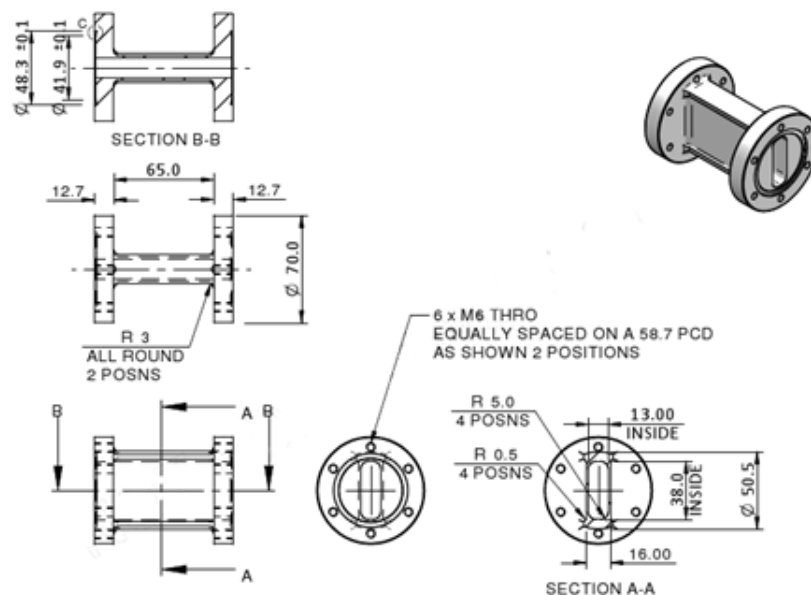


Figure 2.6: Schematic of Inconel[®] reactor cell

transfer. It is also a difficult exercise to consider subsequent sample treatments on that sample, as it involves re-loading the material in to the U-tube reactor and re-connecting the reactor to the gas handling facility. In addition to the challenge of handling potentially pyrophoric materials and the possibility of induced radiation in metal containing catalysts can add a further complication. It is with these limitations in mind that the second generation of reactor cells were commissioned.

2.3.2 Inconel[®] Reactor

One way round the sample handling difficulties mentioned above is to use a solid cell that can be isolated and readily connected/disconnected to/from the gas manifold whilst at the same time being of a design suitable for “in-situ” INS measurements, thereby facilitating direct transfer between the gas handling line and the spectrometer. Figure 2.6 presents drawings of the body of a reaction cell suitable for this task whilst photographs of the assembled cell are shown in figures 2.7 and 3.4. The cell is a variation on an aluminium sample cell

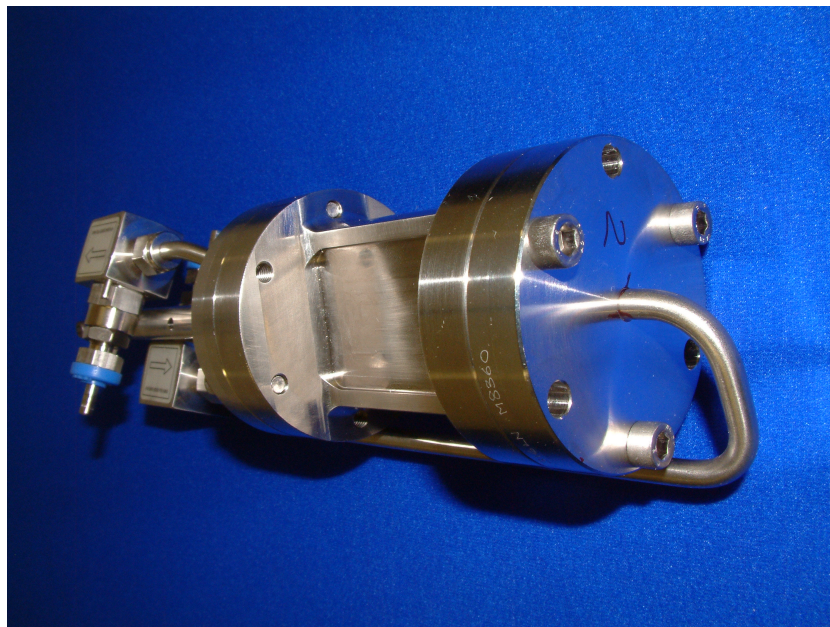


Figure 2.7: Picture of assembled Inconel [®] reactor



Figure 2.8: Picture of assembled Inconel [®] reactor mounted on an INS sample stick prior to measurement

described by Nicol [79] and is an elaboration on the stainless steel tubular reactor designed, built and tested by Parker and co-workers [44]. In our case, the body of the cell is manufactured from Inconel[®] and has an approximately rectangular section between two DN40 ConFlat (CF) flanges. Inconel was selected because it has a higher operating temperature than stainless steel. This specification is necessary for the reforming of methane, which can require temperatures in excess of 800 K over supported nickel catalysts [13] in order to minimise the water gas shift reaction. High pressure operation is also desirable for certain reactions for example the Fischer-Tröpsch process, therefore the INS “windows” through which the neutrons will pass are 1.5 mm thick. These arrangements allow for an upper operating pressure of 20 bar. The width of the internal sample cavity is 13 mm, so that the total neutron path through the cell is therefore 16 mm. CF sealing flanges are made of stainless steel and use standard copper gaskets. 1” o.d. stainless steel tubing passes through the flanges and is centrally welded on the lower cap, but off-centre on the top to accommodate a threaded rod for mounting onto a centre stick for placement in the neutron beam (see figure 3.4). The openings are protected with steel gauze, allowing granulated catalysts to be used directly in the reactor, whilst powdered samples are supported between quartz wool plugs packed above and below the sample area to keep them out of the beam path. Gas flows into the reactor body from below, exiting above, thus providing a degree of pre-heating to the reactant gases. High temperature valves (Parker NV series, rated to 811 K) are mounted above the cell to fit within the 10 cm bore of a standard cryostat [82] and allow the cell to be sealed after reaction. The sample volume is designed to over-fill the beam on the TOSCA spectrometer [62] which has a cross section of 40 mm by 40 mm. The reactor is formally certified by the ISIS environmental section for use at up to 898 K and 20 bar.

2.3.3 Quartz U-Tube Reactor

Whilst the Inconel[®] reactors are designed to go to temperatures of 898 K (625 °C), during the course of the project it became clear that the water gas shift reaction (equation 1.5) was still highly favoured at these maximum operating



Figure 2.9: Picture of high temperature quartz reactor(post steam reforming reaction)

temperatures and so development of a reactor that could achieve operating temperatures of up to 1000 K was commissioned. The design focussed on the use of quartz as the reactor material as it can withstand the high temperatures and is resistant to the corrosive nature of steam. Quartz was also deemed to be suitable as higher pressures (such as those desired in Fischer-Trøpsch chemistry) are not required for the methane reforming studies under consideration here. 1/2" 316 stainless steel tubing was fused to 30 cm long 12 mm diameter quartz tubing. High temperature valves (Parker NV series, rated to 811 K) were situated immediately above the reactor on both the inlet and the outlet allowing the sample to be isolated under helium after reaction. A quartz frit was placed on the outlet side of the reactor to support the catalyst and the two lengths were fused into a "U" using 1/2" quartz. Quartz Raschig rings were located on the inlet before the catalyst in order to create a turbulent flow which allows additional gas mixing as well as preheating of the reactant gasses. The reactor was held inside a bucket furnace (Instron) [2.10](#) attached to a temperature controller (Eurotherm), with a quartz wool plug, ceramic tiles and stainless steel and ceramic baffles were



Figure 2.10: Picture of quartz reactor in furnace (post steam reforming)

inserted in and placed on top of the furnace to minimise heat loss due to convection and to ensure the stainless steel components were kept below 800 K. Official temperature ratings for the reactor were 1000 K and 2 bar respectively.

2.4 Performance Results

The three reactors described above have all been used in the methane reforming studies. The relative performance of the reactors in terms of their ability to prepare samples (*i.e.* reaction performance) will therefore be discussed within the context of the two reforming reactions in later chapters. It is however, important to discuss the results of the *in-situ* Inconel[®] reactor in terms of its performance in obtaining an INS spectrum compared to, for example, the traditional “*ex-situ*” aluminium sample cans. Reactor performance was analysed by performing the adsorption of methanol on η -alumina which has already been reported using the standard alumina sample cans [83].

A known mass of η -alumina (22.9 g Ineos Chlor Ltd. Ref. 25867/19A) was loaded into the Inconel[®] sample cell between quartz wool plugs ensuring that the alu-

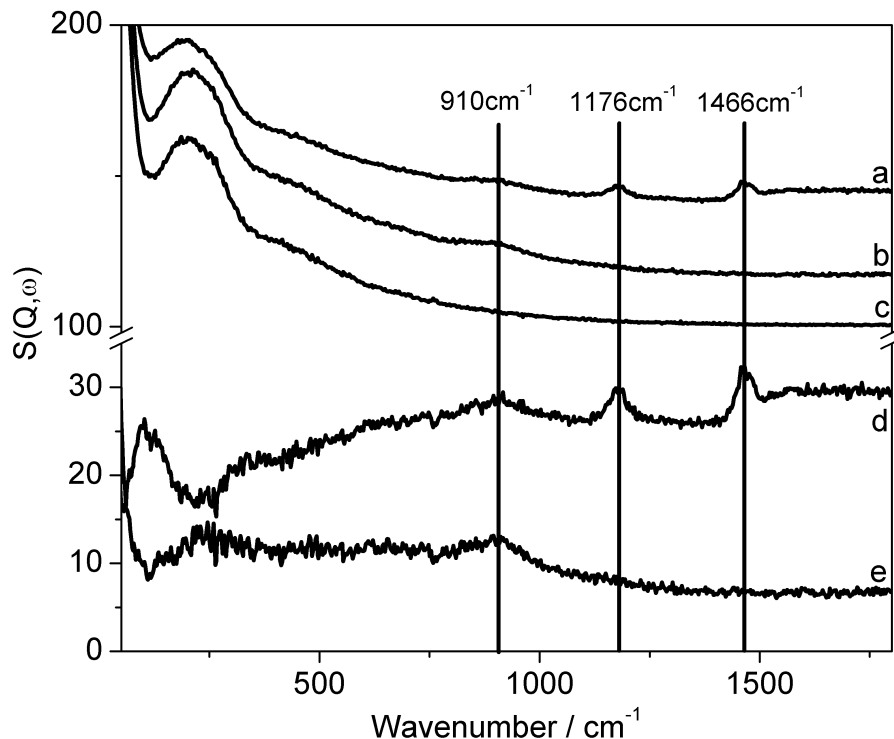


Figure 2.11: Medium energy INS spectra (2017cm^{-1}) (a), alumina and reactor after methanol adsorption, (b), activated alumina and reactor, (c) empty Inconel[®] reactor, (d) alumina post adsorption, (e) alumina pre- adsorption. (d) and (e) are subtracted spectra

mina was all located within the cross section of the neutron beam. The alumina was first activated by heating to 623 K under 100 sccm He for 90 min before the collection of INS data. Subsequently, the sample was reattached to the rig, and the same flow of helium was this time passed through the bubbler unit which contained methanol (Aldrich $\geq 99.9\%$) for an hour at room temperature. This was then heated to 473 K , where a pure He flow was maintained for 60 min to remove physisorbed material. Spectra were collected on the MERLIN spectrometer at the ISIS Facility, Rutherford Appleton Laboratory. By selecting an incident energy close to the vibrational transitions of interest it is possible to achieve good resolution around this vibrational region [60]. It is therefore necessary to perform measurements at a number of different incident energies to achieve the full spec-

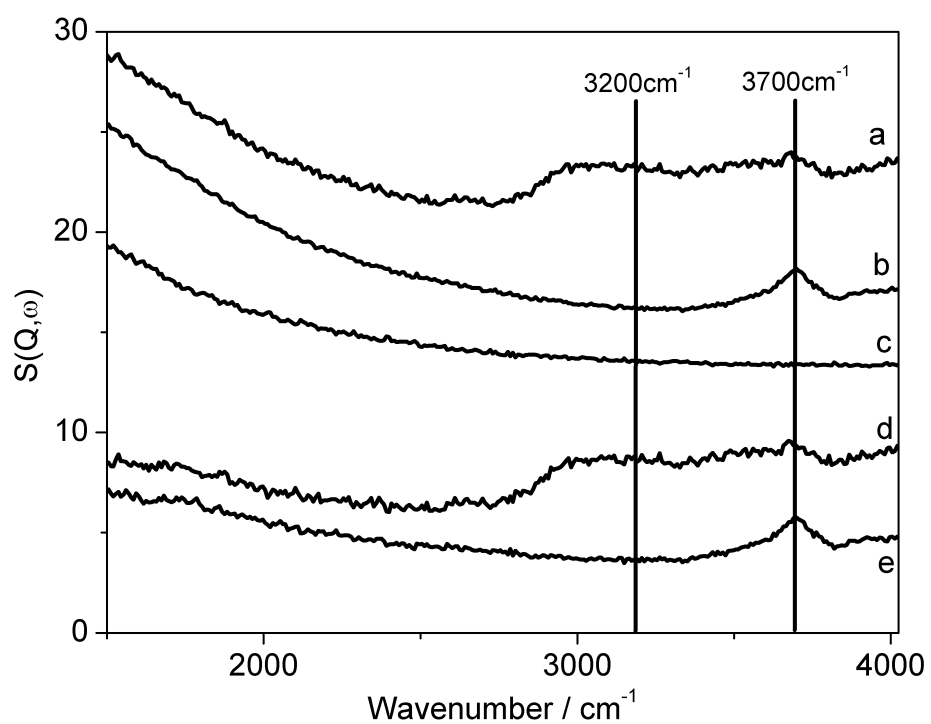


Figure 2.12: High energy INS spectra (4840cm^{-1}) (a), alumina and reactor after methanol adsorption, (b), activated alumina and reactor, (c) empty Inconel[®] reactor, (d) alumina post adsorption, (e) alumina pre-adsorption. (d) and (e) are subtracted spectra.

tral range of 40-4500 cm^{-1} . In this study, two incident energies were selected in order to probe the adsorption of methanol.

Figures 2.11 and 2.12 show the spectra recorded with incident neutron energies of 250 meV (2017 cm^{-1}) and 600 meV (4840 cm^{-1}) respectively. (a), (b) and (c) are raw spectra of alumina post methanol adsorption, activated alumina and the empty reactor. (d) and (e) show the alumina post- and pre- adsorption, after subtraction of the can, i.e. (d) = (a) - (c) and (e) = (b) - (c).

Figure 2.11 displays the spectra collected at the lower incident neutron energy ($E_i = 2017 \text{ cm}^{-1}$). A number of features are worth mentioning. Firstly spectrum (a) shows two peaks that are clearly visible at 1176 and 1466 cm^{-1} . These peaks become even more clear after subtraction (d). The 1176 cm^{-1} band is assigned to the methyl rock whilst the 1466 cm^{-1} feature is assigned to the methyl deformation of chemisorbed methoxy groups. The second of these is a result of the dissociative adsorption of methanol on the alumina surface [83]. A weaker peak at 910 cm^{-1} , present on the activated (Figure 6(e)) and methanol-adsorbed (Figure 6(d)) alumina is due to the deformation of surface hydroxyl groups present on the alumina [83]. As mentioned in the introduction, infrared spectroscopy would be unable to observe the 1176 cm^{-1} peak due to the spectral “cut-off” of alumina that occurs around 1200 cm^{-1} [69; 83]. Figure 2.11 therefore highlights the potential of INS to observe a wide range of spectral information that would not otherwise be available with traditional optical spectroscopy. In fact, the vibrational information available in figure 2.11 goes down to ca. 300 cm^{-1} . Specifically, although the methyl deformation mode is seen in infrared experiments, the important methyl rock is often not readily observable in the optical measurement. Perhaps even more interesting is the observation of the hydroxyl deformation in figure 2.11(e). Hydroxyl groups play an important part in the surface chemistry of the alumina and so it is often desirable to study vibrations associated with this functional group. The O-H deformation can however, complicate infrared spectra, most notably in terms of the Evans hole phenomenon [84]. Essentially this involves the primary overtone of a hydroxyl deformation mode overlapping with the broad O-H stretching bands that are red-shifted by hydrogen bonding [84]. Understanding the actual energy of the alumina hydroxyl deformation mode by

Wavenumber / cm^{-1}	Assignment
3700	Alumina $\nu(\text{OH})$
3200	Methoxy $\nu(\text{CH})$
1466	Methyl deformation
1176	Methyl rock
910	Hydroxy deformation

Table 2.2: Summary of INS Vibrational Assignments Pre and Post Methanol Adsorption

INS is highly beneficial as it can greatly assist in the understanding of the spectral patterns sometimes encountered in the more routine infrared measurement of metal oxide and zeolite surfaces.

In the high energy transfer region displayed in Figure 2.12, the reactor itself shows a significant contribution to the overall spectrum (Figure 5(c)). This shown by a long curve that tails out towards higher wavenumbers. (d) and (e) show how subtraction results in a flatter baseline that enhances the appearance of spectral features. A peak at 3700 cm^{-1} is visible on the activated catalyst (figure 2.12(b) and (e)) and is assigned as the stretching mode of surface hydroxyls associated with the alumina [69]. This feature is less visible on the catalyst plus adsorbate (Figure 2.12a and (d)) possibly due to overlapping contribution from the OH group of the adsorbed alumina. (a) and (d) also show a broad feature centred at around 3200 cm^{-1} , which can be assigned to CH stretching vibrations of the methoxy species [83]. As previously mentioned, further resolution of these peaks is not possible due to the constraints of MERLIN. Background subtraction is an important part of obtaining useful INS spectra of heterogeneous catalysts [44] and both figures 2.11 and 2.12 show this to be possible with the *in-situ* Inconel [®] cell. This is in no small part due to the consistency of the mounting of the sample in the neutron beam path but is also due to the fact that the subtraction involves the original catalyst sample and not a separate sample recorded previously, and then manipulated in the glovebox as would have to be the case with the U-tube reactor configuration. A summary of the vibrational assignments drawn from the INS spectra is presented in table 2.2.

2.5 Discussion of Performance and Challenges

This study has demonstrated that the gas handling system and the *in-situ* INS cell constructed and described here is capable of reacting *ca.* 20 g alumina with methanol. This is an important benchmark as it proves that quantities of catalyst suitable for INS measurements will be able to be reacted in a single operation and not require multiple batches of catalyst to be reacted and subsequently combined for the measurement. It also demonstrates that the saturator works as expected. The use of a combined reactor and sample holder considerably simplifies sample handling, especially where volatile or air sensitive samples may be used. This initial study has also shown that the *in-situ* sample cell has been able to reproduce the spectrum associated with a benchmark adsorption system [83] without the need for external sample manipulation. Probably the biggest advantage of the new experimental methodology is that it is a highly adaptable system that is capable of examining a wide number of reaction systems such as reforming, and Fischer-Tropsch chemistry. The sample cells are robust and can be exposed to a variety of reaction conditions including high pressures and reasonably high temperatures. They are also able to be disconnected from the system thereby allowing as near to *in-situ* INS measurements as is possible to be achieved. Good spectral analysis has also been demonstrated with background subtraction routines that yield the vibrational spectrum of the actual chemisorbed species being reliable and fairly simple. As well as the simplicity of the subtraction, the removal of the background is also greatly improved as the exact same sample, undisturbed, is used before and after reaction. This method should therefore be considered the intended standard for such measurements. It is noted however, that the use of Inconel[®] as the cell construction material does have one significant disadvantage. Figure 2.11 shows spectral intensity to increase on decreasing wavenumber. This intensity is the result of a bulk phonon mode from the Inconel[®] that is centred about 230 cm⁻¹. In practice, this results in a spectral cut-off value of approximately 300 cm⁻¹. Although this is restrictive, it is a significant improvement on traditional infrared spectrometry and the intense elastic peak of the neutrons makes measurements below *ca.* 100 cm⁻¹ difficult in practice anyway.

Although the *in-situ* reactor is of great benefit in the study of working catalysts there are other, more general problems associated with the technique. One factor that needs to be considered is that of obtaining sufficient neutron spectrometer time. Studying small amounts of surface species on catalyst overlayers requires long acquisition times, especially in the case of direct chopper instruments where three separate measures need to be made in order to achieve good resolution across the entire spectral range. Furthermore, in order to cope with high pressures, the *in-situ* cells are of considerable mass. As INS spectra are typically acquired at cryogenic temperatures < 30 K, these cells can take a long time to cool to these temperatures once removed from the flow apparatus (where they may have been operating at up to 898 K. This represents a sizeable change in temperature that a significant amount of time. One way of minimising this dead time is to immerse the isolated cell in liquid nitrogen before it is inserted into the spectrometer cryostat but even then, the samples take hours of valuable beam time to cool.

The second issue with large reactor mass is that of radiation. This problem varies with different neutron spectrometers. As MERLIN and MAPS are chopper spectrometers, the incident neutron flux is relatively low, which minimises the induction of radioactivity in the Inconel[®] cell so that, upon extraction from the spectrometer, the sample holder is readily manageable, even after long acquisition periods (e.g. 16 hours). In contrast, the incident neutron flux is considerably increased on non-chopper inelastic spectrometers such as TOSCA and extended spectral acquisition can lead to the induction of considerable radioactivity of the cell body. Under these conditions, sample extraction procedures have to be more carefully managed and further dead time can result.

One possible solution to these problems is the construction of cells designed to operate at lower pressures and temperatures. Methane reforming catalysis is at the extreme end of heterogeneous catalysis as is Fischer-Tröpsch chemistry. Systems requiring more benign conditions could easily be carried out in similarly designed *in-situ* cells to that described here but with a lot less reactor mass. If the design were to be adapted for less arduous conditions, the reduced cell mass would result in reduced cooling times and possible neutron activation problems. New cell designs addressing these attributes have been commissioned and will be

available from late 2013.

2.6 Calibration and Quantification of Hydrogen Modes

The development of the inelastic neutron scattering technique can be broadly discussed in two categories; 1. development of apparatus and 2. calibration of the spectrometer with respect to hydrogen signals in order to allow quantification of the hydrogen that is present in any given sample. The previous section dealt with the former whilst this section will describe the procedures that will ultimately lead to hydrogen quantification.

2.6.1 Development of Method and Calibration of INS Spectrometer

There are a number of means by which one can measure the quantity of carbon retained by a catalyst during a reaction. One of the most common methods is temperature programmed oxidation (TPO) in which surface carbon is oxidised to CO_2 at elevated temperatures which can then be quantified [37]. What is not so well established, is how to quantify hydrogen retention. Low concentrations of surface hydrogen can render elemental analysis inaccurate and side reactions (such as water gas shift chemistry in the case of reforming [13]) can make hydrogen mass balance calculations difficult if not impossible. To be able to fully quantify surface hydrogen would allow for a more complete analysis of the elementary reactions occurring on a catalyst surface and would also allow for comments to be made on the relative kinetic rates of these steps. Spectroscopy could be a powerful tool in quantifying surface hydrogen as the amount of hydrogen on a surface will be proportional to the vibrational signal it produces. It is however, not a straightforward task. One of the difficulties of using infrared spectroscopy for quantitative analysis is that the extinction coefficient of any mode is specific to a given molecule. This means that it is not possible to transfer extinction coefficients between molecules: each molecule must be individually calibrated.

For adsorbed species on surfaces this is rarely possible and is meaningless when there are a mixture of species present. The problem arises because the infrared intensity is determined by the interaction of electromagnetic radiation with the electrons; since the electronic structure of a molecule is unique, it follows that the intensities will be specific to that molecule. As discussed in the introduction, this problem does not occur in INS spectroscopy since the interaction of the neutron is with the atomic nucleus; the electrons are irrelevant. The observed intensity of an INS spectral band, S , is a function of both the energy, ω , and the momentum, Q , exchanged during the scattering process. The momentum transfer is an experimental variable which can be kept the same between measurements and the cross section is a fundamental property of each element, so only the amplitude of vibration is a molecular property. If we make the assumption that say a CH stretch can be treated as a harmonic oscillator, then the amplitude of vibration is given by equation 2.1:

$$(U_i)^2 = \frac{\hbar^2}{2\mu\omega_i} \quad (2.1)$$

Where U_i is the root mean square displacement of the atoms in the mode, μ is the reduced mass of the oscillator. Thus band intensities are dominated by the number of oscillators and the amplitude of the oscillators. From 2.1 it can be seen that the Debye-Waller factor (the exponential term) in 3.1 is dominated by the low energy modes, since a surface species and the model compounds have many of these, the Debye-Waller factors will be similar. The result is that a calibration is transferable between similar species.

2.6.1.1 Experimental

INS spectra were recorded using the MAPS spectrometer described in the introduction. Spectra were recorded at a single incident energy of 4840 cm^{-1} . This energy is important as it covers the region associated with both the C-H and O-H stretching regions of the vibrational spectrum which will be used to make the

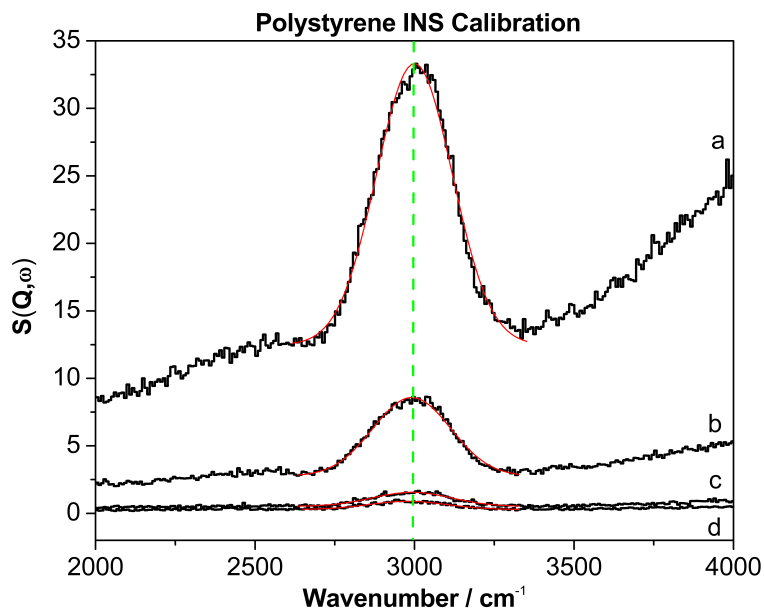


Figure 2.13: INS spectra of the $\nu(\text{C-H})$ and (O-H) region for different known masses of polystyrene (a) 969 mg, (b) 242 mg, (c) 41 mg and (d) 23 mg.

calibrations. A full vibrational spectrum from 40-4500 cm^{-1} was not therefore required.

Two compounds were used as external calibrants: polystyrene ($[-\text{CH}_2\text{CH}(\text{C}_6\text{H}_5)-]_n$, Aldrich, gel permeation chromatography standard, powder, typical molecular weight = 29300) and brucite (magnesium hydroxide, $\text{Mg}(\text{OH})_2$, Fluka, > 99 %). The polystyrene provided a reference for (C-H) stretching modes, whilst the brucite and talc provided reference spectra for compounds for (O-H) stretching modes. Known masses of these compounds were loaded in to sachets made from aluminium foil, which were contained within aluminium sample holders then the spectra recorded. In this manner the integrated vibrational peaks from the INS spectra could be directly correlated with the mass of the reference material for both C-H and O-H modes. Spectral acquisition was performed at 20 K.

Polystyrene $[-\text{CH}_2\text{CH}(\text{C}_6\text{H}_5)-]_n$ was chosen as a reference material and a large molecular weight variant was selected so as to mitigate the effect of terminal groups. This allows the formula to be simplified to $\text{C}_6\text{H}_5\text{C}_2\text{H}_3$, which is equal to 8 hydrogen atoms per monomeric subunit. Figure 2.13 shows the INS spectrum

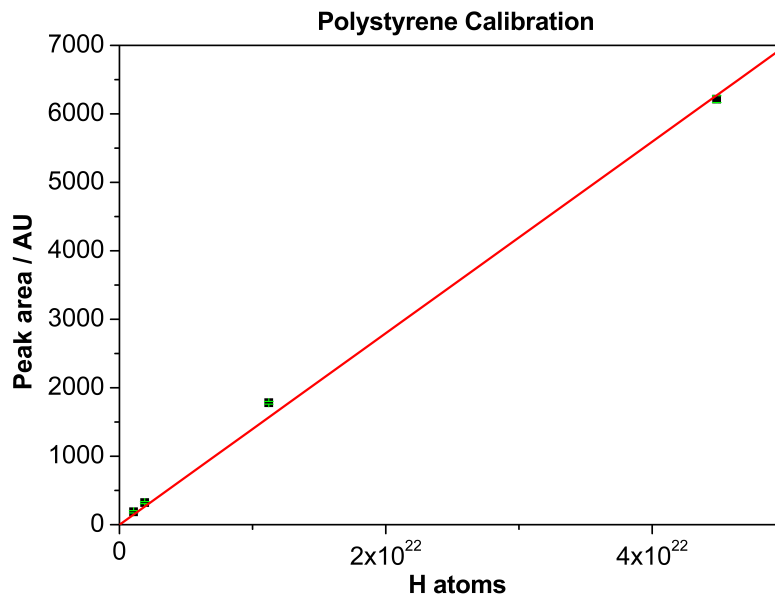


Figure 2.14: Best linear fit of INS peak area against known sample mass of polystyrene

for different masses of polystyrene recorded. 969 mg of sample yields a single broad feature centred at 3000 cm^{-1} , that can be attributed to the C-H stretching modes of polystyrene. A comparison against the corresponding infrared spectrum shows IR to be vastly superior in resolution as a number of discrete vibrational modes are able to be resolved [85]. This highlights the limitations of resolution associated with this technique. That said, it is possible to integrate the intensity of the INS peak to determine the number of H atoms associated with carbon present in the path of the neutron beam. As sample mass is decreased, so too is the INS response for the hydroxyl stretching region. Interestingly, it is still possible to observe and integrate the O-H stretch (and so determine the number of H atoms associated with oxygen) even when only 23 mg of sample is present in the beam. This suggests that INS is perhaps not as insensitive a technique as first thought.

A plot of integrated intensity for the n(C-H) feature as a function of sample mass is presented in Figure 2.14, which reveals a straight line with a correlation coefficient of $R = 0.9995$. The slope of this line corresponds to the response

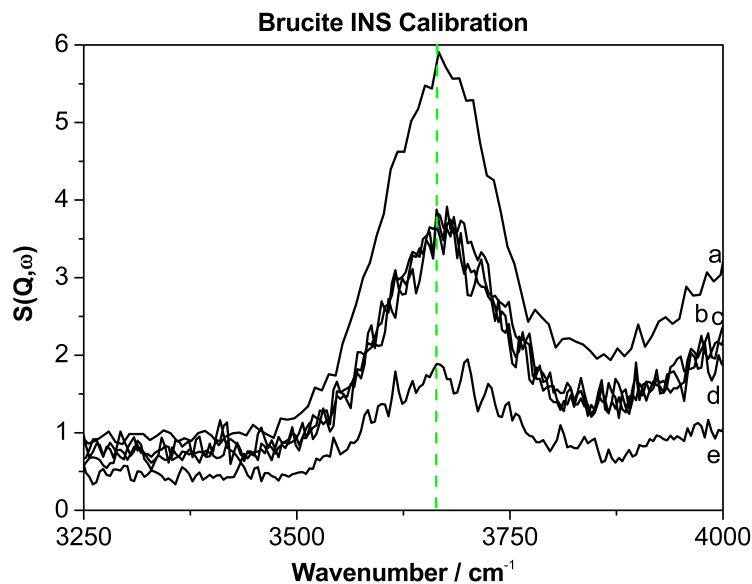


Figure 2.15: INS spectra of the $\nu(\text{C-H})$ and $\nu(\text{O-H})$ region for different known masses of brucite (a) 330 mg, (b) 152 mg, (c) 152 mg, (d) 152 mg and (e) 80 mg

factor for C-H containing species examined using this spectrometer configuration. The linearity of the response is consistent with the observations of Albers *et al* [86]. This confirms that the response of the spectrometer to different masses of molecular species is directly proportional to the number of hydrogen atoms present in the beam.

In order to determine the spectral response for hydroxyl groups (a functional group often present in catalytic overlayers) another standard compound was selected for analysis. Figure 2.15 shows the INS spectrum for different sample masses of brucite, $(\text{Mg}(\text{OH})_2)$, for which the formula mass affords 2 hydrogen atoms. The feature at 3650 cm^{-1} is assigned to the O-H stretch of hydroxyl groups. In a similar manner to that encountered with polystyrene, the intensity of this feature decreases as a function of sample mass. The resulting calibration plot is shown in Figure 2.16, where again peak intensity is shown to be directly proportional to sample mass. The quality of the fit is not as good as with the hydrocarbon ($R = 0.9680$), nevertheless, it is clear from this plot that the trend is linear and that INS is capable of detecting precise amounts of hydroxyl groups

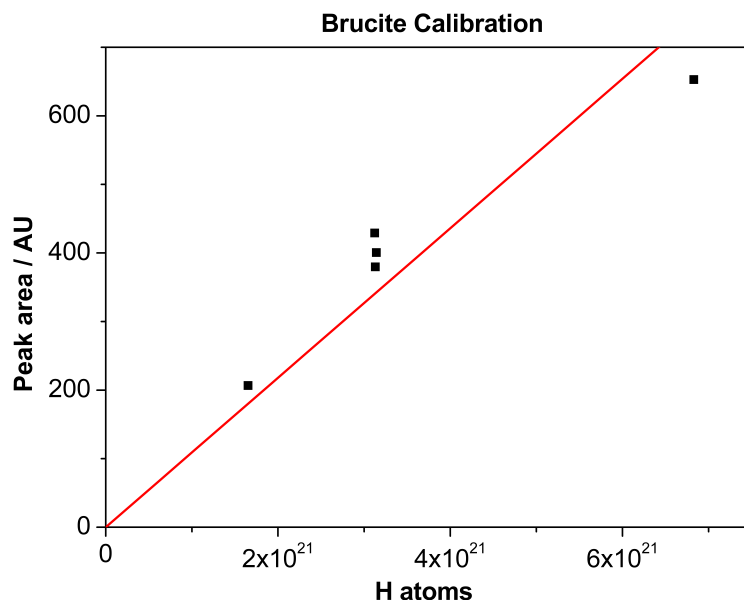


Figure 2.16: Best linear fit of INS peak area against known sample mass of brucite

as well as CH entities. In order to evaluate the degree of error inherent in making these absolute measurements, triplicate measurements were made for a brucite sample mass of 152 ± 1 mg. These measurements involved new samples in new sachets. The data points are contained within a standard deviation of $\pm 6.2\%$, indicating a good degree of precision within these measurements.

2.6.1.2 Discussion

Figures 2.14 and 2.16 show that quantifying the peak area associated with a particular vibrational mode of hydrogen (i.e. C-H or O-H) is possible. Although performed using molecular standards, these calibrations are transferable to measurements on a reacted catalyst. This will make it possible to obtain a value for the number of hydrogen atoms that are associated with both carbon and oxygen on a working catalyst surface. Comparing these values with post reaction temperature programmed oxidation will enable a ratio of surface carbon to hydrogen to be calculated, which in turn will allow comments to be made about the relative rates of a number of the elementary steps that are involved in this reaction.

Chapter 3

CO₂ Reforming of Methane

This section is concerned with the CO₂ or “dry” reforming of methane (equation 1.1). Although perhaps it would seem more obvious to look first at the industrially well established system of steam reforming before moving on to the less understood “dry reforming” reaction, generation and control of steam is not a trivial matter. It is on this basis that the project initially focussed on the experimentally simpler CO₂ system before moving on to examine the reforming of methane using H₂O.

This project has examined a range of Ni/Al₂O₃ and Ni-Au/Al₂O₃ reforming catalysts in an attempt to understand a number of aspects of the chemistry including; the nature and quantity of the carbon overlayers, the nature and quantity of the retained hydrogen and whether using gold as a dopant would offer improved resistance to coke formation. This chapter will be split into two broad categories; catalysts that result in (a) amorphous carbon formation and (b) those that result in graphitic carbon formation. The switch between the form of retained carbon is an inherent function of the catalyst preparative process (mainly selection of support material). That topic was examined at the University of Keele as part of a linked project. This thesis concentrates on the characterisation of catalyst performance and uses these catalysts to explore the form of both types of carbonaceous deposit. Characterisation of each catalyst, before and after reaction will be presented, as will a discussion on each coke forming system.

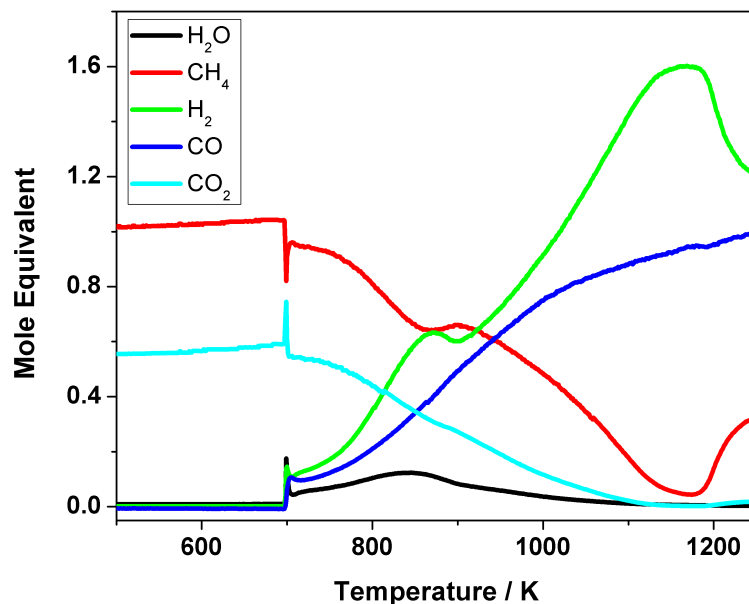


Figure 3.1: Temperature-programmed reaction (500 - 1300 K) of a 2:1 mixture of CH₄ and CO₂ over Ni/Al₂O₃ catalyst

3.1 Amorphous Carbon Characterisation

This first section will focus on the characterisation of the CO₂ reforming of methane over alumina-supported nickel and gold doped nickel catalysts that favour amorphous carbon laydown. It will also demonstrate how the INS technique described earlier can help to compare the performance of the nickel and the gold-doped nickel catalyst in terms of hydrogen retention on the catalyst surface

3.1.1 Results

3.1.1.1 Microreactor Studies

Both the Ni and Ni-Au catalysts were tested for reforming performance, firstly under temperature-programmed conditions. Figure 3.1 shows the temperature-programmed reaction profiles for the Ni/Al₂O₃ catalyst whilst figure 3.2 shows the temperature programmed reaction profile for the gold doped catalyst. The first point to note is that both samples display similar trends. The reaction ini-

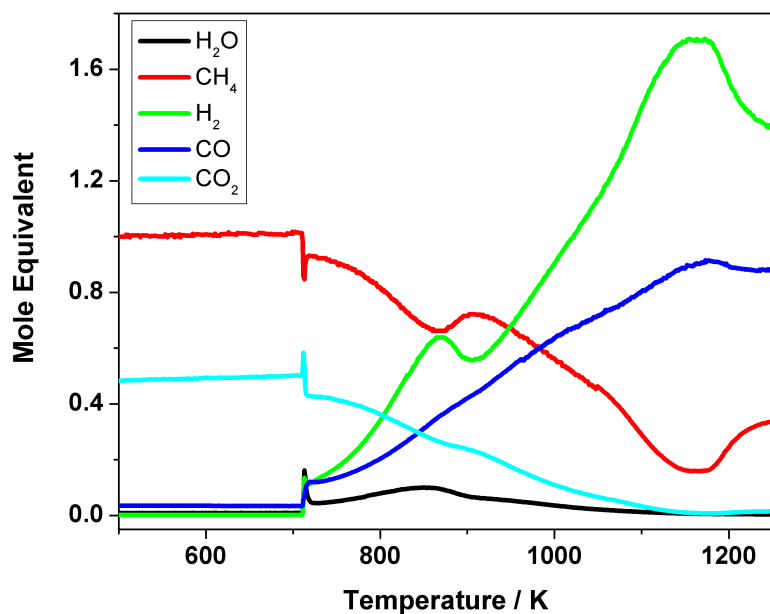


Figure 3.2: Temperature-programmed reaction (500 - 1300 K) of a 2:1 mixture of CH₄ and CO₂ over Ni-Au/Al₂O₃ catalyst

tiates at 708 K and then exhibits three distinct regimes. Hydrogen production increases with temperature until 873 K followed by a slight decrease before hydrogen production increases again. Hydrogen production appears to reach a second maximum at 1183 K before decreasing again. The low temperature maximum in the hydrogen production at 873 K corresponds to increased methane consumption and a maximum in the water production, whilst the CO and CO₂ traces do not show any inflection. This observation suggests that carbon is being retained by the catalyst at this point. Methane decomposition is producing additional H₂, some of which is reacting with CO₂ in the reverse water gas shift reaction, equation 1.6. As the temperature rises, this reaction pathway becomes less important, and H₂O production decreases, whilst the desired synthesis gas product begins to dominate. Above 1100 K total conversion of CO₂ is observed, and although the CH₄ concentration increases, the CO signal also continues to climb. Hydrogen production also decreases in this region and appears to be matched to the CH₄ conversion, indicating rapid and efficient release of hydrogen from the catalyst.

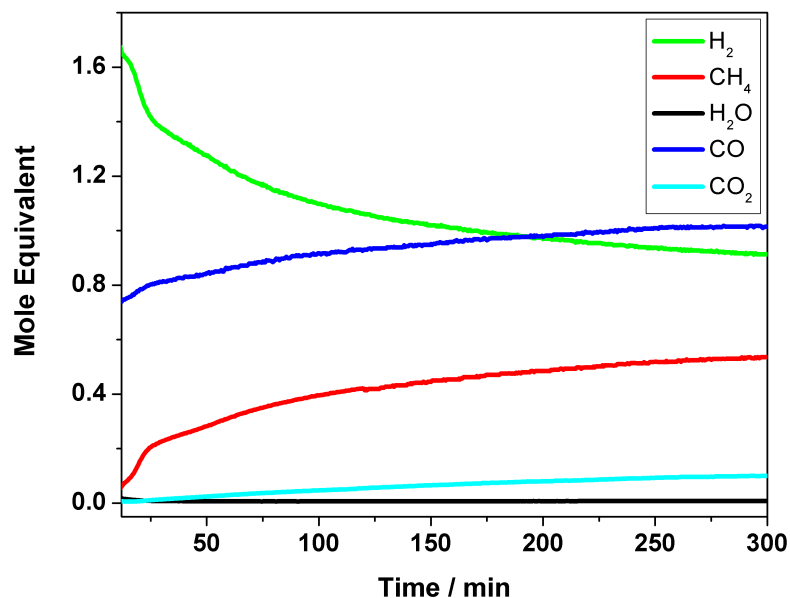


Figure 3.3: Extended reaction at 1073 K of a 2:1 mixture of CH₄ and CO₂ over Ni/Al₂O₃ catalyst

CO production, however, appears more complicated, possibly illustrating deposition of carbon at low temperature, which is later oxidised upon further heating. At 1073 K there is high conversion, with little contribution from the reverse water gas shift reaction, making it a suitable temperature for isothermal measurements.

The reaction profiles for the catalysts under extended reaction at 1073 K are shown in Figures 3.3 and 3.4. As time-on-stream increases, so to does deactivation of the Ni/Al₂O₃ catalyst produces less hydrogen, and more methane is apparent in the exit gases. Production of CO and CO₂ also increase with time. This process appears to continue, even after 300 min. The Ni-Au/Al₂O₃ profile is very similar but the changes in exit gas composition caused by deactivation occur more quickly, indicating a comparatively more rapid deactivation of this sample. For example, the CO concentration for Ni-Au/Al₂O₃ exceeds H₂ production after 15 minutes, yet for Ni/Al₂O₃ this characteristic production profile begins at 180 minutes. Both catalysts appear to approach steady-state operation at *ca.* 300

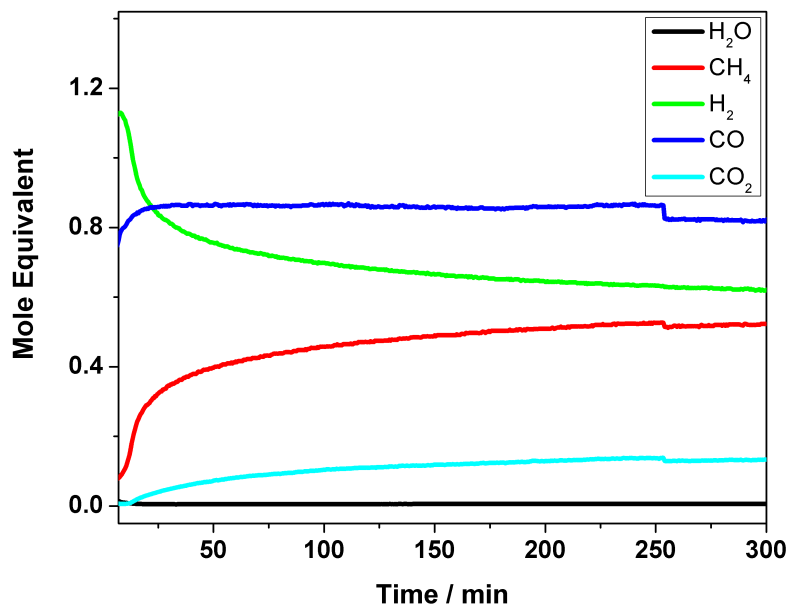


Figure 3.4: Extended reaction at 1073 K of a 2:1 mixture of CH₄ and CO₂ over Ni-Au/Al₂O₃ catalyst

minutes. It is noted that control reactions using only the support alumina showed no reforming activity.

Post-reaction TPO measurements of the micro-reactor samples are presented in Figures 3.5 and 3.6. Both are dominated by a single broad and intense feature with a desorption maximum at about 900 K for both the Ni/Al₂O₃ and Ni-Au/Al₂O₃ catalysts. The desorption range of 710 - 1010 K is indicative of a polymeric amorphous coke, C β [87]. The maxima for the two samples differ by around 70 K, which suggests there is some variation in morphology of the carbonaceous deposits. It is noted however, that this difference could be due to different catalytic effects if the Ni and the Ni-Au on the oxidation process [38]. The system was calibrated via the oxidation of graphite which yields a sharp peak at 1060 K, suggesting that the detected carbon is not of a graphitic nature. It is therefore concluded that further experimental evidence is required before a classification of the deposited carbonaceous material can be safely attempted.

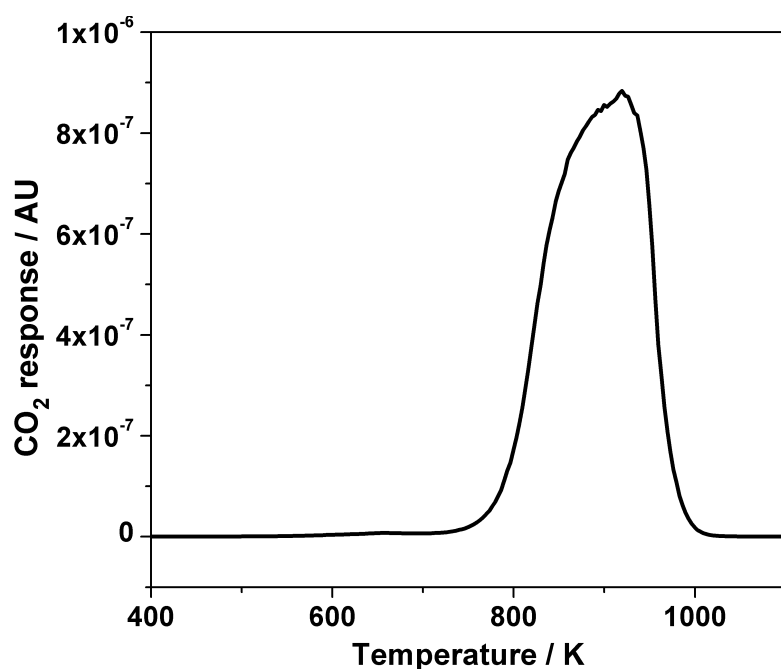


Figure 3.5: Temperature-programmed oxidation profile for Ni/Al₂O₃ after isothermal micro-reactor runs at 1073 K.

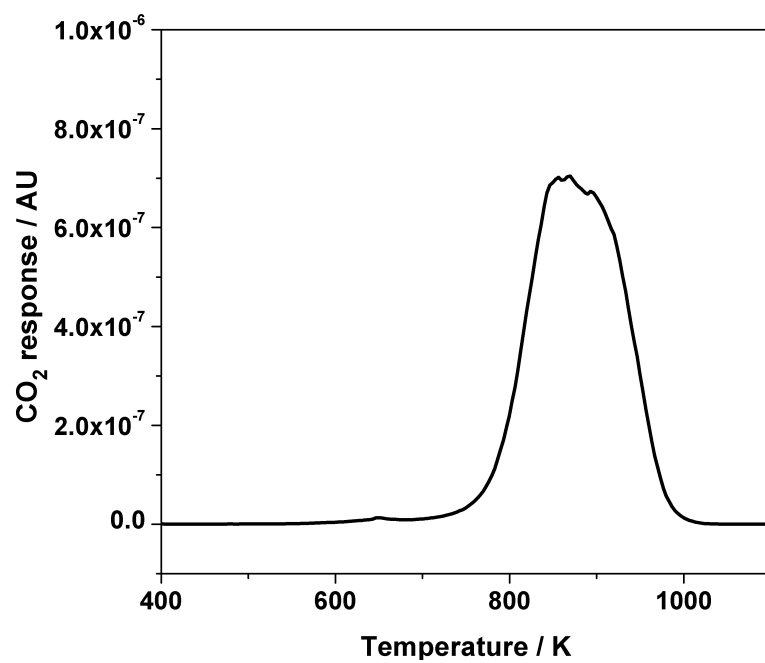


Figure 3.6: Temperature-programmed oxidation profile for Ni-Au/Al₂O₃ after isothermal micro-reactor runs at 1073 K.

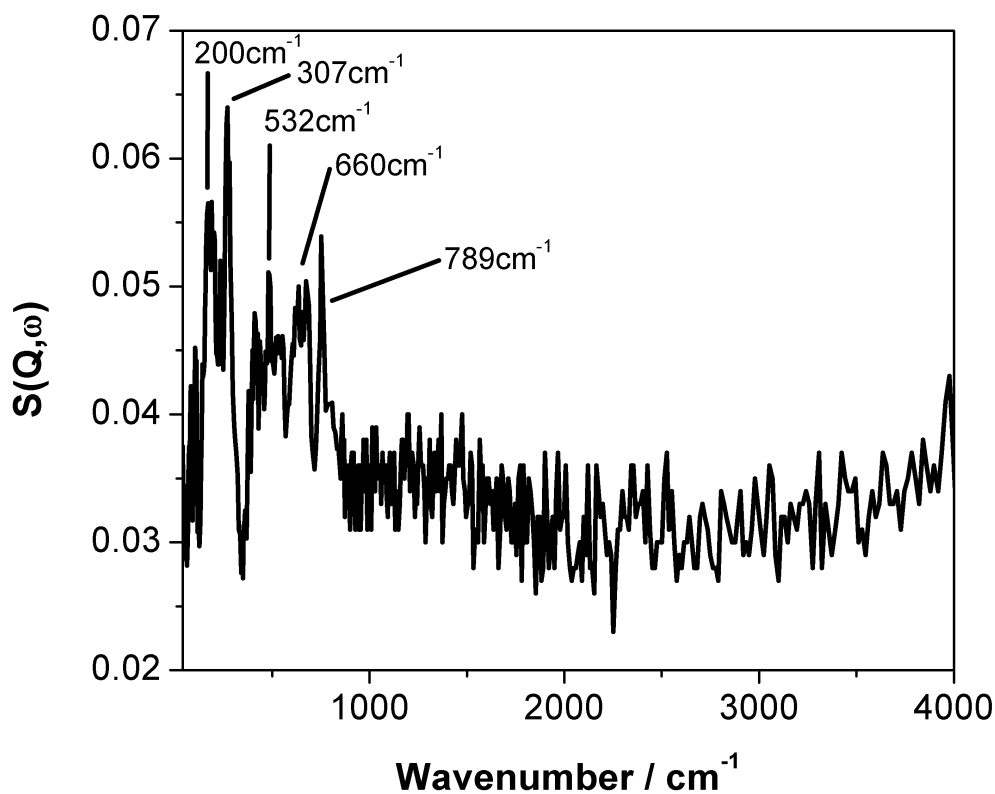


Figure 3.7: TOSCA INS spectrum of the alumina support after 6 hours reaction of a 2:1 mixture of CH_4 and CO_2 at 1073 K

3.1.1.2 Inelastic Neutron Scattering Measurements, TOSCA

The INS spectrum for the reacted alumina support is shown in figure 3.7. It can be seen from the spectrum that there is an extremely low signal : noise ratio. This indicates a low level of hydrogen which is probably not surprising as the sample has first been reduced (which removes any physisorbed hydroxyls) and then as it is a blank sample, no overlayers will have been formed.

The $\text{Ni}/\text{Al}_2\text{O}_3$ and $\text{Ni-Au}/\text{Al}_2\text{O}_3$ samples are presented in figures 3.8 and 3.9. Again, the spectra shown suffer from very low signals. Although consistent with

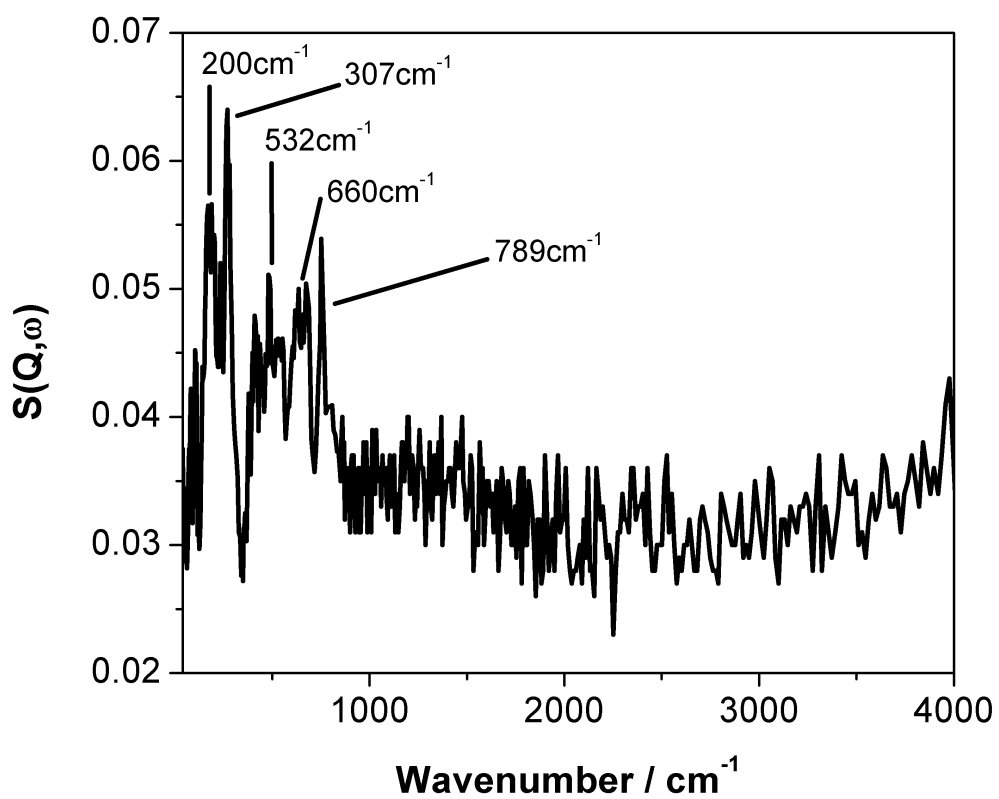


Figure 3.8: TOSCA INS spectrum of the Ni/Al₂O₃ catalyst after 6 hours reaction of a 2:1 mixture of CH₄ and CO₂ at 1073 K

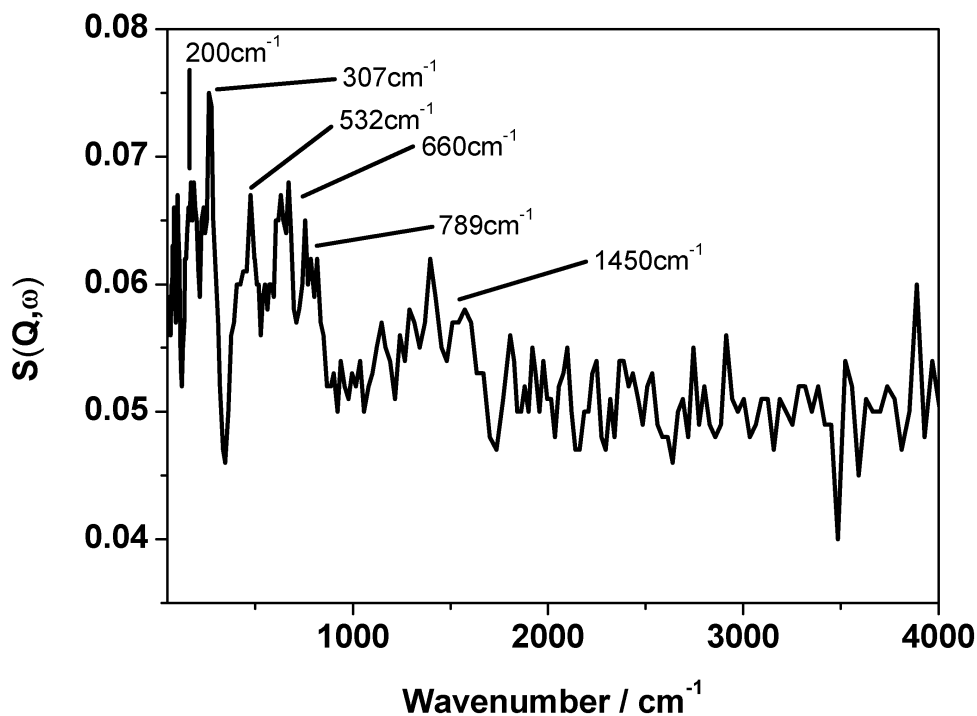


Figure 3.9: TOSCA INS spectrum of the Ni-Au/Al₂O₃ catalyst after 6 hours reaction of a 2:1 mixture of CH₄ and CO₂ at 1073 K

elemental analysis results 3.3, this is perhaps surprising as surface overlayers have been formed. Spectral features are evident at 789, 660, 532, 307 and 200 cm⁻¹ in all the figures. The bands at 789, 660 and 532 cm⁻¹ are assigned to in-plane hydroxyl deformation modes of the support material, whilst the bands at 307 and 200 cm⁻¹ are attributed to out-of-plane hydroxyl deformation features [88].

In figure 3.9 it is possible to suggest the presence of a very weak and broad peak centered around 1450 cm⁻¹. This is due to differences in the processing of the raw data compared to 3.7 and 3.8. In the Ni-Au spectrum, the intensity has been summed or “binned” over wider frequency ranges. This gives the benefit of increased signal but at a cost of resolution. If the band at 1450 cm⁻¹ is a real feature and not just background noise, it could be assigned to methyl defor-

Wavenumber / cm^{-1}	Assignment
1450	Methyl deformation
789	In-plane OH deformation
660	In-plane OH deformation
532	In-plane OH deformation
307	Out-of plane OH deformation

Table 3.1: Summary of the TOSCA INS Vibrational Assignments Pre and Post Methane Reforming Resulting in Amorphous Carbon Laydown.

mations resulting from methane adsorption and subsequent decomposition. This would be consistent with the elementary steps shown in the introduction and of a hydrocarbonaceous coke layer that has formed on the catalyst surface.

The resolution broadening on increasing wavenumber of the TOSCA spectrometer [60] means that the associated support hydroxyl stretching features are not observed in the spectrum. Whereas background subtraction routines for the 26 wt% Ni/Al₂O₃ TOSCA spectrum revealed a weak spectrum characteristic of an industrial grade carbon black examined previously [88], no new features are observed on background subtraction for the higher loading Ni/Al₂O₃ sample under investigation here. This indicates, in agreement with other studies [89], that the nature and extent of the carbon formed is sensitive to the catalyst specification. It is also noted that there is no evidence for graphitic domains, which are discernible with this spectrometer [90], or for any C-H stretching vibrations around 2900 cm^{-1} . A summary of the TOSCA vibrational assignments is given in table 3.1.

3.1.1.3 Inelastic Neutron Scattering Measurements, MAPS

Figure 3.10 shows an example of a mitre plot (the raw data) of an unreacted catalyst sample received from the MAPS spectrometer. It can be seen that the spectra is a 2D plot of energy transfer versus momentum transfer with intensity given as a colour range . In order to produce a standard spectrum more akin to an infrared spectrum, the intensity (summed across u_1 (Q)) is plotted versus energy transfer.

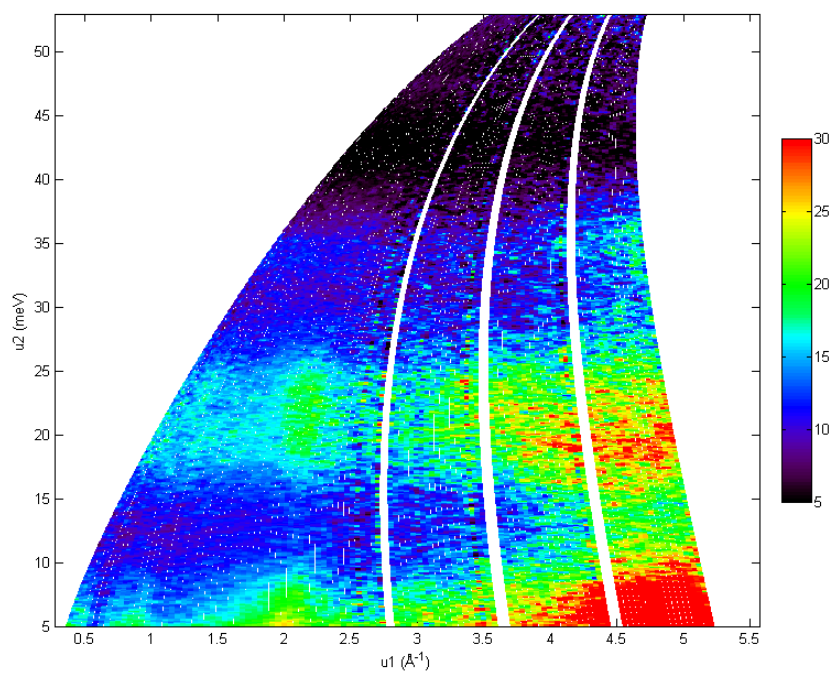


Figure 3.10: MAPS Mitre plot of Low energy-transfer INS spectra of post reaction Ni/Al₂O₃

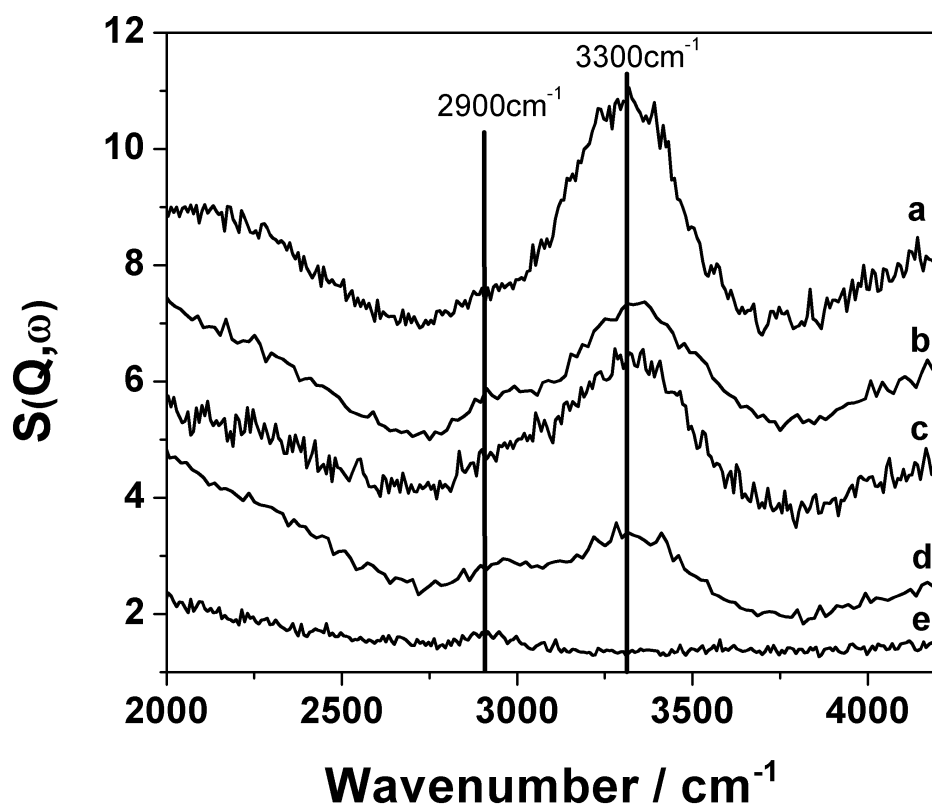


Figure 3.11: MAPS High energy-transfer INS spectra of (a) reduced Ni/Al₂O₃, (b) reacted Ni/Al₂O₃, (c) reduced Ni-Au/Al₂O₃, (d) reacted Ni-Au/Al₂O₃ and (e) reduced alumina. Incident energy of 4840 cm⁻¹

As explained in the introduction, the MAPS spectrometer operates differently to the TOSCA spectrometer and so the reacted samples were also examined using the direct geometry instrument. Figure 3.11 presents the spectra in the 2000-4500 cm⁻¹ region of all the studied samples. The spectrum of alumina that has experienced a reduction treatment is shown in (e) and is characterised by a flat background with the exception of a very small feature observed at 2900 cm⁻¹ which is thought to originate in a C-H stretch of residual aliphatic hydrocarbon. α -alumina has a low hydroxyl density [91] and no $\nu(\text{O-H})$ is evident in the spectrum. Spectrum (a) shows the reduced Ni/Al₂O₃ catalyst whilst 3.11(b)

Wavenumber / cm^{-1}	Assignment
3300	Alumina $\nu(\text{OH})$
2900	$\nu(\text{CH})$
1460	Methyl deformation
760	In-plane OH deformation
560	In-plane OH deformation
290	Out-of plane OH deformation
170	Nickel phonon

Table 3.2: Summary of the MAPS INS Vibrational Assignments Pre and Post Methane Reforming Resulting in Amorphous Carbon Laydown.

presents the spectrum the same catalyst post-reaction. The spectrum displayed in a) is dominated by a relatively intense band measured at 3300 cm^{-1} , which is assigned to $\nu(\text{O-H})$ of hydroxyl groups that are thought to be present on the alumina support material. Given the absence of such a feature in (e), it can safely be assumed that the hydroxyl population has been introduced to the catalyst during the preparative stage. The tendency of α -alumina to retain hydroxyl groups during impregnation of a metal component is thought to be specific to the type and sample history of that particular alumina. Post reaction, the spectrum of $\text{Ni}/\text{Al}_2\text{O}_3$ exhibits an attenuated $\nu(\text{O-H})$ band that is accompanied by a feature centred at 2940 cm^{-1} (b), which is attributed to a C-H stretch of aliphatic hydrocarbon species. The intensity of this band is low, indicating a relatively low hydrocarbon concentration and is in agreement with the TOSCA spectrum.

The same sets of spectra are presented in figure 3.12 and 3.13 as in figure 3.11 for the respective energy ranges of $400 - 1700$ and $60 - 400 \text{ cm}^{-1}$. For $400 - 1700 \text{ cm}^{-1}$, the spectrum in figure 3.12 shows the alumina to have a flat background. The reacted $\text{Ni}/\text{Al}_2\text{O}_3$ and $\text{Ni-Au}/\text{Al}_2\text{O}_3$ catalysts exhibit a small feature observed at 1460 cm^{-1} that is attributed to a C-H deformation mode. Features recorded at 760 and 560 cm^{-1} are assigned to hydroxyl deformation modes [92]. For $60 - 400 \text{ cm}^{-1}$, Figure 3.13 shows the two reacted catalyst samples to exhibit broad features measured at 290 and 170 cm^{-1} . The former is thought to be an out-of-plane deformation of hydroxyl groups [92], $\gamma(\text{O-H})$, whereas the latter is ascribed to a nickel phonon mode [93].

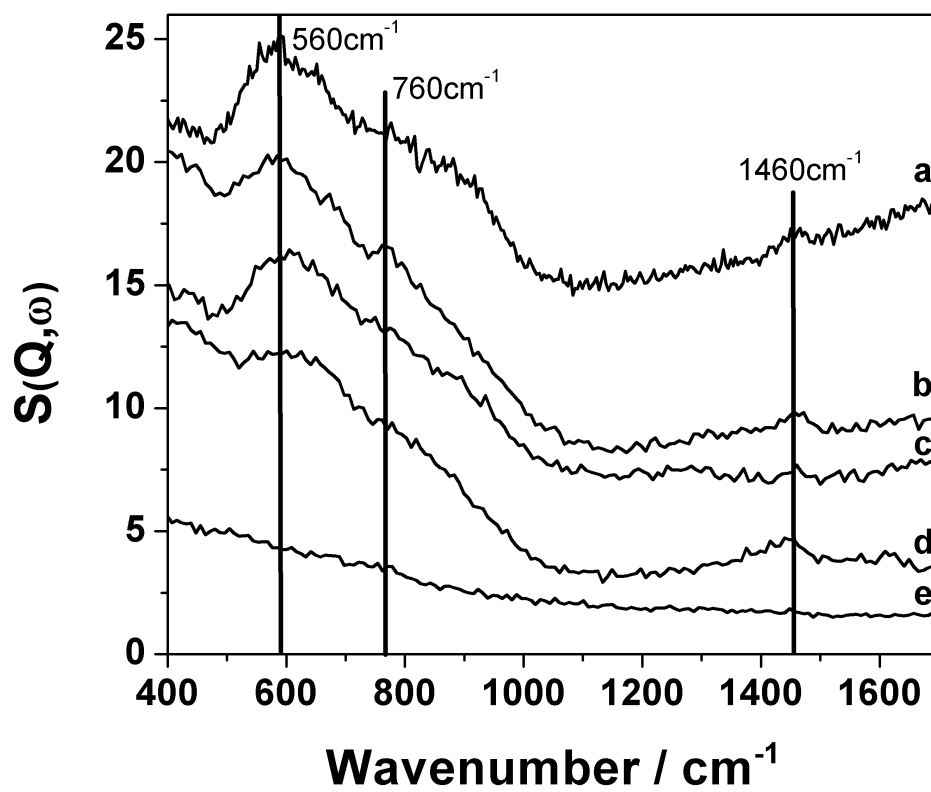


Figure 3.12: MAPS Medium energy-transfer INS spectra of (a) reduced Ni/ Al_2O_3 , (b) reacted Ni/ Al_2O_3 , (c) reduced Ni-Au/ Al_2O_3 , (d) reacted Ni-Au/ Al_2O_3 and (e) reduced alumina. Incident energy of 2017 cm^{-1}

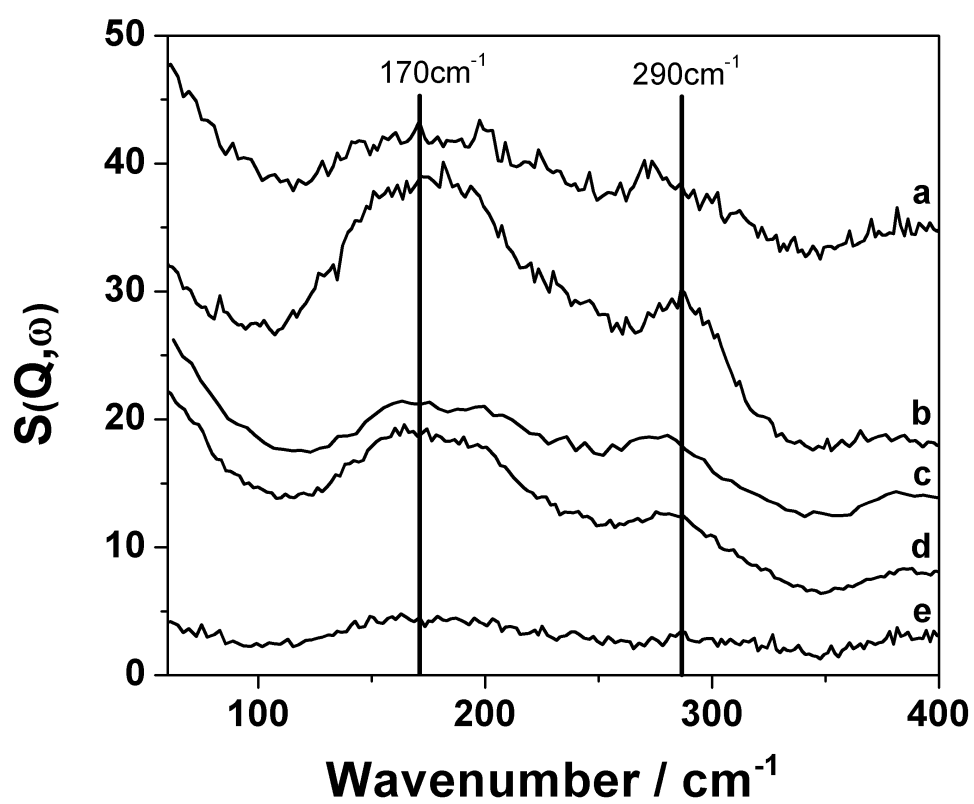


Figure 3.13: MAPS Low energy-transfer INS spectra of (a) reduced Ni/Al₂O₃, (b) reacted Ni/Al₂O₃, (c) reduced Ni-Au/Al₂O₃, (d) reacted Ni-Au/Al₂O₃ and (e) reduced alumina. Incident energy of 484 cm⁻¹

	Ni/Al ₂ O ₃
C (Elemental Analysis)	30-35%
H (Elemental Analysis)	0%
Carbon _(ad) TPO (micro-reactor)	22 mmol C g ⁻¹ _{cat} (26.84%) ± 8%
Carbon _(ad) TPO (INS-reactor)	11 mmol C g ⁻¹ _{cat} (13.63%) ± 8%
ν (O-H)	728 μ mol H g ⁻¹ _{cat}
ν (C-H)	66 μ mol H g ⁻¹ _{cat}
C _{INS} : H _{ν(C-H)}	175:1

Table 3.3: Carbon and hydrogen retention values for Ni/Al₂O₃ post micro-reactor and INS CO₂ reforming. Values in parenthesis are % by mass

	Ni-Au/Al ₂ O ₃
C (Elemental Analysis)	32-38%
H (Elemental Analysis)	0%
Carbon _(ad) TPO (micro-reactor)	23 mmol C g ⁻¹ _{cat} (27.61%) ± 8%
Carbon _(ad) TPO (INS-reactor)	15 mmol C g ⁻¹ _{cat} (18.59%) ± 8%
ν (O-H)	195 μ mol H g ⁻¹ _{cat}
ν (C-H)	87 μ mol H g ⁻¹ _{cat}
C _{INS} : H _{ν(C-H)}	171:1

Table 3.4: Carbon and hydrogen retention values for Ni-Au/Al₂O₃ post micro-reactor and INS CO₂ reforming. Values in parenthesis are % by mass

The grouping of the spectra recorded at the three primary energies (Figures 3.11 - 3.13) produces the vibrational spectrum for reduced and activated samples over a wide spectral range (60 - 4000 cm⁻¹) and a summary of the MAPS vibrational assignments is given in table 3.2. Few techniques could achieve this outcome. Importantly, the spectra for both catalyst samples are remarkably similar and indicate a low hydrocarbon population that co-exists with a slightly greater hydroxyl population, which is thought to reside on the support material. There is insufficient spectral information contained within Figures 3.11 - 3.13 to specify unequivocally the nature of the hydrocarbonaceous deposit.

Utilising the procedures described in the introduction, the spectral intensities of the MAPS C-H and O-H stretching modes (figure 3.11 can be used to determine the number of hydrogen atoms associated with oxygen and carbon atoms at the

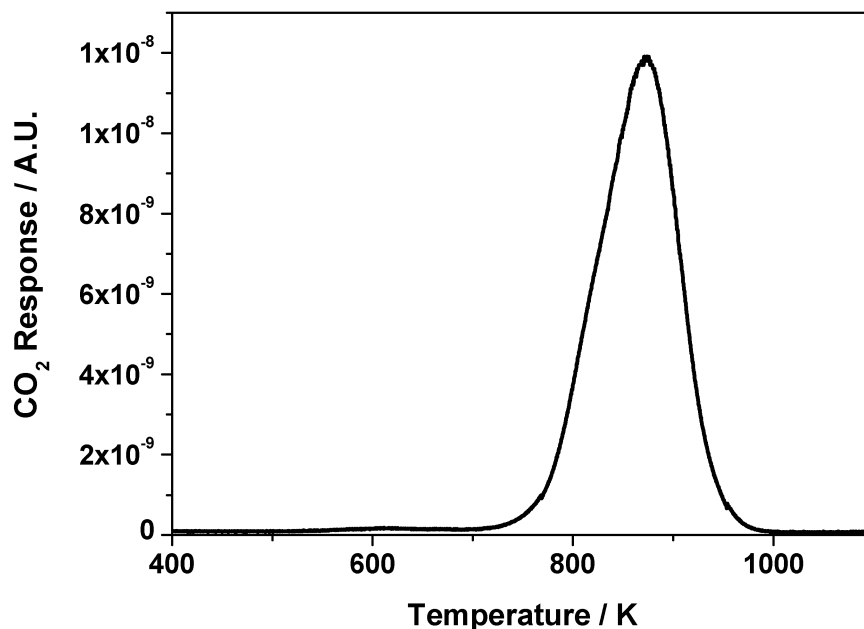


Figure 3.14: Temperature-programmed oxidation profile for Ni/Al₂O₃ INS runs after 6 hours reaction at 1073 K

surface of the two catalysts. This information is presented in tables 3.3 and 3.4. Post reaction, the $\nu(\text{O-H})$ and $\nu(\text{C-H})$ modes for the Ni/Al₂O₃ sample equate to respectively $728 \mu\text{mol H g}^{-1} \text{ cat}$ and $66 \mu\text{mol H g}^{-1} \text{ cat}$; the equivalent values for the Ni-Au/Al₂O₃ sample are $195 \mu\text{mol H g}^{-1} \text{ cat}$ and $87 \mu\text{mol H g}^{-1} \text{ cat}$. This corresponds to around 170 carbon atoms : 1 hydrogen atom for both the Ni and Ni-Au catalysts. Clearly, this suggests that the cokes formed during reactions are lean in hydrogen and can perhaps be described as carbonaceous rather than hydrocarbonaceous.

3.1.1.4 Post-reaction Temperature Programmed Oxidation of INS Samples

The TPO profiles for the post reaction INS samples are shown in Figures 3.14 and 3.15, where both samples exhibit peak maxima at approximately 880 K, closely

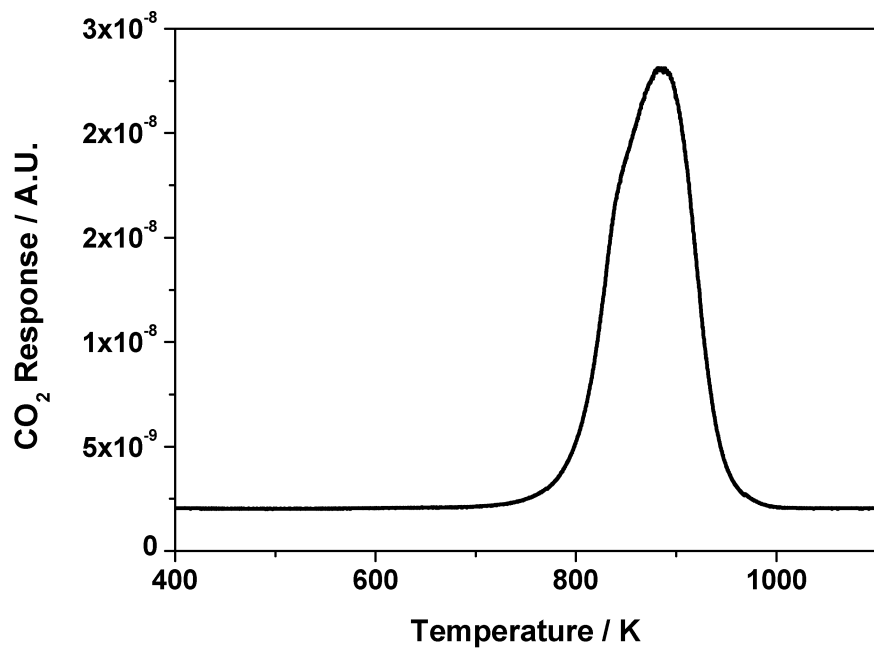


Figure 3.15: Temperature-programmed oxidation profile for Ni/Al₂O₃ INS runs after 6 hours reaction at 1073 K

matching the profiles observed in the micro-reactor experiments (figures 3.5 and 3.6). This coincidence suggests formation of a comparable form of carbon for both catalysts operated in the micro-reactor and the larger volume INS reactor. The quantity of retained carbon for each sample is also presented in the table above, with the Ni and Ni-Au samples equating to $11 \text{ mmol C g}^{-1} \text{ cat}$ (13.63%) $\pm 8\%$ and $15 \text{ mmol C g}^{-1} \text{ cat}$ (18.59%) $\pm 8\%$, respectively. What seems to be counter-intuitive based on the earlier discussion on gold doping is that the gold modified catalyst retains the larger proportion of carbon. This fact, combined with the observation that the Ni-Au catalyst does not appear to offer any advantage in terms of sustained syngas yield in the isothermal measurements (figure 3.4) indicates that in contrast to studies on steam reforming, the Au additive is providing little beneficial effect for reforming using CO_2 .

3.1.1.5 Post-Reaction Raman scattering and Infrared spectroscopy

Raman spectra for the reacted Ni/ Al_2O_3 and Ni-Au/ Al_2O_3 samples are shown in Figure 3.16. The sharp band observed at 1556 cm^{-1} originates in an atmospheric oxygen plasma and is an artefact of the measurement technique. Two bands consistent with the formation of a carbonaceous overlayer are measured. The G band, which occurs in spectra of all graphitic materials, is recorded at 1582 cm^{-1} [94]. The band detected at 1351 cm^{-1} is the D band, which arises from structural disorder breaking the translation symmetry of the material [95][96]. Although the ratio of intensities of these two bands is often used as a measure of disorder and may be related to the in-plane crystallite size of existing graphite domains [97], the laser excitation wavelength should also be taken into account. Cançado *et al.* [98] have developed a method for the determination of in-plane crystallite sizes of nano-structured graphites which is based on the following relationship:

$$L_a(nm) = (2.4 \times 10^{-10}) \lambda_l^4 \left(\frac{I_G}{I_D} \right) \quad (3.1)$$

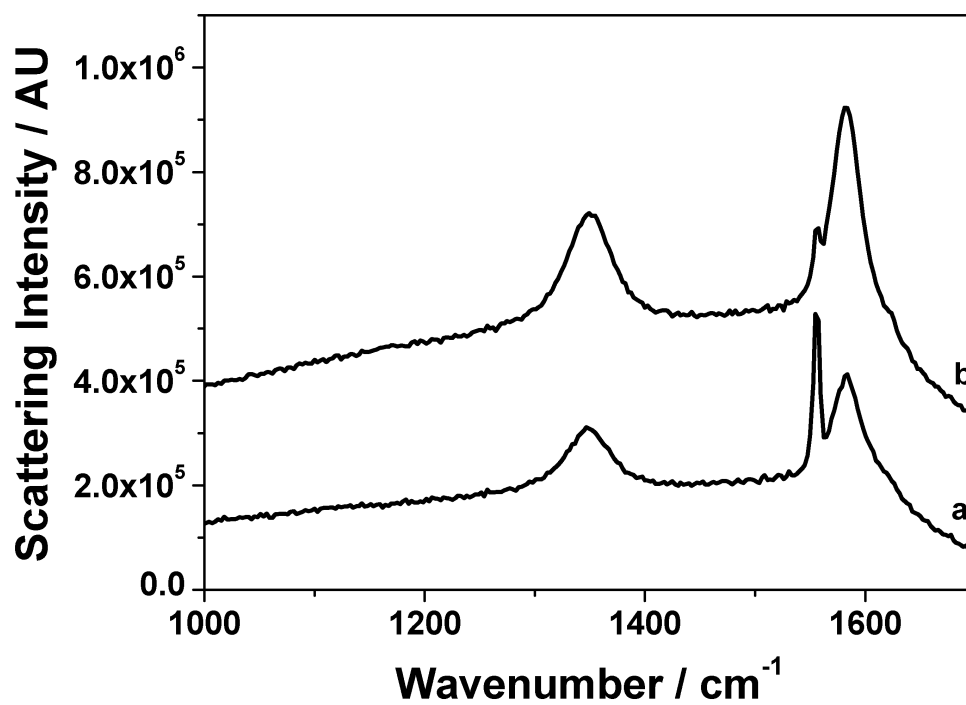


Figure 3.16: Raman spectra of (a) Ni/Al₂O₃ and (b) Ni-Au/Al₂O₃ catalysts after reaction and INS measurement

with L_a denoting the in-plane crystallite size, λ_l representing the laser wavelength (measured in nm), and I_G and I_D characterising the integrated peak intensities of the G and D bands, respectively. Calculations using the experimental data presented in Figure 9 provide crystallite domains of 27 nm for the Ni/Al₂O and 39nm Ni-Au/Al₂O, respectively.

These values would lead to a C : H ratio that is greater than the 170 : 1 reported in the table above. The recorded Raman spectra show contributions from sample fluorescence and were collected close to the limit of the detector, where non-linearity may complicate the instrument response. Further, the existence of the G band does not necessitate the presence of graphite, as merely six conjugated rings are needed to reproduce this spectrum [99]. Benzene has also been shown to give rise to a G band [100; 101]. Whilst the intensity ratio approach has been shown to work successfully for well-ordered homogeneous materials, justification for its application is weaker with materials of uncertain character [102]. Caution must consequently be exercised for interpretation of the data relating to the calculated graphite crystallite size. Nevertheless, the fact that the two bands in Figure 9 are separated and well defined suggests that heterogeneity within the coke is relatively low [103]. Signals that may be assigned to hydrogenous species are not observed [104].

The infrared absorption spectra of the two catalysts post reaction are displayed in Figure 3.17, which shows the two spectra to be very similar. The broad hydroxyl stretch observed at 3373 cm⁻¹ is due to the presence of surface hydroxyls on the alumina support and will also be due to water that has absorbed into the catalyst between the reaction and the the infrared measurement. A small C-H stretching region with two peaks at 3036 and 3057 cm⁻¹ could be either aromatic or alkene groups. The larger C-H stretching peak at around 2900 cm⁻¹ is evidence for the presence of saturated hydrocarbons. There is an extremely weak feature present at 1732 cm⁻¹ and is assigned to a carbonyl stretch which would suggest the incorporation of some oxygen into the coke matrix. The deformation mode of water can be seen at 1610 cm⁻¹. There are a number of peaks below 1500 cm⁻¹ and could be due to either hydrocarbon deformations (1457, 1415, 1381, 1361 and 1298 cm⁻¹), skeletal aromatic ring vibrations (1583, 1510 cm⁻¹) or carbon-

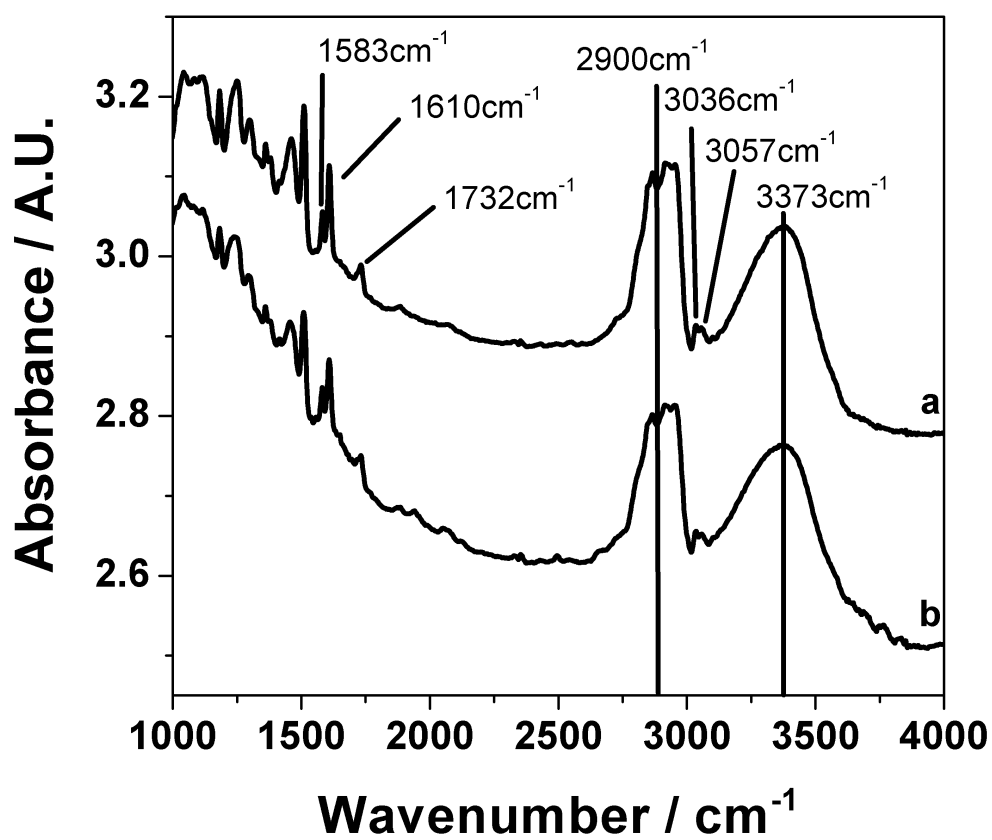


Figure 3.17: Transmission IR spectra of (a) Ni/Al₂O and (b) Ni-Au/Al₂O catalysts after reaction and INS measurement

Technique	Wavenumber / cm^{-1}	Assignment
Raman	1582	G Band
	1556	Oxygen Plasma
	1351	D Band
Infrared	3373	Alumina and adsorbed H_2O $\nu(\text{OH})$
	3057	Unsaturated $\nu(\text{CH})$
	3036	Unsaturated $\nu(\text{CH})$
	2900	Saturated $\nu(\text{CH})$
	1732	$\nu(\text{CO})$
	1610	H_2O deformation
	1583	Methyl deformation
	<1500	CH deformations

Table 3.5: Summary of the Raman and Infrared Vibrational Assignments Post Methane Reforming for Ni/ Al_2O_3 and Ni-Au/ Al_2O_3 Catalysts Resulting in Amorphous Carbon Laydown.

ate species, which may be connected with the alumina support or as suggested for the C=O stretch, they could be associated with the carbonaceous overlayer (1583, 1510, 1457, 1415 cm^{-1}). The peak measured at 1583 cm^{-1} has previously been characterised as a “coke band” and is attributed to the carbon-carbon stretch of microcrystalline graphite [105]. Almost all of the features in the infrared absorption spectrum may be exclusively connected to the persistent carbonaceous deposits formed during reaction, with great similarity apparent between the two catalysts. A summary of the Raman and IR vibrational assignments is given in figure 3.5.

3.1.1.6 Post Reaction Transmission Electron Microscopy (TEM) and X-ray Diffraction (XRD)

TEM images of Ni/ Al_2O and Ni-Au/ Al_2O recorded after reaction are shown in figures 3.18 and 3.19. The micrographs show large, dispersed, dense structures which represent nickel particles covered by amorphous carbon. The distribution of the particle sizes (20 - 100 nm) is a reflection of the high calcination, reduction

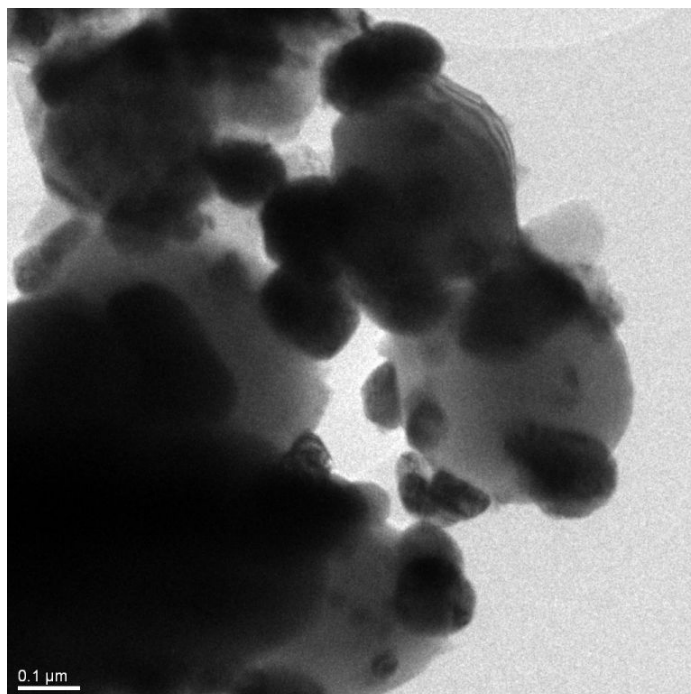


Figure 3.18: TEM of Ni/Al₂O₃ post INS reaction.

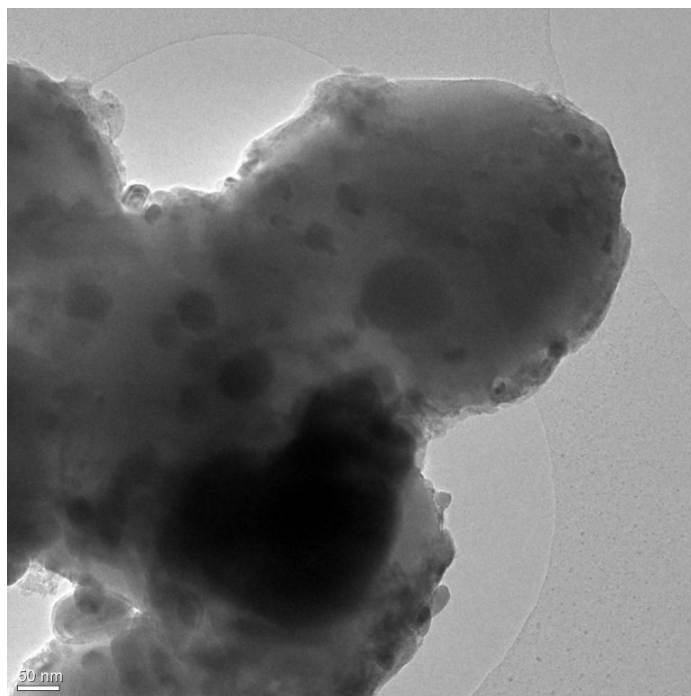


Figure 3.19: TEM of Ni-Au/Al₂O₃ post INS reaction.

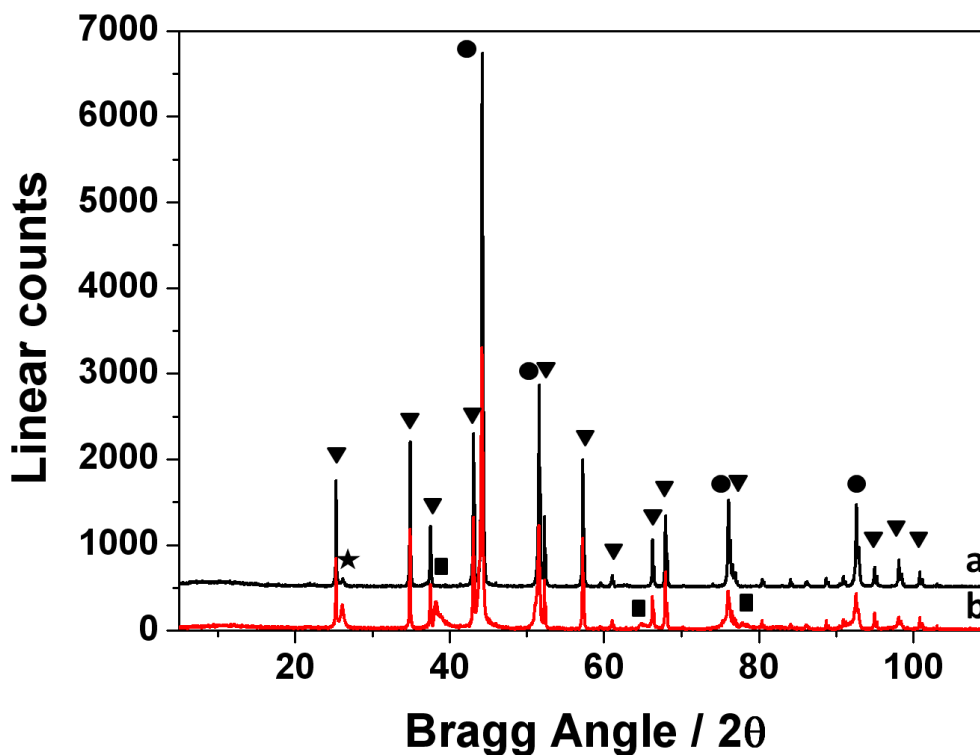


Figure 3.20: Powder XRD patterns of post-reaction (a) Ni/Al₂O and (b) Ni-Au/Al₂O catalyst samples showing reflections for α -alumina (triangle), nickel (circle), graphite (star) and gold (square) phases.

and reaction temperatures used. Evidence for filamentous carbon formation was not detected.

Diffraction patterns for post-reaction Ni/Al₂O and Ni-Au/Al₂O are shown in Figure 3.20. The major peaks of all identified phases are labelled; minor peaks are consistent with these assignments, but have not been labeled for clarity. The patterns of both catalysts are dominated by the alumina support and nickel. Peaks that are close in position, for example Ni at 51.6 and Al₂O at 52.3 °, are resolved, although this may not be apparent from the figure. Small, broad peaks due to crystalline gold are visible in the Ni-Au/Al₂O catalyst at 38.2 °, 64.8 ° and

77.9 °. The pattern displayed in Figure 12 shows no evidence for alloy formation. A peak at 26.2 ° is visible with patterns for both catalysts, which is assigned to graphite, indicating that coking has occurred. As the graphite peak is precluded, determination of the size of the graphite domains via the Scherrer equation is not possible[40]. It is suggested that graphite formation has occurred during reaction (XRD and Raman G band) but TEM and TPO measurements give the impression that it is of a low concentration. This perspective is further endorsed by the absence of graphitic features in the TOSCA INS spectrum (figures 3.8 and 3.9).

3.1.2 Discussion

The temperature-programmed reaction measurements presented in figures 3.1 and 3.2 show that there is no major difference between the Ni and the Ni-Au activity under the reaction conditions studied. Extended isothermal measurements (figure 3.3 and figure 3.4 do show a minor difference in that the undoped catalyst appears to have a slightly more favourable deactivation profile, which contrasts with other studies on presented on steam reforming [47].

The coke formed during the reforming process does appear to be essentially the same in terms of morphology and quantity irrespective of which catalyst is used. Although the bulk of the coke is carbon, evidence for hydrogen and oxygen containing functional groups has been observed with both INS and infrared spectroscopies. It is noted that the fine detail of the functionalities present on the overlayer are not visible with INS, but only with IR. INS measurements have also quantified the amount of hydrogen associated with the catalyst and describe a coke that is predominantly carbon with very small quantities of hydrogen. What this suggests kinetically is that both the Ni and the Ni-Au catalysts are extremely efficient at cycling hydrogen. The TPO, TEM, XRD and Raman data indicate the coke to be in the form of an amorphous carbon, and the quantities of hydrogen suggest that it could be decorating the edges of the amorphous carbon.

Temperature-programmed oxidation of the coke shows carbon deposits that are oxidised across a wide temperature range. This is consistent with the type of

the carbon being amorphous and composed of domains varying in size [90; 106]). Polycyclic aromatic hydrocarbons (PAHs) show similar bonding to that found in graphene planes, and have been detailed in highly carbonaceous materials such as carbon blacks and coals [107; 108]. A difference between PAHs and small graphene sheets is that the PAH is strictly terminated in hydrogen. Graphene terminations can be left as dangling bonds or may be hydrogenated. For bulk crystals, this is not important, but for nanocrystalline graphite, the edge may constitute a significant fraction of the material. It is also likely that some of the graphite nanocrystals will terminate with sp^3 bonded carbon. The location of the carbon on the catalyst is not clear. However, it can not apparently significantly obstruct the active metal, at least under reaction conditions, as only minor deactivation is observed. It may cover the metal, but be sufficiently porous to allow the reactants access and products escape.

The INS and infrared absorption spectra have shown the presence of hydrogen bonded to carbonaceous deposits, with the infrared spectra displaying the C-C ring stretch of the coke band. Bartholomew describes the mechanisms of coke formation in steam reforming as either reactions between atomic $C\alpha$ to form pure carbons, or CH_x fragments to generate hydrocarbon cokes, which may be dehydrogenated to form pure carbons [21; 22]. Both of these pathways will probably be present in the “dry” reforming reaction.

The different techniques applied in this study have all contributed to an understanding of the matrix deposited in the dry reforming reaction. Each technique emphasises a different aspect of the matrix and demonstrates the benefits of a multi-technique approach to describe these materials, which are notoriously difficult to characterise. The Raman and XRD measurements suggest that the bulk of the material is a framework of carbon rings, although the oxidation temperature and TOSCA spectrum suggest the extent of graphitisation to be relatively low. TEM does not observe the production of filamentous carbon, and the best descriptor of the carbon must therefore be “amorphous”. The MAPS spectra have enabled detection, specification and quantification of hydrogen between OH and CH forms, whilst the higher resolution infrared absorption spectra show that the retained hydrogen in the coke occurs in a variety of chemical forms.

Rigorous quantification of the hydrogen associated with carbon is difficult,

but INS has permitted an unambiguous characterisation that shows very low hydrogen content. This observation leads to kinetic insight into aspects of the reaction under consideration.

$C_{n(ad)}$ (equation 1.27) is equivalent to $C\beta$ (figure 1.28). The rate determining step is the dissociation of methane (equation 1.9(k_2)), which demands a high temperature (above 700 K, Figure 3.1) for the reaction to progress [13][109]. The almost complete lack of hydrogen retained in the reaction (INS results) shows that k_6 (equation 1.20) and k_7 (equation 1.21) must be greater than the CO reaction k_8 (equation 1.22). This leads to a reservoir of adsorbed atomic carbon that polymerises with rate k_{10} (equation 1.27), in this case to form amorphous carbon. Key to the minimisation of coke is maximising k_8 and k_9 with respect to k_{10} in order to produce gas phase CO.

This hypothesis leads to a generalised kinetic scheme that may account for the partitioning of carbon and hydrogen throughout the reaction system. For simplicity, the elementary reactions are approximated to the following four generic processes: (a) dissociative adsorption of methane, (b) recombinative desorption of adsorbed hydrogen atoms, (c) oxidation of adsorbed carbon atoms and (d) polymerisation of adsorbed carbon to form amorphous carbon. The rate coefficients for these processes are respectively denoted k_a , k_b , k_c and k_d . If we accept that k_a is rate limiting, the trends observed in this work may consequently be described by the magnitudes of the associated rate coefficients in the following order:

$$k_b \gg k_d > k_c \quad (3.2)$$

It is acknowledged that the scheme shown above is similar to other schemes that have been used to describe this and related chemical systems [28; 108; 110; 111; 112], with the proposals of Wei and Iglesia [111] and Xiancai and co-workers [28] in particular describing comparable pathways. However, this scheme is presented here from the perspective of a better quantitative understanding of the partitioning of hydrogen within the reaction system, that additionally endorses some of the concepts explored by the other workers.

The high carbon to hydrogen ratio of the overlayer of the active catalysts

indicates that molecular hydrocarbon species are neither formed nor retained in any appreciable quantity. Indeed, the bulk of the carbon is predominantly bonded to other carbon atoms. Terminations of these carbonaceous regions, or possibly surfaces, dominate the infrared absorption spectra and are accessible in the INS spectra. Interestingly, this work also shows that under the conditions used here, the addition of the gold modifier does not provide any benefit for applications to supported nickel catalysts and the CO₂ reforming of methane.

3.2 Graphitic Carbon Characterisation

The previous section of this chapter has demonstrated that both the 45 % Ni and Ni-Au catalysts synthesised were highly efficient at cycling hydrogen. It also demonstrated (via the determination of C : H ratios for the retained overlayers) a proposed reaction scheme that invokes a rate of polymerisation of carbon that is greater than the rate of oxidation of the adsorbed carbon atoms to CO product (equation 1.27). The “s” subscript in equation 1.27 refers to solid carbon which is unspecified in nature. In the previous section, the combination of catalyst composition, catalyst sample history and reaction conditions created an environment that resulted in the production of an overlayer that was comprised mainly of amorphous carbon. Thus, in that case, equation 1.27 can be stated more specifically as equation 1.28. Methane reforming on an industrial scale however, is more typically compromised by the formation of filamentous carbon [36]. Here, “whisker” formation is prevalent and it is often the loss of mechanical strength of the catalyst matrix that induces the need for a replacement catalyst charge. This phenomenon of “whisker” formation in methane reforming reactions is also described elsewhere [2; 113; 114].

The form of the carbon produced during “dry” methane reforming over supported metal catalysts (whether it be amorphous or filamentous whiskers) is known to be sensitive to catalyst composition, reaction conditions and sample history [5][115][116][117][89]. Further, Joo and Jung [113] and Chen and co-workers [32] have also signified the importance of calcination temperature. This chapter examines the 26 % wt Ni/Al₂O₃ catalyst which, was prepared using a different support material, a lower metal loading and a milder calcination temperature of 873 K. The latter parameter minimizes the possibility of forming nickel aluminates, which may further complicate matters [32][118]. Thus, this section specifically studies the carbon polymerization process represented by equation 1.29.

The previous section is based around an appreciation of how hydrogen was partitioned within the reaction system. In this section micro-reactor isotopic substitution experiments will be employed, swapping ¹²C¹⁶O₂ for ¹³C¹⁶O₂, to explore the role of the carbon dioxide in the carbon laydown process over an alumina-

supported nickel catalyst. Previous studies have also attempted to elucidate the source of carbon in the reaction process in order to make comments on various mechanistic steps taking place in the “dry” reforming reaction. Verykios has suggested that the major source of coke in “dry” reforming over supported rhodium catalysts is from the CO₂ oxidant, and that the hydrogen content of the carbonaceous overlayer is negligible [119]. Mirodatos and co-workers have made extensive use of isotopes to look at the elementary steps that occur in CO₂ reforming of methane [120; 121; 122]. Specifically, SSITKA and TAP reactors have been used to determine isotopic scrambling of carbon and hydrogen during reaction. By combining isotopic studies with the INS technique already described it should be possible to develop a number of elementary steps and kinetic schemes for representative industrial methane reforming catalysts.

3.2.1 Results

3.2.1.1 Microreactor Studies

Initial testing was carried out in the microreactor in order to determine reaction parameters for the INS measurements. Figures 3.21 and 3.22 show the temperature reduction profile for both the Ni and the Ni-Au catalysts (scanning for mass 18 (water)). It can be seen from figure 3.21 that reduction commences at 600 K and reaches a maximum at around 675 K. Over this temperature range there is a concomitant decrease in the mass 2 signal (hydrogen) though this has been omitted for clarity. At temperatures of around 900 K and above, the reduction of the metal is complete. The high temperature tail is a function of the increased time it takes for water vapour to leave the microreactor system. A reduction temperature of 898 K was deemed to be necessary to ensure full reduction to Ni⁰. This temperature also coincides with the maximum operating temperature of the Inconel[®] INS sample reactors. Figures 3.23 and 3.24 show the temperature-programmed profiles for the dry reforming of methane over the Ni/Al₂O₃ and the Ni-Au/Al₂O₃ over the temperature range 300-1150 K. It can be seen in both figures that the dry reforming reaction has a sharp starting temperature of around 650 K for the Ni and 700 K for the Ni-Au. Full conversion of methane seen at about 1050 K for the Ni catalyst and 1100 K for the Ni-Au.

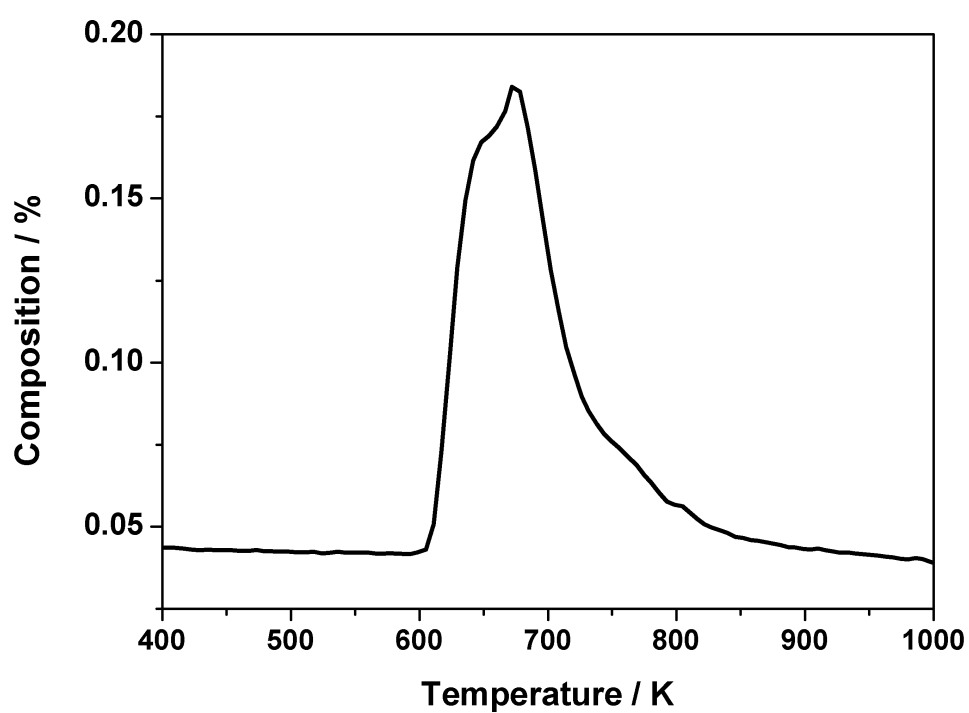


Figure 3.21: Temperature-programmed reduction profile (400 - 1000 K) for Ni/Al₂O₃ catalyst. Measurements performed using the micro-reactor arrangement using a heating rate of 10 K min⁻¹ and scanning for mass 18 (H₂O)

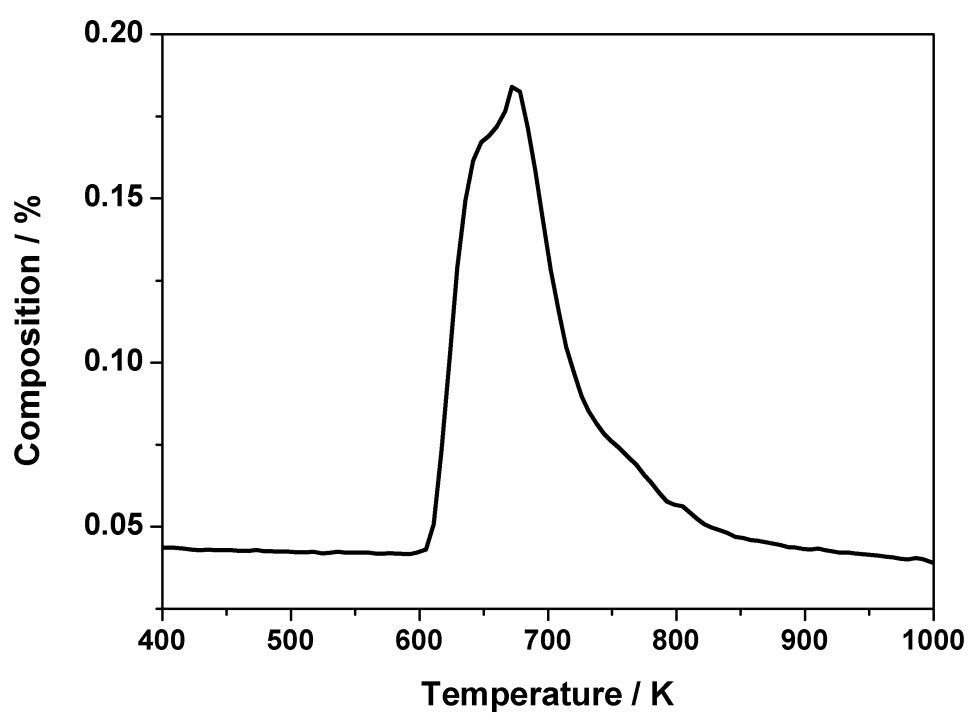


Figure 3.22: Temperature-programmed reduction profile (400 - 1000 K) for Ni-Au/Al₂O₃ catalyst. Measurements performed using the micro-reactor arrangement using a heating rate of 10 K min⁻¹ and scanning for mass 18 (H₂O)

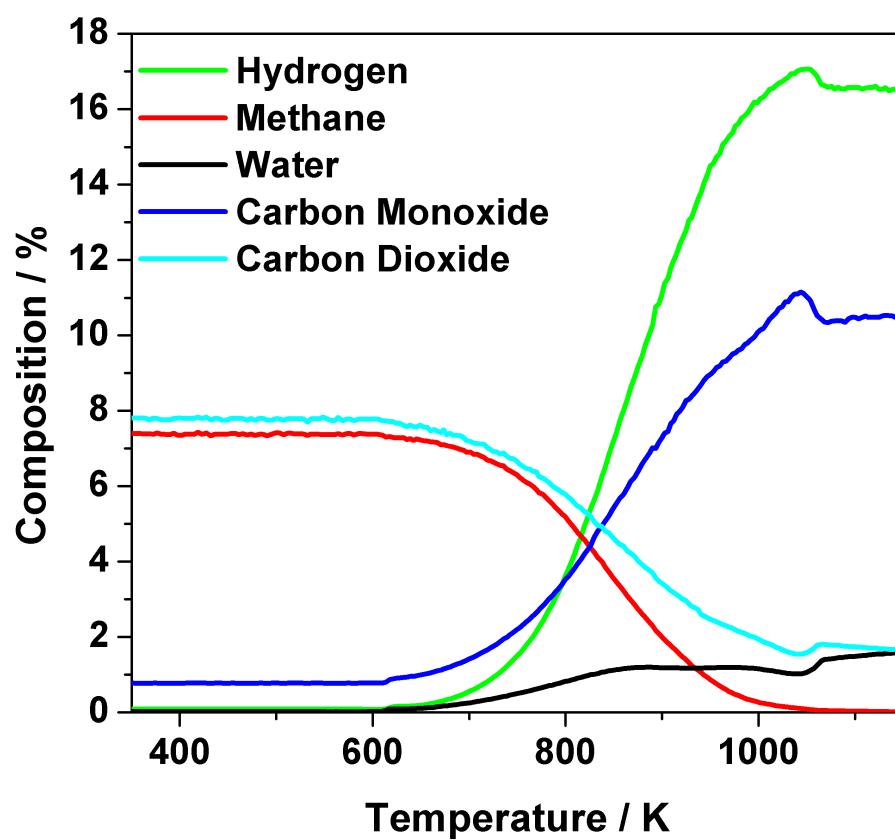


Figure 3.23: Temperature-programmed reaction profile (350 - 1150 K) for Ni/Al₂O₃ catalyst. Measurements performed using the micro-reactor arrangement using a heating rate of 10 K min⁻¹

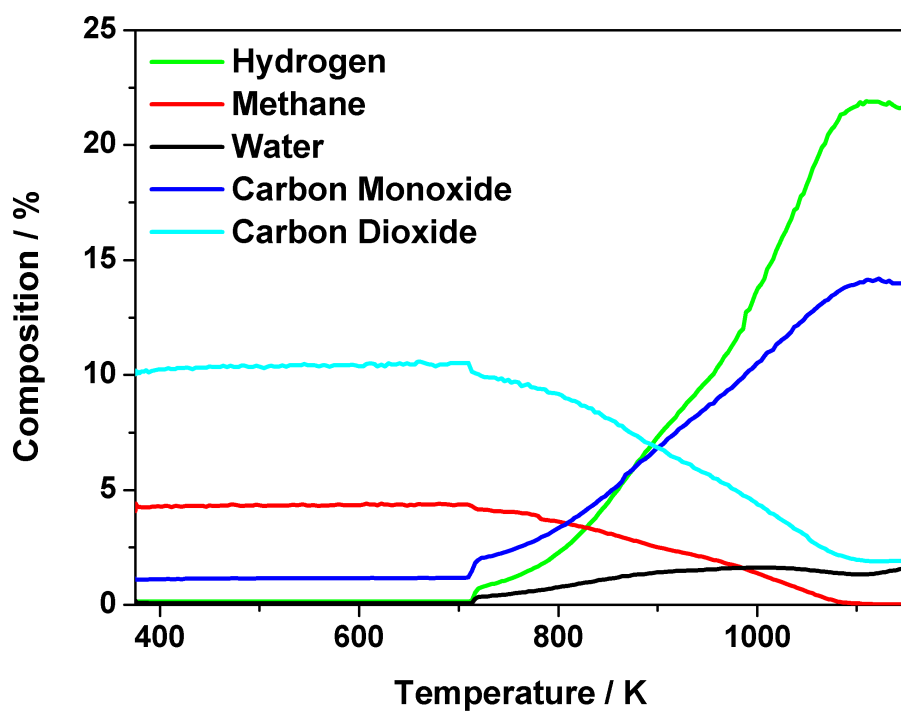


Figure 3.24: Temperature-programmed reaction profile (350 - 1150 K) for Ni-Au/Al₂O₃ catalyst. Measurements performed using the micro-reactor arrangement using a heating rate of 10 K min⁻¹

For the Ni catalyst, CO₂ consumption is not complete at this stage and levels out at higher temperatures. This may reflect water gas shift activity, which can also explain the presence of water in the same region where syngas is produced. CO₂ consumption does appear to reach 100 % at the same time as full methane conversion in the Ni-Au catalyst. At the highest temperatures (above 1100 K) deactivation can be seen to be occurring in the Ni-Au catalysts. This is observed as falling CO and H₂ levels.

A reasonably wide range of methane conversions at given temperatures exist in the literature. This is in no small part due to each study having differences in Ni loading, metal particle size and GHSV. There is however a general trend that reactions reach around 70 % methane conversion at around 950 K and achieve 90 % and above conversions at around 1050 K [123; 124; 125]. Based on these studies, it appears that the catalysts are comparing within the same general area as others in the literature.

A temperature of 898 K was selected for isothermal measurements as it is within the operational range of the Inconel[®] INS cell as well as providing significant catalytic activity. Figures 3.25 and 3.26 show the reaction profile for the micro-reactor isothermal measurements (898 K) that correspond to an initial methane conversion of approximately- 51 % for the Ni and 75 % for the Ni-Au catalyst. A modest degree of deactivation is apparent over the initial period of reaction in both catalysts, as evidenced by gradual CH₄ and CO₂ breakthrough alongside falling H₂ and CO levels. The extent of deactivation is different for the two products: for the Ni catalyst, although H₂ formation is reduced by approximately 24 % over 165 minutes, CO formation is only reduced by approximately 9 % over the same period. Hydrogen formation decreases in the Ni-Au catalyst by 48 % with CO formation falling by around 20 %. Despite these reductions in product yields, it is noted that sustained syngas production remains prevalent throughout the reaction period presented.

The TPO profiles for the post micro-reactor reformed Ni and Ni-Au are presented in figures 3.27 and 3.28. Both the samples display comparable peak maxima of 915-920 K. This coincidence in T_{max} suggests that similar carbons are formed in both cases. Earlier in the section a calibration of graphite vs MS response was presented (figure 2.2). In this experiment a T_{max} of 1086 K was observed for the

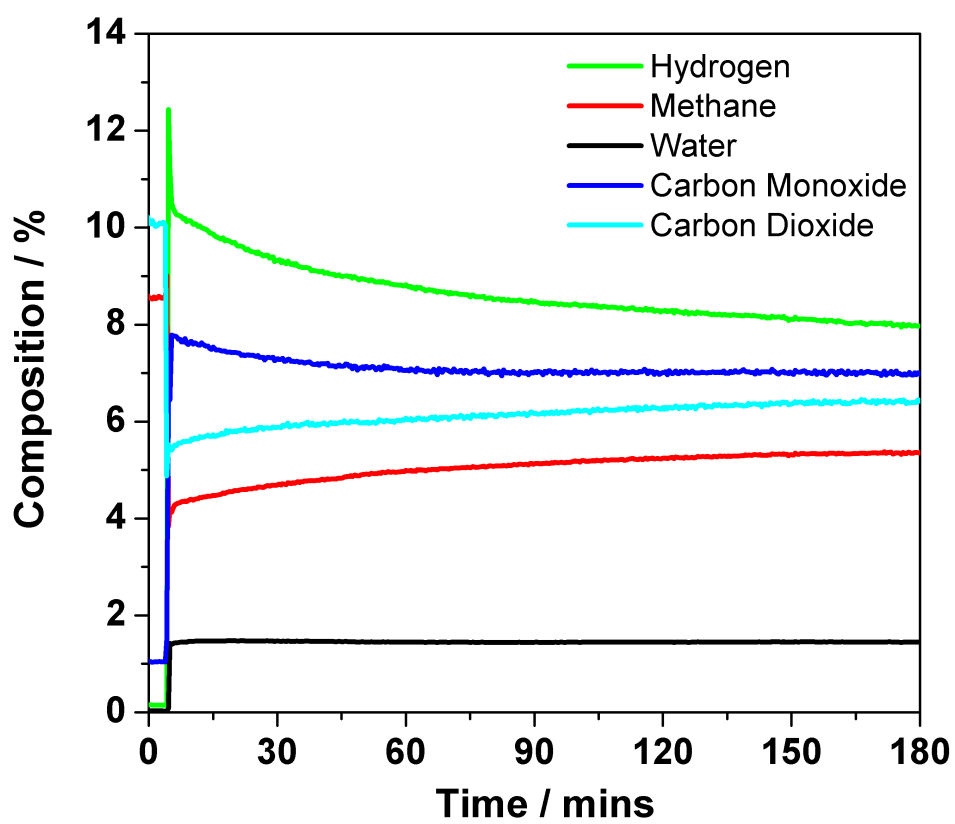


Figure 3.25: Isothermal reaction profile at 898 K of a 1:1 mixture of CH₄ and CO₂ over Ni/Al₂O₃ catalyst. Measurements performed using the micro-reactor arrangement

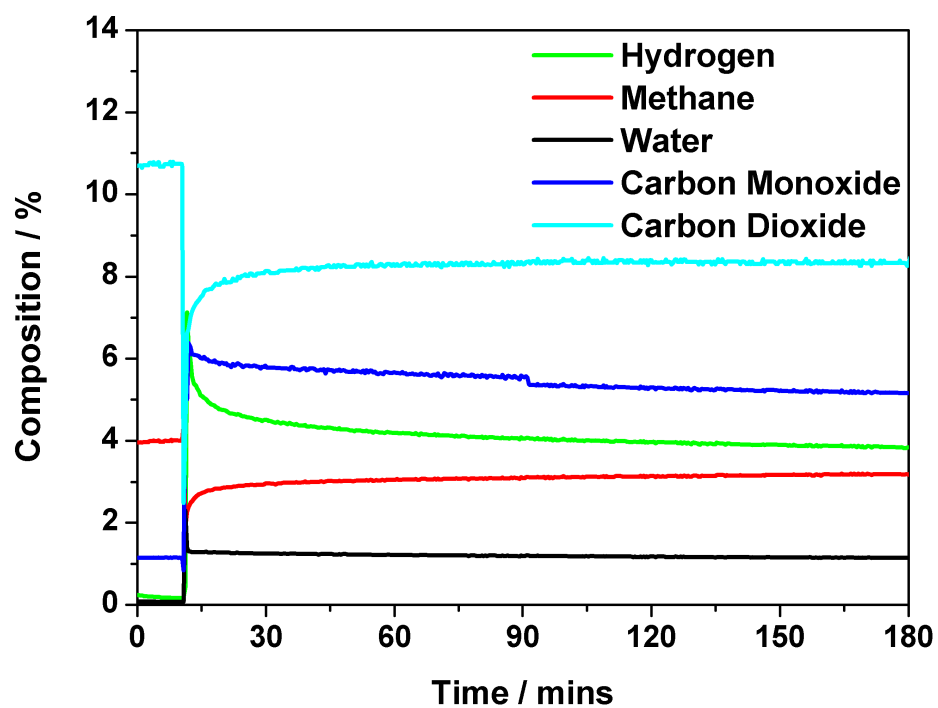


Figure 3.26: Isothermal reaction profile at 898 K of a 1:1 mixture of CH_4 and CO_2 over Ni-Au/ Al_2O_3 catalyst. Measurements performed using the micro-reactor arrangement

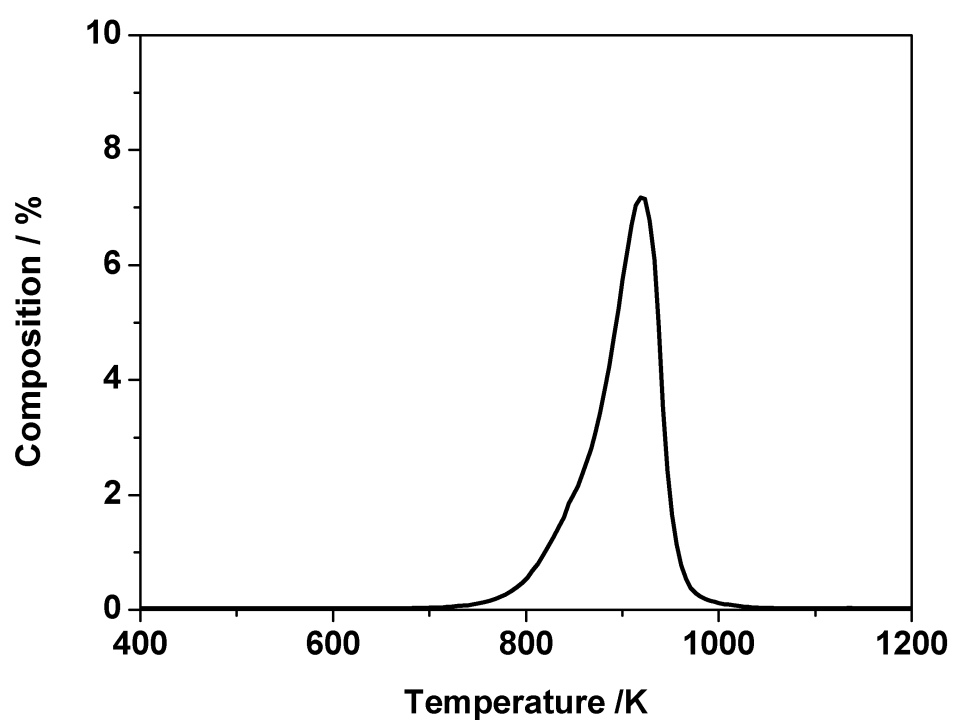


Figure 3.27: Temperature-programmed oxidation profile for Ni/Al₂O₃ catalyst post reaction at 898 K. Measurements performed using the micro-reactor arrangement

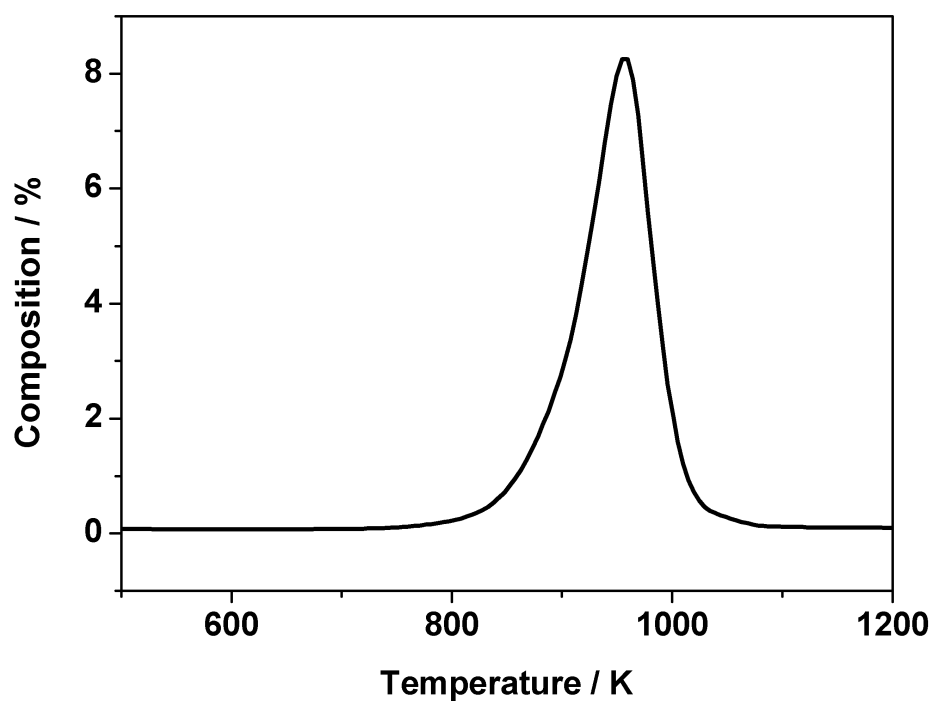


Figure 3.28: Temperature-programmed oxidation profile for Ni-Au/Al₂O₃ catalyst post reaction at 898 K. Measurements performed using the micro-reactor arrangement

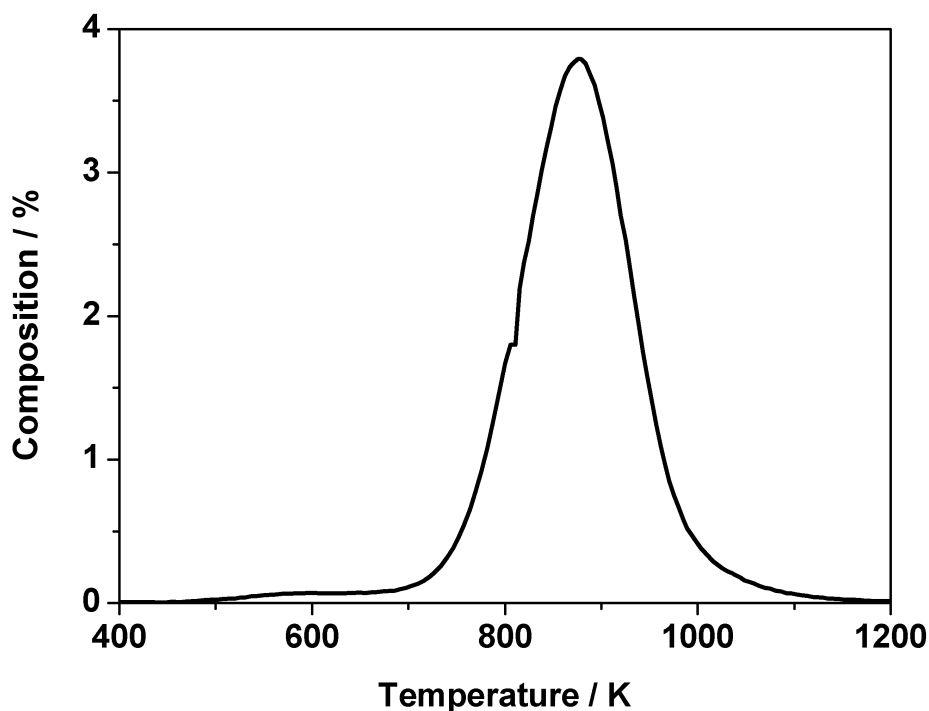


Figure 3.29: Temperature programmed hydrogenation profile (15 amu mass spectrometer signal) for Ni/Al₂O₃ catalyst after 3 hours reaction of a 1:1 mixture of CH₄ and CO₂ in the quartz micro-reactor at 898 K. Measurements were performed using a temperature ramp of 10 K min⁻¹ and a carrier gas mixture of 5 % H₂ in He

TPO of graphite. This value is close to that seen in figures 3.27 and 3.28, which may indicate that graphitic type structures have formed in this case. It is also to be noted that similar quantities of coke are formed in both reactions (both around 50 mmol C g_(cat)⁻¹ or 66 % by mass, from integration of the CO₂ peak). The significance of this value will be discussed in greater detail later on in the section.

The technique of temperature-programmed hydrogenation (TPH) has been used before to discern distinct carbonaceous populations retained within overlayers [119; 126], and so the technique has been employed here to examine a sample of

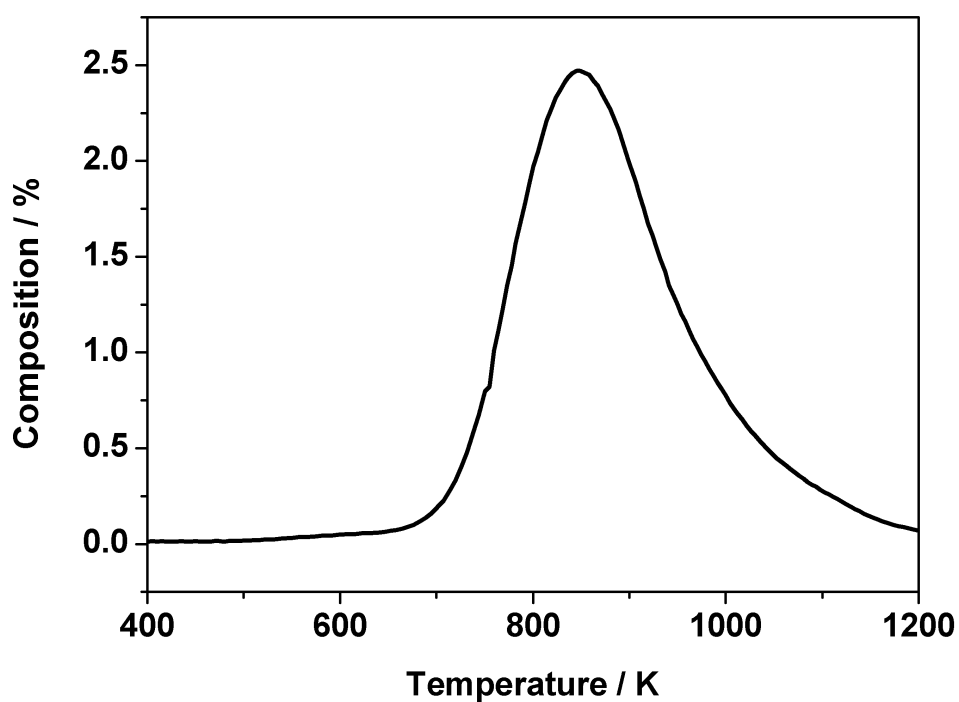


Figure 3.30: Temperature programmed hydrogenation profile (15 amu mass spectrometer signal) for Ni-Au/ Al_2O_3 catalyst after 3 hours reaction of a 1:1 mixture of CH_4 and CO_2 in the quartz micro-reactor at 898 K. Measurements were performed using a temperature ramp of 10 K min^{-1} and a carrier gas mixture of 5 % H_2 in He.

this catalyst after 3 hours continuous reaction in the micro-reactor. The resulting profiles in figure 3.29 and 3.30 both show a single peak centered just above 850 K. The singularity of this feature is further evidence that the carbon population is homogeneous, with no indication of discrete interactions, for instance of carbonaceous deposits associated with different “active sites” of the metal crystallites.

3.2.1.2 INS Sample Preparation, Carbon Analysis and INS Measurements for Ni/Al₂O₃

The rest of the results focus solely on the Ni/Al₂O₃ catalyst. This is for a number of reasons not least because of the limitations in neutron beam time. Also, similarly to the previous section in this chapter, in order to quantify the hydrogenous component of the overlayer, scale-up samples of *ca.* 10 g had to be prepared for INS measurements. Synthesising large quantities of Ni-Au catalyst would be relatively costly compared to synthesis of the undoped catalyst and was not justifiable unless the catalyst was exhibiting vastly superior reforming results. As the microreactor results presented in figures 3.24, 3.26 and 3.28 were all broadly similar to the undoped catalyst, a decision was made to concentrate solely on the Ni/Al₂O₃ catalyst. The reaction profile for the INS reactor measurements is presented in figure 3.31. As in the previous section, the larger reactor configuration forces the operating regime to be at a reduced GHSV (longer space time) compared to the more conventional micro-reactor arrangement. The profile of the INS reactor exit stream is only intended to indicate relative trends in gas composition as the catalyst is brought on-line and reaction stabilized. The apparent delay seen at the beginning of the reaction profile is due to a combination of the reactor attaining reaction temperature and the switching of the gas feed from the by-pass line. The data from 60 minutes onwards define the actual reaction profile. Figure 3.31 shows conversion of the CH₄ and CO₂ whilst at the same time, production of H₂ and CO can be observed. As with the isothermal micro-reactor profile for the Ni catalyst (figure 3.25), some degree of deactivation is apparent for continuing time-on-stream. The perturbations in the signals that can be observed in figure 3.31 are thought to originate from occasional changes to the gas

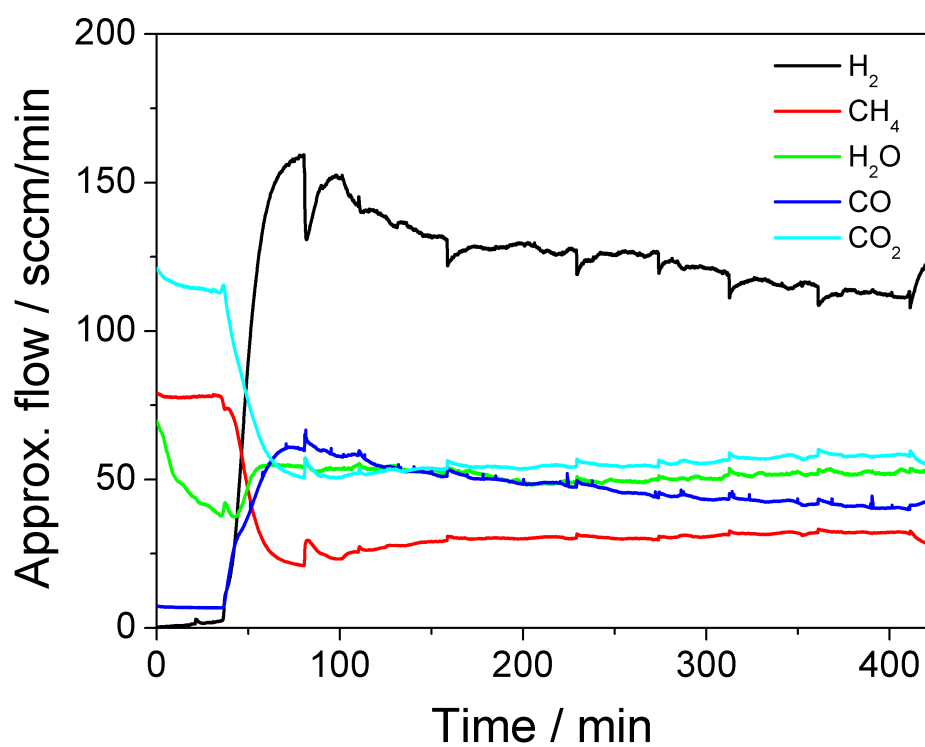


Figure 3.31: Isothermal reaction profile at 898 K of a 1:1 mixture of CH₄ and CO₂ over Ni-Au/Al₂O₃ catalyst. Measurements performed using the INS arrangement

	Ni/Al ₂ O ₃
C (Elemental Analysis)	45-48%
H (Elemental Analysis)	0%
Carbon _(ad) TPO (micro-reactor)	51.1 ± 4.1 mmol C g ⁻¹ _{cat}
Carbon _(ad) TPO (INS-reactor)	44.33 ± 3.54 mmol C g ⁻¹ _{cat}
$\nu(\text{O-H})$	none observed
$\nu(\text{C-H})$	17.4 $\mu\text{mol H g}^{-1}$ _{cat} ± 1 $\mu\text{mol H g}^{-1}$ _{cat}
C _{INS} : H _{$\nu(\text{C-H})$}	2550 ± 204 : 1

Table 3.6: Carbon and hydrogen retention values for Ni/Al₂O₃ post micro-reactor and INS CO₂ reforming.

flow as the gases pass through the extended catalyst bed. What is important to note is that qualitatively there are comparable trends seen with the micro-reactor and the INS reactor. On significant difference between the two measurements is that of pressure. The large sample and reactor volume caused a large pressure build-up during the course of the reaction - atmospheric pressure to 9.6 bar over the course of the reaction. This is in no doubt due to the formation of large quantities of carbon during the reaction. Weighing the reactor after reaction indicated an increase in catalyst mass corresponding to 53.2% carbon. This mass would certainly cause restricted gas flow and result in pressure build-up.

The results of elemental analysis (C and H) of catalyst samples extracted from the INS reactor after the 6 hour reaction period reaction are presented in Table 3.6. No hydrogen response was observed, indicating the hydrogen content of the sample to be below the 0.3 % detection limit of the instrument for this element. The range of carbon values for a number of samples taken from different regions of the INS reactor were 45-48 %. Figure 3.32 shows the TPO of the INS sample post reaction. The TPO profile is described as a single intense peak that is skewed with a low temperature tail. This simple profile indicates the retained carbon populations to be reasonably homogeneous, as no separate peaks are evident. As can be seen, the T_{max} is just below 930 K. This is a similar temperature to the microreactor sample in figure 3.27 and suggests that the coke formed is of a similar morphology in each sample.

The carbon levels are reported in Table 3.6, with the micro-reactor and INS

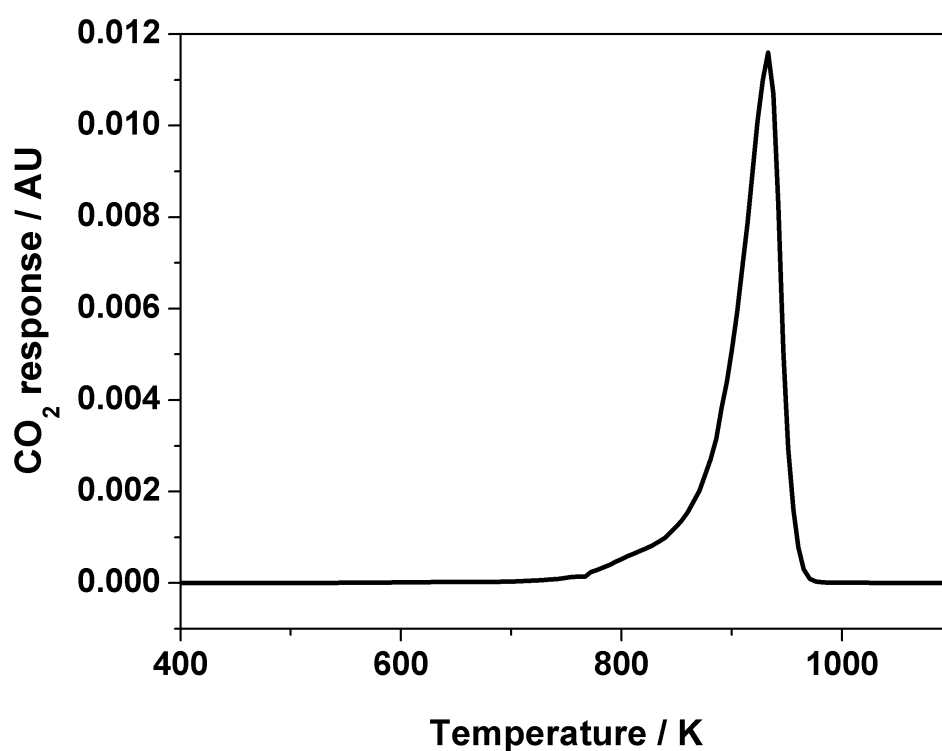


Figure 3.32: Temperature-programmed oxidation profile for Ni/Al₂O₃ catalyst after 3 hours reaction of a 1:1 mixture of CH₄ and CO₂ at 898 K in the INS Inconel[®] reactor. Measurements were performed using a temperature ramp of 10 K min⁻¹ and a carrier gas mixture of 5 % O₂ in He

reactor samples respectively comprising 51.1 ± 4.1 mmol C g⁻¹(cat) and 44.33 ± 3.54 mmol C g⁻¹(cat).). In the former case this corresponds to a carbon content of 61.3%, whereas this represents 53.2% in the latter case. The value for the INS reactor is in reasonable agreement with the elemental analysis and is consistent with the increase in mass of the reactor post-reaction. It is also reasonable to assume that this build-up of carbon within the catalyst bed is connected with the increase in pressure-drop observed with the INS reactor. It is indeed noteworthy that despite substantial carbon laydown, corresponding to approximately 50% of the catalyst mass after a 6 hour period of reaction, the catalyst continues to operate and produce syngas to a significant degree.

Figure 3.33 shows the high energy spectrum (primary energy of 4840 cm⁻¹) for the reacted Ni/Al₂O₃ catalyst. The design of the Inconel[®] can has allowed the spectrum to be displayed as a difference spectrum (i.e. reacted spectrum + sample can - reduced catalyst spectrum + sample can). Figure 3.33 is characterized by a single weak feature centered at 3050 cm⁻¹, which can be assigned as either an aromatic or olefinic C-H stretching vibration. One of the most striking features of this spectrum is the poor signal : noise ratio especially compared to figure 3.11, the corresponding figure for the amorphous carbon characterisation. There are two main reasons for the difference in signal. Firstly, the weak signal can partially be attributed to the use of a different chopper package in the MAPS instrument. In this instance, the “A” chopper package has been installed compared to the “S” chopper package used previously [60]. The rationale behind this is improved resolution. The “A” chopper package is able to achieve higher resolution than the “S” chopper and this was selected in the hope that different hydrocarbonaceous motifs could be discerned from each other (e.g. olefinic and aromatic units). This however, has not been possible and the result has actually just been a decreased signal. What is worth noting, is that the “A” chopper can, and indeed has, been calibrated to known hydrogen masses in exactly the same way as described in the previous chapter for the “S” chopper. Perhaps though, the most obvious reason for the weak signal is lack of retained hydrogen. Calibration of C-H scattering intensity for the C-H stretch permits the number of hydrogen atoms associated with carbon atoms to be determined as before. This information is presented in Table 2, which indicates a value of 17.4 μmol H g⁻¹

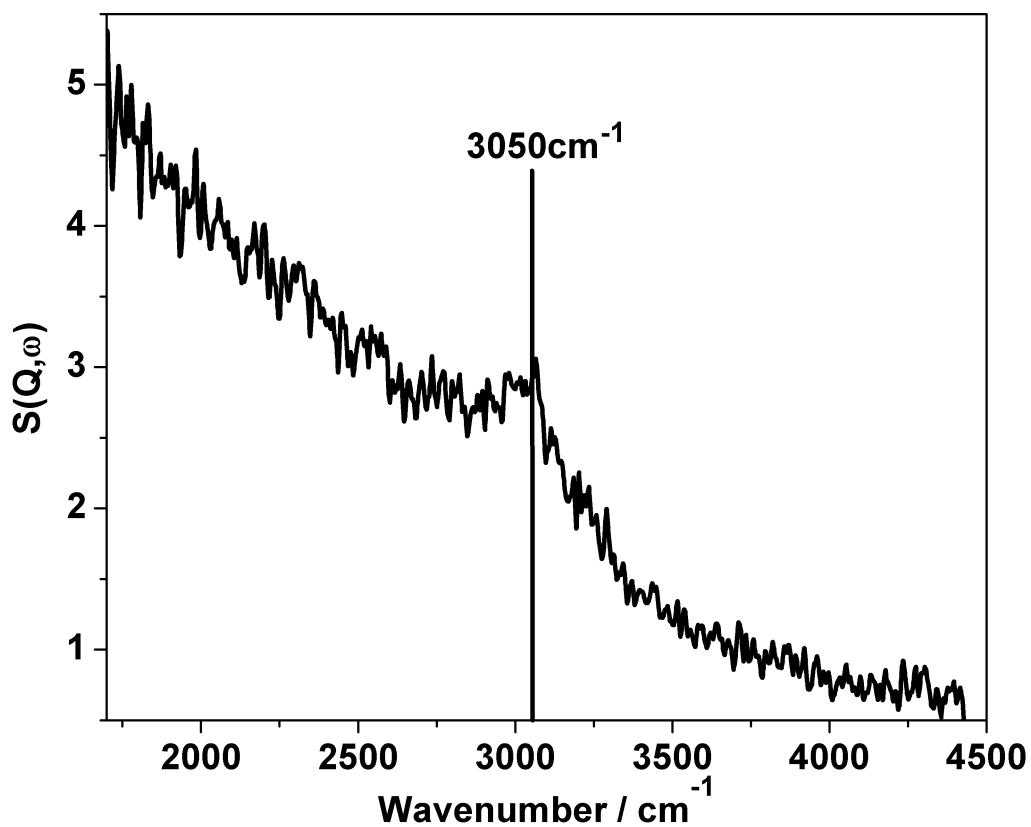


Figure 3.33: High energy transfer INS spectrum of reacted Ni/Al₂O₃ after 6 hours reaction of a 1:1 mixture of CH₄ and CO₂ at 898 K. The spectrum is a difference spectrum (reacted spectrum - spectrum of reduced catalyst) acquired using the MAPS spectrometer operating at an incident energy of 4840 cm^{-1}

$cat \pm 1 \mu\text{mol H g}^{-1} cat$. This value is significantly lower than the value of $68 \pm 4 \mu\text{mol H g}^{-1} cat$ determined in the previous section. Another major difference between the high energy data in the previous section and figure 3.33 above, is the absence of any $\nu(\text{O-H})$ features. A minimal hydroxyl density is associated with α -alumina [91] so it is not too surprising that one is not observed however, the lack of hydroxyls can be further explained. The hydroxyl signal associated with the 45.1% Ni/Al₂O₃ sample was connected to the catalyst preparative process involved with that particular catalyst. A different α -alumina was used to prepare the Ni/Al₂O₃ catalyst under investigation here. What this “missing” O-H suggests is that hydroxyls do not appear to be required during the various surface steps taking place in the reforming process. This result also suggests that not all α -aluminas can be considered the same and this should be considered when selecting a support for a particular chemical system.

The spectrum for the reacted catalyst recorded at a medium energy (2017 cm^{-1}) is presented in figure 3.34. This spectrum suffers again from low signal to noise ratios (confirming lack of retained hydrogen) but is nonetheless characterized by four bands observed at 1410, 1200, 840 and 620 cm^{-1} . The 1410 cm^{-1} band is close in energy to a CH₂ scissors vibration, however, the $\nu(\text{C-H})$ region in the previous figure is more suggestive of the carbon existing in more of an unsaturated guise. Instead, this mode may consist of a coupled C-C stretch and C-H bend, as previously reported by Albers and co-workers [127]. The broad band centered at 1200 cm^{-1} is assigned to a C-H bending mode [127; 128; 129]. The band at 840 cm^{-1} is assigned to an aromatic CH bend [127; 130; 131] which is consistent with the the mode observed at 3050 cm^{-1} in the previous figure. That said, there is a possibility that the band could be attributed to a C-C stretch at 875 cm^{-1} [129; 132] although the lack of hydrogen in this mode perhaps makes it less likely. The 620 cm^{-1} band is attributed to an sp² carbon network deformation mode [128; 131]. Collectively, the spectra in figures 3.33 and 3.34 are similar to other studies on cokes and hydrocarbonaceous materials [127; 131; 133]. The overall picture is one a low presence of hydrocarbonaceous species that is of an aromatic character.

The low energy INS spectrum is given in figure 3.35. No obvious vibrational

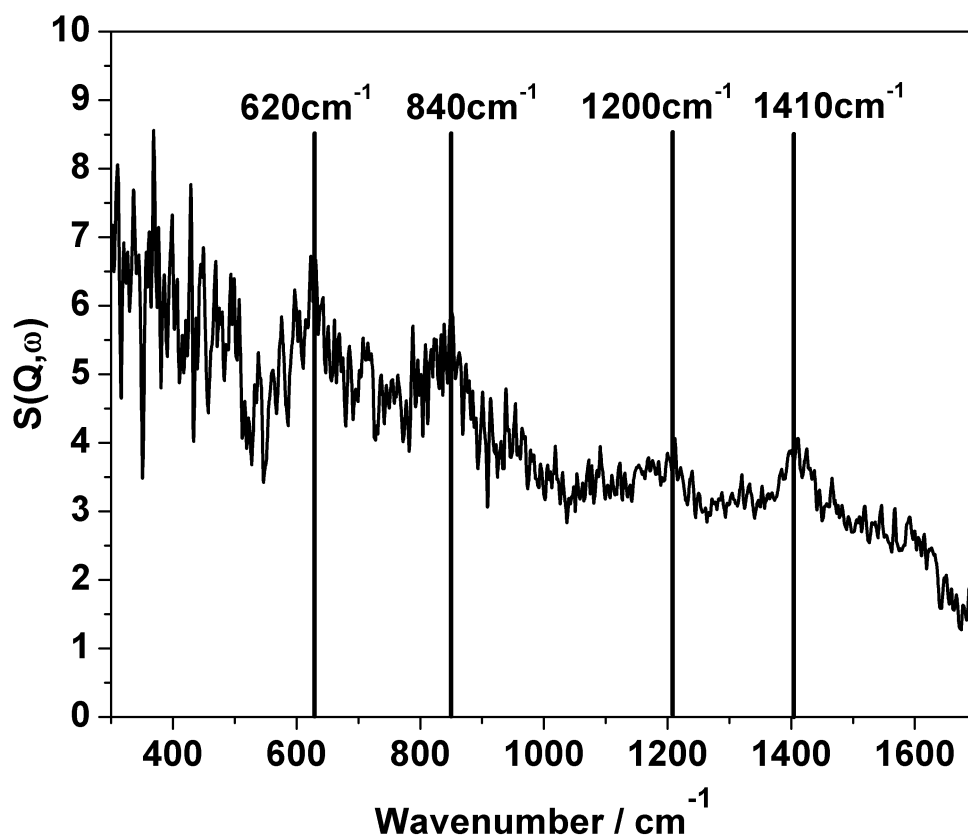


Figure 3.34: Medium energy transfer INS spectrum of reacted Ni/Al₂O₃ after 6 hours reaction of a 1:1 mixture of CH₄ and CO₂ at 898 K. The spectrum is a difference spectrum (reacted spectrum - spectrum of reduced catalyst) acquired using the MAPS spectrometer operating at an incident energy of 2017 cm⁻¹

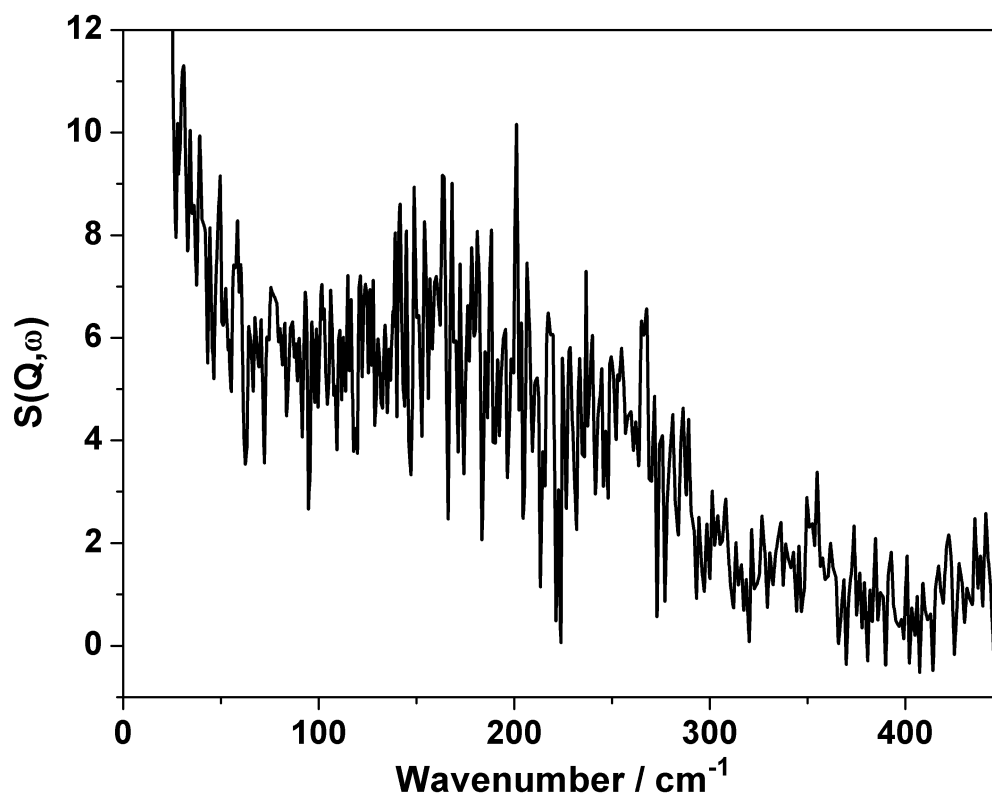


Figure 3.35: Low energy transfer INS spectrum of reacted Ni/Al₂O₃ after 6 hours reaction of a 1:1 mixture of CH₄ and CO₂ at 898 K. The spectrum is a difference spectrum (reacted spectrum - spectrum of reduced catalyst) acquired using the MAPS spectrometer operating at an incident energy of 484 cm^{-1}

Wavenumber / cm^{-1}	Assignment
3050	$\text{sp}^2 \nu(\text{CH})$
1410	Coupled $\nu(\text{CC})$ and $\delta(\text{CH})$
1200	$\delta(\text{CH})$
840	Aromatic $\delta(\text{CH})$
620	sp^2 carbon network deformation

Table 3.7: Summary of the MAPS INS Vibrational Assignments Post Methane Reforming Resulting in Graphitic Carbon Laydown.

modes are observable. Whilst the spectrum is clearly dominated by noise (at the expense of all other signal) it does demonstrate that the subtraction methods utilised (both in terms of the sample methodology and the experimental hardware) and the subtraction routine itself is robust. A poor subtraction would show phonon modes related to the nickel from the catalyst or even the Inconel [®] can. A summary of the vibrational modes measured via INS are given in table 3.7.

The powder X-ray diffraction pattern for the post-reaction INS sample is presented in figure 3.36. Reflections due to the alumina support and metallic nickel are apparent. A moderately broad and intense reflection due to graphite is observed at 26.1° ((002) lattice plane), indicating that a substantial degree of coking has taken place and that it is of a graphitic nature rather than amorphous [134]. Graphite particle sizing using the Scherrer equation was not possible due to the overlap of this feature with a feature attributed to alumina.

Transmission electron micrographs of the post-reaction sample are presented in figures 3.37 and 3.38. Figure 3.37 shows the same area using; zero energy loss (a) and elemental mapping analysis (b-d). Most obvious to note from the zero energy loss map (figure 3.37(a)) are a number of long strands that terminate in small but dense “spheres”. These strands are further highlighted in figure 3.37(b) which is an energy-filtered carbon image. This set-up causes carbon to appear as white whilst all other elements fade into the background. The grey region in the top left hand side of the image is the “holey carbon” film that supports the sample whilst it is being analysed. From the carbon map it can be confirmed that the

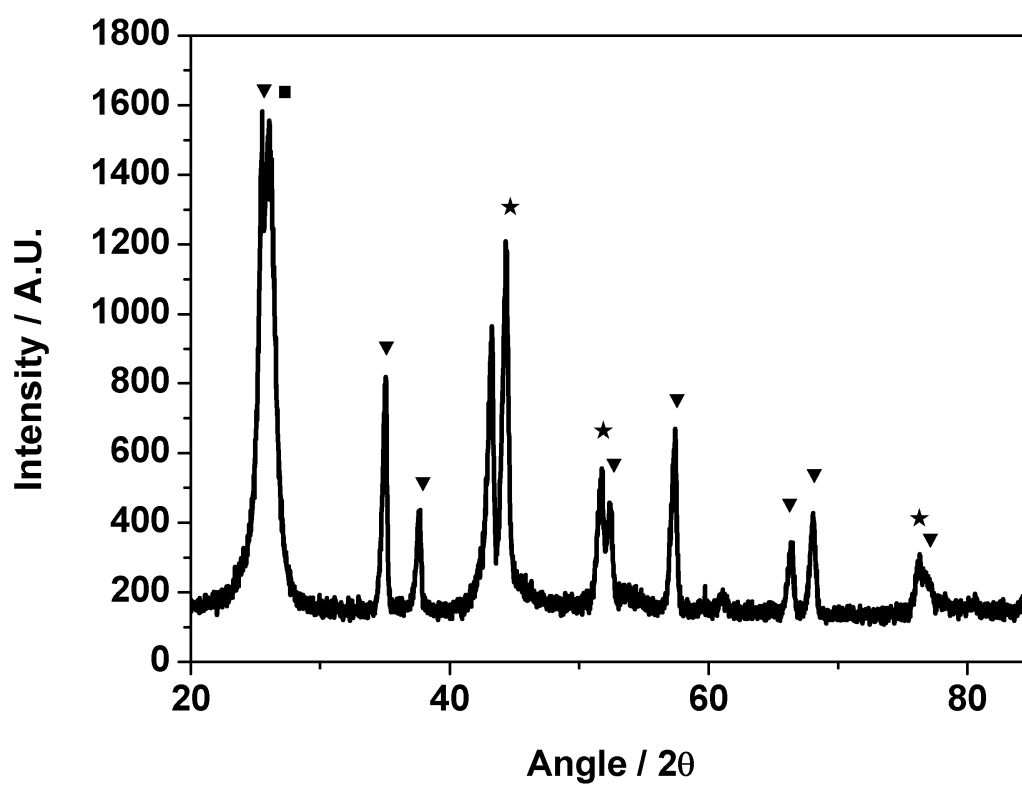


Figure 3.36: Powder X-ray diffraction pattern of Ni/Al₂O₃ recorded after reaction and INS measurement. Reflections for α-alumina (triangle), nickel (star) and graphite (square) phases

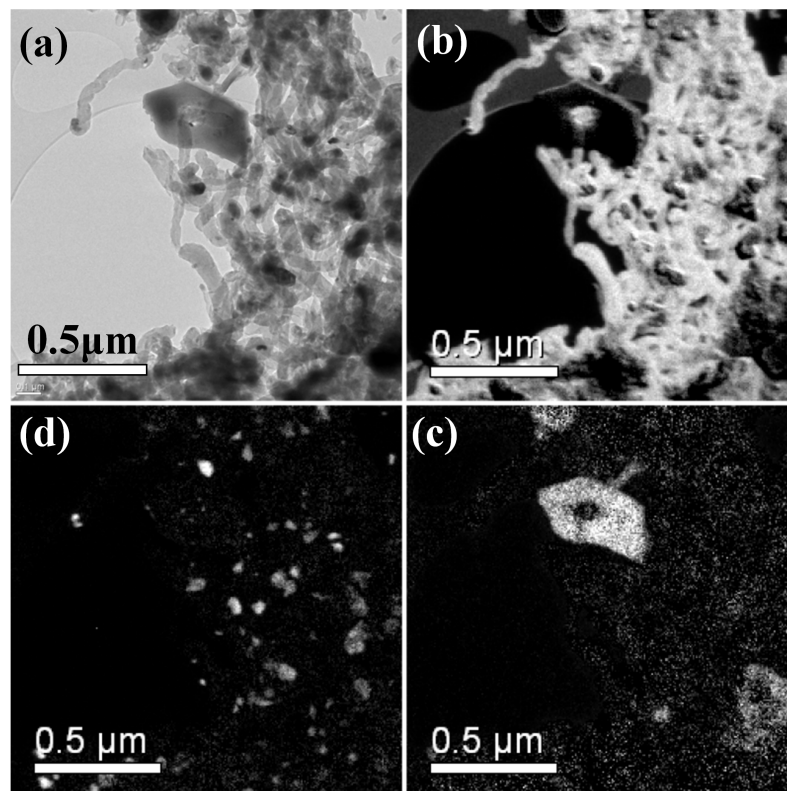


Figure 3.37: Transmission electron micrographs of Ni/Al₂O₃ recorded after reaction and INS measurement: (a) zero loss micrograph, i.e. no energy filtering, (b) carbon map, (c) nickel map and (d) oxygen map

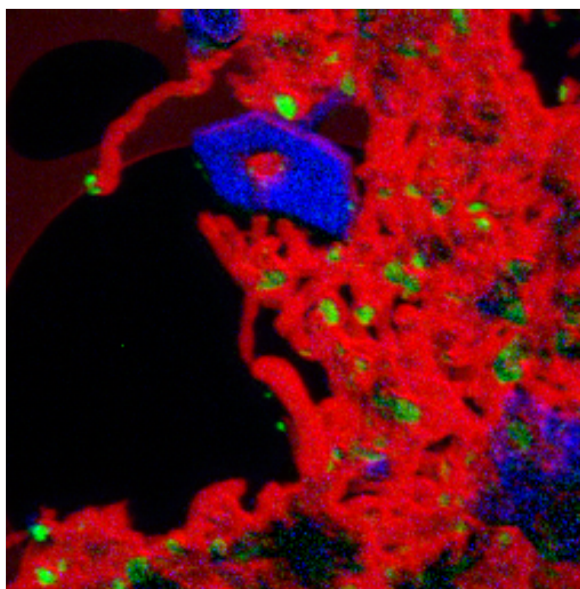


Figure 3.38: Colour-coded energy map transmission electron micrograph of Ni/Al₂O₃ recorded after reaction and INS measurement: red = carbon, green = nickel and blue = oxygen. The spectral scan is taken over the same area of sample presented in figure 3.37

strands or “whiskers” are composed of carbon. These whiskers are also known as filamentous carbon [2; 5; 114; 123] and are graphitic in nature. A small dark shape is discernible at the end of each whisker and figure 3.37(c) is the energy filtered image for nickel, which highlights these dark shapes. It can be concluded then that these are nickel particles that “cap” the carbonaceous whiskers at the end of each strand. In fact, these nickel particles are the reaction centre associated with the methane reforming reaction. These caps are present in a range of sizes, with diameters from 20-70 nm. Figure 3.37(d) presents the oxygen map and is present to highlight the alumina support as the K-edge of aluminium is such that it cannot be easily highlighted using this technique. It is apparent by the quantity of nickel particles capping the carbon filaments that the mechanism of filament growth has removed a large proportion of the active metal from the support. This phenomenon has been extensively reported [114][2][5][113] and is produced during the reforming process. Figures 3.37(b-d) can be recombined into (a) but as a colour coded map that is presented in figure 3.38 and provides a dramatic visual image of the spent catalyst post-reforming. The nickel particles are well dispersed but occur as terminations of carbonaceous “whiskers”, representative of filamentous carbon. It is clear that the carbonaceous matrix has lifted small nickel crystallites from the alumina support material, which the oxygen signal shows remain clustered in particular regions. Overall the picture is of a very mobile active site that continues to react long after separation from the support.

Prior to carrying out Raman measurements, diffuse reflectance UV-vis absorption measurements were performed in order to confirm that no unanticipated electronic effects could occur at the Raman wavelengths used for studying the reacted catalyst. Figure 3.39 shows UV-vis spectra of both the as received (a) and the reacted catalyst (b) as well as BaSO₄ (used as a diluent) as a reference (c). It can be seen from 3.39(b) and (c) that there are no features arising from the reacted catalyst and that the modes at 470 and 520 cm⁻¹ can be attributed to diluent. The same two bands also appear in figure 3.39(a) however the as-received sample also has a small adsorption band at 375 cm⁻¹ and a large broad feature at 310 cm⁻¹. These bands are associated with NiO electronic transitions

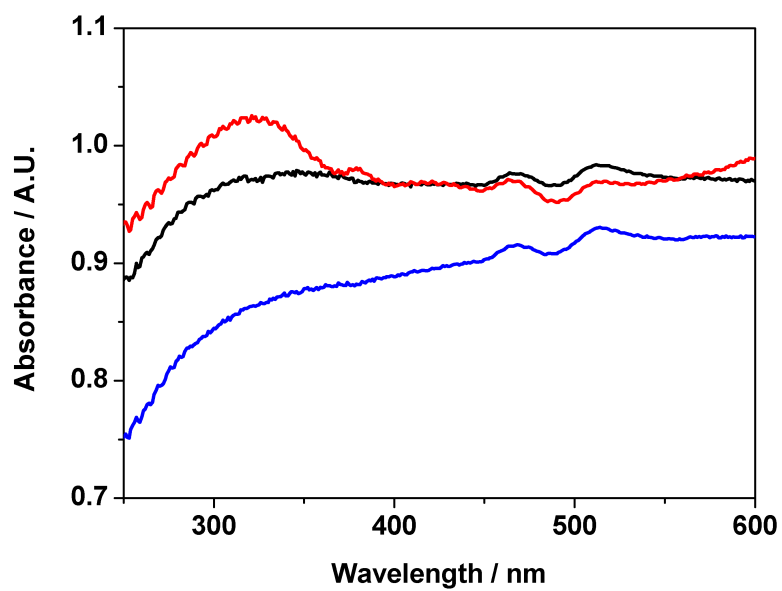


Figure 3.39: UV-vis spectra of (red) Ni/Al₂O₃ as received, (blue)Ni/Al₂O₃ post dry reforming reaction and (black) Barium sulphate which was used as a diluent

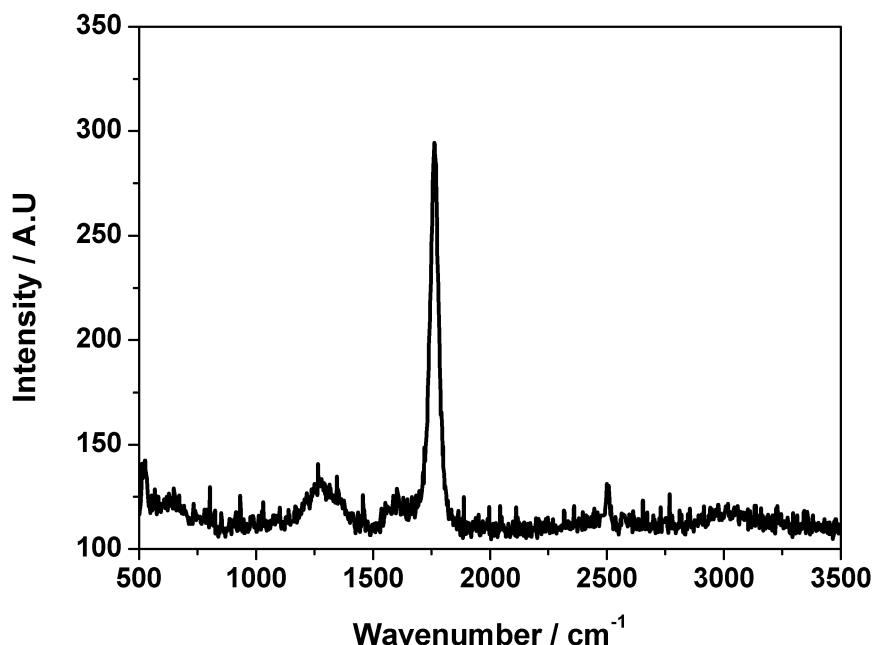


Figure 3.40: Raman measurement of post INS reaction Ni/Al₂O₃ catalyst, 325nm laser

from the pre-reduced nickel particles on the catalyst surface[135][136]. The laser wavelengths used in the Raman measurements are 325 and 532 nm respectively and from figure 3.39 it can be concluded that no distinct electronic adsorption should arise from the samples at these wavelengths.

Figure 3.40 shows the shows the 325 nm Raman spectrum in the range 500 - 3000 cm⁻¹ for the Ni/Al₂O₃ sample after 6 hours in a 1 : 1 mixture of CH₄ and CO₂ at 898 K in the INS reactor. Vibrational bands can be seen at 3000, 1750, 1620 and 1275 cm⁻¹. The band at 3000cm⁻¹ is a C-H stretching mode that is only visible using a UV laser source [104]. The large mode at 1750 cm⁻¹ is a combination band made up from the vibration at 1620 cm⁻¹ and radial breathing mode at 180 cm⁻¹ [95]. The small 1620 cm⁻¹ band is assigned to carbon - carbon double bond stretches [104] as is the mode at 1275 cm⁻¹. Figure 3.41(a) shows the 532 nm Raman spectrum in the range 500 - 3000 cm⁻¹ for the Ni/Al₂O₃ sample after 6 hours in a 1 : 1 mixture of CH₄ and CO₂ at 898 K in the mi-

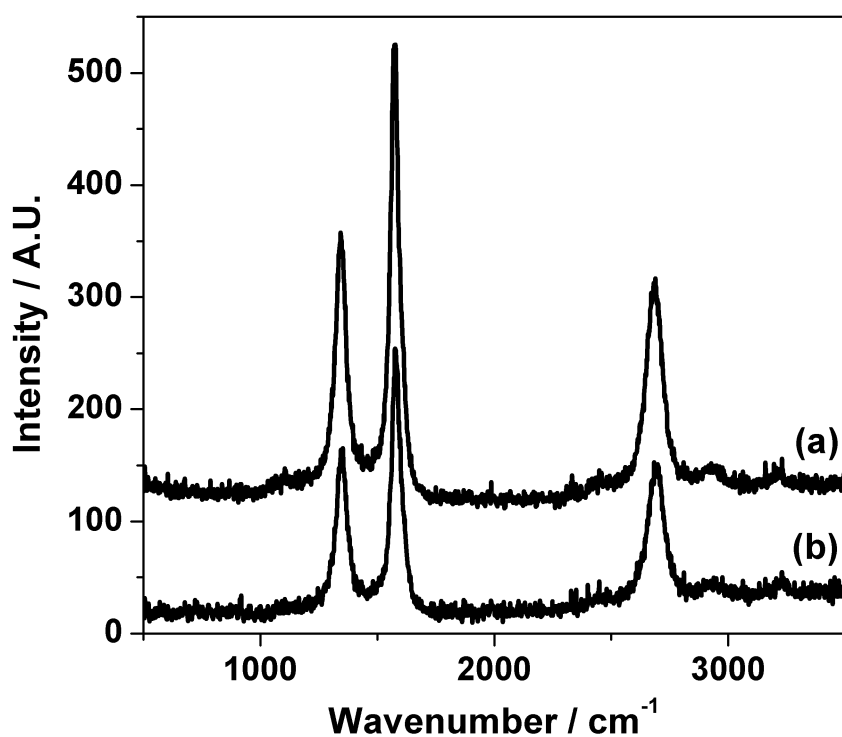


Figure 3.41: Raman measurement of post INS reaction Ni/Al₂O₃ catalyst, 532nm laser (a) Raman spectrum of Ni/Al₂O₃ recorded after reaction and INS measurement. (b) Raman spectrum of the sample in (a) after it has been exposed to a continuous stream of 5 % H₂ in He at 700 K for 1 hours

cro reactor. What is interesting when compared to the previous figure, is that two intense peaks at 1342 and 1580 cm^{-1} are observed (assigned to 1342 cm^{-1} - D and 1580 cm^{-1} - G bands of carbon that has been formed on the surface as before)[94; 96]. What figures 3.40 and 3.41 demonstrate is that different incident energies can highlight vibrational modes to different extents and so care should be taken when performing Raman measurements that are quantitative. Aside from the D and G bands, there are also two bands between 2500 and 3000 cm^{-1} (major band at 2685 cm^{-1}), which is due to the overtone of the D band ($2 \times 1342 \text{ cm}^{-1} = 2684 \text{ cm}^{-1}$) (and G band). This suggests an ordered carbonaceous matrix, which may be also further attributed to 3-dimensional ordering in the c direction (along the plane) of a graphitic like matrix [95][137][138].

In figure 3.29 temperature-programmed measurements demonstrated that hydrogenation of the carbonaceous overlayer at elevated temperature formed methane gas. Is it possible to incorporate hydrogen into the carbon matrix by passing H_2 over the spent catalyst at temperatures just below that which allows methane to form? If this could be achieved, the modified overlayer could then be exploited by INS as the extra hydrogen could amplify any existing modes. Figure 3.41(b) shows the Raman spectrum recorded after the sample examined in (a) had been maintained in a H_2/He feed-stream at 700 K for 30 minutes. Unfortunately no new features are present in the spectrum. Instead a slight reduction in intensity with respect to (a) is observed which indicates partial decomposition of the carbonaceous overlayer in this instance. Other combinations of temperature and flow rate were explored but no new spectral features were observed. These Raman experiments are consistent with a highly ordered carbonaceous overlayer, but the distribution of which is not amenable to further analysis by partial hydrogenation techniques.

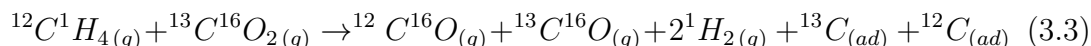
3.2.1.3 Isotopic Substitution Experiments

The previous experiments in this section have described the form and quantity of both the carbon and the hydrogen present in the overlayers of the reacted reforming catalysts. In order to complete the picture, it is imperative that the

Laser Wavelength (nm)	Wavenumber / cm ⁻¹	Assignment
352	3000	$\nu(\text{CH})$
	1750	Combination band
	1620	$\nu(\text{CC})$
	1275	$\nu(\text{CC})$
532	2685	D-band overtone
	1580	D band $\nu(\text{CC})$
	1342	G band $\nu(\text{CC})$

Table 3.8: Summary of the Raman Vibrational Assignments Post Methane Reforming Resulting in Graphitic Carbon Laydown.

source of the carbon is examined. In the steam reforming reaction, carbon is only available from methane, however in the “dry” reforming analogue, the oxidant could perceptibly contribute to the carbon formation. In order to evaluate this possibility, reaction testing measurements at 898 K for 1.5 hours were performed in the micro-reactor where $^{13}\text{C}^{16}\text{O}_2$ was used as a reagent alongside $^{12}\text{C}^1\text{H}_4$ in place of $^{12}\text{C}^{16}\text{O}_2$. A shorter reaction time was used in this instance due to the excessive cost of the $^{13}\text{C}^{16}\text{O}_2$ feedstock. The results are presented in figure 3.42. This experiment provides the opportunity to assess how the carbon connected with the CO_2 oxidant partitions in the reaction and whether it contributes to the carbon deposition process. In the absence of scrambling, the following (unbalanced) equation applies:



As the reaction progresses, the signal at mass 16 ($^{12}\text{C}^1\text{H}_4$) and mass 45 ($^{13}\text{C}^{16}\text{O}_2$) are seen to reduce over time, indicating the catalyst to be slowly deactivating, as seen in the earlier isothermeal reaction 3.25. At the same time, masses 28 ($^{12}\text{C}^{16}\text{O}$), 29 ($^{13}\text{C}^{16}\text{O}$) and 2 amu ($^1\text{H}_2$) also decrease. Figure 3.42 reproduces the same overall trends evident in the non-labelled experiment and shows increasing breakthrough of reactant alongside decreasing product formation which is due to a slow deactivation route. The fact that signals for both mass 28 and 29 decrease indicates that both the methane and oxidant are being consumed as part of the reaction process.

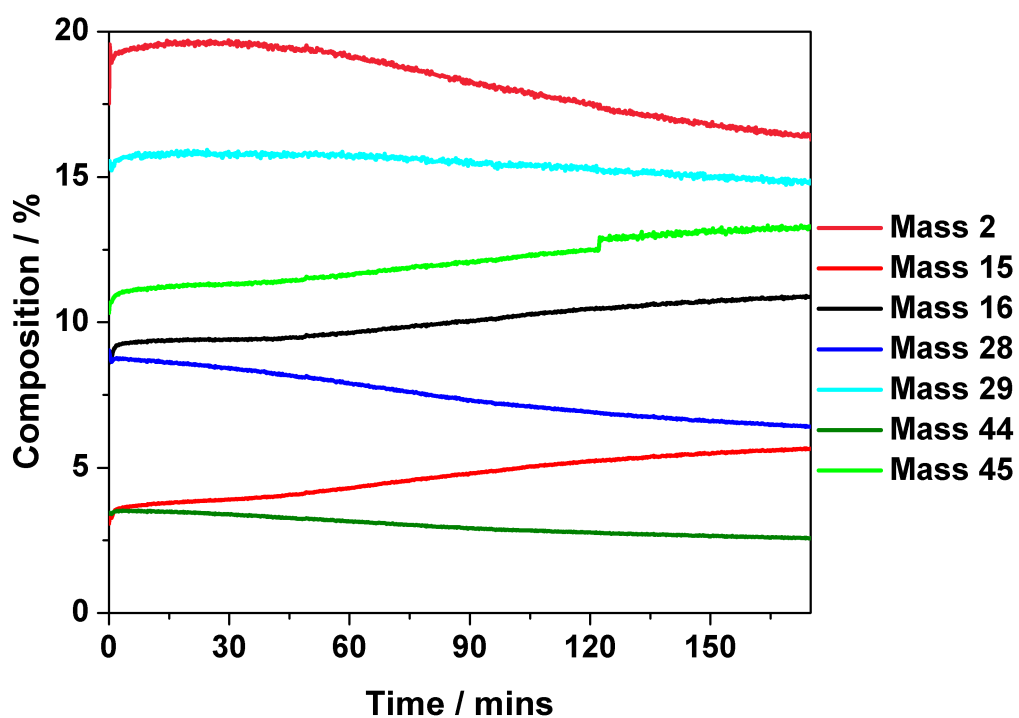
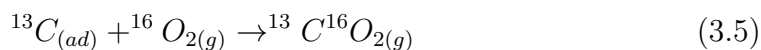
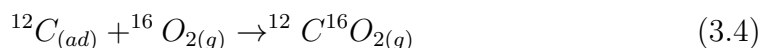


Figure 3.42: Isothermal reaction profile at 898 K of a 1:1 mixture of $^{12}\text{C}^1\text{H}_4$ and $^{13}\text{C}^{16}\text{O}_2$ over $\text{Ni}/\text{Al}_2\text{O}_3$ catalyst. Measurements performed using the micro-reactor arrangement

The equation above (3.3) demonstrates that carbon from the oxidant could conceivably contribute to the carbon deposition process. Figure 3.43 shows two TPO plots of post reforming with (a) $^{12}\text{C}^1\text{H}_4$ and $^{12}\text{C}^{16}\text{O}_2$ or (b) $^{12}\text{C}^1\text{H}_4$ and $^{13}\text{C}^{16}\text{O}_2$. The two equations 3.4 and 3.5 show that by mass analysing for 44 and 45 it is possible to determine whether the isotopically labelled carbon is present at the catalyst surface and thus conclude what role the oxidant is playing in the coking process.



The TPO profile above is of a post reaction sample after 1.5 hrs time-on-stream using conventional reagents ($^{12}\text{C}^1\text{H}_4 + ^{12}\text{C}^{16}\text{O}_2$) and shows a single and intense $^{12}\text{C}^{16}\text{O}_2$ feature ($T_{max} = 900$ K) skewed to low temperature, which is consistent with figure 3.27. A small signal for $^{13}\text{C}^{16}\text{O}_2$ is also seen, representing 1.1 % of the integrated intensity of the $^{12}\text{C}^{16}\text{O}_2$ peak, corresponding to the natural abundance of the ^{13}C isotope. This signal could equally be derived from the $^{12}\text{C}^1\text{H}_4$ or $^{12}\text{C}^{16}\text{O}_2$ and simply represents background levels of ^{13}C in the reactants.

The post-reaction TPO profile observed for a $^{12}\text{C}^1\text{H}_4$ and $^{13}\text{C}^{16}\text{O}_2$ feed-stream (figure 3.43b) shows a single $^{12}\text{C}^{16}\text{O}_2$ peak centered at 890 K but it also shows a significant $^{13}\text{C}^{16}\text{O}_2$ peak at the same temperature. The $^{13}\text{C}^{16}\text{O}_2$ peak intensity represents 31 % of the $^{12}\text{C}^{16}\text{O}_2$ peak. This value clearly exceeds ^{13}C natural abundance levels. Figure 3.43(b) shows that both the fuel and the oxidant (albeit to a lesser extent) are contributing to the carbon retained at the catalyst surface as part of the “dry” reforming process.

Schuurman and Mirodatos have performed similar TPO experiments over a silica-supported nickel catalyst but using $^{13}\text{C}^1\text{H}_4$ and $^{12}\text{C}^{16}\text{O}_2$ as reagents [120; 122]. In that case, the intensity of their $^{13}\text{C}^{16}\text{O}_2$ peak exceeded the intensity of their

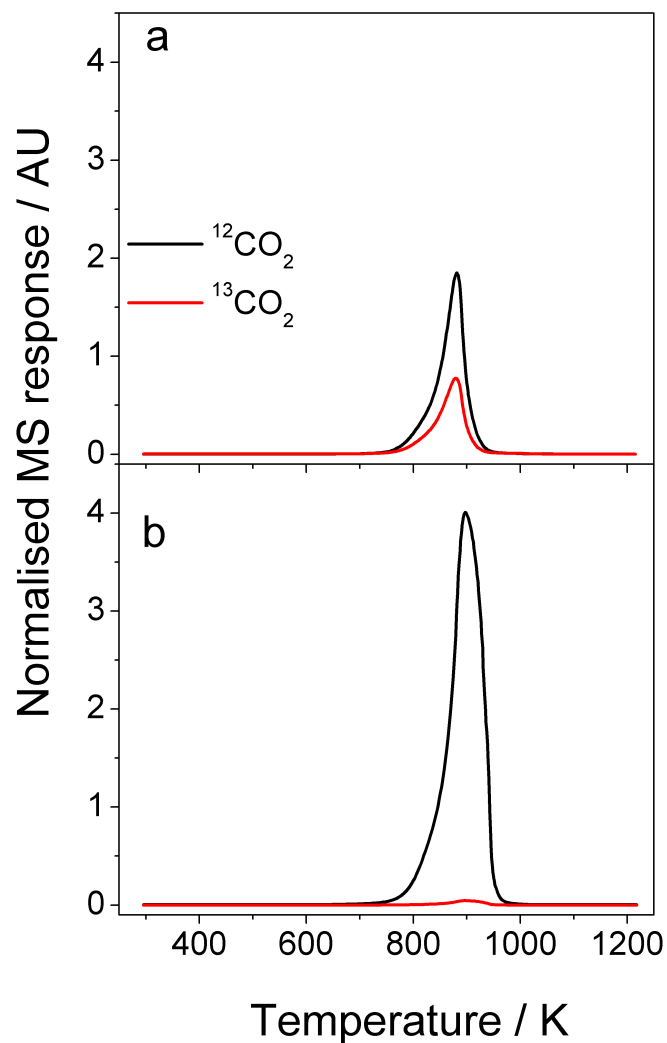


Figure 3.43: Temperature-programmed oxidation profile for Ni/Al₂O₃ catalyst after 1.5 hours isothermal run at 898 K of a 1:1 mixture of (a) ¹²C¹H₄ and ¹³C¹⁶O₂ and (b) ¹²C¹H₄ and ¹²C¹⁶O₂ over Ni/Al₂O₃ catalyst. Measurements performed using a temperature ramp of 10 K min⁻¹ and a carrier gas mixture of 5 % ¹⁶O₂ in ²He

$^{12}\text{C}^{16}\text{O}_2$ peak. That outcome is consistent with the results presented here.

3.2.2 Discussion

Compared to the previous section on “dry” reforming in this chapter, a combination of different preparative procedures (calcination temperature, support material, metal loading) and reaction conditions have been employed in order to synthesise a catalyst that favours the formation of filamentous carbon rather than amorphous carbon as the major side reaction. Thus equation 1.27 can be specifically written as equation 1.29 for this section.

Although the form of carbon is different in the two studies, the source of carbon is thought to be comparable in both regimes. Schuurman and Mirodatos have previously reported the carbon oxidation reaction to be rate limiting [122] and this would agree with the work presented here based on the large quantities of carbon being deposited on the surface coupled to the gradual deactivation of the catalyst over time.

The transmission electron micrographs (figures 3.37 and 3.38) are visually striking images that clearly describe the form of filamentous carbon, and this evidence is further supported by the presence of the graphite signal in the XRD diffractogram (figure 3.36). Temperature-programmed oxidation (figures 3.43 and 3.21) and hydrogenation (figure 3.29) describe an overlayer that is homogeneous in form and of a more graphitic than amorphous nature. The presence of a strong G band in the Raman spectrum (figures 3.41 and 3.40) further strengthen this conclusion. The extremely weak INS spectra presented in figures 3.33, 3.34 and 3.35 describe a carbonaceous overlayer that has practically no hydrogen and hints that hydrogen is perhaps only terminating the graphitic whiskers.

Quantification of both the hydrogenous and the carbonaceous components of the overlayers has been made possible by employing a range of techniques including elemental analysis, TPO and INS measurements. Table 3.6 shows the quantities of carbon resulting from the INS TPO and the elemental analysis. By

comparing the INS TPO measurements with the hydrogen quantification measurements, a carbon : hydrogen ratio of $2550 \pm 204 : 1$ is presented. This value significantly exceeds that of the previous section where the overlayer was predominantly amorphous in nature. These two ratios are justifiable as amorphous carbon domains would have many more termination sites than extended graphitic regions. These INS results show that hydrogen partitioning during the reaction differs depending on the regime in which that particular catalyst is operating (*i.e.* amorphous or graphitic).

The previous section identified a series of elementary reactions relevant to the operation of alumina-supported nickel catalysts active for the methane “dry” reforming reaction under amorphous conditions. The observed kinetic steps were then encapsulated within a scheme demonstrating that polymerisation occurs quicker than oxidation with steps involving hydrogen being the fastest of them all. The extra isotopic substitution measurements presented in this section allow more detailed postulation of the reaction mechanism, especially regards the oxidant. This chapter will conclude then, with a series of elementary reaction steps and their relative kinetic importance considered.

First to consider is the dissociative adsorption of methane, which proceeds in a stepwise manner to give us adsorbed carbon and hydrogen (equations 1.8-1.12). The results above show that temperatures in excess of 600 K are required to dissociate the methane molecule. From the different integrated areas in the TPO plot in figure 3.43(b) the process defined by equation 1.12 is most likely to be the major source of retained carbon. The next step is recombinative desorption of hydrogen which from the INS results is thought to proceed rapidly and efficiently:



Although the surface carbon atom in equation 1.12 goes on to polymerise into graphitic carbon (equation 1.29), it can also react with oxygen from the CO₂ to

form the CO product. However, as shown in figure 3.43(b), CO₂ is also a source of surface carbon and so a number of additional equations have to be considered that explain how the oxidant can contribute to carbon deposition and polymerisation. The first to consider is the dissociative adsorption of CO₂ (equation 1.17) which is the direct route for the oxidant to contribute to the coking process (equations 1.17 - 1.19). It is also possible that CO₂ could be cycled via the reverse water gas shift reaction to form CO (equation 1.6), which could then lead on to surface carbon via the dissociative adsorption of CO (equation 1.19).

Furthermore, CO₂ could additionally contribute to the Boudouard reaction, (equation 1.2). This latter option is thought to be dominant on the basis that equations 1.17 and 1.19 lead to chemisorbed oxygen atoms, that can then go on to oxidise the adsorbed carbon and hydrogen atoms 3.8 and 3.9.



Whereas this work has required application of a wider number of elementary reactions than proposed for the catalyst exhibiting amorphous carbon laydown in the previous section, both schemes are equally valid and transferable as long as one differentiates between amorphous and graphitic carbon.

It is possible to sum this second section up with a generic reaction scheme as presented in figure 3.44. Other schematics similar to figure 3.44 have been reported by others. For instance, Ferreira-Aparicio *et al* present a reaction scheme for the reforming of methane with carbon dioxide over a Ru/SiO₂ catalyst [139]. Rostrup-Nielsen and Sehested have also examined details of whisker carbon formation [46]. Froment's examination of producing synthesis gas by steam and CO₂ reforming of natural gas also includes a model outlining the elementary steps of methane cracking on a nickel/alumina catalyst [13].

Ultimately this section builds on the work done in the previous section of this chapter and adds specific insight into filamentous carbon formation in the "dry" reforming reaction. It has also further developed the methodology of the INS hydrogen quantification procedures.

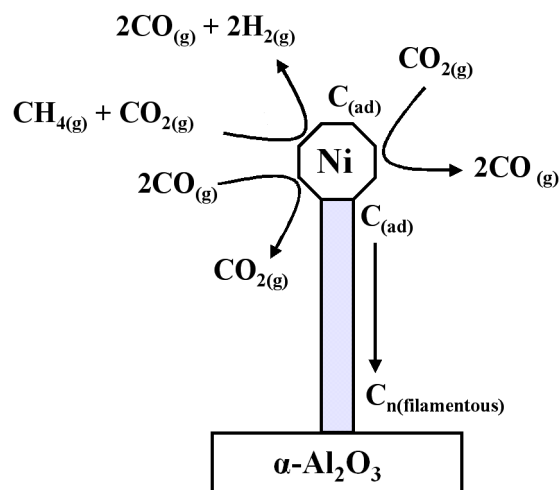


Figure 3.44: Schematic diagram illustrating some of the main reactions active during the “dry” reforming of methane and the formation of filamentous carbon.

Chapter 4

Steam Reforming of Methane

The propensity for coke build-up on supported metal catalysts during the steam reforming of methane reaction can be minimised by using a high ratio of steam : methane or via dopants such as gold [14; 24]. Producing steam in quantities sufficient for reforming on an industrial scale is extremely costly and so it would be beneficial to operate the reaction at low steam ratios, whilst still minimising the deposition of carbon. By accurately characterising and quantifying the coke deposited on the catalyst during the reaction, it may be possible suggest improvements to the system such that carbon free operation can be achieved even at low steam ratios. This chapter will seek to extend on that of the previous chapter by attempting to use some of the spectroscopic methods above with thermal methods and transmission electron microscopy to characterise and quantify the surface carbon. INS will also be employed as before to make statements about the retention of hydrogen by the catalyst during the reaction. Unlike the “dry” reforming reaction which was found to be extremely lean in hydrogen, the steam reforming alternative harbours the possibility of a more hydrogen rich overlayer based on equation 1.24 where larger quantities of hydrogen are being processed by the catalyst. If this were to prove true, the steam reforming of methane would be ideally suited to analysis by INS.

This chapter discusses three separate bodies of work based on developing the understanding of carbon and hydrogen deposition and retention in the steam reforming of methane reaction. Similarly to the previous chapter, the first section focusses on a catalyst that favours amorphous carbon formation, whilst the

second section looks at a catalyst where filamentous carbon is prevalent. Section three is a brief discussion on attempts to carry out high temperature steam reforming measurements in a bid to negate the water gas shift reaction.

4.1 Amorphous Carbon Characterisation

This section is concerned with characterising amorphous overlayers that are formed during the steam reforming of methane over the 45 wt % Ni / Al₂O₃ catalyst. The reforming reactions were carried out in relatively steam rich conditions to reflect the industrial scenario.

4.1.1 H₂O Calibration

One major problem in the steam reforming reaction that does not need to be considered in the “dry” reforming alternative is the supply and more importantly the quantification of H₂O as steam. Steam has to be created via the evaporation of water and can then be transported to the reactor via a carrier gas (e.g. helium). This is reasonably facile and the experimental setup described above allows steady flow rates of steam for extended periods of time. The problem of quantification is not so readily solved. Two possible methods of quantifying steam flow rates were devised for this project. The first was to install a length of swagelok after the reactor that could be placed in ice water and act as a “catch pot” for the steam to condense in. It could then be possible to set up a flow rate of He through the bubbler at a specific temperature for an extended time (e.g. 10 hours). At the end of this time, water condensed in the catch pot could be weighed and the total mass of water divided by the time to give a flow rate of H₂O (steam) in sccm. In practice, there were a number of issues that rendered this infeasible. Firstly, it could not be assumed that 100 % of the steam was condensing in the catch pot. Secondly, as only small amounts of steam are created, the error in weighing the pot could constitute a significant error in calculating the steam flow rates.

The second method was to oxidise H₂ in excess O₂ over the Ni/Al₂O₃ catalyst at elevated temperatures. Figure 4.1 shows how the mass spectrometer response (mass 18) varies with the oxidation of different known flow rates of hydrogen. Hydrogen flow rates of 8 sccm to 1 sccm were oxidised in 1.5 x O₂ to ensure 100 % conversion. As can be seen from the figure, the mass 18 response decreases in a stepwise manner when the flow rate of H₂ is decreased by 1 sccm. Figure 4.2 shows the average mass spectrometer (mass 18) response plotted against the flow rate of hydrogen oxidised to give that specific signal. It is clear from the

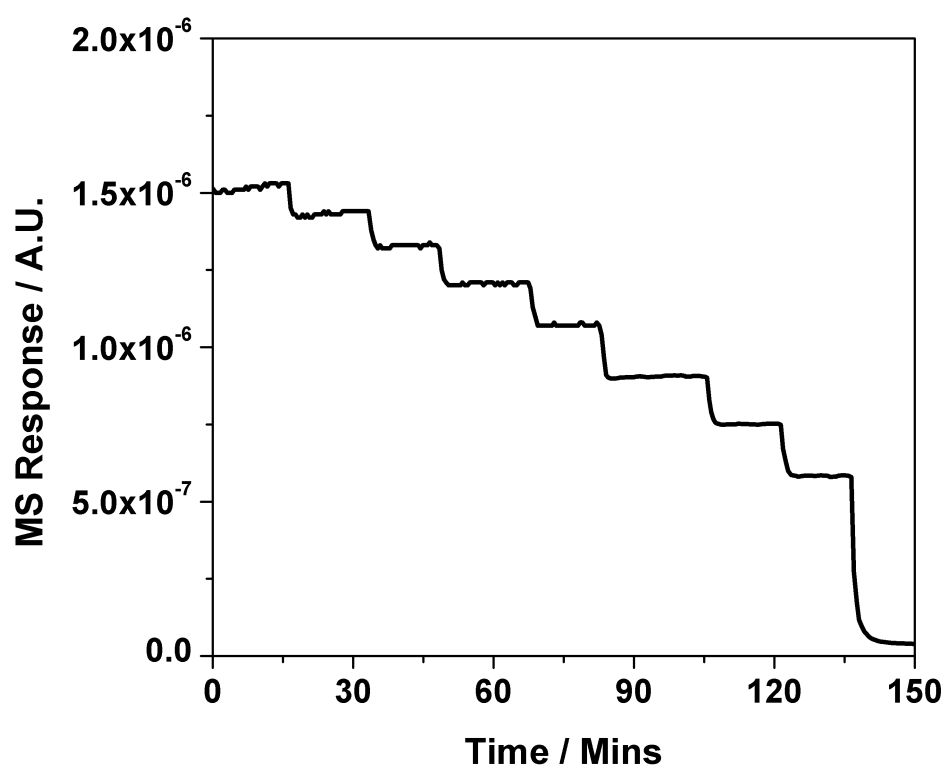


Figure 4.1: Mass 18 (H_2O) response of oxidation of varying known flow rates of H_2 in O_2 . Oxidation performed over the $\text{Ni}/\text{Al}_2\text{O}_3$ catalyst at a temperature of 898 K

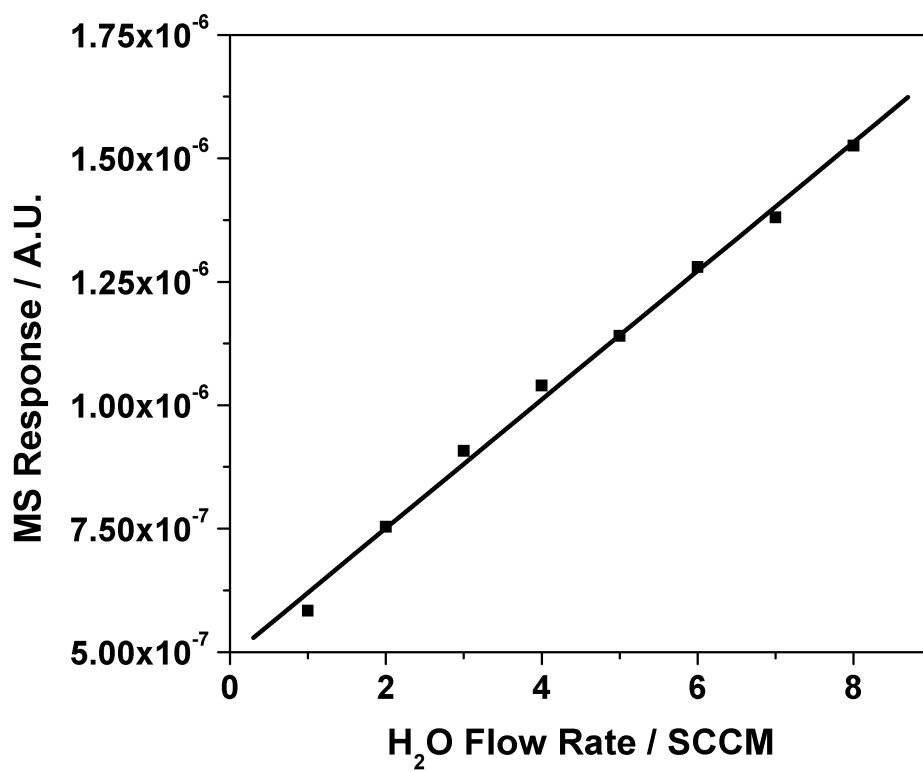


Figure 4.2: Average mass 18 (H₂O) response vs H₂O flow rate (Assuming 100 % hydrogen conversion)

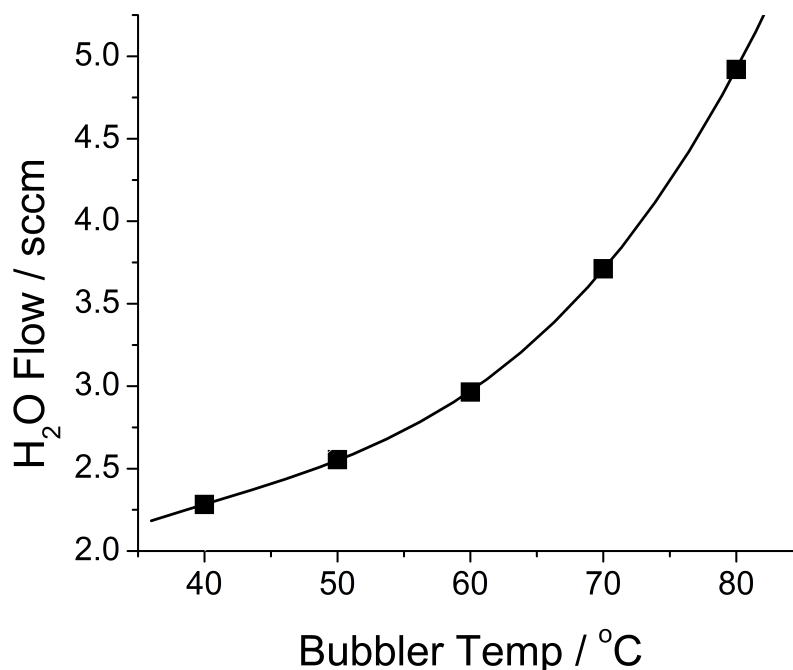


Figure 4.3: Variation of H₂O flow rate (based on mass 18 (H₂O) response as temperature of bubbler is increased.

plot that there is a linear relationship between the H₂O flow rate and the mass spectrometer response. Figure 4.3 is a plot of how the mass spectrometer mass 18 signal varies as the temperature of the bubbler is varied (at a constant He flow rate). The data were well described by a cubic polynomial obtained via curve fitting using the Origin software package. By relating the mass spectrometer response to the flow rate (figure 4.2) the temperature can be calculated at which to hold the oil bath for any flow rate of steam within the calibrated range. This approach was therefore selected as the way by which all steam flow rates were calculated in both the microreactor and the INS experiments.

4.1.2 Microreactor Results

Initial steam reforming measurements were performed in the microreactor in order to assess catalyst performance. Figure 4.4 is the temperature programmed reaction for the steam reforming reaction. It can be seen from the figure that

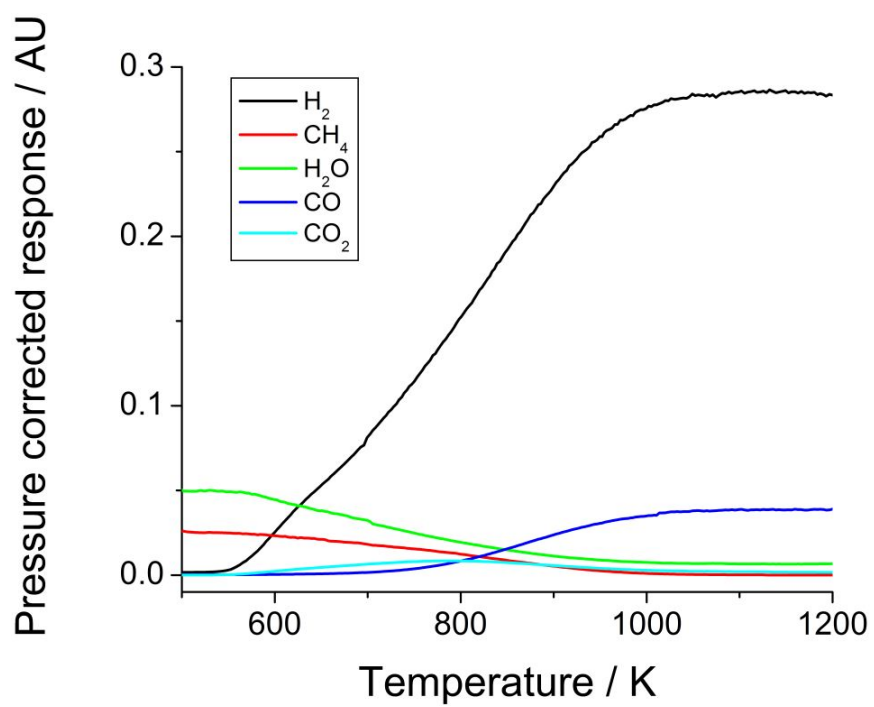


Figure 4.4: Temperature programmed reaction for steam reforming over 45 wt % Ni/Al₂O₃ catalyst

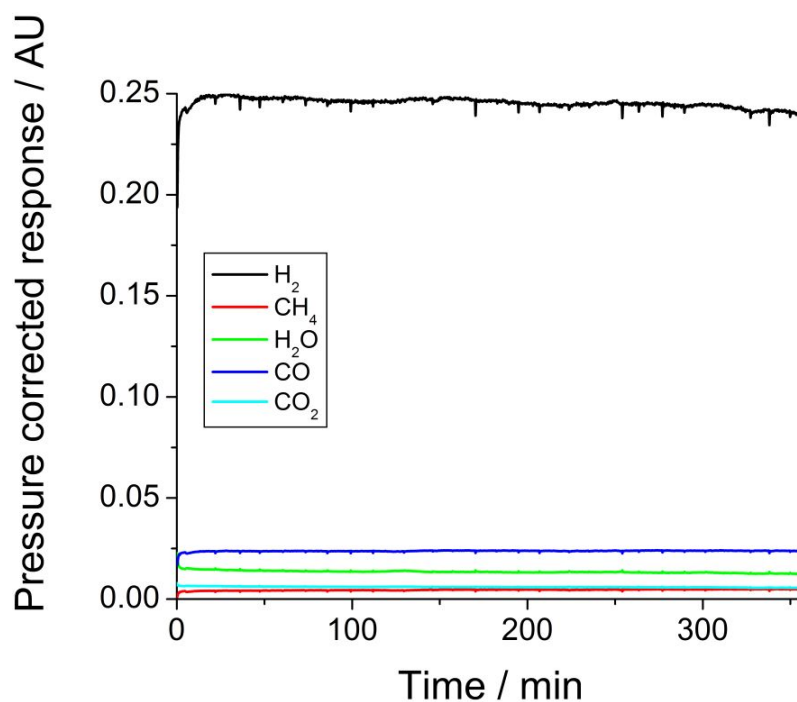


Figure 4.5: Isothermal reaction for steam reforming at 893 K over 45 wt % Ni/Al₂O₃ catalyst

hydrogen production commences just above 650 K. The evolution of CO₂ can also be seen at this temperature. This is due to the water gas shift reaction that is discussed in the previous section and is competes favourably over the reforming reaction at this temperature. It is not until around 750 K that the production of CO is observed. At temperatures approaching 1000 K, 100 % conversion is attained and this is seen by a plateau of both reactants and products. It is to be noted that the CO₂ levels have tailed off at this temperature which is a result of the WGS reaction being less favoured. As expected, the production of hydrogen is considerable, and demonstrates why this reaction is favoured industrially for hydrogen production.

Figure 4.5 shows the extended isothermal reaction in the microreactor at 893 K, This temperature was selected in order to allow comparisons to be made between the microreactor studies and the INS measurements. Minimal deactivation was seen over the six hour reaction, with methane conversion dropping from 82 to

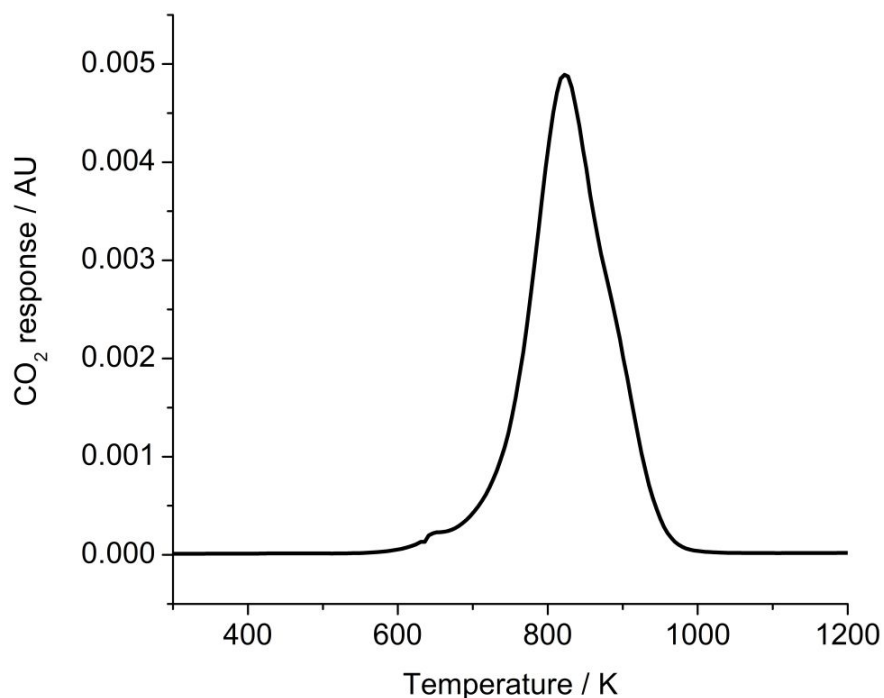


Figure 4.6: Temperature programmed oxidation of catalyst after extended isothermal reaction at 893 K (Figure 4.5)

79 %. CO and H₂ are the majority products although some production of CO₂ persists which is in agreement with the temperature programmed reaction in Figure 4.4. Overall though, the catalyst shows promising activity over the extended time.

Figure 4.6 shows the TPO of catalyst after the extended isothermal reaction at 893 K (Figure 4.5). The peak maximum is 826 K, suggesting a material that has not formed an extensive graphitic network. For comparison, the crystalline graphite that was used for calibration had a peak maximum of 1086 K. Integration of the peak area gives a value of 2.047 mmol C g⁻¹ *cat*. Temperature programmed hydrogenation of a post-reaction sample is displayed in Figure 4.7 and shows the ms response to mass 15 (methane). There are two peaks in this figure, a small low temperature peak at 570 K which suggests a minor species of reactive coke to have formed on the surface. The higher temperature peak at around 850 K is consistent with the TPO measurement (figure 4.6) and suggests

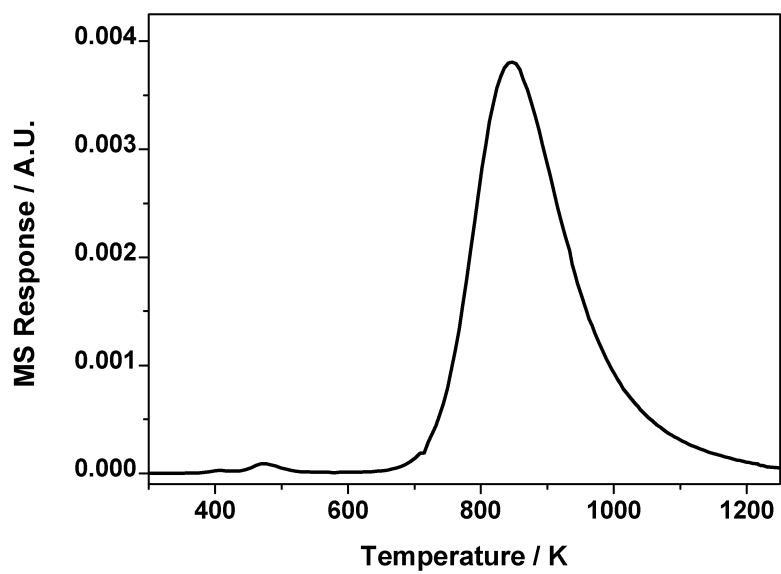


Figure 4.7: Mass 15 (methane) Temperature programmed hydrogenation of catalyst after extended isothermal reaction at 893 K

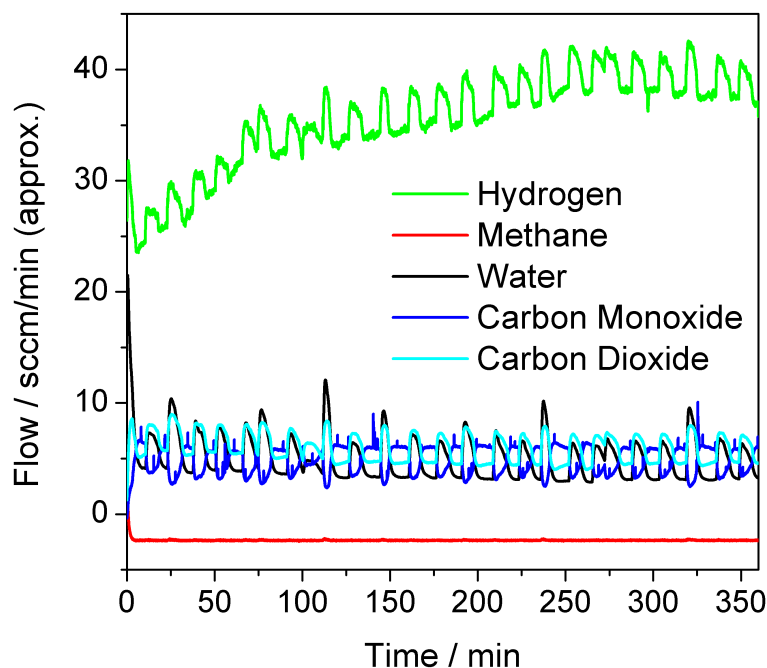


Figure 4.8: Extended reaction at 893 K of 18 sccm CH_4 and 30 sccm H_2O over reduced $\text{Ni}/\text{Al}_2\text{O}_3$ catalyst. Sample prepared in INS reactor and denoted INS18

an amorphous coke has been formed.

4.1.3 Inelastic Neutron Scattering Measurements

As discussed in the experimental section, two INS steam reforming samples were prepared, INS6 and INS18. INS18 represents a higher methane ratio and the representing isothermal reaction measurement can be seen in figure 4.8 with INS6 (a lower methane flow rate) shown in figure 4.9. What is most notable from both the figures is the instability of the flow rates. This is due to the way the steam is produced in the system. The saturator is controlled via a PID (Proportional Integral Derivative) controller which should reduce fluctuations in the temperature of the saturator by continuously regulating the power output via a feedback loop. In practice however, a steady temperature is not able to be maintained and

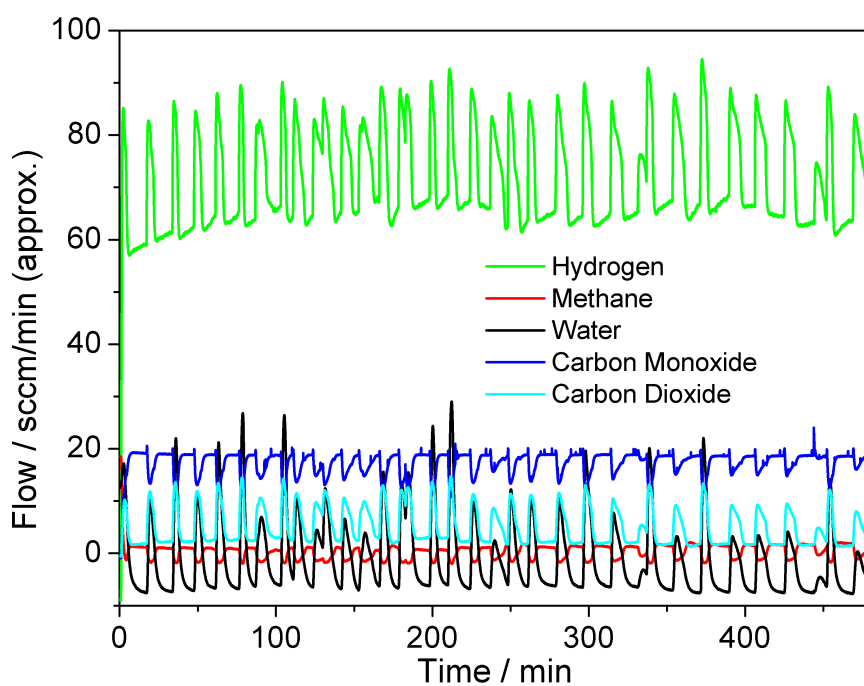


Figure 4.9: Extended reaction at 893 K of 5.6 CH₄ and 30 H₂O over reduced Ni/Al₂O₃ catalyst. Sample prepared in INS reactor and denoted INS6

so the saturator tends to overshoot the desired temperature. When this occurs, the heater switches off and the temperature falls below the one desired. This continuous fluctuation is then seen as unsteady steam production in the mass spectrometer. What is interesting, is that the microreactor rig is set up to produce steam in a very similar manner yet the steam response is much more linear. This demonstrates the higher heat capacity of the INS reactor cell and is a further complication in the generation of steam. Figures 4.8 and 4.9 demonstrate this difficulty that is inherent in controlling large quantities of steam.

Although the isothermal INS measurements are not ideal, they do show that the reforming reaction is taking place as CO and H₂ are being produced while at the same time CH₄ is being consumed. No deactivation is readily apparent, which is consistent with the microreactor studies.

Whilst two samples were prepared for INS, experimental constraints prevented collection of a complete set of data for INS6. This is due to the INS6 isothermal reaction being too oxidant rich a regime and so no hydrogen signals were observed in the spectrometer, *i.e.* the high steam ratio had oxidised any retained hydrocarbonaceous deposits. INS spectra are therefore only shown for the catalyst after reaction with the higher methane flow (INS18/INS18H). INS18H represents an attempt to incorporate additional hydrogen into the matrix of the carbonaceous overlayer. This was done, in part, to determine if different operating conditions affected the hydrocarbonaceous retention properties of these catalysts. As described in the experimental section, hydrogen was passed over the reacted catalyst at temperatures just below that which methane begins to form from the surface coke. A similar experiment was performed in the previous chapter using Raman as the resultant probe. The results were negative, but as INS has increased sensitivity to hydrogen, it was hoped that any hydrogen incorporated into the matrix would be observed. Those recorded with an incident neutron energy (E_i) of 4840 cm⁻¹ (600 meV) are shown in Figures 4.10 and 4.11.

The poor signal to noise ratio indicates a very low concentration of hydrogen within the neutron beam. Using the calibration method described in an earlier chapter, the quantity of hydrogen associated with the overlayer is calculated at

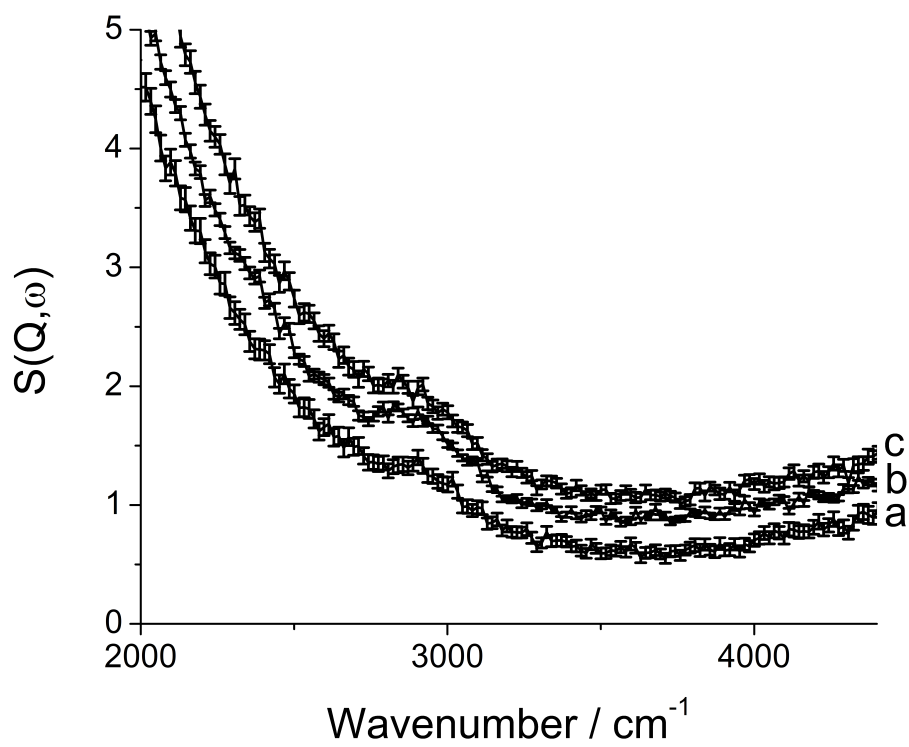


Figure 4.10: INS spectra of catalyst (a) after reduction (b) after reaction (INS18) (c) after hydrogenation (INS18H) of reaction-deposited layer recorded with incident neutron energy of 4840 cm^{-1}

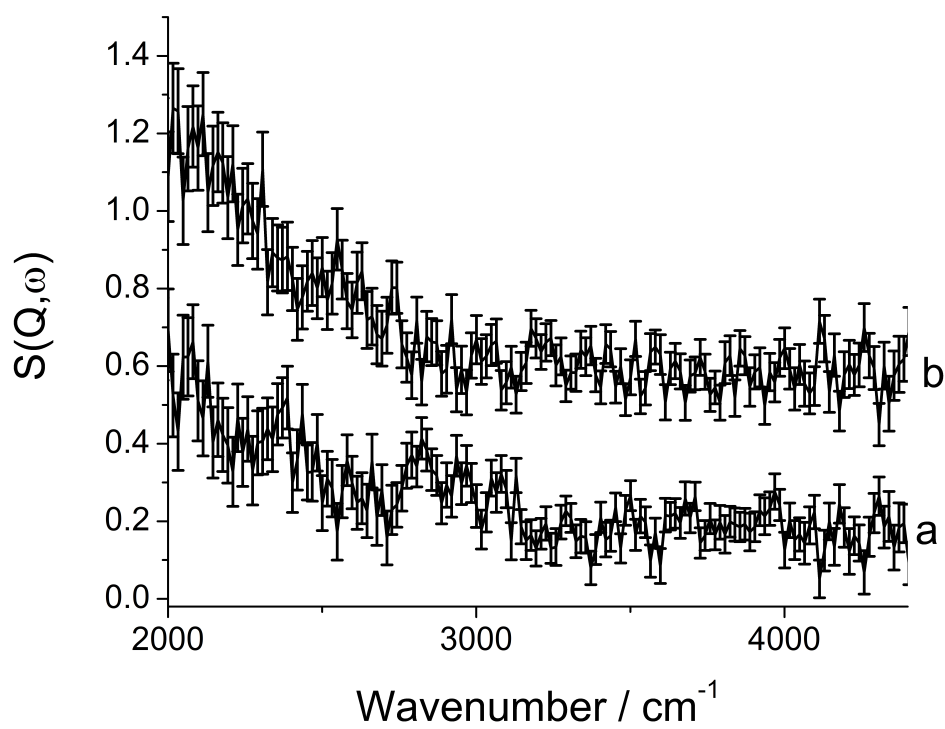


Figure 4.11: Subtracted INS spectra of catalyst overlays recorded with incident neutron energy of 4840 cm^{-1} (a) after reaction (INS18) and (b) after hydrogenation INS18H of reaction-deposited layer

	Ni/Al ₂ O ₃ (INS18)
Carbon _(ad) TPO (micro-reactor)	2.0 mmol Cg ⁻¹ cat
Carbon _(ad) TPO (INS-reactor)	N/A due to post reaction hydrogenation
$\nu(\text{O-H})$	not observed
$\nu(\text{C-H})$	7.9 $\mu\text{mol Hg}^{-1}\text{cat}$
$C_{tot} : \text{H}$	253:1

Table 4.1: Carbon and hydrogen retention values for post H₂O reforming at a 2:1 steam to methane ratio.

7.9 $\mu\text{mol}(\text{C-H})/\text{g}_{\text{cat}}$ for INS18, but values were not obtained for INS6 or INS18H, due to poor signal intensities. Figure 4.10 shows the raw data for the catalyst after the reduction, reaction and hydrogenation steps. All samples show a peak around 2930 cm^{-1} which may be assigned to aliphatic C-H stretching vibrations. The fact a low intensity band is present at this position on the reduced catalyst suggest some degree of contamination within the system due to organic materials, such as oil or grease, possibly on the walls of the cryostat. This is a problem that has manifested itself here because of the low concentration of hydrogen connected with these particular samples. Figure 4.11 show the sample spectra after subtraction of the reduced catalyst spectrum, which should nullify the effect of contamination and any contribution of the catalyst to the spectra, assuming it is unchanged by the reaction. Figure 4.11a displays three weak features in the C-H stretching region, at 2820, 2952 and 3080 cm^{-1} . This suggests that the material formed has a combination of saturated and unsaturated character. Figure 4.11b shows no discernible C-H stretching vibration. From this result, it is clear that attempts to incorporate additional hydrogen into the overlayer have been unsuccessful with desorption being the favoured process. If we compare the quantification of carbon from the TPO measurement, figure 4.6 with the quantification of hydrogen from figure 4.10 we can calculate an estimated ratio of carbon to hydrogen present in the overlayer. Table 4.1 shows this value to be around 250 : 1 carbon to hydrogen atoms. This result demonstrates again, the relative efficiency of reactions involving hydrogen compared to those involving carbon. INS spectra collected at E_i of 2017 cm^{-1} (250 meV) are shown in Figure 4.12 with the samples displaying peaks at 172 and 379 cm^{-1} ; the lower peak has a shoulder at 231 cm^{-1} . The 172/231 cm^{-1} band is assigned to a nickel phonon mode.

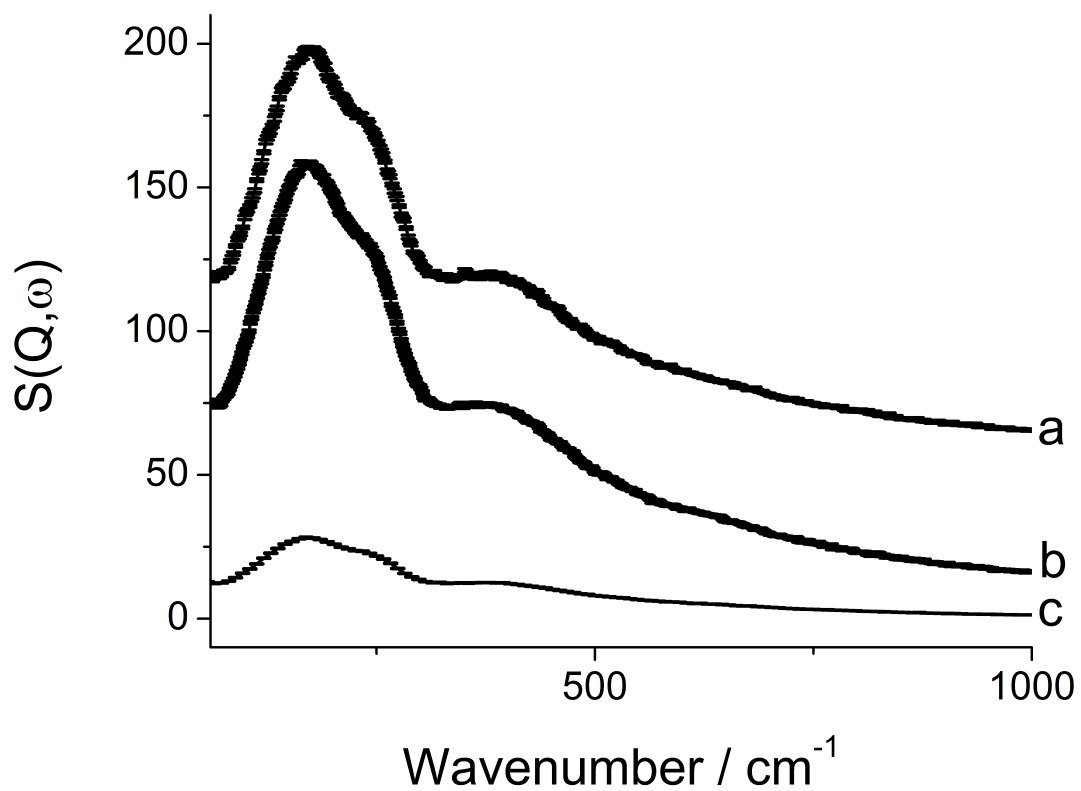


Figure 4.12: INS spectra of catalyst (a) after reduction (b) after reaction (c) after hydrogenation of reaction-deposited layer recorded with incident neutron energy of 2017 cm^{-1}

Wavenumber / cm^{-1}	Assignment
3080	$\text{sp}^2 \nu(\text{CH})$
2952	$\text{sp}^3 \nu(\text{CH})$
2820	$\text{sp}^3 \nu(\text{CH})$
379	Uncertain
231	Nickel phonon
172	Nickel phonon

Table 4.2: Summary of the INS Vibrational Assignments Pre and Post Methane Steam Reforming Resulting in Amorphous Carbon Laydown.

The origin of the 379 cm^{-1} feature are uncertain. The observation that spectral intensity is substantially attenuated on hydrogenation indicates some change in the Ni environment. This matter is considered further upon presentation of the x-ray diffraction data later in this chapter. A summary of the INS vibrational assignments is presented in table 4.2

4.1.4 Post INS Characterisation

4.1.4.1 Raman

Prior to taking Raman measurements of the sample, UV-vis spectra were recorded in order to better understand the Raman spectra in terms of any possible resonance effects. These are presented in Figure 4.13. It can be seen from figure 4.13(b) that increasing the methane ratio with respect to oxidant has resulted in increased UV absorbance, especially at wavelength below 400 nm. The grey lines indicate the wavelength at which Raman spectroscopy was performed. It is clear that the sample does not exhibit any distinct absorptions at these wavelengths. Figure 4.14 shows the Raman spectra collected with 532 nm excitation. Figure 4.14 shows both INS6 and INS18H post reaction. There is a single weak peak at 834 cm^{-1} which is due to the microscope slide upon which the samples are supported. The rising background at higher wavenumber is due to fluorescence, which is induced in the material after the hydrogen treatment. Although vibrational information is not apparent in these results, it demonstrates that the catalyst's morphology has been affected by the hydrogenation step, as fluorescence has been

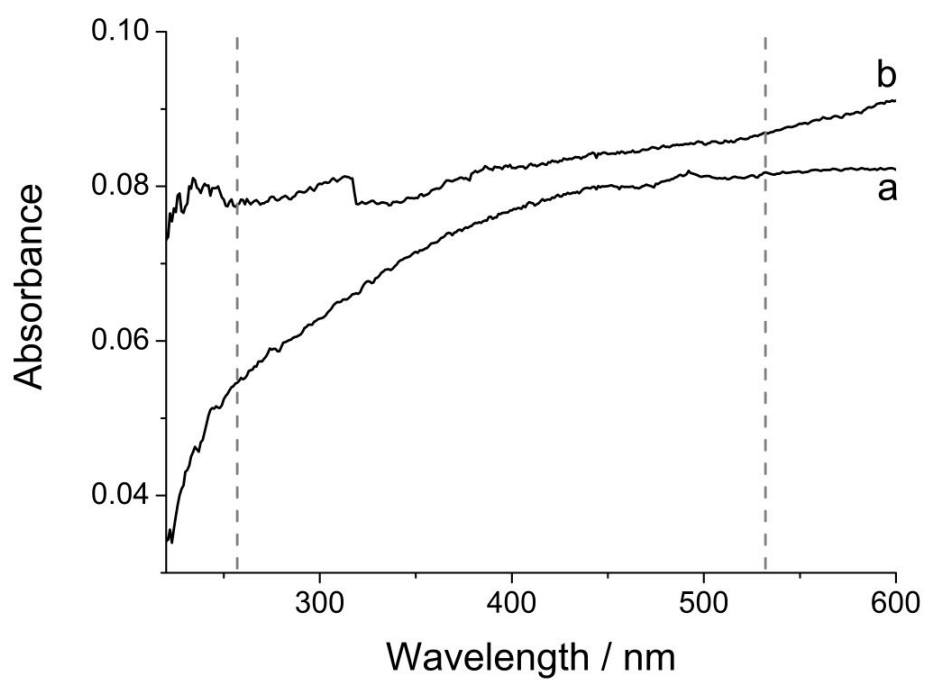


Figure 4.13: Diffuse reflectance UV-Vis spectra of samples after (a) reaction at low methane flow (INS6) and (b) reaction at high methane flow followed by hydrogen treatment (INS18H). Dashed grey lines indicate Raman laser wavelengths (257, 532 nm).

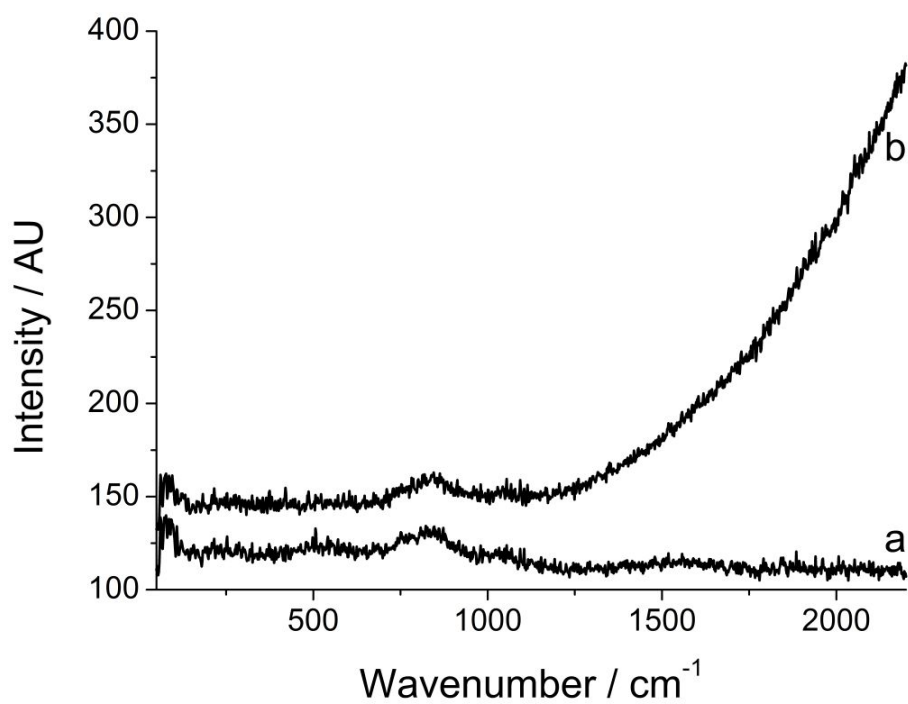


Figure 4.14: Raman spectra of catalyst after (a) reaction at low methane flow (INS6) and (b) reaction at high methane flow followed by hydrogen treatment (INS18H).

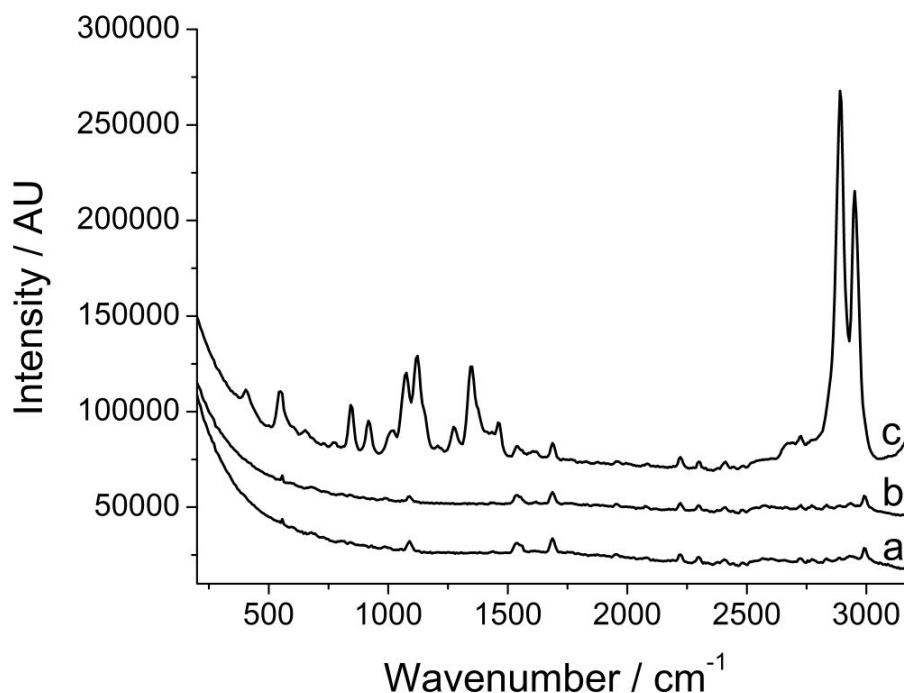


Figure 4.15: UV-Raman spectra of (a) KBr diluent, (b) catalyst after reaction with low methane flow (INS6), and (c) glucose reference

induced. Furthermore, the absence of the D and G bands of graphite suggest that the quantity of carbon on these materials is low and has no apparent long range order. The Raman spectra collected with 257 nm excitation are shown in Figure 4.15. The UV Raman spectrum of post reaction samples is present in fig4.15. The glucose spectrum (c) was collected as an example of the quality of data that may be obtained under ideal conditions. However in (a) and (b) we see no modes like those associated with the glucose. Again, this suggests minimal formation of coke on the sample during the reforming process. The peaks that are observed in (a) and (b) are due to either plasma lines from the laser or fluorescence within the instrumental optics.

4.1.4.2 X-ray Diffraction Measurements

Figure 4.16 shows the XRD patterns corresponding to the catalyst, (a) before reduction, (b) INS6 after reduction and reaction, (c) the sample hydrogenated

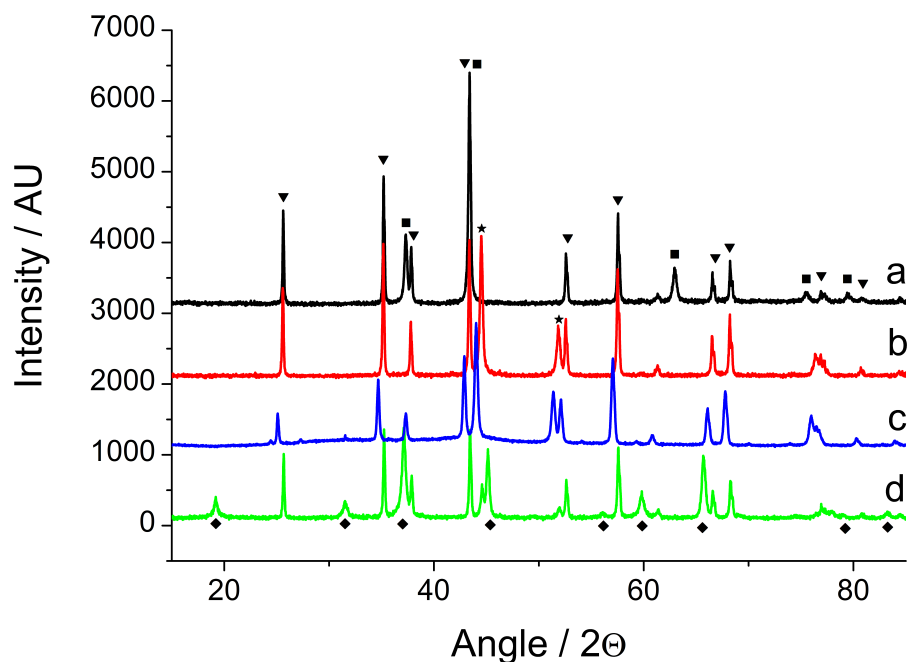


Figure 4.16: X ray diffraction pattern for the catalysts (a) as received, (b) INS6 post reaction, c) INS18 hydrogenated in the microreactor post-reaction and (d) INS18H after reduction, reaction and hydrogen treatment. Triangles indicate corundum reflections, squares indicate NiO, stars are reflections from metallic nickel and diamonds indicate reflections from the spinel structure (NiAl_2O_4). Trace (c) is slightly shifted due to calibration issues with the instrument

in the microreactor post-reaction, and (d) INS18H after reduction, reaction and hydrogen treatment. The catalyst before reduction is composed of nickel oxide on α -alumina (corundum), showing no trace of the spinel structure. INS6 shows peaks from metallic nickel and corundum, indicating that the pre-reaction reduction has transformed the nickel oxide into the active metal. This can be regarded as the active phase, and despite the relatively higher concentration of steam in this reaction, the spinel has not formed. INS6 represents the active catalyst after reaction. The post-reaction hydrogenation carried out in the microreactor has not affected the structure of the catalyst, with metallic nickel and α -alumina being the phases present after this treatment. The INS18H sample however, shows decreased intensity from metallic nickel. The corundum peaks are also present, but weaker and a new phase is apparent due to formation of a nickel aluminate spinel

(NiAl₂O₄), indicating reaction between the metal and support. The absence of serious deactivation in 4.5 and 4.8 suggest the catalyst has not transformed in the reaction itself, but through post-reaction treatment. INS18 is therefore expected to have been of similar structure to INS6 before hydrogenation to INS18H. The reaction of Ni/Al₂O₃ to NiAl₂O₄ is formally an oxidation, yet appears to have occurred under reducing conditions. This surprising result is explored further in view of other data in the discussion. No evidence is apparent in any sample for the presence of nickel carbides or graphite.

4.1.4.3 Transmission Electron Microscopy

Energy filtered TEM images of the samples are shown in Figure 4.17 (INS6) and Figure 4.18 (INS18H). Figure 4.17 shows well defined nickel particles of *ca.* 5–60 nm diameter supported on the oxide support. Dark spots on the zero energy loss image are associated with high intensity in the nickel map, and a low intensity in the oxygen map. This indicates a clear boundary between the metal and support. In Figure 4.18 large dark areas in the standard transmission image appear predominantly due to the thickness of the sample. Some of these regions however, also appear to contain a higher concentration of nickel. The boundary between the nickel and surrounding support has become indistinct. Both light and dark areas in the zero energy loss micrograph show a high oxygen concentration. This can be interpreted as an intimate mixing of the nickel with the alumina, as would be expected in a nickel aluminate phase. The metal appears to have diffused into the alumina support and formed the aluminate spinel during the post-reaction hydrogenation step.

4.2 Discussion

Although less than ideal steam generation was achieved in the INS sample preparation, the steam reforming reaction is clearly active and a persistent carbonaceous deposit with a degree of hydrogenation forms with the higher methane flow rate (INS18). With the lower methane flow, it appears that the high relative steam concentration prevents extensive carbon deposition. INS has shown

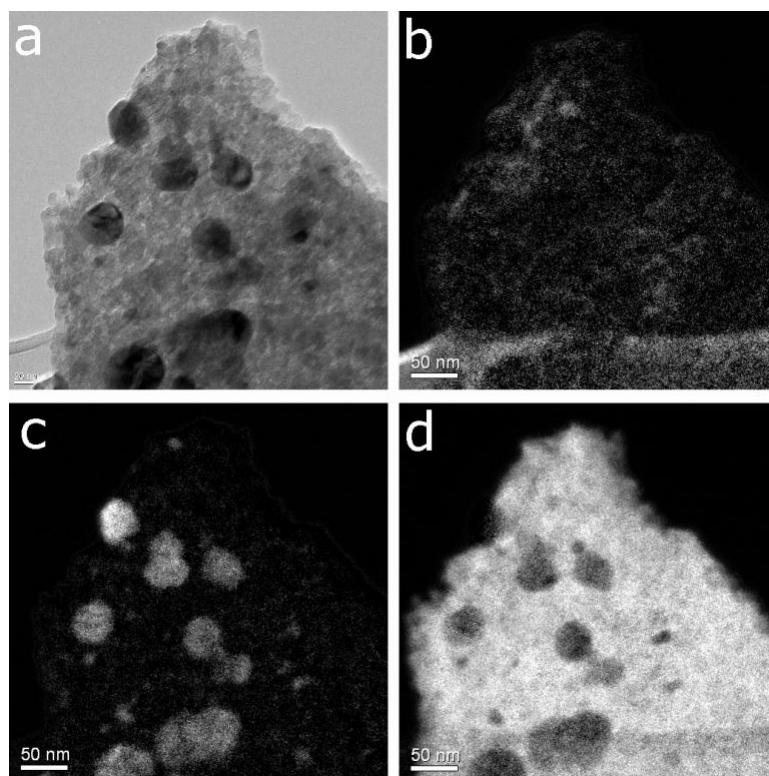


Figure 4.17: Transmission Electron Micrograph of INS6 after reduction and reaction at low methane flow. (a) zero energy loss image, (b) carbon map, (c) nickel map, (d) oxygen map

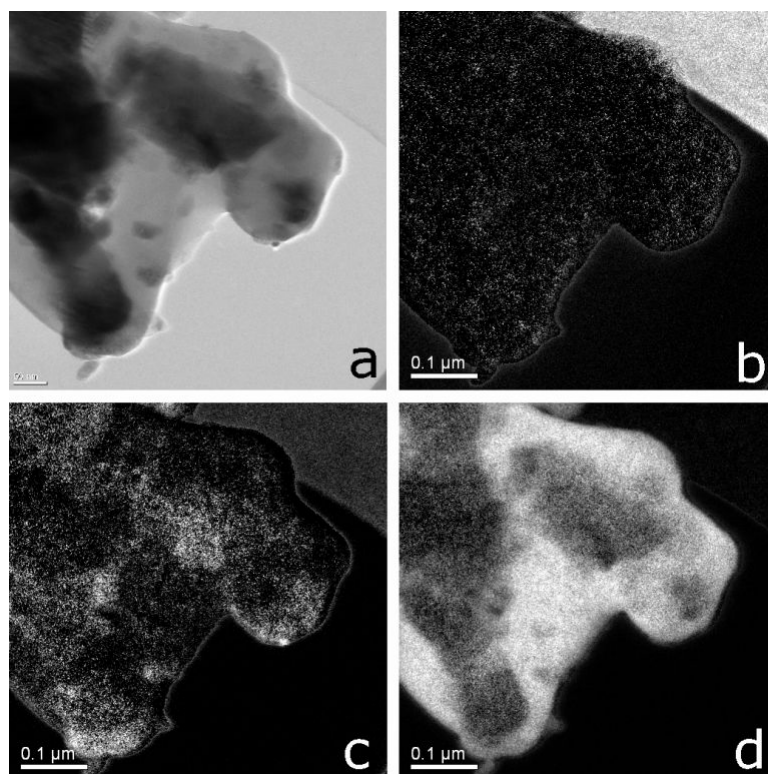


Figure 4.18: Transmission Electron Micrograph of INS18 after reduction, reaction and hydrogen treatment (a) zero energy loss image, (b) carbon map, (c) nickel map, (d) oxygen map

hydrogenous deposits to be of both saturated and unsaturated character. An attempt to increase its degree of hydrogenation to facilitate spectral collection was unsuccessful and it seems that some degree of coke hydrogenation has in fact taken place. This step has also fundamentally affected the catalyst itself, encapsulating some of the metallic nickel into a nickel aluminate spinel, as shown by the XRD pattern 4.16, and loss of defined metallic particles in the TEM. It can also explain the reduction of Ni phonon intensity seen in the INS spectra of figure 4.12. This observation is somewhat counter-intuitive, since the reaction is an oxidation, yet occurs under reducing conditions. Furthermore, bulk formation of the spinel is believed to occur at 1073 K in oxygen with only very slow formation of 873 K, where our hydrogenation was carried out at 773 K. An attempt to reproduce this behaviour in the microreactor was unsuccessful, with the process not affecting the XRD patterns obtained. This indicates an inconsistency in the structural phase of the Ni/Al₂O₃ catalyst operating in the two reaction configurations.

Overall, this section illustrates a complex deactivation pathway, where coke deposition appears to result in a phase transformation and shows that interaction between the reacting components may be more complicated than previously appreciated. It has also shown the relative abundance of hydrogen and carbon partitioning in a steam reforming overlayer. Unlike the dry reforming reaction however, comparing relative rates of CO formation against deactivation is not so straight forward. This may be because H₂O is a superior oxidant or it may simply be that the oxidant rich reaction conditions prevented any significant carbon buildup. In order to further examine this last point, the following section not only deals with graphitic carbon formation, but also steam lean conditions (i.e. a 1 : 1 ratio) which will not only accelerate coke formation but would be the desired ratio to achieve on an industrial scale.

4.3 Graphitic Carbon Characterisation

This section is concerned with the characterisation of graphitic overlayers in the steam reforming reaction formed using the 26 wt % Ni/Al₂O₃ catalyst. It also develops the understanding of the steam reforming reaction by attempting to

accelerate deactivation by carrying out the reforming at a 1 : 1 ratio which should allow coke to form more readily than the previous section whilst allowing accurate quantification of the hydrogen present in the overlayers.

4.3.1 Results

4.3.1.1 Microreactor Studies

Initial testing was carried out in the microreactor in order to determine reaction parameters for the INS measurements. As the catalyst is the same as examined in section two of the previous chapter, the temperature programmed reduction is also the same and so a reduction temperature of 898 K was selected. Figure 4.19 shows the temperature-programmed reaction profile for the steam reforming of methane over the Ni/Al₂O₃ catalyst over the temperature range 500-1200 K. It can be seen that the reaction initiates sharply at 650 K. Interestingly, this is the same temperature that is observed in the “dry” reforming reaction and suggests that this is the probably the minimum activation energy for the methane dissociation step (equation 1.9).

Full conversion of methane seen at about 1000 K. H₂O consumption is not yet complete at this temperature and there are two possible reasons for this. Firstly, it is possible that due to the inherent difficulties involved in controlling steam, the oxidant could be in a slight excess. More likely though is that the disparity is due to water gas shift activity (equation 1.5). This would explain the continued presence of water which diminishes at higher temperatures as this side reaction becomes less favoured, and the reverse water gas shift becomes more dominant (equation 1.6).

At the highest temperatures (above 1100 K) deactivation is not readily apparent as no tailing of the CO and H₂ levels is apparent. What can be seen though is a drop then a plateau in CO and H₂ which is due to H₂O reaching full conversion.

A temperature of 898 K was selected for isothermal measurements as it is within the operational range of the Inconel[®] INS cell as well as providing significant

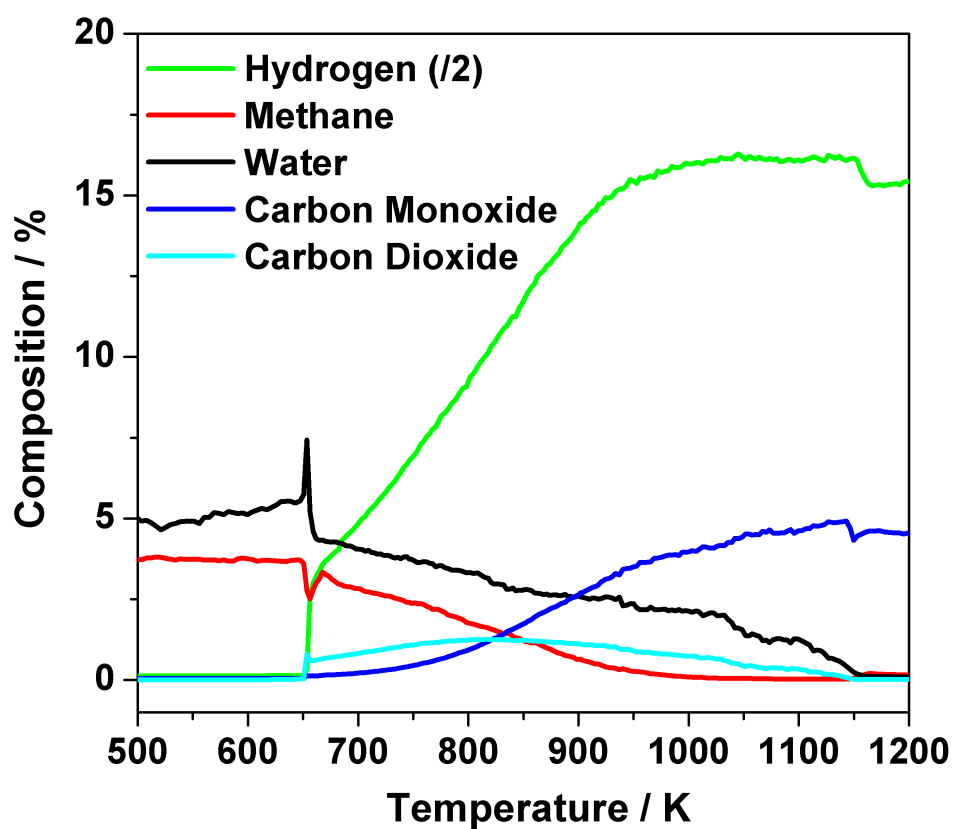


Figure 4.19: Temperature-programmed reaction (500 - 1200 K) of a 1:1 mixture of CH_4 and H_2O over reduced $\text{Ni}/\text{Al}_2\text{O}_3$ catalyst. Measurements performed using the micro-reactor arrangement using a heating rate of 10 K min^{-1}

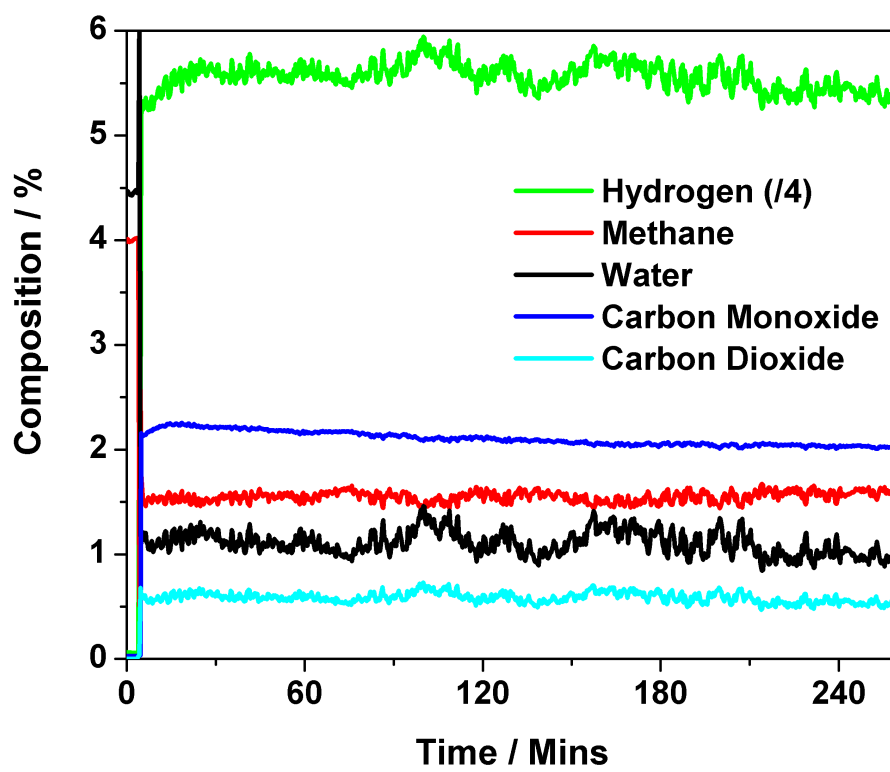


Figure 4.20: Extended microreactor reaction at 898 K of a 1:1 mixture of CH_4 and H_2O over reduced $\text{Ni}/\text{Al}_2\text{O}_3$ catalyst.

catalytic activity. Figure 4.20 shows the reaction profile for the micro-reactor isothermal measurements. An initial methane conversion of 72.5 % is observed at this temperature. Deactivation is not readily apparent over the course of the reaction as methane and water levels stay fairly constant throughout. There is however, a small tailing of the CO levels, which could suggest some loss of activity however there is no concomitant loss in H₂ levels. Variation in H₂ is solely due to fluctuations in the steam level which stand to highlight the difficulty in controlling this reactant. Certainly the extent of deactivation is different for the steam reforming reaction and the dry reforming in the previous chapter. This suggests that even in a steam lean environment of 1 : 1 ratios, the H₂O is a superior oxidant to that of CO₂ and allows the catalyst to react for longer without deactivation. Finally it is noted that water-gas shift chemistry is taking place at this temperature and is confirmed by the presence of CO₂, however the dominant reaction is by far the reforming process. The TPO profile for the post micro-reactor reformed Ni can be seen in figure 4.21. A single peak is observed with a maximum at 810 K. When comparing this value to the the TPO profiles for the amorphous and the graphitic “dry” reforming reactions, the temperature is closer to that observed for the amorphous carbon than the graphitic although it is acknowledged that the oxidation of the carbon could be aided catalytically [38]. Integration of the peak results in a quantity of coke of 76.38 mmol C g_{cat}⁻¹ or 47 % by mass, from integration of the CO₂ peak. This represents a significant quantity of carbon and it is perhaps surprising that the isothermal 4.20 reaction continues without any significant deactivation.

4.3.1.2 Inelastic Neutron Scattering Results

The reaction profile for the INS reactor measurements is displayed in figure 4.22. As in the previous “dry” reforming section, the larger reactor configuration and subsequent increase in catalyst mass necessitates the reaction to be performed at a reduced GHSV (longer space time) compared to the more conventional micro-reactor arrangement. It can be seen in the figure that the reaction is active for methane reforming as conversion of the CH₄ (initial conversion of 60 %) and H₂O

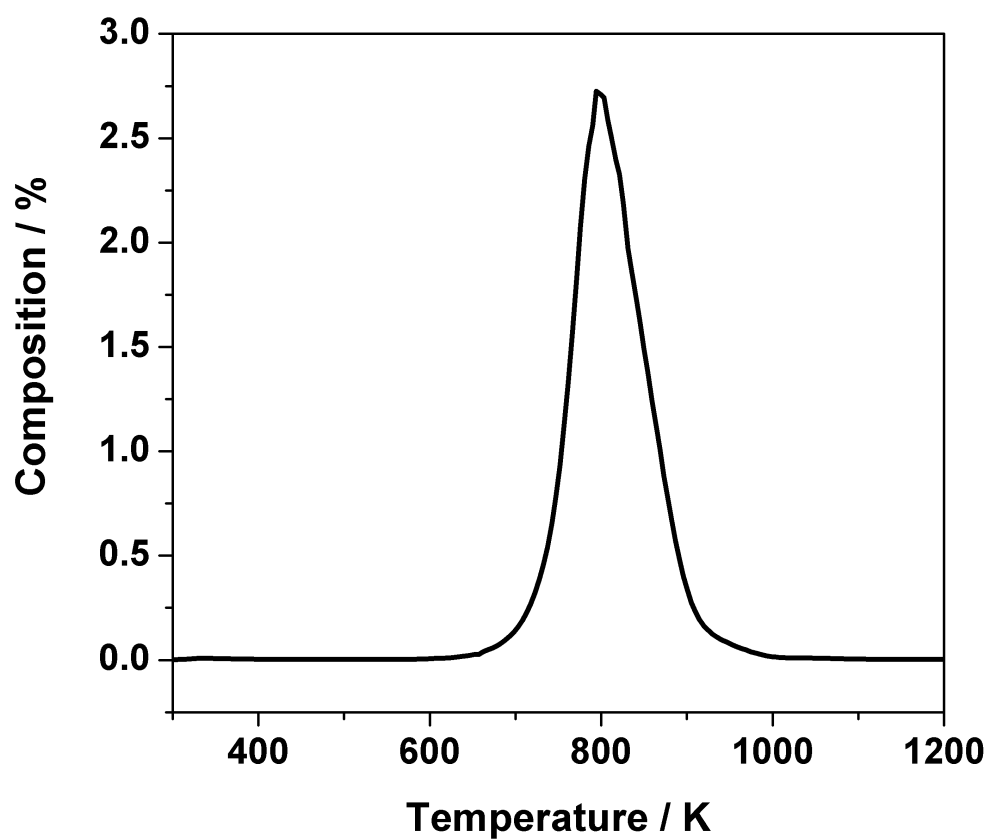


Figure 4.21: Temperature-programmed oxidation profile for Ni/Al₂O₃ catalyst post reaction at 898 K. Measurements performed using the micro-reactor arrangement using a heating rate of 10 K min⁻¹

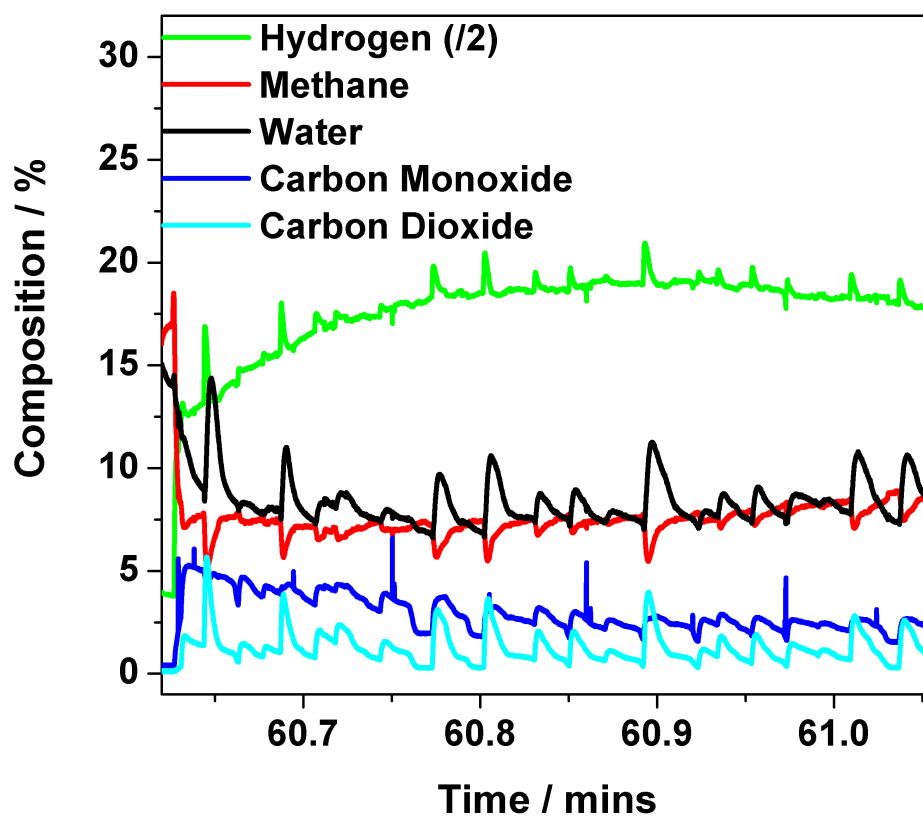


Figure 4.22: Extended reaction at 898 K of a 1:1 mixture of CH₄ and H₂O over reduced Ni/Al₂O₃ catalyst.

whilst at the same time, production of H₂ and CO can be observed. The most obvious point to note is that large perturbations can be seen in the water signal. The reason for this lies in the control mechanism for the saturator. Producing large quantities of steam consistently over a long period of time in a medium volume reactor is non-trivial and the temperature controller for the saturator struggles to stay at a constant temperature. This results in small changes in the temperature of the steam and as figure 4.3 shows, relatively large changes in the steam flow rates can occur. It is acknowledged that this change in the H₂O flow rates will result in the reaction going through periods of being steam lean and steam rich. Over the whole course of the reaction though, the average steam levels are at a ratio of 1 : 1 with methane. Some degree of deactivation is apparent over the course of the reaction (decreasing CO and H₂). Qualitatively there are similar trends seen with the micro-reactor and the INS reactor that suggest that the samples are comparable.

The post INS reaction TPO profile is shown in figure 4.23. Unlike the microreactor study, two peaks can be observed, one small peak is observed with a maximum at 605 K and a second, much larger peak at 890 K. The low temperature peak is a minority species and is possibly a reactive monotomic carbon [87] and could be formed in the steam lean periods of the proceeding isothermal reaction. The high temperature peak is close in desorption temperature to the graphitic “dry” reforming TPO. This suggests the carbon to be of a graphitic nature [87]. Integration of the high temperature peak results in a quantity of coke of 12.25 mmol C g_{cat}⁻¹ or 14 % by mass. This is a much lower quantity of carbon than that observed for all the other reactions studied and may well be due to the steam rich periods that occur in the INS isothermal reaction. It is noted that the final pressure in the INS reactor was 5 bar which confirms that carbon buildup is perhaps not as serious as in the “dry” reforming reaction.

Elemental analysis (C and H) of post INS catalyst samples was performed. Results showed 8.7 % by mass of retained carbon but hydrogen concentration was below detection limits which indicates the hydrogen content of the sample to be less than 0.3 % by mass.

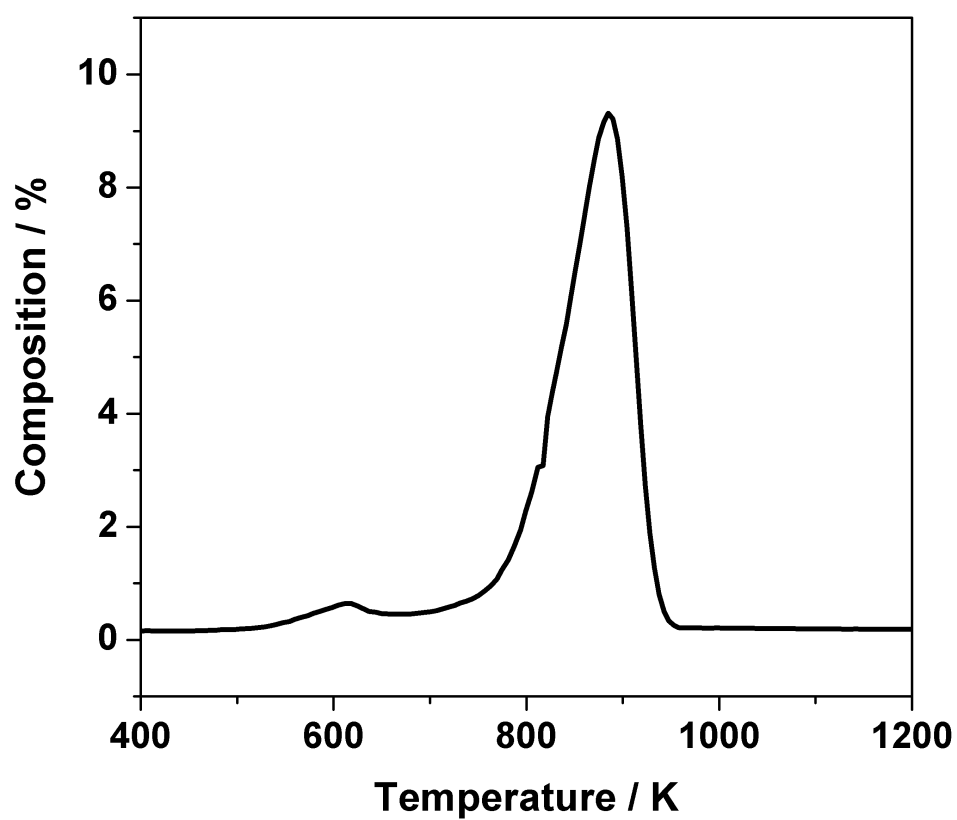


Figure 4.23: Temperature-programmed oxidation profile for Ni/Al₂O₃ catalyst post INS reaction at 898 K. Measurements performed using the micro-reactor arrangement using a heating rate of 10 K min⁻¹

After the INS isothermal reaction was carried out, the Inconel[®] can and sample were detached from the gas manifold and INS measurements were performed at two energies; 4840 cm⁻¹ and 2017 cm⁻¹. The high energy spectrum (primary energy of 4840 cm⁻¹) for the reacted Ni/Al₂O₃ catalyst is presented in figure 4.24. The spectrum is displayed as a subtracted difference spectrum similarly to the second section of the previous chapter. Figure 4.24 is characterized by a number of features at 3692, 3029 and 2900 cm⁻¹. The features at 2900 cm⁻¹ and 3029 cm⁻¹ are assigned as C-H stretching vibrations related to unsaturated and aliphatic hydrocarbons [83]. The feature at 3692 cm⁻¹ can be assigned as hydroxyl stretching modes [69]. It is possible that this peak is actually two peaks as there is asymmetric tail on the left hand side. Due to the constraints of the chopper, it is not possible to further resolve the spectrum so it is not possible to determining how many OH modes are actually present. This same catalyst was presented in the graphitic section of the previous chapter. In that study, no O-H stretching mode was observed. This suggests that the stretching mode observed here is most likely due to the oxidant being adsorbed onto the catalyst surface. Similarly to all the other INS spectra presented in this study, the signal to noise ratio is poor and indicates minimal hydrogen retention by the catalyst. Calibration of C-H and O-H scattering intensity permits the number of hydrogen atoms associated with carbon and hydrogen atoms to be determined as before. This information is presented in Table 3, alongside the elemental analysis results and the TPO results. Integration of the C-H peaks give a combined value of 1.048 μmol Hg_{cat}⁻¹ and integration of the O-H region gives 0.748 μmol Hg_{cat}⁻¹. Thus, the ratio of hydrogen associated with carbon corresponds to 11689 C : 1 H. This really is a minimal amount of hydrogen and is at the low end of what is quantifiable currently by the INS technique.

The medium energy spectrum (2017 cm⁻¹) for the reacted catalyst is presented in figure 4.25. This spectrum also has a low signal to noise ratios but four weak bands are observable bands observed at 1445, 810, 763, and 640 cm⁻¹. The band at 1445 cm⁻¹ band is close in energy to a CH₂ scissors vibration, or a coupled C-C stretch and C-H bend, as reported by Albers and co-workers [127]. The band at 810 cm⁻¹ is assigned as an aromatic CH bend [127; 130; 131], or a C-C

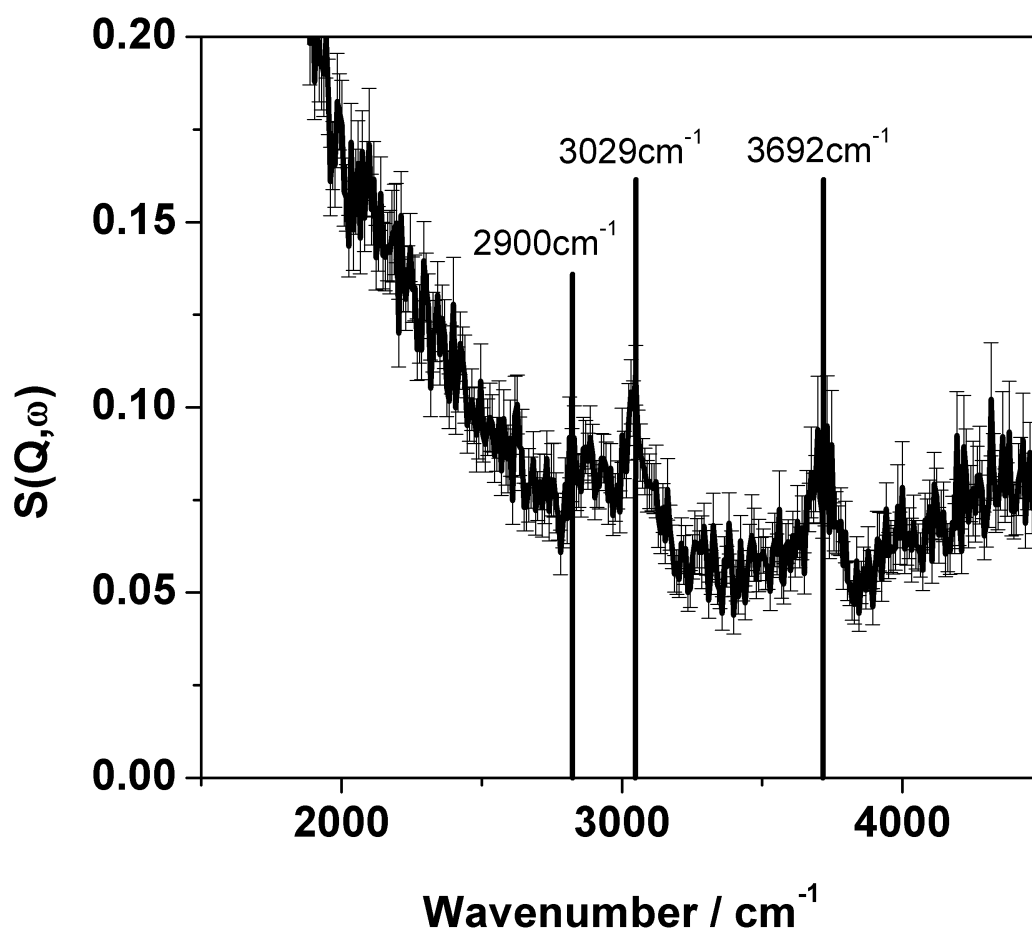


Figure 4.24: High energy transfer INS spectrum of reacted Ni/Al₂O₃. The spectrum is a difference spectrum (reacted spectrum - spectrum of reduced catalyst) acquired using the MAPS spectrometer operating at an incident energy of 4840 cm⁻¹

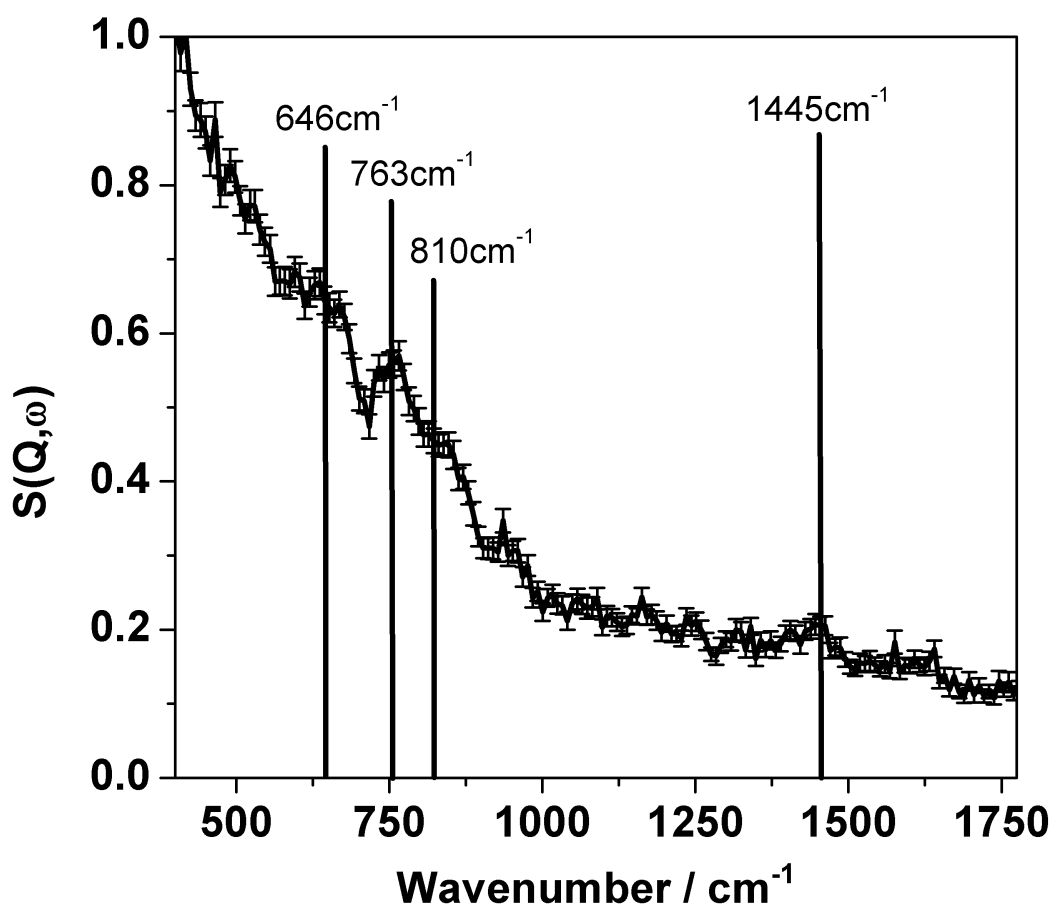


Figure 4.25: Medium energy transfer INS spectrum of reacted Ni/Al₂O₃. The spectrum is a difference spectrum (reacted spectrum - spectrum of reduced catalyst) acquired using the MAPS spectrometer operating at an incident energy of 2010 cm^{-1}

	Ni/Al ₂ O ₃
C (Elemental Analysis)	8.7%
H (Elemental Analysis)	Below detection limits%
Carbon _(ad) TPO (micro-reactor)	76.38 mmol Cg ⁻¹ cat ± 8 %
Carbon _(ad) TPO (INS-reactor)	12.25 mmol Cg ⁻¹ cat ± 8 %
$\nu(\text{O-H})$	0.728 $\mu\text{mol Hg}^{-1}\text{cat} \pm 6 \%$
$\nu(\text{C-H})$	1.048 $\mu\text{mol Hg}^{-1}\text{cat} \pm 6 \%$
C _{tot} : H	11689 ± 935 : 1

Table 4.3: Carbon and hydrogen retention values for Ni/Al₂O₃ post micro-reactor and INS CO₂ reforming.

Wavenumber / cm ⁻¹	Assignment
3692	$\nu(\text{OH})$
3029	sp ² $\nu(\text{CH})$
2900	sp ² $\nu(\text{CH})$
1445	Coupled $\nu(\text{CC})$ and $\delta(\text{CH})$
810	Aromatic $\delta(\text{CH})$
763	Aromatic $\delta(\text{CH})$
640	sp ² Carbon network deformation

Table 4.4: Summary of the INS Vibrational Assignments Pre and Post Methane Steam Reforming Resulting in Graphitic Carbon Laydown.

stretch at 875 cm⁻¹ [129; 132]. The mode at 640 cm⁻¹ band is thought to be an sp² carbon network deformation mode [128; 131]. As with the graphitic “dry” reforming spectra in the previous chapter this overlayer appears to be similar in nature to other studies on cokes and hydrocarbonaceous materials [127; 131; 133] and suggests an overlayer that is graphitic in nature. A summary of the vibrational assignments is shown in table 4.4

Diffuse reflectance UV-vis measurements were performed on the post reaction sample to make sure that bands in the Raman spectra were due solely to surface species and not due to any other unanticipated electronic effects resulting from the specific laser energies used for the measurements. Figure 4.26 shows the diffuse reflectance UV-vis spectra of (a) as received Ni/Al₂O₃, (b) the reacted catalyst and (c) BaSO₄ which was used as a diluent. It can be seen from the figure that there are no bands at the the laser wavelengths used in the Raman

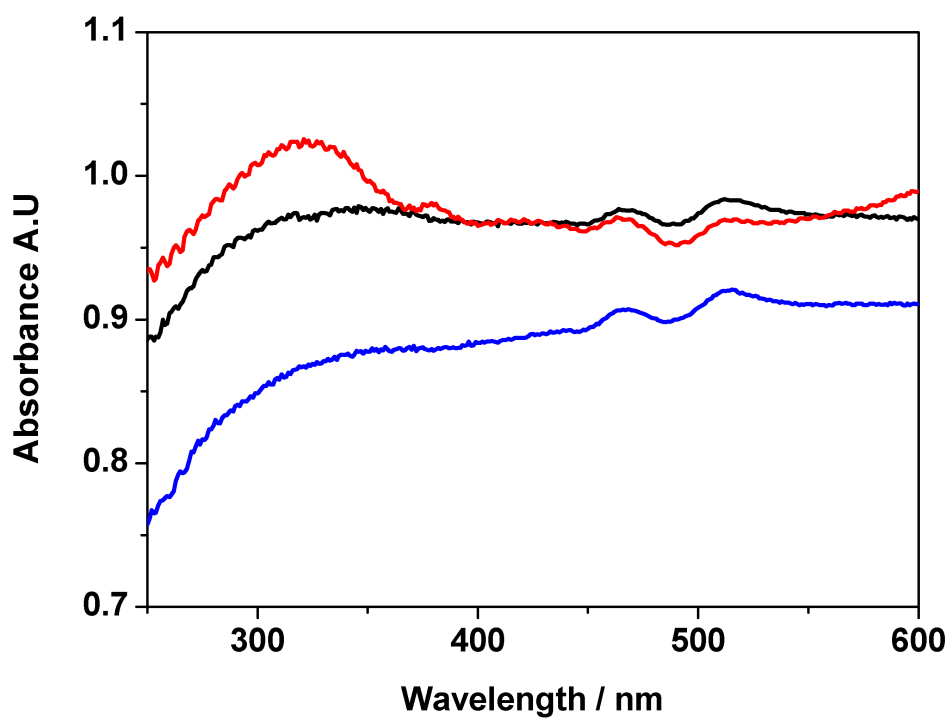


Figure 4.26: UV-vis spectra of (red) Ni/Al₂O₃ as received, (blue)Ni/Al₂O₃ post steam reforming reaction and (black) Barium sulphate which was used as a diluent

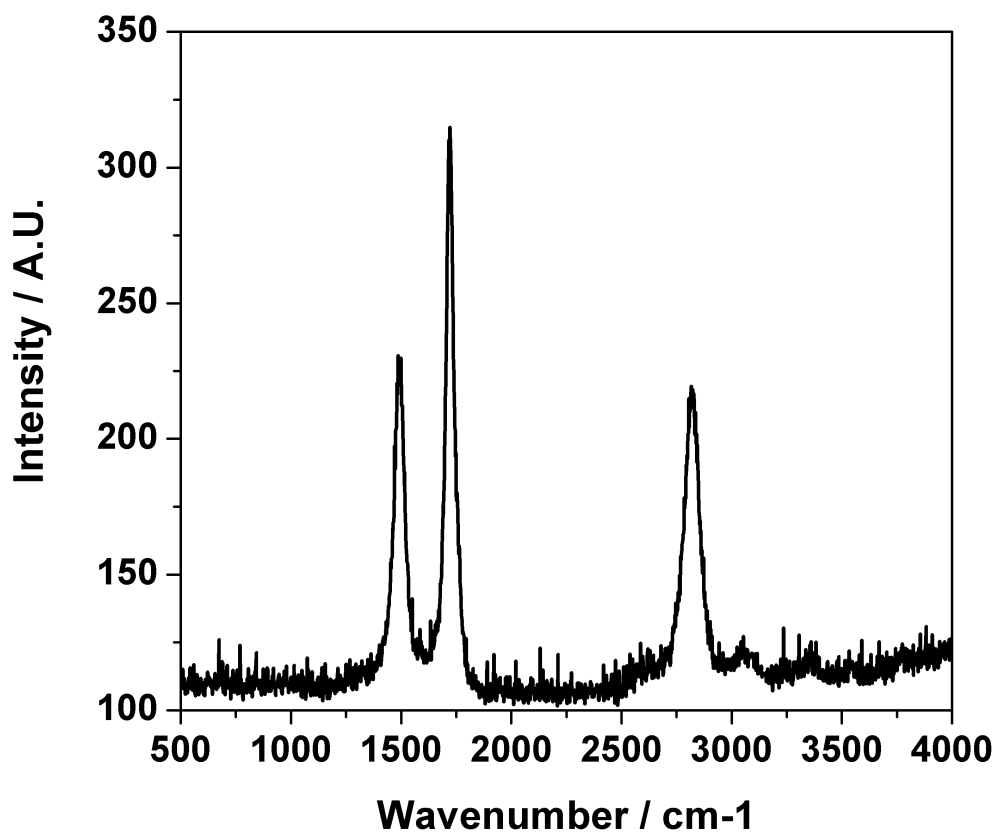


Figure 4.27: Raman measurement of post INS reaction Ni/Al₂O₃ catalyst, 532nm laser

measurements (325 and 532 nm) and so any Raman bands that are active will be from the catalyst and the overlayer. The features present at 470 and 520 cm⁻¹ are seen in all three samples and can be attributed to the diluent. It should be noted however, that there is also a small adsorption band at 375 cm⁻¹ and a large broad feature at 310 cm⁻¹ in the as-received spectrum. These bands are most likely associated with electronic transitions from the pre-reduced nickel particles on the catalyst surface.

Figure 4.27 shows the 532 nm Raman spectrum in the range 500 - 4000 cm⁻¹ for the Ni/Al₂O₃ sample after the INS steam reforming measurement. Two intense

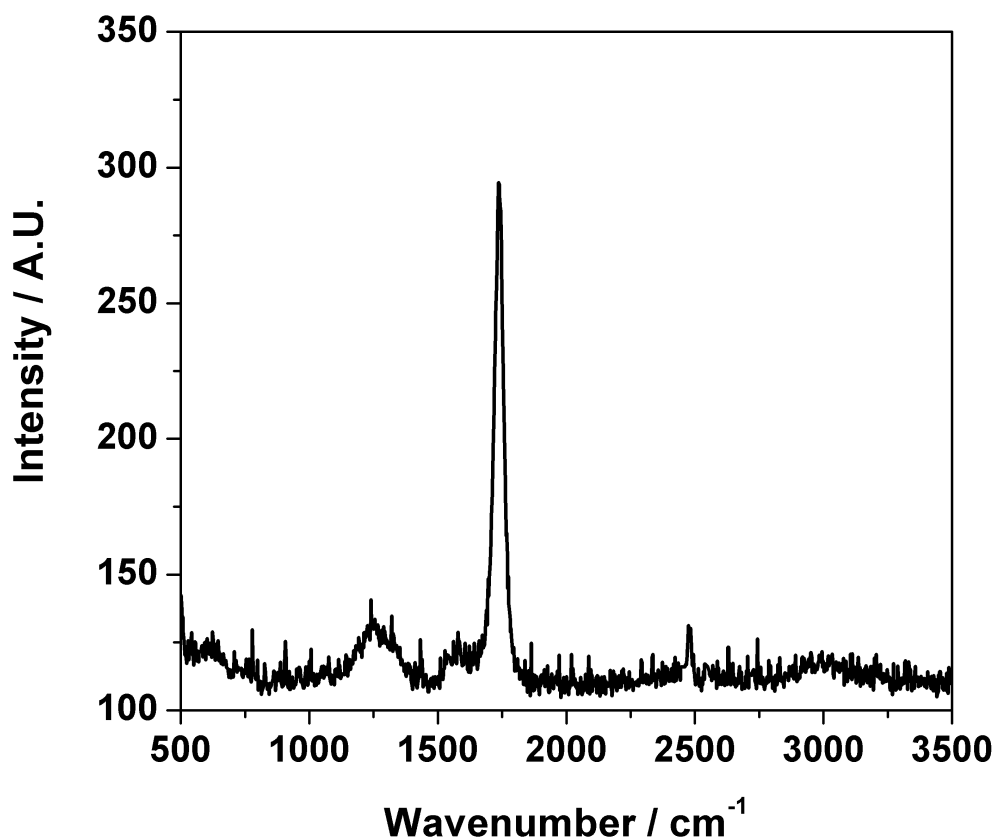


Figure 4.28: Raman measurement of (a) post INS reaction Ni/Al₂O₃ catalyst and (b) reduced Ni/Al₂O₃, 325nm laser

peaks at 1342 and 1580 cm⁻¹ are observed and are assigned to the D and G bands of carbon that has been formed on the surface [94; 96]. As before, the G band suggests a level of order in the deposited coke however the presence of the D band allows us to conclude that the sample is not pure graphite. There are also two bands between 2500 and 3000 cm⁻¹ (major band at 2685 cm⁻¹), which is due to the overtones of the D and G band. These higher wavenumber bands show that the carbon overlayer has a high level of 3D order [138]. Figure 3.40 shows the shows the 325 nm Raman spectrum in the range 500 - 3500 cm⁻¹ for the Ni/Al₂O₃ sample after 3 hours in a 1 : 1 mixture of CH₄ and CO₂ at 898

Laser Wavelength (nm)	Wavenumber / cm^{-1}	Assignment
352	3000	$\nu(\text{CH})$
	1750	Combination band
	1620	$\nu(\text{CC})$
	1275	$\nu(\text{CC})$
532	2685	D-band overtone
	1580	D band $\nu(\text{CC})$
	1342	G band $\nu(\text{CC})$

Table 4.5: Summary of the Raman Vibrational Assignments Post Methane Reforming Resulting in Graphitic Carbon Laydown.

K in the micro reactor. Four vibrational modes can be observed at 3000, 1750, 1620 and 1275 cm^{-1} . The 3000 cm^{-1} band is a C-H stretching mode that is only visible using a UV laser source [104]. The dominating band at 1750 cm^{-1} is a combination band made up from the vibration at 1620 cm^{-1} and radial breathing mode at 180 cm^{-1} [95] that is not observable using this technique. The small 1620 cm^{-1} band is assigned to carbon - carbon double bond stretches [104] as is the mode at 1275 cm^{-1} .

The powder X-ray diffraction pattern for the (a) reacted and (b) reduced INS sample is presented in figure 4.29. Most of the reflections are due to the alumina support and metallic nickel (triangle and square respectively) and it is clear that the catalyst undergoes very little change during the reaction. An intense reflection due to graphite is observed at 26.1 degrees, which indicates the coke to be graphitic. Graphite particle sizing using the Scherrer equation was not possible due to the overlap of this feature with a feature attributed to alumina.

Transmission electron micrographs of the post-reaction sample are presented in figures 4.30 and 4.31. Four images are shown in 4.30 (a) zero energy loss map, (b) carbon map, (c) nickel map and (d) oxygen map. All four images are of the same area. The zero energy loss map (figure 4.30(a)) shows an overview of the reacted catalyst and it is clear to see that there are a number of long, whisker like strands that are similar in appearance to the whiskers shown in section two of the previous chapter. These filaments are highlighted in figure 4.30(b) and can therefore be attributed to carbon that is deposited during the reforming process. These whiskers are also known as filamentous carbon [2; 5; 114; 123] and are

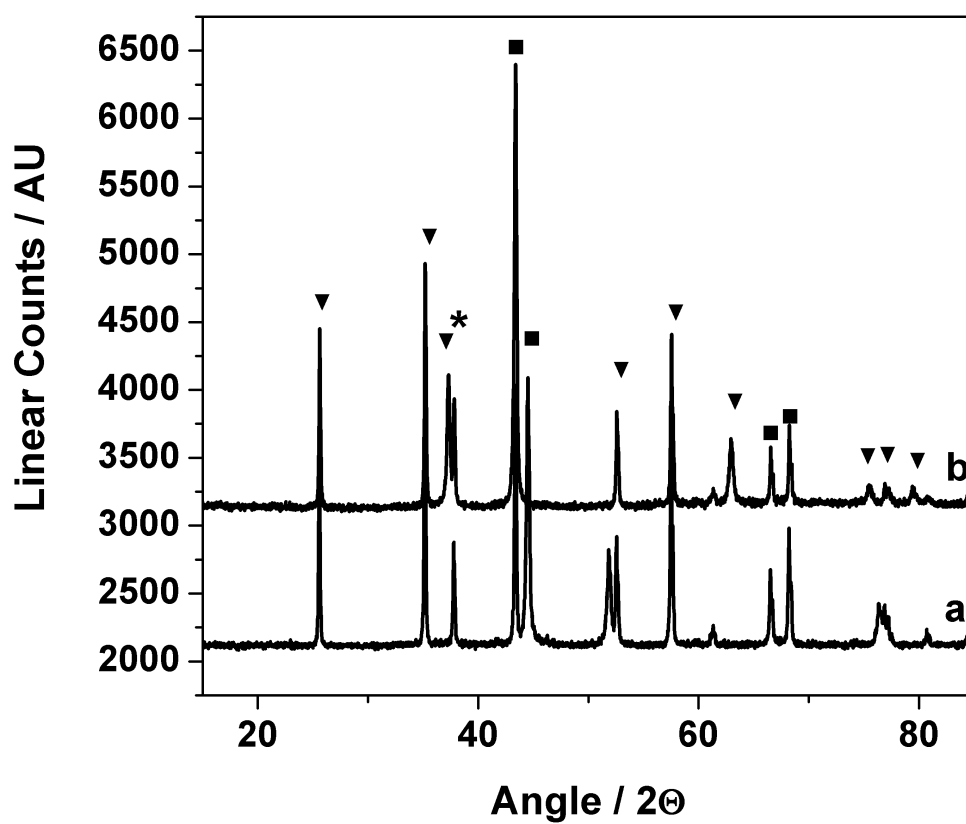


Figure 4.29: Powder X-ray diffraction pattern of Ni/Al₂O₃ recorded (a) after reduction and (b) after reaction and INS measurement. Reflections for α-alumina (triangle), nickel (square) and graphite (star) phases

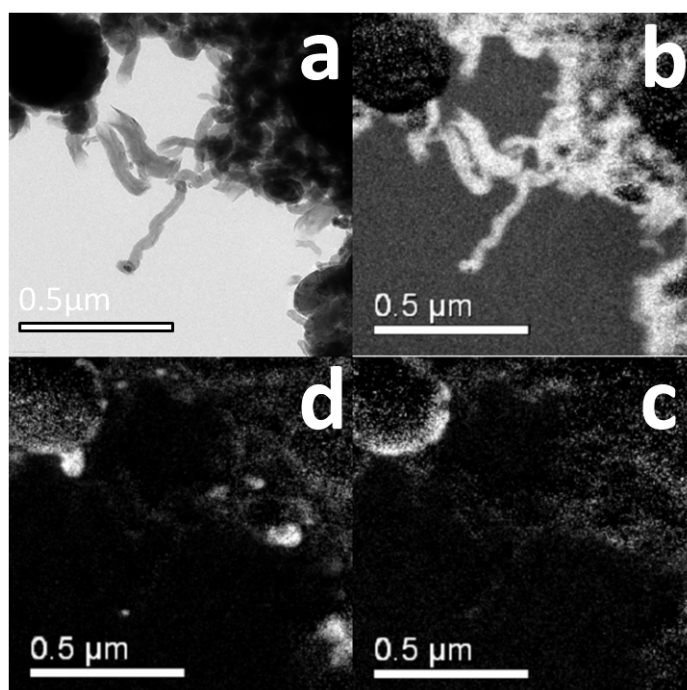


Figure 4.30: Transmission electron micrographs of Ni/Al₂O₃ recorded after reaction and INS measurement. (a) zero loss micrograph, i.e. no energy filtering, (b) carbon map, (c) oxygen map and (d) nickel map

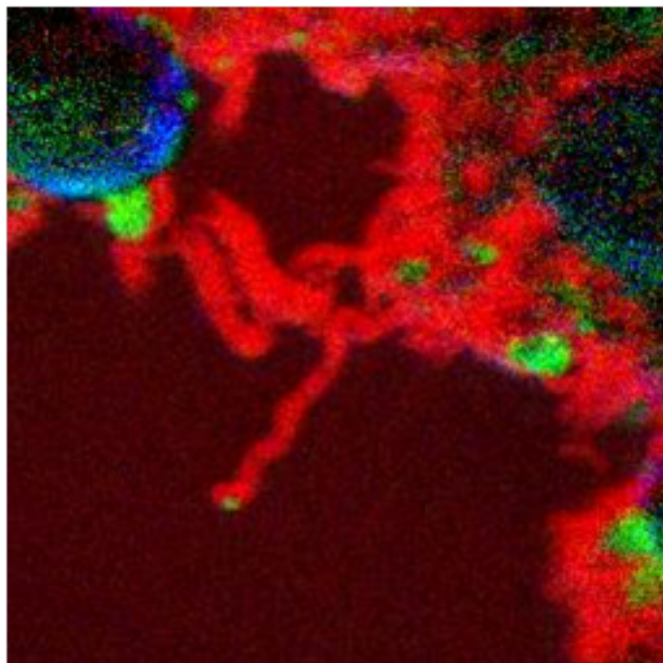


Figure 4.31: Colour-coded energy map transmission electron micrograph of Ni/Al₂O₃ recorded after reaction and INS measurement. red = carbon, green = nickel and blue = oxygen. The spectral scan is taken over the same area of sample presented in figure [3.37](#)

graphitic in nature. Figure 3.37(d) presents the oxygen map and represents the alumina support. From the image it is clear that the support is homogeneous across the sample area. Figure 4.30(c) is the energy filtered image for nickel, and it is clear that the metal is capping the whiskers as before. The nickel particles have diameters ranging from around 20-70 nm. They are also well dispersed. It is noted again, that from the reaction data observed in figures 4.20 and 4.22 the metal particles are still catalysing the reaction even after being separated from the support and suggests that aside from dispersing the nickel and giving the catalyst mechanical strength, the support is probably not responsible for the chemistry occurring.

Figures 4.30(b-d) can be recombined into but as a colour coded map that is presented in figure 4.31. This provides a striking image of the post reforming catalyst.

4.3.2 Discussion

Manipulation of calcination temperature, support material, and metal loading during the catalyst synthesis stage has resulted in a Ni/Al₂O₃ catalyst that favours the formation of filamentous carbon during the steam reforming of methane. The formation of this carbon suggests that the oxidation step reaction (equation 3.8), where surface atomic carbon forms CO, is slower than the polymerisation reaction (equation 1.27) in the same manner as the “dry” reforming reaction. This polymerisation step is confirmed by TPO 4.23 as significant quantities of carbon are measured. TEM images 4.30 and 4.31 describe a filamentous coke rather than an amorphous one. The strong G band in the Raman spectrum (figures 4.27 and 4.28) and the graphite band in the XRD 4.29 support this conclusion. The extremely weak INS spectra presented in figures 4.24, 4.25 allow the conclusion that the coke is carbonaceous rather than hydrocarbonaceous and that the measured hydrogenous features are most likely decorating the edges of the graphitic planes. A surprising outcome of the TPO experiments in both the “dry” and the steam reforming chapters is that the temperature in which surface carbon is oxidised is not always consistent, and care has to be taken not to make it the only tool in which to probe carbon morphology.

Quantification of both the hydrogenous and the carbonaceous components has been possible, although the hydrogen signal is near the limits of the sensitivity of the technique. A ratio of 11689 ± 935 carbon atoms : 1 Hydrogen has been calculated. This value suggests that the catalyst is extremely efficient at cycling hydrogen and is perhaps a little surprising given that both reactant and oxidant contain a total of $3\text{H}_2 : 1\text{C}$. INS results also highlighted the presence of an insignificant population of hydroxyls on the surface that probably originate from dissociatively adsorbed water.

The previous chapter identified a series of elementary reactions for the methane “dry” reforming reaction. Many of the observed steps are also present here:

Dissociative adsorption of methane is seen to occur in the same manner as the “dry” reforming reaction to give one adsorbed carbon and four hydrogen atoms (equations 1.8 - 1.12).

The oxidant also undergoes dissociative adsorption to produce one adsorbed oxygen atom and two hydrogen atoms (equation 1.25), which is analogous to CO_2 dissociation in the “dry” reforming reaction. This adsorbed oxygen can then react with the deposited carbon from the methane to give the CO product.

The recombinative desorption of hydrogen is then a rapid and efficient process, again similarly to the “dry” reforming process (equations 1.20 and 1.21).

Other reactions such as the water gas shift reaction and the polymerisation reaction are also occurring which makes the overall scheme complicated. What this study has shown, is that the steam reforming oxidant is superior to that of CO_2 as although carbon deposition does occur, it is to a much lesser extent. It has also quantified the hydrogen content in a representative industrial methane reforming process and offers a new perspective on this important and relevant problem.

4.4 High Temperature INS Steam Reforming

The final section in this chapter briefly discusses attempts to carry out steam reforming at temperatures above 1000 K on the 26 wt % Ni catalyst. Isothermal reforming in the previous two sections was carried out at around 900 K which reflects the material limitations of the Inconel[®] reactor. At this temperature,

the water gas shift reaction is significant and in industry, higher reaction temperatures are used to mitigate its effects [2]. The conclusions drawn in the previous section are probably, but may not, be transferable to the industrial scenario as water-gas shift chemistry could be altering the coke. It would be an important step therefore, to examine the overlayers formed at this higher temperature so that direct comparisons could be made to the industrial problem. This section has been included to complete the record of experiments taken and to demonstrate the progression towards replicating the industrial scenario. Serious materials problems were encountered however, when attempting to operate INS reactors under these demanding conditions. In essence, although an INS reactor arrangement was developed that demonstrated promise and was able to generate results, it ultimately proved to be unreliable and prone to fracture. This seriously hindered attempts at reproducibility. Thus, the results presented here are preliminary. Although not taken further, they do indicate probable developments in cell design that could be attempted in future work.

4.4.1 Results

4.4.1.1 Microreactor Studies

Figure 4.32 shows the reaction profile for the micro-reactor isothermal measurements carried out at 1123 K. A methane conversion of 100 % is achieved at this temperature which agrees with the temperature programmed reaction profile in section two 4.19. The water signal does not reach zero however and this suggests the water is in slight excess. The stability of the steam signal over the course of the 350 minutes is very good indeed, and reflects the increased control of the microreactor system compared to the INS gas manifold. A small decrease in the water signal is seen, but only after three hours and is probably due to the depleting reservoir of water in the saturator. Overall, little deactivation is observed, as the decrease in hydrogen mirrors the water decline with CO remaining unaffected. Finally, and most importantly, the water-gas shift reaction does not take place in any significant manner at this temperature which is reflected by the absence of CO₂. It can be concluded then that any surface coke formed is due to the reforming reaction rather than the water gas shift. Figure 4.33 shows

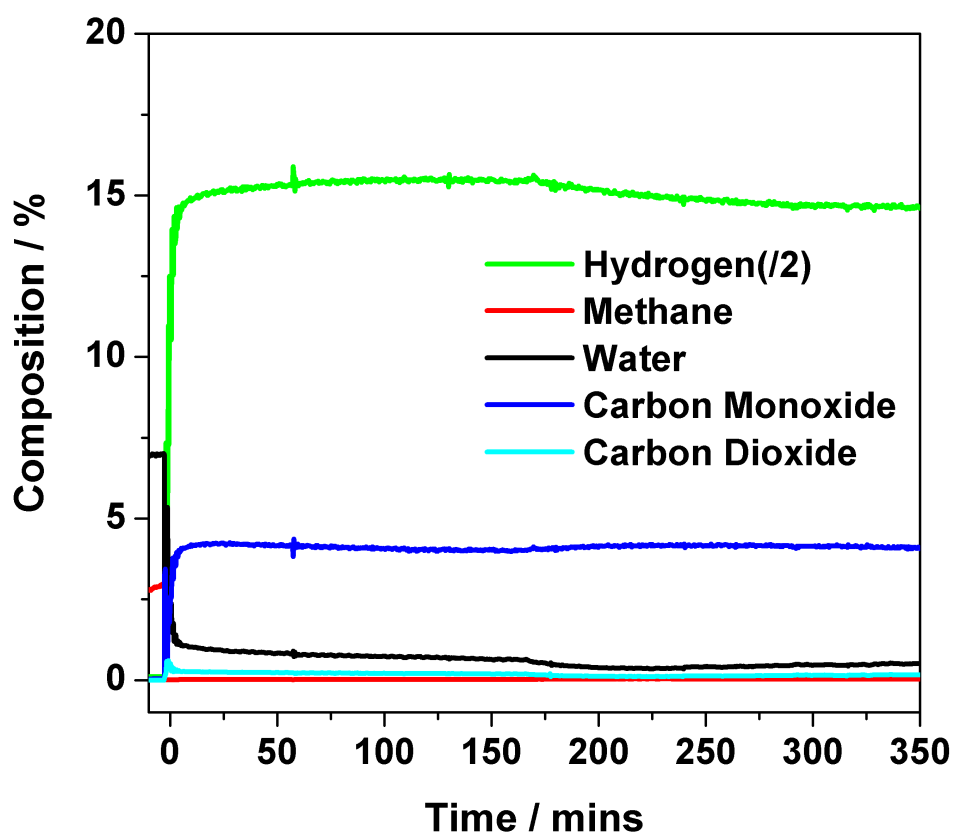


Figure 4.32: Extended reaction at 1123 K of a 1:1 mixture of CH_4 and H_2O over reduced $\text{Ni}/\text{Al}_2\text{O}_3$ catalyst. Measurements performed using the micro-reactor arrangement

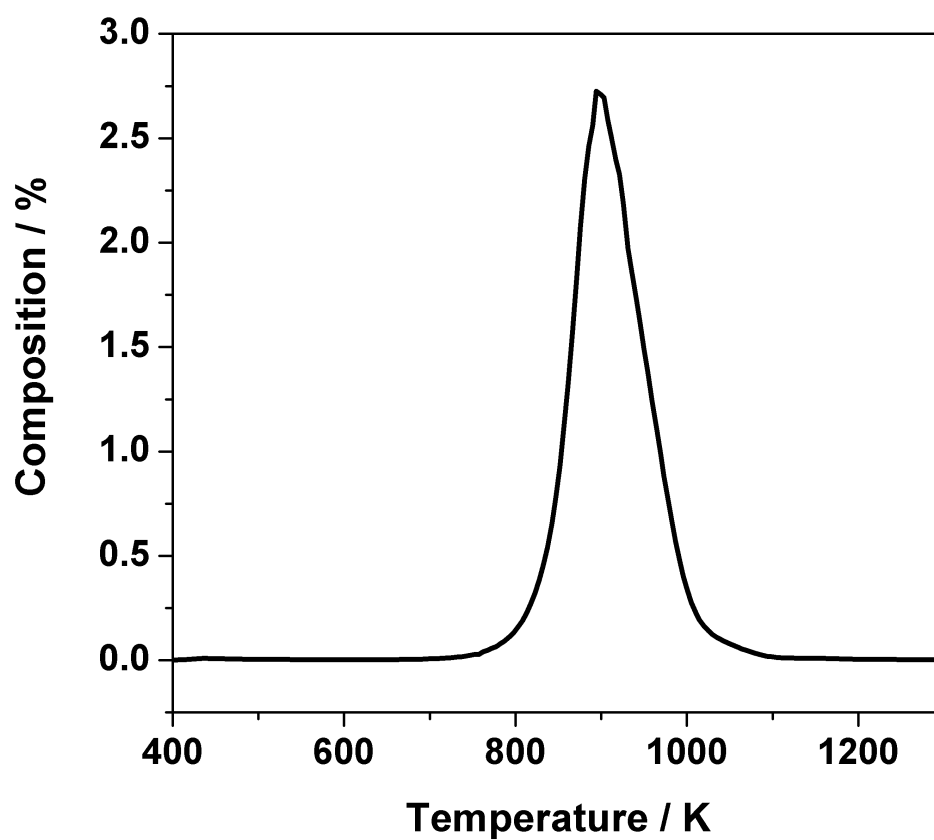


Figure 4.33: Temperature-programmed oxidation profile for Ni/Al₂O₃ catalyst post reaction at 1123 K. Measurements performed using the micro-reactor arrangement

the post-reaction TPO measurement of the micro-reactor sample. The plot is dominated by a single broad and intense feature with a desorption maximum at about 900 K, suggesting a polymeric amorphous coke, C β [87].

4.4.1.2 Inelastic Neutron Scattering Studies

Sample preparation for INS measurements was made extremely difficult for two reasons. Firstly, the u-tube reactor was rated for a maximum operating pressure of two bar. Due to the design of the cell and the amount of catalyst to be reacted (*ca.* 7 g), flow rates had to be reduced significantly in order to keep the pressure of the cell low. This necessitated recalibration of the saturator system as described in section one of this chapter. This calibration was made impossible as the back up turbo pumps in the mass spectrometer failed which prevented the use of the mass spectrometer for use in calibration measurements and reactor monitoring. A steam reforming reaction was attempted nonetheless, however it could not be determined if the reaction was proceeding in a steam lean or steam rich environment. After 6 hours reaction at 1123 K, the reaction was stopped and the sample taken to the spectrometer. Figure 4.34 shows the high energy, 4840 cm⁻¹ (600 meV) spectrum of the reacted sample. The spectrum is dominated by two overlapping ν (C-H) modes of fairly high intensity the are centered around 3010 cm⁻¹. There are also peaks centred around the 1250 and 750 cm⁻¹ wavenumber regions. This spectrum presents a level of detail not yet observed for this reaction system and suggests that a significant quantity of hydrogen has been retained within the carbonaceous matrix. Unfortunately, due to the fact that that it is impossible to quantify the ratio of steam to methane it cannot be determined whether the carbonaceous buildup is from side products of the methane reforming reaction, or simply a buildup of adsorbed methane. When compared to all the previous measurements shown in this study of the post-reaction samples (figures 3.11, 4.10 and 4.24, the signal to noise ratio is vastly improved. This suggests that the reaction was running in an extremely steam lean regime which has allowed a substantial hydrocarbonaceous buildup on the surface. This is a disappointing outcome as we observe an interesting

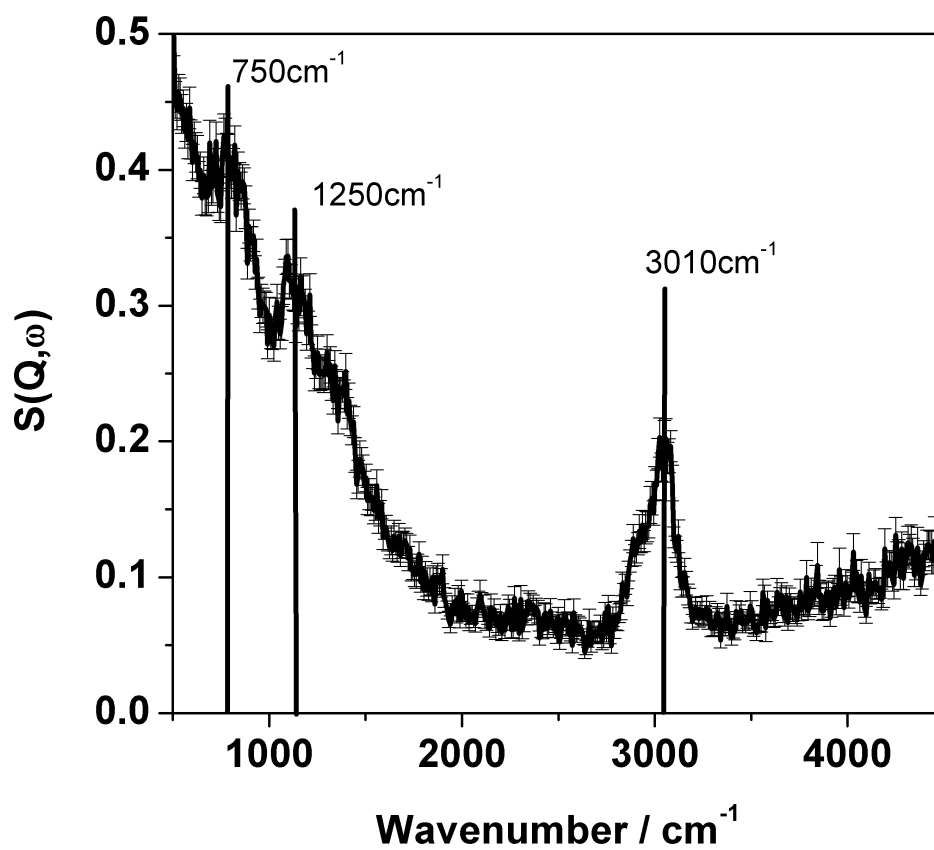


Figure 4.34: High energy transfer INS spectrum of reacted Ni/Al₂O₃ (1123 K). The spectrum is a difference spectrum (reacted spectrum - spectrum of reduced catalyst) acquired using the MAPS spectrometer operating at an incident energy of 4840 cm^{-1}

spectrum but cannot confirm the operating conditions which it corresponds to. Several efforts to refine the experimental arrangements were attempted but on each occasion the quartz cells fractured (four in total). Consequently, it has not been possible to reproduce this intriguing experiment. At this point the project was terminated and no further measurements were taken at this temperature, not least because no fully intact quartz cells remained.

4.4.2 Discussion

High temperature steam reforming was possible in the microreactor regime and yielded positive results. Control of the steam was satisfactory and high methane conversions was observed. The high temperature also prevented any significant contribution to the overall chemistry from the water gas shift reaction. Any comments made relating to the formation of carbonaceous overlayers could then be attributed solely to the methane reforming reaction. The scale up reaction for INS samples was not as successful. Although capable of high temperatures, the limits of pressure coupled to the failure of the mass spectrometer system and sample cells meant that it was impossible to predict steam : methane ratios. This probably resulted in a steam lean regime where the large ν (C-H) signals observed were possibly due to methane adsorption. Unfortunately, this reactor design is not suitable for the reaction system and will not be used further. From discussions with the ISIS Facility Sample Environment team, it has been concluded that the quartz u-tube arrangement cannot tolerate the thermal gradients associated with the high temperature steam reforming measurement. One possible way forward would be to construct u-tube reactors from Hastelloy [®] steel and transfer the samples in a glove box. Hastelloy [®] closely resembles the steel used in industrial steam reforming reactors, however this development is deemed to be beyond this current PhD project.

Chapter 5

Conclusions and Future Work

Both the H_2O and CO_2 reforming of methane has been studied in an attempt to characterise the coke formed on the surface of Ni and Ni-Au alumina catalysts. This has been performed using a wide range of techniques and has allowed characterisation of the nature, quantity and in the case of the “dry” reforming reaction, the source of the carbon. What is perhaps interesting is that sample preparation plays a key role in determining the morphology of the carbon and either amorphous and filamentous carbon has been observed to form almost exclusively depending on the catalyst preparation history. Also worth noting is that in this study, Au doping has not improved the catalysts’ resistance to coke formation and in actual fact may have accelerated deactivation. This is contrary to other studies and suggests that carbon formation is either inevitable or perhaps simply that the gold dopant used in this study was not properly alloyed to the nickel. The contribution of hydrogen to the overlayers has also been studied via inelastic neutron scattering. This technique has permitted quantitative measurements of the extent of hydrogen retention in both CO_2 and H_2O systems for the first time and has allowed elementary steps associated with the reaction to be explored from a new perspective.

In order for these measurements to take place a range of inelastic neutron scattering reactors have been designed, built and tested under reforming conditions. The most successful of these reactors is the Inconel [®] in-situ reactor that has allowed large samples to be prepared, and has permitted excellent background spectra to be achieved. Future work will see the construction of sample cells

System	Carbon Form	C : H Ratio	TPO (Microreactor)
Dry Reforming	Amorphous	175 : 1	11 mmol Cg ⁻¹ cat
	Graphitic	2550 : 1	51 mmol Cg ⁻¹ cat
Steam Reforming	Amorphous	253 : 1	2 mmol Cg ⁻¹ cat
	Graphitic	11689 : 1	76 mmol Cg ⁻¹ cat

Table 5.1: Summary of the Ni/Al₂O₃ C : H ratios for dry and steam reforming systems which lead to amorphous and graphitic carbon deposition. Microreactor TPO values are also given.

made out of Hastelloy[®], most likely of a U-tube design, which will allow much higher temperatures to be achieved while still permitting high reaction pressures. Although the ultimate desire would be to construct in-situ cells from Hastelloy[®], this may be difficult from a machining perspective and expensive from a materials point of view.

Although the hydrogen quantities observed in this system are extremely small, the technique has been shown to work on what is a difficult but highly relevant industrial system. Work is currently under way to apply this technique to a range of CO hydrogenation catalysts which are expected to retain much greater amounts of hydrogen in the overlayers.

What the INS results have shown in both the “dry” and steam reforming reaction is that reactions involving hydrogen are shown to be fast and efficient compared to those involving carbon. This is the first time that comments on hydrogen retention have been able to be made on this system.

Table 5.1 summarises the C : H ratios for all the Ni reforming reactions examined in this study. It also recaps the microreactor TPO values for the same systems. First to note is that in all reactions, the amount of carbon formed is always greater than that of hydrogen. This shows that reactions that reactions involving hydrogen are much faster than those involving either oxidation or polymerisation to carbon.

The ratio also highlights the marked difference between the amorphous and graphitic cokes in terms of the amount of retained hydrogen to that of carbon. Graphitic C : H values are very much higher than amorphous systems. This is

not that surprising when one considers that large graphitic domains will have very few termination points available for hydrogen binding. Conversely, amorphous carbon is much less well structured and there will be many opportunities for hydrogen to terminate the coke.

The extremely low C : H ratio calculated in the amorphous steam reforming system is perhaps misleading. In this instance, the microreactor TPO data has been compared with the INS hydrogen data, unlike the other systems that compared the INS with the post INS TPO. A degree of care has to be taken then when discussing this ratio with the others. As this reaction was also performed with excess oxidant, the values for both carbon and hydrogen are probably underestimated as the excess steam will have cleaned off a portion of the overlayer compared to the other studies that were performed at stoichiometric ratios.

The microreactor TPO measurements have been included to highlight that although C : H ratios differ between systems, carbon laydown occurs regardless of the oxidant type, or the catalyst sample preparation. This suggests that although CO₂ is perhaps a less efficient oxidant than the steam variant, carbon formation cannot be avoided and so it may be more beneficial to utilise an environmentally undesirable oxidant (CO₂) that does not require as much energy to generate as H₂O in steam form. It can be concluded therefore that the CO₂ “dry” reforming of methane may have an important role to play in future environmental chemistry.

References

- [1] Bp statistical review of world energy, www.bp.com/reportsandpublications, 2011. [1](#)
- [2] Jens Rostrup-Nielsen and Lars J. Christiansen. *Concepts in Syngas Manufacture: Catalytic Science Series, Vol 10*. Imperial College Press, 2011. [1](#), [5](#), [7](#), [92](#), [118](#), [172](#), [178](#)
- [3] R. Zennaro C. Perego, R. Bortolo. *Catalysis Today*, 142:9, 2009. [1](#)
- [4] M. L. H. Green J. B. Claridge A. P. E. York, T. Xiao. *Catal. Rev: Sci. Eng.*, 49:511, 2007. [1](#), [5](#)
- [5] J. R. Rostrup-Nielsen. *Catalysis Science and Technology Vol 5*. Springer-Verlag, 1984. [2](#), [3](#), [6](#), [92](#), [118](#), [172](#)
- [6] H. Tropsch F. Fischer. *Brennst. Chem*, 4:276, 1923. [2](#)
- [7] A.J. Silvestri J.J. Wise. Mobil process for the conversion of methanol to gasoline. *University of Pittsburgh, Annual International Conference on Coal Gasification and Liquefaction, 3rd*, page 15, August 1976. [2](#)
- [8] Y. Zhang W. Ding S. Chen W. Fang Y. Yang Wang, L. Yang. *Fuel Process. Technol.*, 91:723, 2010. [2](#)
- [9] M. E. Dry. *Catalysis Today*, 71:227, 2002. [2](#)
- [10] J.M. Parera R. Frety F. Lefebvre F. C.L. Pieck, E.L. Jablonski. *Industrial and Engineering Chemistry Research*, 31:1017–1021, 1992. [2](#)

REFERENCES

- [11] C. H. Bartholomew J. Xu. *Journal of Physical Chemistry B*, 109:2392–2403, 2005. [2](#)
- [12] H. Xu W. Li Y. Cui, H. Zhang. *Applied Catalysis A: General*, 318:79–88, 2007. [2](#), [5](#)
- [13] G. F. Froment. *Journal of Molecular Catalysis A: Chemical*, 163:147–156, 2000. [2](#), [5](#), [46](#), [55](#), [90](#), [129](#)
- [14] J. Weitkamp G. Ertl, H. Knozinger, editor. *Handbook of Heterogeneous Catalysis - Vol 4, Ch3*. Wiley-VCH, 1997. [5](#), [131](#)
- [15] Y. Wang, Y. Chin, R. Rozmiarek, B. Johnson, Y. Gao, J. Watson, A. Tonkovich, and D. Vanderwiel. *Catalysis Today*, 98(4):575–581, December 2004. [5](#)
- [16] A.J. Brungs C. Marquez-Alvarez J. Sloan S.C Tsang M.L.H. Green J.B. Claridge, A.P.E York. *Journal of Catalysis*, 180:85, 1998. [5](#)
- [17] S. Rokni J.R. Rostrup-Nielsen J. Sehested, C.J.H Jacobsen. *Journal of Catalysis*, 201:206, 2001. [5](#)
- [18] JLG Fierro J. Santamaria JC Rodriguez, E. Romeo and A. Monzon. *Catalysis Today*, 37:255, 1997. [6](#)
- [19] D. Lennon S.D. Jackson, J. Hargreaves, editor. *Catalysis in Application p16*. RSC Publishing, 2003. [6](#)
- [20] C.H. Bartholomew R.J. Farrauto, editor. *Fundamentals of Industrial Catalytic Processes*. Blackie, 1997. [6](#), [30](#)
- [21] C.H. Bartholomew. *Applied Catalysis A*, 212:17–60, 2001. [6](#), [7](#), [89](#)
- [22] C.H. Bartholomew. *Catalysis Reviews, Science and Engineering*, 24:67–112, 1982. [6](#), [89](#)
- [23] L. Kepinski. *Carbon*, 38:1845, 2000. [6](#)

REFERENCES

- [24] F. Besenbacher, I. Chorkendorff, B. S. Clausen, B. Hammer, A. M. Molenbroek, J. K. Nørskov, and I. Stensgaard. *Science*, 279:1913–1915, 1998. [6](#), [8](#), [9](#), [131](#)
- [25] N. V. Parizotto, K. O. Rocha, S. Damyanova, F. B. Passos, D. Zanchet, C. M. P. Marques, and J. M. C. Bueno. *Appl. Cat. A*, 330:12–22, 2007. [6](#)
- [26] J. Schwank L. Suljo N. Eranda, H. Adam. *Journal of the American Chemical Society*, 128:11354–11355, 2006. [6](#)
- [27] B.J.H Hansen J.R., Rostrup-Nielsen. *Journal of Catalysis*, 144:38–49, 1993. [6](#), [7](#)
- [28] Y. Yifeng W. Min-H. Fei L. Xiancai, L. Shuigen. *Catalysis Letters*, 118:59–63, 2007. [7](#), [90](#)
- [29] A.M. Vannice M.C.J. Bradford. *Catalysis Today*, 50:87–96, 1999. [7](#)
- [30] X. Zheng T. Yashima P. Chen, Z. Hou. *React. Kinet. Catal. Lett.*, 86:51–58, 2005. [7](#)
- [31] A.M. Vannice M.C.J. Bradford. *Applied Catalysis A*, 142:73–96, 1996. [7](#)
- [32] J. Ren Y-G. Chen. *Catalysis Letters*, 29:39–48, 1994. 10.1007/BF00814250. [7](#), [92](#)
- [33] B. Bower A.M. Gadalla. *Chemical Engineering Science*, 43:3049–3062, 1988. [7](#)
- [34] X. Zheng J. Guo, H. Lou. *Carbon*, 45:1314–1321, 2007. [7](#)
- [35] Juliana D.O. Borio M.N. Pedernera, J. Piña. *Chem. Eng. J.*, 134, 2007. [7](#)
- [36] D. L. Trimm. *Catalysis Today*, 37:233–238, 1997. [7](#), [9](#), [92](#)
- [37] C. A. Querini and S. C. Fung. *Catalysis Today*, 37:277–283, 1997. [7](#), [55](#)
- [38] D. McKee. *Carbon*, 8:623, 1970. [7](#), [65](#), [160](#)

REFERENCES

- [39] J. Bilbao A.G. Gayubo-P. Castano M. Ibanez, B. Valle. *Catalysis Today*, <http://dx.doi.org/10.1016/j.cattod.2012.04.030>, 2012. [8](#)
- [40] J.W. Niemantsverdriet, editor. *Spectroscopy in Catalysis, An Introduction. 3rd Ed.* Wiley-VCH, 2007. [8](#), [10](#), [16](#), [17](#), [18](#), [88](#)
- [41] P.C. Stair Y.T. Chua. *Journal of Catalysis*, 213:39, 2003. [8](#)
- [42] J. Datka, Z. Sarbak, and R. P. Eischens. Infrared study of coke on alumina and zeolite. *Journal of Catalysis*, 145:544–550, 1994. [8](#)
- [43] J.E. Lester D.G. Blackmond, J.G. Goodwin. *Journal of Catalysis*, 78:34–43, 1982. [8](#)
- [44] P. C. H. Mitchell, S. F. Parker, A. J. Ramirez-Cuesta, and J. Tomkinson. *Vibrational spectroscopy with neutrons*. Series on Neutron Techniques and Applications. [8](#), [19](#), [21](#), [38](#), [46](#), [52](#)
- [45] J. Tomkinson P. Mitchell. *Catalysis Today*, 9(1-2):227–235, March 1991. [8](#), [19](#)
- [46] J. Sehested B.S. Clausen L.P. Nielsen A.M. Molenbroek J. Rostrup-Nielsen H. S. Bengaard, J.K. Nørskov. *Journal of Catalysis*, 209:365–384, 2002. [8](#), [129](#)
- [47] B.S. Clausen A.M. Molenbroek, J.K. Nørskov. *Journal of Physical Chemistry B*, 105:5450–5458, 2001. [8](#), [9](#), [88](#)
- [48] H-S. Roh Y. Wang S.M. Heald Y-H. Chin, D.L. King. *J. Catal*, 224:153, 2006. [8](#)
- [49] J. Rostrup-Nielsen. *Journal of Catalysis*, 85(1):31–43, January 1984. [9](#)
- [50] G. Zhu. *Huagong Shikan*, 23:17, 2009. [9](#)
- [51] S.G. Neophytides N.C. Triantafyllopoulos. *Journal of Catalysis*, 239:187–199, 2006. [9](#)

REFERENCES

- [52] O. Geszti-I. Saj Z. Pszti A. Tompos Z. Schay L. Guzci, G. Stefler. *Appl. Catal.*, 375:236, 2010. [9](#)
- [53] J. de Haseth P. Griffiths, editor. *Fourier Transform Infrared Spectrometry 2nd Ed.* Wiley, 2007. [10](#), [11](#), [12](#), [13](#), [14](#), [15](#), [16](#)
- [54] V.I. Lygin A.V. Kiselev, editor. *Infrared Spectroscopy of Adsorbed Species.* Academic Press - New York, 1966. [10](#)
- [55] W.A. Pliskin R.P. Eischens. *Adv. Catal.*, 10:1, 1958. [10](#)
- [56] P. Felgett. *Aspen Int Conf on Fourier Spec.*, 1970. [11](#)
- [57] J. M. Stencel, editor. *Raman Spectroscopy for Catalysis.* Van Nostrand Reinhold, New York, 1990. [16](#), [18](#)
- [58] Jack Loader, editor. *Basic Laser Raman Spectroscopy.* Heyden-Sadtler, 1970. [18](#)
- [59] A.A. Demidov D.L. Andrews, editor. *An Introduction to Laser Spectroscopy.* Plenum Press, New York, 1995. [18](#)
- [60] P.W. Albers S.F. Parker, D. Lennon. *Applied Spectroscopy*, 65,12:1325, 2011. [19](#), [21](#), [38](#), [49](#), [71](#), [109](#)
- [61] P. A. Lindgard K.N. Clausen M.F. Hansen F. Bodker S. Morup-M. Telling S.N. Klausen, K. Lefmann. *Journal of Magnetism and Magnetic Materials*, 266:68, 2003. [19](#)
- [62] F. Cilloco R.J. Newport S.F. Parker R. Albertini V. Rossi F. Sacchetti J. Tomkinson M. Zoppi D. Colognesi, M. Celli. *Applied Physics A*, 74:S64–S66, 2002. [20](#), [21](#), [46](#)
- [63] Sacchetti F. Rossi-Albertini V. Ricci F.P. Parker S.F. Newport R.J. Colognesi D. Cilloco F. Checchi C. Celli M. Zoppi M., Tomkinson J. [20](#), [21](#)
- [64] <http://www/isis.ral.ac.uk/excitations/maps/maps.htm>. Website, 2006. [21](#)

REFERENCES

- [65] S.F Parker, C.J Carlile, T Pike, J Tomkinson, R.J Newport, C Andreani, F.P Ricci, F Sacchetti, and M Zoppi. *Physica B: Condensed Matter*, 241(0):154 – 156, 1997. [Proceedings of the International Conference on Neutron Scattering](#). [21](#)
- [66] G. Prescher K. Seibold S.F. Parker P. Albers, H. Angert. *Chemical Communications*, (17):1619 – 1620, 1999. [21](#)
- [67] S.F. Parker P. Albers, J. Pietsch. *Journal of Molecular Catalysis A*, 173:275–286, 2001. [21](#)
- [68] D.K. Ross R.G. Heidenreich K. Kohler S.F. Parker P.W. Albers, J.G. Krauter. *Langmuir*, 20(19):8254–8260, September 2004. [21](#)
- [69] A. Mcinroy, D. Lundie, J. Winfield, C. Dudman, P. Jones, S. Parker, and D. Lennon. The interaction of alumina with hcl: An infrared spectroscopy, temperature-programmed desorption and inelastic neutron scattering study. *Catalysis Today*, 114(4):403–411, May 2006. [21](#), [38](#), [51](#), [52](#), [165](#)
- [70] R. Osborn P.D. McK A.T. Boothroyd G. Aeppli T.G. Perring, A.D. Taylor. *Proceedings. ICANS XII, p I-60, RAL Report 94-025*, 1994. [21](#)
- [71] J.R. Treadgold R.L.S. Coleman D.W.J. Bellenger N.J. Rhodes K.A. McEwan S.M. Hayden M.T. Dove R.I. Bewley, R.S. Eccleston. *16th Meeting of the International Collaboration on Advanced Neutron Sources*, 2003. [22](#)
- [72] T. Guidi R.I. Bewley and S. Bennington. *Notiziario Neutroni e Luce di Sincrotrone*, 14:22. [22](#)
- [73] K.A. McEwen S.M. Hayden M.T. Dove S.M. Bennington J.R. Treadgold R.L.S. Coleman R.I. Bewley, R.S. Eccleston. *Physica B*, 385:10291031, 2006. [22](#)
- [74] L.L. Daemen J. Eckert W.D. Goodman S. Chinta, T.V. Choudhary. *Angewandte Chemie International Edition*, 41(1):144–146, 2002. [34](#), [36](#)
- [75] L.L. Daemen J. Eckert W.D. Goodman S. Chinta, T.V. Choudhary. *Journal of the American Chemical Society*, 126(1):38–39, January 2004. [34](#), [36](#)

REFERENCES

- [76] I.H. McColl C.D. Syme L. Hecht K. Nielsen L.D. Barron, E.W. Blanch. *Spectroscopy*, 17:101, 2003. [37](#)
- [77] R.A. Mosher J.J.M. O'Reilly. *Carbon*, 21:47–51, 1983. [38](#)
- [78] P. Concepcion A. Corma H. Garcia R Juarez, S.F. Parker. *Chemical Science*, 1:731, 2010. [38](#)
- [79] J. M. Nicol. *Spectrochimica Acta*, 48A:313, 1992. [38](#), [46](#)
- [80] J. Dreyer W. I. F. David J. F. C. Turner, R. Done and C. R. A. Catlow. *Rev. Sci. Instrum*, 70:2325, 1999. [38](#)
- [81] T. H. Free C. J. Benmore K. W. Herwig . F. C. Turner, S. E. McLain and J. E. Siewenie. *Rev. Sci. Instrum*, 74:4410, 2003. [38](#)
- [82] I. F. Bailey. A review of sample environments in neutron scattering. *Zeitschrift fr Kristallographie*, 218(2/2003):84–95, February 2003. [46](#)
- [83] J.M. Winfield C.C. Dudman P. Jones S.F. Parker J.W. Taylor D. Lennon A. R. Mcinroy, D.T. Lundie. *Physical Chemistry Chemical Physics*, 7:3093–3101, 2005. [48](#), [51](#), [52](#), [53](#), [165](#)
- [84] D. Lennon J. Tomkinson, S.F. Parker. *J.Chem.Phys*, 133:034508, 2010. [51](#)
- [85] A. T. Todorovskii and Plotkin. Prediction of the ir spectra of polystyrene and its deuterated analogs. *Journal of Applied Spectroscopy*, 51(4):1050–1055, October 1989. [58](#)
- [86] I. Udrea, M. Udrea, and L. Frunza. Methane synthesis from CO/H₂O mixture on supported nickel catalysts, III. Formation of of surface carbon and its role in the reaction mechanism. *Reaction Kinetics and Catalysis Letters*, 21(3):265–268, 1982. [59](#)
- [87] C.H. Bartholomew. *Catal. Rev: Sci. Eng.*, 24:67, 1982. [65](#), [163](#), [181](#)
- [88] J.Z. Staniforth C.J. Laycock S.F. Parker R.M. Ormerod D. Lennon I.P. Silverwood, N.G. Hamilton. *Catalysis Today*, 155:319, 2010. [70](#), [71](#)

REFERENCES

- [89] M.J. Illan-Gomez J. Juan-Juan, M.C. Roman-Martinez. *Appl. Cat. A*, page 355, 2009. [71](#), [92](#)
- [90] C.J. Liu X. Zhu, Y.P. Zhang. *Catal. Lett.*, 118:306–312, 2007. [71](#), [89](#)
- [91] B. Xu J. Shen-J. Ma C. Joll A. Heitz F. Qi, Z. Chen. *App. Cat. B: Gen.*, 84:684, 2008. [73](#), [111](#)
- [92] C.C. Dudman P. Jones-D. Lennon J.M. Winfield I.W. Sutherland, N.G. Hamilton. *App. Cat. A: Gen.*, 339:1, 2011. [74](#)
- [93] R. Stevens J.Y.Y Li-B. Fultz M. Kresch, O. Delaire. *Phys. Rev. B.*, 75:104301, 2007. [74](#)
- [94] M. A. Pimenta, G. Dresselhaus, M. S. Dresselhaus, and L. G. Cançado. *Physical Chemistry Chemical Physics*, 9:1276–1291, 2007. [80](#), [122](#), [171](#)
- [95] G. Dresselhaus P. Kwizera, M.S. Dresselhaus. *Carbon*, 21,2:121, 1983. [80](#), [120](#), [122](#), [172](#)
- [96] J.L. Koenig F. Tuinstra. *J. Chem. Phys*, 53:1126, 1970. [80](#), [122](#), [171](#)
- [97] P. Jagodzinski L. Nikiel. *Carbon*, 31:1313, 1993. [80](#)
- [98] T. Enoki M. Endo-Y.A. Kim H. Mizusaki A. Jorio L.N. Coelho R. Magalhes-Paniago M.A. Pimenta L.G. Cancado, K. Takai. *Appl. Phys. Lett*, 88:163106, 2006. [80](#)
- [99] K.J. Schmidt A. Savage-R.H. Hall J.T. Bulmer G.R. Loppnow, L. Shoute. *Phil. Trans. R. Soc. Lond. A*, 362:2461–2476, 2004. [82](#)
- [100] V. Batori H. Ehrhardt-S.R.P. Silva J. Schwan, S. Ulrich. *J. App. Phys.*, 80:440, 1996. [82](#)
- [101] E.P.J. Parrott J.A. Zeitler-K.L. Nguyen J.M. Rawson A. Carley T.W. Hansen J-P. Tessonnier D.S. Su D.Teschner E.M. Vass A.Knop-Gericke R. Schlgl L.F. Gladden J. McGregor, Z. Huang. *J.Catal*, 269:329, 2010. [82](#)

REFERENCES

- [102] J. Laureyns A.A. Martínez-J.M.D. Tascón A. Cuesta, P. Dhamelincourt. *Carbon*, 32(8):1523–1532, 1994. [82](#)
- [103] D. Su R. Schlögl-R. Niessner N.P. Ivleva M. Knauer, M.E. Schuster. *J. Phys. Chem. A*, 113:13871, 2009. [82](#)
- [104] P.C. Stair Y.T. Chua. *J. Catal*, 213:39, 2003. [82](#), [120](#), [172](#)
- [105] E. Gallei D. Eisenbach. *Journal of Catalysis*, 56:377–389, 1979. [84](#)
- [106] K. Ito J. Jia-H. Morioka T. Shishido K. Takehira P. Wang, E. Tanabe. *Applied Catalysis A*, 231:35–44, 2002. [89](#)
- [107] A. Tomita H. Aso, K. Matsuoka. *Energy & Fuels*, 17(5):1244–1250, September 2003. [89](#)
- [108] H. Grothe R. Niessner-U. Pöschl A. Sadezky, H. Muckenhuber. *Carbon*, 43:1731, 2005. [89](#), [90](#)
- [109] H. Xu W. Li Y. Cui, H. Zhang. *Applied Catalysis A*, 318:79–88, 2007. [90](#)
- [110] A.M. Vannice M.C.J. Bradford. *Applied Catalysis A*, 142:97–122, 1996. [90](#)
- [111] E. Iglesia J. Wei. *Journal of Catalysis*, 224:370–383, 2004. [90](#)
- [112] Y. Chen K. Yokoyama-X. Li K. Fujimoto K. Tomishige, O. Yamazaki. *Catalysis Today*, 45:35–39, 1998. [90](#)
- [113] K-D. Jung O-S. Joo. *Bull. Korean. Chem. Soc.*, 23 , 8:1149, 2002. [92](#), [118](#)
- [114] J. Sehested P. L. Hansen B. S. Clausen J. R. Rostrup-Nielsen-F. Abild-Pedersen J. K. Norskov. S. Helveg, C. Lopez-Cartes. *Nature*, 427:246, 4272004. [92](#), [118](#), [172](#)
- [115] J. R.; Grant B. Baird, T.; Fryer. *Carbon*, 12:591, 1974. [92](#)
- [116] J. R.; Grant B. Baird, T.; Fryer. *Nature*, 233:329, 1971. [92](#)
- [117] M. G.; Rodda E. J. Tibbetts, G. G.; Devour. *Carbon*, 25:367, 1987. [92](#)

REFERENCES

- [118] Z. Hong C. Dingfeng Z. Xiaoming J. Guo, L. Hui. *Applied Catalysis A: General*, 273(12):75 – 82, 2004. [92](#)
- [119] X. Verykios. *Appl. Cat. A.*, 255:101, 2003. [93](#), [103](#)
- [120] P. Ferreira-Aparicio I. Rodreguez-Ramos A. Guerrero-Ruiz Y. Schuurman, C. Mirodatos. *Catalysis Letters*, 66:33–37, 2000. 10.1023/A:1019022917507. [93](#), [125](#)
- [121] P. Ferreira-Aparicio C. Mirodatos Y. Schuurman, V.C.H. Kroll. *Catalysis Today*, 38(1):129 – 135, 1997. [93](#)
- [122] Y. Schuurman and C. Mirodatos. *Applied Catalysis A: General*, 151(1):305 – 331, 1997. [Transient Kinetics](#). [93](#), [125](#), [127](#)
- [123] C. Guimon-R. Bilbao R. Martinez, E. Romero. *App. Cat. A: Gen*, 274:139, 2004. [98](#), [118](#), [172](#)
- [124] J. Wang H. Li. *Chemical Engineering Science*, 59:4861, 2004. [98](#)
- [125] S.C. Dhingra A. Nandini, K.K. Pant. *Applied Catalysis A: General*, 290(12):166 – 174, 2005. [98](#)
- [126] M.G. White Q. Yan, H. Toghiani. *J. Phys. Chem. C*, 111:18646–18662, 2007. [103](#)
- [127] J. Krauter S.F. Parker P. W. Albers, J. Pietsch. *Physical Chemistry Chemical Physics*, 5:1941–1949, 2003. [111](#), [165](#), [168](#)
- [128] J.R. Philips R.M. Ibberson S.F. Parker D. Lennon, J. McNamara. *Physical Chemistry Chemical Physics*, 2:4447–4451, 2000. [111](#), [168](#)
- [129] R.J. Newport J.K. Walters. *Journal of Physics: Condensed Matter*, 7:1755–1769, 1995. [111](#), [168](#)
- [130] S.F. Parker W.S. Howells J.K. Walters, R.J. Newport. *J. Phys. Condens. Matter*, 7:10059–10073, 1995. [111](#), [165](#)

REFERENCES

- [131] G. Prescher K. Seibold D.K. Ross S.F. Parker P. Albers, S. Bösing. *Applied Catalysis A: General*, 187:233–243, 1999. [111](#), [165](#), [168](#)
- [132] P. J. R. Honeybone, R. J. Newport, and J. K. Walters. *Physical Review B*, 50:839–845, 1994. [111](#), [168](#)
- [133] K. Siebold D.K. Ross F. Fillaux P. Albers, G. Prescher. *Carbon*, 34:903–908, 1996. [111](#), [168](#)
- [134] E. Paimozed M. Asghari, A. Ghasemi. *Current Nanoscience*, 8(2):239–243, 2012. [114](#)
- [135] F.B. Passos D.C.R.M. Santos, L. Madeira. *Catalysis Today*, 149:401, 2010. [120](#)
- [136] P.R.J. Silva H. Saitovitch F.B. Passos J.S. Lisboa, L.E. Terra. *Fuel Process. Technol.*, 92:2075, 2011. [120](#)
- [137] J.T. Nicholls J.S. Speck M.S. Dresselhaus G.L. Doll, R.M. Sakya. *Synthetic Materials*, 23:481, 1988. [122](#)
- [138] R. A. Shatwell P. Xiao E. Lopez-Honorato, P. J. Meadows. *Carbon*, 48:881, 2010. [122](#), [171](#)
- [139] J.A. Anderson A. Guerrero-Ruiz P. Ferreira-Aparicio, I. Rodriguez-Ramos. *Applied Catalysis A: General*, 202:183–196, 2000. [129](#)